NOTICE

The quality of this microform is heavily dependent upon the quality of the original thesis submitted for microfilming. Every effort has been made to ensure the highest quality of reproduction possible.

If pages are missing, contact the university which granted the degree.

Some pages may have indistinct print especially if the original pages were typed with a poor typewriter ribbon or if the university sent us an inferior photocopy.

Reproduction in full or in part of this microform is governed by the Canadian Copyright Act, R.S.C. 1970, c. C-30, and subsequent amendments.

AVIS

La qualité de cette microforme dépend grandement de la qualité de la thèse soumise au microfilmage. Nous avons tout fait pour assurer une qualité supérieure de reproduction.

S'il manque des pages, veuillez communiquer avec l'université qui a conféré le grade.

La qualité d'impression de certaines pages peut laisser à désirer, surtout si les pages originales ont été dactylographiées à l'aide d'un ruban usé ou si l'université nous a fait parvenir une photocopie de qualité inférieure.

La reproduction, même partielle, de cette microforme est soumise à la Loi canadienne sur le droit d'auteur, SRC 1970, c. C-30, et ses amendements subséquents.

Canada

THE OXYGEN ISOTOPE EFFECT IN Pr, Ca, AND Zn SUBSTITUTED $YBa_2Cu_3O_{7-d}$

by

Georg Johannes Soerensen

B.Sc., University of Waterloo, 1986

A THESIS SUBMITTED IN PARTIAL FULFILLMENT OF

THE REQUIREMENTS FOR THE DEGREE OF

DOCTOR OF PHILOSOPHY

in the Department

of

PHYSICS

SIMON FRASER UNIVERSITY

June 1993

APPROVAL

Name:	Georg Johannes Soerensen
Degree:	Doctor of Philosophy
Title of Thesis:	The Oxygen Isotope Effect in Pr, Ca, and Zn substituted $YBa_2Cu_3O_{7-\delta}$.

Examining Committee:

Chairman: Dr. Michael Thewalt

Dr. Suso Gygax
Professor
Senior Supervisor

Dr. Daryl Crozier
Professor

Dr. Chuck Irwin
Professor
Internal Examiner

Dr. Albert Curzon
Professor

Dr. John Harrison
Professor, Dept. of Physics
Queens University, Kingston
External Examiner

Dr. Michael Plischke
Professor

PARTIAL COPYRIGHT LICENSE

I hereby grant to Simon Fraser University the right to lend my thesis, project or extended essay (the title of which is shown below) to users of the Simon Fraser University Library, and to make partial or single copies only for such users or in response to a request from the library of any other university, or other educational institution, on its own behalf or for one of its users. I further agree that permission for multiple copying of this work for scholarly purposes may be granted by me or the Dean of Graduate Studies. It is understood that copying or publication of this work for financial gain shall not be allowed without my written permission.

Title of Thesis/Project/Extended Essay

The Oxygen Isotope Effect in Pr, Ca, and Zn Substituted $YBa_2Cu_3O_{7-\delta}$

Author: _____
(signature)

GEORG SORENSEN
(name)

Aug 20 / 1993
(date)

ABSTRACT

The oxygen isotope effect in *Pr*, *Ca*, and *Zn* doped superconducting $YBa_2Cu_3O_{7-\delta}$ was investigated. *Pr* and *Ca* substitute predominantly at the *Y* site while *Zn* goes into the *Cu* plane site. The shift in critical temperature (ΔT_c) between samples oxygenated in ^{18}O and ^{16}O was obtained via dc resistance measurements, and low field dc magnetization and ac susceptibility measurements in a SQUID magnetometer. Confirmation of the substitution of the oxygen was achieved with Raman and SIMS measurements.

The *Pr*, *Ca*, and *Zn* substitutions change T_c of the superconductor in different ways. Increasing *Pr* concentration lowers T_c and increases ΔT_c with the isotope coefficient, α, approaching $^1/_2$. The addition of *Ca* reduces the size of both ΔT_c and α. Both exhibit a small parabolic effect with increasing *Ca* substitution. An increase in *Zn* substitution lowers T_c but ΔT_c remains nearly constant, or perhaps gets slightly smaller, with α increasing to approximately $^1/_3$.

We find that there is a linear relationship between the width of the normal to superconducting transition and the size of ΔT_c. We believe that this dependency may be related to the sample quality.

There does not appear to be a universal correlation between T_c and α, however, both are dependent on the number of mobile holes and our values do follow closely a universal relationship that has been proposed between these two quantities.

We find that a modification to the BCS theory, involving a logarithmic Van Hove singularity in the density of states, does qualitatively fit the general trend of our data. More success is achieved with the use of Eliashberg type calculations

in which the change in α and T_c can be made to resemble our data provided we use a pair-breaking mechanism as well as a modification of the Coulomb pseudopotential which includes an attractive electronic pairing interaction. Both models predict α to be a minimum at the maximum T_c, and as T_c decreases, α increases. Also common to both is the apparent dependence of both T_c and α on the mobile hole concentration.

This work shows that an isotope effect does exist in the high temperature superconductors and that large values of α comparable to those found in conventional superconductors exist. It is also evident from our results that the mobile hole concentration must play an important role in the mechanism for superconductivity in these materials.

DEDICATION

To my parents, Carl and Gerta, my brothers Karl, Roger and Chris and my sister Mayken for their love, and support throughout my academic career, and

For My Lady

ACKNOWLEDGMENTS

I would like to acknowledge the support of my senior supervisor, Dr. Suso Gygax, for his guidance in writing this thesis and for allowing me the freedom to do things the way I thought they should be done.

I would like to thank Dr. Richard Akis for both providing the computer program from which the Eliashberg equations were solved and for answering my many question involving this model.

Gerry Rynders and Les Wakida in the Glass Shop; Ken Stowe, Roger Turner, Dick Van Der Wal, and James Shoults of the Machine Shop, and Mike Billany were invaluable in providing technical assistance.

I would like to thank Ernesto Altshuler, University of Havana, for his friendship and help in measuring a number of the Zn substituted samples on his stay at S.F.U.

I would also like to thank Nancy Bean for proof reading this thesis for me.

TABLE OF CONTENTS

LIST OF TABLES

LIST OF FIGURES

1.0 INTRODUCTION

Superconductivity has its roots at the beginning of this century when in 1911, Kamerlingh Onnes[1], while investigating the low temperature electrical properties of mercury, witnessed an abrupt drop in the resistance to below any measurable value at $4.2K$. In the years that followed, numerous other superconductors and a set of unique properties were found. These properties distinguished the superconductors from being other than "perfect" conductors. The Meissner effect[2], Josephson tunneling[3] and other properties established that superconductivity is not a classical result. Only quantum mechanics could explain these phenomena. One of the effects discovered was that the critical temperature of mercury was altered by an isotopic substitution[4,5]. This provided strong support that a mechanism involving an electron-phonon interaction was responsible for superconductivity. This, along with Cooper's discovery that a state of lower energy (pairing of electrons - Cooper pairs) results from an attractive interaction between two electrons near the Fermi surface, gave rise to the Bardeen-Cooper-Schrieffer (BCS) theory of superconductivity[6]. The majority of the superconductors discovered were metals (poor conductors) or inter-metallic compounds, but a number were also "oxides", one of which, $SrTiO_3$ ($T_c = 0.3K$)[7], has the pervoskite crystal structure, a variation of which is found in the high temperature superconductors. Prior to the high temperature superconductors, Nb_3Ge ($T_c = 23.2K$)[8] had the highest critical temperature (T_c is defined as the temperature at which the transition between the superconducting state and normal states occur). The BCS theory was quite successful in explaining the characteristics of superconductors, but failed in providing the correct quantitative results for a number of these materials. The extent of the disagreement between BCS and the observed characteristic(s) is different from

material to material. These differences can be largely attributed to the fact that the BCS theory is oversimplified. Corrections[9-11] to the BCS theory involving other theoretical methods, such as the Eliashberg[12] theory, followed BCS and have been very successful in providing accurate quantitative results. BCS methods are still used quite often as they are simple and are thus able to provide insight into the physics involved in the system. Eliashberg equations on the other hand, are based on solving many body Green's functions, and as this must be done numerically, no analytic form exists and so the basic insight into the physics of what is occurring is lost.

Seventy five years after the initial discovery of superconductivity, a new class of superconductors was discovered. In 1986, J.G. Bednorz and K.A. Müller reported evidence for superconductivity in a *La-Ba-Cu-O* material[13]. This was confirmed and a number of other superconducting oxides came into existence in a very short time. The maximum critical temperature climbed from the previous high of 23.2*K* to 35*K* in $La_{1.85}Ba_{0.15}CuO_4$[14,15], then to 38*K* in $La_{1.8}Sr_{0.2}CuO_4$[16]. With the discovery of $YBa_2Cu_3O_{7-\delta}$ with $T_c = 93K$[17], superconductivity moved out of the range of low temperature physics in that a liquid He dewar was no longer required in order to achieve the necessary temperatures. The next year brought about two more systems, *Bi-Sr-Ca-Cu-O*, $T_c = 110K$[18] and the *Tl-Ba-Ca-Cu-O* system, $T_c = 125K$[19]. The highest T_c to date is the $130K$[20] phase in the *Hg-Ba-Ca-Cu-O* system.

Since the discovery of high T_c superconductors, there have been tens of thousands of papers presented in journals and at conferences concerning the properties of these materials. There have been numerous conflicting results and unsubstantiated claims, primarily due to the difficulty associated with synthesizing these materials. It is therefore important to follow a well defined

method of synthesis, ensure careful measurements are carried out, and to confirm that the results are reproducible. It is generally believed that these new materials do not follow in the same theoretical framework of the conventional BCS theory. However, current evidence does support the pairing of charge carriers as in the BCS case, although in high temperature superconductors, the charge carriers are in most cases holes as opposed to electrons as found in the conventional superconductors.

The high temperature superconductors must be classified as extreme type-II superconductors since they have large penetration depths (λ_L - length scale over which the magnetic field can penetrate into the superconductor - the region in which shielding currents can flow), and a short coherence length (ξ - typical length over which the Cooper pairs are coherent - the length scale of the order parameter in the Ginzburg-Landau theory). This allows for the formation of quantized magnetic vortices (fluxoids) when the materials are exposed to a magnetic field.

In conventional superconductors governed by the BCS theory, one finds that the critical temperature varies by $T_C \propto M^{-\alpha}$, where M is the mass of the element that is isotopically substituted This will be shown in chapter 4. For materials consisting of more than one element, each can be isotopically substituted. The partial isotope exponent, α_i, for elemental mass M_i, can then be defined by

$$\alpha_i = -\frac{\partial \log T_c}{\partial \log M_i} \quad . \qquad [1.1]$$

The α_i are positive and the net isotope coefficient, α, is just the sum of the α_i. A large number of materials exhibit values of $\alpha = 1/2$, consistent with the weak-

coupling limit in the BCS theory. BCS theory also allows for values that deviate from the simple result of $\alpha = 1/2$ by incorporating more sophisticated information regarding phonon modes and electron-phonon interactions[21], and thus a value of $\alpha = 0$ does not indicate a failure in the theory's reliance on the interaction mechanism between electrons and phonons. The converse however, is not true. If superconductivity were due to a mechanism that did not involve an electron-phonon pair coupling then $\alpha = 0$. The existence of an isotope effect in high T_c materials may then prove essential in determining the mechanism for superconductivity.

Ideally, one should be able to make an isotope substitution for any of the constituents of the high temperature superconductor $YBa_2Cu_3O_{7-\delta}$. The effects of the substitutions ^{135}Ba for ^{138}Ba[22], ^{134}Ba for ^{138}Ba[23], and ^{63}Cu for ^{65}Cu[22,24,25] have been measured, but the small shift that is observed ($< 0.2K$) is of the same order of the uncertainty involved in the measurements. Of course, the expected shift in T_c would only be as much as $0.7K$ and $1.4K$ in $YBa_2Cu_3O_{7-\delta}$ ($T_c = 90K$), with the substitutions ^{138}Ba for ^{134}Ba and ^{65}Cu for ^{63}Cu respectively, assuming a coefficient of $\alpha = 1/2$. Thus there is no evidence of a shift in the critical temperature with isotope substitution for these heavy cations. Oxygen, being the lightest element in these superconductors with $\Delta m/m = 12\%$ compared to 2% and 3% for *Ba* and *Cu*, is expected to give the largest shift in T_c. Assuming $\alpha = 1/2$, the substitution of ^{18}O for ^{16}O is expected to give $\Delta T_c = 5.5K$ in $YBa_2Cu_3O_{7-\delta}$.

The largest number of investigations have been performed using the oxygen substitution of ^{18}O for ^{16}O, although some experiments have used ^{17}O. The earliest experiments were performed on the *La-Sr-Cu-O* system[22,26] but found no shift. Later experiments did confirm a downward shift in T_c with this

isotopic substitution. In the *La-Sr\Ca-Cu-O* system[24,27,28], shifts in T_c between $0K$ and $1.3K$ ($\alpha = 0$ to 0.54) are common. The shift measured in the $YBa_2Cu_3O_{7-\delta}$ system, however, is much smaller. Shifts measured in this system[29-32] are typically on the order of $0.4K$ ($\alpha = 0.08$), but shifts as much as $2K$ have been seen. Shifts of $0.3K$ and $0.4K$ have also been reported for the $110K$ and $75K$ phases in the *Bi-Sr-Ca-Cu-O* system[33].

The majority of the systems studied have revolved around the "optimum" T_c that can be achieved. The preparation methods and constituent concentrations have been selected in order to maximize the critical temperature. One of the more striking results was reported by Crawford[34] et al. who found that α was dependent on the concentration of *Sr*, *x*, in the $La_{2-x}Sr_xCuO_4$ system. The *Sr* concentration was varied from 3.8% to 26.3%. The critical temperature appears parabolic with *x* and passes through a maximum of $38K$ at 15% *Sr*. No obvious correlation between α, which varies $0.06 \leq \alpha \leq 0.64$, and T_c was found although high T_c values correspond generally to a low α, and low T_c values correspond to a high α. More recently, the system $YBa_{2-x}La_xCu_3O_{7-\delta}$[35] has been studied. The increasing *La* concentration has the effect of reducing T_c and at the same time increases α. Again, high T_c values correspond to a low α and low T_c values correspond to a high α, but in this case, a strong correlation is reported between α and T_c.

The isotope effect as a function of *Sr* concentration in the *La-Sr-Cu-O* system poses some interesting questions. What is the effect of an elemental substitution on the isotope coefficient? As the substitution affects T_c, is there then a relationship between T_c and α? The purpose of our research is to confirm whether a relationship between the elemental substitution (and hence T_c) and α exists in the high temperature superconductors. This thesis reports on

the work done in the investigation of the oxygen isotope effect in the high T_c superconductor - $YBa_2Cu_3O_{7-\delta}$. The oxygen isotopes used are ^{16}O and ^{18}O. In this system we alter the critical temperature of the superconductor by the substitution of:

1) *Pr* for the *Y* giving $(Y_{1-x}Pr_x)Ba_2Cu_3O_{7-\delta}$ for $0 \leq x \leq 0.5$;

2) *Ca* for the *Y* with a constant *Pr* concentration of 20% giving $(Y_{0.8-y}Pr_{0.2}Ca_y)Ba_2Cu_3O_{7-\delta}$ for $0 \leq y \leq 0.25$; and

3) *Zn* for *Cu* giving $YBa_2(Cu_{1-z}Zn_z)_3O_{7-\delta}$ for $0 \leq z \leq 0.09$.

These substitutions have the general effect of lowering the critical temperature as well as altering the charge carrier concentrations. The critical temperatures are determined from dc resistance as well as dc magnetization and ac susceptibility measurements. Other aspects of this investigation such as the preparation of the samples and some of the characterization were performed by other groups. The samples were prepared by J. Franck's group at the University of Alberta, who also performed some of the measurements (where noted). G.I. Sproule of the National Research Council (NRC) in Ottawa performed SIMS (Secondary Ion Mass Spectroscopy) on the samples to obtain an indication of the completeness of the isotopic substitution. Raman measurements conducted by J.C. Irwin's group at S.F.U. were performed, at various oxygen sites, to confirm the isotopic substitution.

The second chapter provides background information concerning the isotope effect, properties of the $YBa_2Cu_3O_{7-\delta}$ system, and the effects of *Pr*, *Ca*, and *Zn* substitution. Chapter three is concerned with the sample preparation and characterization, and the design and operating principles of the

experimental apparatus used for resistivity and magnetic measurements. Chapter four provides a brief outline of the isotope effect in the BCS theory, and the two models used in comparison with our isotope data. Chapter five reports on the method used for determining the critical temperature and the isotope shift. Chapters six through eight present the results of the magnetization, susceptibility and resistance measurements for the three series of data: *Pr*, *Pr* & *Ca*, and *Zn* substitutions respectively. Chapter nine discusses the results and the possible relationships between these results and the current theoretical calculations. Chapter ten closes with the conclusions.

2.0 BACKGROUND

This chapter deals with the general preparation method and characteristics of the high T_c superconductors that (may) have an effect on critical temperature; the effects of *Pr*, *Ca*, and *Zn* substitution on the $YBa_2Cu_3O_{7-\delta}$ system crystal structure and T_c; an outline of previous measurements performed on high T_c superconductors; and what to look for in the dc resistance and ac susceptibility and dc magnetization measurements.

2.1 CHARACTERISTICS OF HIGH T_C SUPERCONDUCTORS

2.1.1 GENERAL PREPARATION

The samples prepared are polycrystalline pellets as opposed to single crystals. There are two primary reasons for this choice. First, it is difficult to obtain large specimen single crystals. Second, the gaseous exchange of $^{16}O/^{18}O$ requires that the sample be porous enough to allow the oxygen to penetrate into the sample. As we desire as complete an oxygen substitution as possible, it was decided that a bulk ceramic material would be best.

The preparation of bulk polycrystalline samples is via a ceramic processing technique. Oxides and/or carbonates of the metal constituents are thoroughly mixed via ball-milling machines, by hand via mortar and pestal, or through a chemical precipitation route. They then undergo an extensive heat treatment program similar to the following:

calcination:

1) react mixed powder in air at temperatures around 900°*C* for a minimum of 24 hours

2) regrind into powder

repeat steps 1) and 2) several times (usually two or three times)

sintering:

3) press into pellets (hydraulic press at a few *kbar* pressure)

4) heat to around 950°*C* in oxygen for at least several hours

5) slowly cool to room temperature (1 - 2½ °*C/min*)

The above "shake and bake recipe" should not be taken as "the method" of preparation. The preparation of these compounds is far from an exact science and there are many different heat treatments used by practically every different group - with varying times, temperatures and cooling characteristics. Different preparation methods emphasize different characteristics; for example, the heating rate and the thoroughness of mixing have a direct effect on the density of the material and hence the size of the polycrystalline grains[36]. The precise preparation technique used for our samples, designed to maintain a fully oxygenated system, is given in the following chapter. The above recipe is a typical method for obtaining a $YBa_2Cu_3O_{7-\delta}$ superconductor with $T_c > 90K$ and $\delta < 0.1$, and to minimize the amount of impurity phases present. During the calcination process, the precursors react in order to form $YBa_2Cu_3O_y$, and its basic crystal structure. The multiple regrindings are to help reduce the impurity phases that occur: primarily CuO, $BaCuO_2$, and $Y_2Cu_2O_5$. A number of factors

influence the critical temperature and perhaps the most important, the oxygen stoichiometry, is determined during the sintering process.

2.1.2 RESISTANCE PROPERTIES

Electrical resistance is caused by the scattering of electrons. The two main causes of this scattering are from other electrons or from lattice vibrations (phonons). The resistivity of metals varies linearly with temperature until the temperature is about 1/3 the Debye temperature, below which it has a T^2 dependence. Conventional superconductors have metallic-like resistance vs. temperature although they tend to have higher normal state resistivities than good conductors. These high resistivities are attributed to the strong interaction between the electrons and phonons. This interaction is also responsible for the electron pairing mechanism that creates this superconducting state. High temperature superconductors also exhibit a higher normal state resistivity than good metals, but have a linear change in resistivity[37] with temperature in contrast with that found in the conventional superconductors.

Resistance is measured by applying a current (ac or dc) across a sample and measuring the voltage drop. As such, it is only a *1-D* phenomenon as only a single zero-resistance percolation path is required to establish T_c.

The sharpness of the transition is traditionally an indicator of the purity of the sample and the degree of order within the crystal structure. A pure, physically perfect, good single crystal, can have an extremely sharp transition while an impure, imperfect crystal structure will have a broader transition. Polycrystalline samples have broader transitions than single crystals as the inter-grain or coupling between (single crystal) grains is poorer than the intra-grain or

intrinsic properties in the high T_c materials. Resistively, the grains can be in the superconducting state but the link between the grains is weak enough that the current density required to make the measurement is sufficiently large to keep the link in the normal state. Other effects such as the self-field produced by the measuring current, noise, contact potentials and sample geometry, or measuring equipment uncertainties can also affect the measured width of the transition.

2.1.3 MAGNETIC PROPERTIES

Magnetization and ac susceptibility measurements on superconductors detect signals inductively, originating from circulating persistent shielding currents as well as any magnetic properties of the material. The shielding currents flow on the surface of the superconductor and penetrate only a small amount into the superconductor. Thus, these measurements are *2-D* in nature as a current sheath is required to shield the bulk within.

The depth to which the magnetic field penetrates into the material is known as the penetration depth λ_L. The penetration depth is temperature dependent - it is essentially infinite at T_c but becomes finite and shorter as the material cools below T_c. For conventional materials, the penetration depth near the transition temperature is found to fit very closely to:

$$\lambda_L = \frac{\lambda_o}{\sqrt{1-t}} \qquad [2.1]$$

where $t = T/T_c$, and λ_o is of the order of a few hundred angstroms. In high T_c materials, λ_o is much larger but λ_L is believed to behave similarly (near T_c) with temperature. The flow of current within the superconductor is also confined to the surface of the material to a depth of λ_L. As the temperature approaches T_c,

λ_L becomes larger and the fraction of the superconductor which is field free becomes smaller. Thus the magnetic signal decreases, becoming 0 at T_c as the penetration depth becomes infinite.

As in the resistive case, the sharpness of the transition will depend on the purity and the crystallographic order. Again, the polycrystalline nature of the samples may result in two transitions; one from the diamagnetic shielding caused by the coupling between the grains and the other from the intrinsic diamagnetic shielding. The intrinsic transition will have the higher T_c; however, these two transitions may not be separate enough to see them distinctly. The short coherence length, in high temperature superconductors, causes small regions of size ξ to undergo noticeable fluctuations when the superconductor is held near T_c. When the temperature is just above T_c, these regions fluctuate into the superconducting state and when T is just below T_c, the regions fluctuate into the normal state. These fluctuations also occur in conventional superconductors[38] but are normally too small to be observed. The net effect of these fluctuations is to widen the transition from normal to superconducting states[39,40].

Cooling the material (ideally to $T = 0K$) in zero field, applying a dc field, and measuring while warming the superconductor through T_c is known as a ZFC (Zero Field Cooling) curve and demonstrates flux shielding (or flux exclusion). Cooling the superconductor through T_c in the presence of an applied field is known as a FC (Field Cooled) curve and demonstrates the Meissner effect (or flux expulsion). These two curves are the standard dc magnetization curves that are obtained. The ac susceptibility, χ, given by $\chi = \frac{dM}{dH}$, measures the shielding

properties of the superconductor regardless of whether warming or cooling. The temperature response of both the ac susceptibility and the dc magnetization is dependent on the shape of the sample. Demagnetizing factors and return-flux corrections are necessary to account for this shape dependence in the overall magnitude of the signal. However, these factors are difficult to determine for materials with irregular shapes. The samples dealt with in this investigation are basically cylindrical in shape and even though calculations on these demagnetizing factors for cylinders[41] and return-flux corrections[42] (through the pick-up loop) do exist, no attempt will be made to incorporate them as the absolute magnitude of the signal is not a concern and all samples have roughly the same shape.

For more information regarding the magnetic susceptibility of superconductors, the interested reader is referred to an article by R.B. Goldberg et al.[43], "Alternating-Field Susceptometry and Magnetic Susceptibility of Superconductors" and references therein.

2.1.4 CRYSTAL STRUCTURE, OXYGEN STOICHIOMETRY

Superconducting $YBa_2Cu_3O_7$ has an orthorhombic crystal structure whereas the tetragonal phase, $YBa_2Cu_3O_6$, is not superconducting. The phase change from tetragonal to orthorhombic normally occurs at an oxygen stoichiometry of $\delta = 0.6$[44], although significantly lower stoichiometries of $\delta = 0.8$ were initially reported[45,46].

The $YBa_2Cu_3O_{7-\delta}$ (Figure 2.1) crystal structure is orthorhombic and is characterized by the space group *Pmmm* with $a = 3.8198(1)$ Å, $b = 3.8849(1)$ Å, and $c = 11.6762(3)$Å when $\delta = 0.1$. The unit cell's *c* axis is nearly three times the *a* or *b* axis length which change slightly with δ. The copper atoms are situated on two inequivalent positions of the space group *Pmmm* and there are five inequivalent positions for the oxygen, labeled *O(1)* through *O(5)*. In the case $\delta = 0$, the *O(1)*, *O(2)*, *O(3)* and *O(4)* sites are fully occupied and the *O(5)* site is vacant. As the oxygen content, δ, increases, the *O(1)*[47] site becomes depleted and the *O(5)* site is filled. At $\delta = 0.5$, the *O(5)* and *O(1)* sites are both partially occupied (50%) and upon reaching $\delta = 1$, *O(1)* and *O(5)* are both vacant giving a tetragonal crystal structure for $YBa_2Cu_3O_6$. This structural instability between the tetragonal (semiconducting) and orthorhombic (superconducting) phases is a clear indication that oxygen plays a key role in superconductivity. The oxygen exists in these layered perovskites in $Cu\text{-}O_2$ planes, *Cu-O* chains, and at the apical site - *O(4)*. This apex oxygen is believed to play an important role in the oxygen isotope effect[48]. It is now generally accepted that the conduction takes place primarily in the $Cu\text{-}O_2$ planes while the other intercalated layers provide a reservoir of carriers and possibly the *3-D* coupling mechanism. The clearest example for support for this is that the conductivity within the $Cu\text{-}O_2$ plane (the *a-b* axis' plane) has been measured to be as much as 10^5 times greater than the conductivity perpendicular to the plane (along the *c* - axis direction).

The oxygen is "driven" out of the material for temperatures exceeding 650°*C* in 1*atm* of oxygen, the structure becomes tetragonal, and as the partial pressure of oxygen decreases. The tetragonal phase can exist to even lower temperatures[44]. As the material cools, at an oxygen pressure of 1*atm*, the oxygen is reabsorbed and the phase shifts to the orthorhombic crystal structure.

Figure 2.1

Crystal Structure of $YBa_2Cu_3O_x$

Both the orthorhombic ($x = 6$, $\delta = 1$; both *O(1)* and *O(5)* vacant) state and the tetragonal ($x = 7, \delta = 0$; *O(1)* occupied and *O(5)* vacant) state are indicated. The *O(5)* oxygen site (empty circle) is vacant when $\delta = 0$ or $\delta = 1$, but becomes occupied with a change in δ and is 50% occupied when $\delta = 0.5$. The apical oxygen site is *O(4)*.

The charge reservoir consisting of the *Ba* atoms and the *Cu-O* chains (along the *b*-axis) are shown.

The conduction layer(s) consisting of the $Cu\text{-}O_2$ planes (*a-b* plane) are shown. The importance of the *Y* atoms to the coupling between the 2 $Cu\text{-}O_2$ planes can be seen.

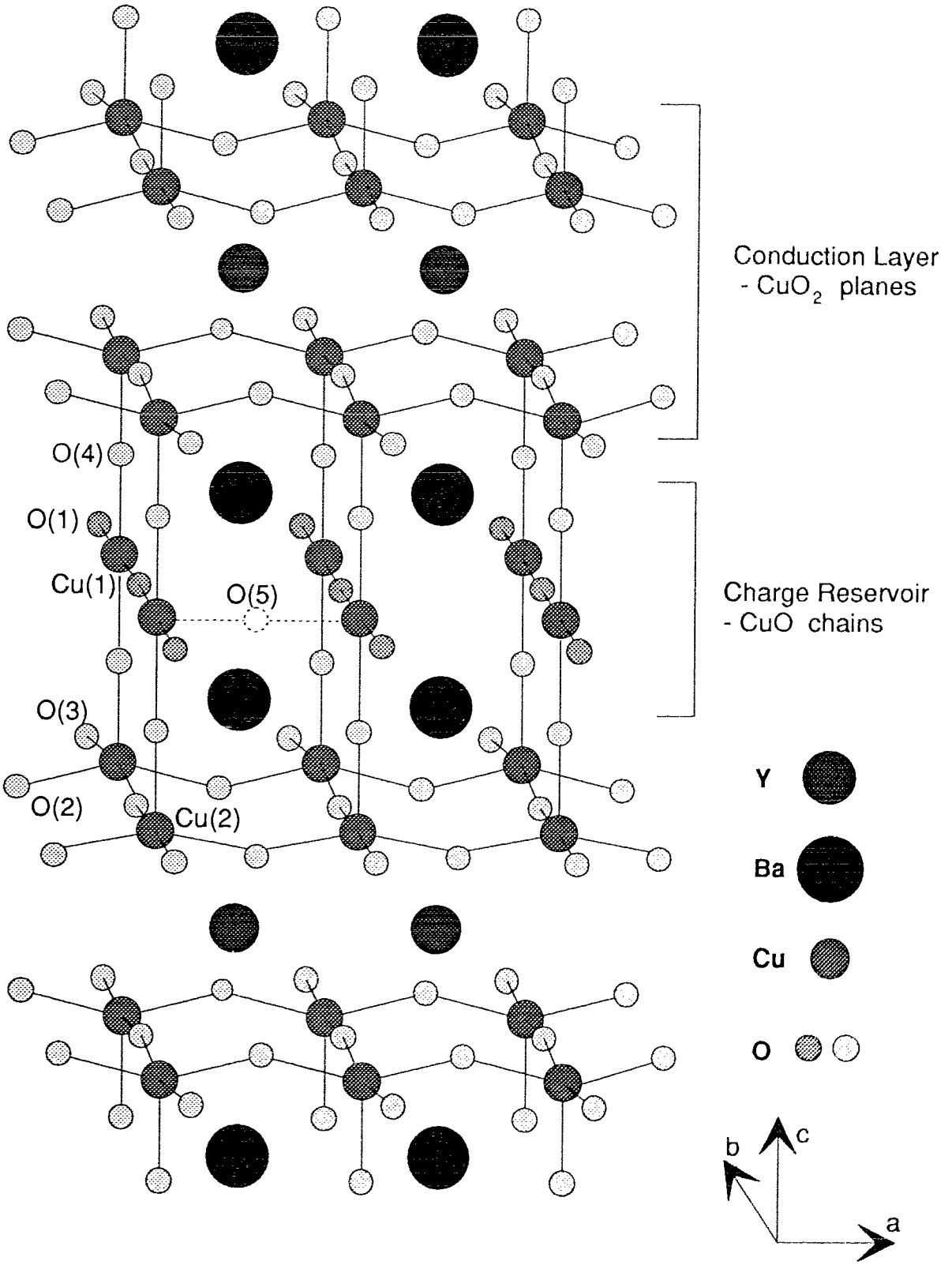
Conduction Layer
- CuO_2 planes
Charge Reservoir
- CuO chains
O(4)
O(1)
Cu(1)
O(5)
O(3)
O(2)
Cu(2)
Y
Ba
Cu
O
b
c
a

The mobility of the oxygen atoms in the crystal structure is dependent on temperature and decreases with decreasing temperature. Thus the amount of oxygen absorbed, that is, the oxygen stoichiometry, depends on the cooling profile. In order to obtain oxygen deficient $YBa_2Cu_3O_{7-\delta}$ (i.e. $\delta = 0.22$[44]), the material would be held at an elevated temperature ($520^{\circ}C$), with a reduced oxygen partial pressure ($0.3atm$), in the orthorhombic regime for a number of hours ($75hr$) and then rapidly quenched. The two standard methods of achieving a fully oxygenated material ($\delta \approx 0.1$) are to cool the material slowly and continuously over a period of several hours, or to hold the temperature for several hours at a number of intermediate temperatures as the material cools. The fully oxygenated state has the most consistent oxygen concentration that can be achieved, and it also corresponds to the highest T_c that is attained. This turns out to be very important as the critical temperature is highly dependent on the oxygen concentration. As the oxygen concentration decreases (i.e. larger δ), so does the critical temperature until the crystal structure is no longer orthorhombic ($\delta \geq 0.6$) and $T_c = 0K$. Current evidence[44,46,49,50] suggests that there are two plateau regimes in which T_c changes only slightly with δ. A $90K$ plateau exists for oxygen stoichiometry of $0 \leq \delta \leq 0.2$, and a $60K$ plateau for $0.3 \leq \delta \leq 0.4$. Outside these regimes T_c changes dramatically with δ, a $30K$ change in T_c for a change of 0.1 in δ. The Raman active modes are also found to be dependent on the oxygen stoichiometry (section 3.6).

The high mobility of oxygen at elevated temperatures allows this isotopic substitution to occur with little disruption of the crystal structure. The high mobility also means that the calcination process is best carried out in a gaseous environment that contains only the desired isotope - ^{16}O or ^{18}O. The majority of researchers[27,35,51] employ a gaseous exchange method of substitution in which

pairs of ^{16}O samples are placed in separate $^{16}O\backslash^{18}O$ environments for a parallel heat processing. Other groups[52,53] have used only $^{16}O\backslash^{18}O$ starting constituents and environments and find shifts that agree with previous work. A test of the effectiveness of the gaseous exchange substitution method is to prepare a set of $^{16}O\backslash^{18}O$ samples, measure the shift, resubstitute ^{16}O for ^{18}O and ^{18}O for ^{16}O and measure again. Franck et al.[51], using the preparation technique described in section 3.1, measured shifts of $0.65K$ for both situations. This is a good indication that the observed shifts are due to some type of an isotope effect.

2.2 ELEMENTAL SUBSTITUTION - *Pr, Ca, Zn*

There are two basic methods that can be used to change the critical temperature of the high T_c *YBCO* superconductor. One would be to change the substitution of one (or more) of the constituents of the superconductor and the other would be to change the oxygen stoichiometry. The stoichiometric precursor concentrations can be weighed out very accurately prior to the preparation of the sample while the oxygen stoichiometry can only be measured after the sample has been prepared. Partial substitution can be done with little effect on the crystal structure while at the time maintaining its fully oxygenated state. Because of the current experimental difficulties in obtaining consistent oxygen stoichiometries (other than the nominal) and the effects that oxygen depletion has on the crystal structure, the second method is currently unsuitable for making isotope samples.

2.2.1 *Pr* - $Y_{1-x}Pr_x Ba_2Cu_3O_{7-\delta}$

It was discovered that the substitution of any of the lanthanide's for *Y*, with the exception of *Ce*, *Pr*, and *Tb*, yields a similar superconducting phase material with a critical temperature close to the *Y* compound[54,55]. The substitution of a small amount of *Ce* and *Tb* for *Y* both yield a multiphase material whereas *Pr* substitution results in an orthorhombic single phase material (even though there is a small tendency to shift towards the tetragonal structure) throughout the entire concentration range, $0 \leq x \leq 1$, in $(Y_{1-x}Pr_x)Ba_2Cu_3O_{7-\delta}$[56]. The increasing *Pr* concentration causes the critical temperature to fall continuously until at a concentration of $x \approx 0.55$, the material fails to be superconducting. A number of other properties are associated with the increase in *Pr* concentration. The normal state resistivity increases and begins to take on a semiconducting behaviour, the width of the transition increases, and the Meissner fraction decreases[57]. The changes in the transition width and the Meissner fraction are not likely to be intrinsic properties, but rather, due to the polycrystalline nature of the sample. Thus, comparisons are made with other polycrystalline materials.

The cause of the depression of the critical temperature is not fully understood. Studies involving susceptibility measurements on the magnetic moment[56,58,59] indicate that *Pr* enters the material with a mixed valence state between +3 and +4 for *Y* (+3) with a magnetic moment of $\approx 2.7\mu_b$ and reduces the number of carriers in the *Cu-O*$_2$ planes. Evidence for a reduction in the number of holes was obtained from Hall-effect measurements[60]. A second factor affecting T_c is thought to be the magnetic pair-breaking effects due to the hybridization of *Pr 4f* orbital with the hole conduction band[57,59]. Other studies, X-ray absorption spectroscopy[61], and electron energy loss spectroscopy[62]

indicate that the *Pr* is strictly trivalent. The reduction in holes is then attributed to a localization of the mobile holes. The interpretation of X-ray photoemission[63] and polarized Raman scattering studies[64] was that this localization takes place at the *Ba* site. Lytle et al.[65] using near edge X-ray absorption spectroscopy (XANES) have determined that a small amount of the *Pr* substitutes for the *Cu(2)* site in the $Cu\text{-}O_2$ planes with a valence of +4 while the rest of the *Pr* substitutes as +3 for *Y*. A recent model[66] for the electronic structure of $PrBa_2Cu_3O_7$ has been proposed which may help in clearing up some of the inconsistency in the *Pr* valence measurements.

Whatever the cause, it appears clear that the concentration of mobile holes is decreased with an increasing *Pr* concentration.

2.2.2 *Zn* - $YBa_2(Cu_{1-z}Zn_z)_3O_{7-\delta}$

The substitution of *Zn* into $YBa_2Cu_3O_{7-\delta}$ has the effect of rapidly reducing the critical temperature. The linear dependence of T_c, the lack of any changes in the orthorhombic crystal structure, and the independence of the oxygen content with changes in the concentration of *Zn*[67-71] are all common features observed in this system. The highest *Zn* concentration at which the material still remains superconducting varies from group to group but is in the range of 6% to 13.5%.

There is great controversy over where the *Zn* substitutes and its rapid depression of the critical temperature is not well understood. Because the ionic radii of *Zn* (0.74Å) and *Cu* (0.72Å) are so close, it is reasonable to conclude that *Zn* will substitute entirely for *Cu*. There are two possible sites for the substitution, *Cu(1)* and *Cu(2)*, associated with the *Cu-O* chains and $Cu\text{-}O_2$ planes respectively. For the *Cu(1)* site[66,71], it has been surmised that the *Zn*,

with its filled *3d* orbitals, diminishes the overlap of the *d* orbital with the oxygen *p* orbital which impairs the charge transfer process causing local disorder and this reduces the carrier concentration and hence depresses T_c. The more convincing evidence has the *Zn* occupying the *Cu(2)* site[68-70,72]. In this case, it is believed that the lack of structural change indicates that the *Cu(1)* chain sites remained undisturbed. It is believed that the *Cu(1)* chain state has a mixed valence between +2 and +3 whereas *Cu(2)* is +2. Thus the *Zn*, with a +2 valence would prefer the *Cu(2)* site. In support of this is neutron scattering data and a study of the effects of *Ga* substitution for *Zn* in $La_{1.85}Sr_{0.15}CuO_4$[73] and $YBa_2Cu_3O_{7-\delta}$[69]. *Ga* has a valency of +3, and would then tend to substitute for *Cu(1)* in $YBa_2Cu_3O_7$, but since the *Cu(1)* do not play a major role in the mechanism for superconductivity, it would thus not affect T_c greatly - this was observed. Moreover, the *La* system consists only of CuO_2 planes and thus the *Ga* would have to substitute in for a plane *Cu* atom. In fact, *Zn* and *Ga* depress T_c in this system similarly. This indicates then that *Zn* substitution of *Cu(2)* in the *Cu-*O_2 plane, and not at the *Cu(1)* site of the *Cu-O* chains, is the leading cause of the depression of T_c. Xiao et al.[73] have experimentally determined that the addition of the non-magnetic impurity *Zn* into the *Cu-*O_2 planes then introduces a magnetic moment of approximately 1.0 to 1.2μ_B.

In regard to the hole concentrations, measurements to establish the carrier concentrations in this system also gave some conflicting results. Alloul et al.[74], using NMR measurements claim no change in hole concentration (carried out on only one doping concentration - 4% *Zn*), while others, using Hall measurements, report a slight increase[71,75] with an increasing *Zn* concentration. In the analysis by Shafer et al.[75], they have found an increase in the number of mobile holes per *Cu* site by the addition of *Zn* impurities. The increase in mobile

sheet holes per *Cu* site (p_{sh}) leads to a decrease in the critical temperature, from a maximum T_c at $p_{sh} = 0.22$ to $T_c = 0K$ at about $p_{sh} = 0.32$. A linear relation between p_{sh} and T_c is proposed although the correlation is not particularly good. A similar result for *Ca* was found except that there was an increase in T_c before a decrease resulting in a maximum, occurring near $p_{sh} = 0.22$ as well. More regarding *Ca* substitution is given in the next section.

Inevitably, there is more to learn regarding the mechanism of the T_c depression for *Zn* substitution, as well as the effects on hole concentration. However, the current belief is that the increase in *Zn* leads to an increase in the concentration of mobile holes.

2.2.3 *Ca* - $Y_{0.8-y}Pr_{0.2}Ca_y Ba_2Cu_3O_{7-\delta}$

There is little in the literature regarding the substitution of *Ca* for *Y*[59,75,76]. X-ray measurements indicate that the structure remains orthorhombic and single phase. It is also believed that the addition of *Ca* may lead to a slight decrease in the oxygen stoichiometry. The analysis of Tokura et al[76] on the effect of change in hole concentration in the $Cu\text{-}O_2$ plane and the oxygen stoichiometry leads to the conclusion that the *Ba* site acts as a center for the localization of holes. There is also believed to be no hybridization between the *Ca* and the valence-band states. The net effect is then that Ca^{+2} adds holes to the unit cell - mainly in the $Cu\text{-}O_2$ planes.

In the investigation by Neumeier et al.[59], the effects of *Pr* and *Ca* substitution together were studied. In the 20% *Pr* system into which *Ca* was doped, there was a net increase in the critical temperature by 2.5*K* at 10% *Ca*, and a net decrease of 1.9*K* at 20% *Ca*. Both these and the results of Shafer[74] on

the modification of hole concentrations, lead to the conclusion that an optimum hole concentration for a maximum T_c is an important characteristic feature of these layered copper-oxide superconductors. Neumeier[59] also proposed an expression for the critical temperature based on the concentrations of *Pr, x,* and *Ca, y:*

$$T_c(x,y) = T_{co} - A(\gamma - \beta x + y)^2 - Bx \qquad [2.1]$$

where T_{co} is the maximum obtainable value of T_c, γ is the optimal hole concentration, β is the deviation of the effective valence of *Pr* from +3. The second term represents the effects of hole generation by *Ca* and hole filling (or localization) by *Pr.* The third term, $-Bx$, represents the overall depression of T_c due to *Pr* pair breaking interactions. A fit of their data give $T_{co} = 97K$; $A = 425K$; $\gamma = 0.1$; $\beta = 0.95$; and $B = 96.5K$. The relative change in the mobile hole concentration is given by $\Delta p = -\beta(x/2) + y/2$ since there are two CuO_2 planes per unit cell.

3.0 EXPERIMENTAL SETUP

Measuring the oxygen isotope effect involves measuring the critical temperature of the ^{16}O samples, T_c, and the shift in the critical temperature for the ^{18}O samples, ΔT_c. Using equation [1.1] we get

$$\alpha = -\frac{\partial \log T_c}{\partial \log M} = -\frac{\log T_c(^{18}O) - \log T_c(^{16}O)}{\log(18) - \log(16)} \qquad [3.1]$$

setting

$$T_c(^{18}O) = T_c(^{16}O) - \Delta T_c = T_c - \Delta T_c \qquad [3.2]$$

gives

$$\alpha = -\frac{\log\left(1 - \Delta T_c / T_c\right)}{\log(1.125)} \qquad [3.3]$$

where T_c is the critical temperature of the ^{16}O sample. For $\Delta T_c << T_c$, one has

$$\alpha \propto \frac{\Delta T_c}{T_c} \,. \qquad [3.4]$$

In this thesis, the critical temperature of the superconductors is determined from measurements on their conductivity - resistance and resistivity, and their magnetic properties - dc magnetization and ac susceptibility. The purpose of this chapter is to outline the sample preparation method as well as to describe the experimental apparatus used in order obtain these values.

3.1 SAMPLE PREPARATION

The experimental technique is always a prime concern in any research. It plays an important role in determining the validity of the results. In the relatively new high T_c research arena, one of the prime concerns is the sample preparation technique which tends to be slightly different for every research group. This is not unexpected since we are still learning what the effects on the sample are that pertain to the different preparation procedures. Unfortunately, the quality of the samples and perhaps the experimental technique as well as the rush to publish often lead to extraordinary results such as: irreproducible isotope shifts of $34K$ for $^{18}O\backslash^{16}O$ and $17K$ for an $^{17}O\backslash^{16}O$ substitution[77]; the previous lack of any observed isotope effect to the now well-established, but small, effect; or even the lack of experimental agreement on the substitution effects in $YBa_2Cu_3O_{7-\delta}$ noted in the previous chapter. It is therefore clear that a good understanding of the experimental technique is essential.

The isotope effect in high temperature superconductors involves the comparison of the critical temperature between sets of two isotopically different samples. In this case, the substitution of ^{18}O for ^{16}O in a series of *Zn*, *Pr*, and *Pr & Ca* doped $YBa_2Cu_3O_{7-\delta}$ samples is investigated. It is therefore important that the samples be as similar as possible. As the different oxygen isotopes are unlikely to cause any structural differences, this essentially requires that both the composition stoichiometry and the preparation technique be identical for both samples.

Preparation of the superconducting compounds from the starting constituents requires the following:

1) measuring and mixing the proper stoichiometric proportions;

2) controlling the temperature profile of the samples to a maximum of approximately 925°C;

3) the substitution of ^{18}O for ^{16}O in the oxygen environment while the samples are being heat treated; and

4) ensuring that all samples undergo the same process, preferably at the same time.

The samples were prepared at the University of Alberta, from high purity oxides and carbonates: Y_2O_3 (Alpha, 99.99%), $BaCO_3$ (Johnson-Matthey, 99.995%), CuO (Anderson Laboratories, 99.999%), ZnO (BDH Inc., 99.99%), $CaCO_3$ (BDH Inc., 99.99%), and Pr_6O_{11} (Johnson-Matthey, 99.99%), all in powder form. For each different concentration, the stoichiometric proportions were mixed in an agate mortar in air. The powder was then placed in an alumina crucible for the calcination process. Following the calcination, the powders were weighed into three equal measures of approximately 250*mg* and formed into pellets, of diameter 6.35*mm*, in a hydraulic press at a pressure of 4*kbar*. They were then placed in the parallel processing system, described next, for sintering. The calcination and sintering procedures for the three different sets of samples are somewhat different and are given in sections 6.1, 7.1, and 8.1 for the *Pr*, *Pr & Ca*, and the *Zn* series respectively. The procedures are designed to obtain good single phase material (calcinating) that is fully oxygenated (sintering process) with $\delta \leq 0.1$.

A single processing line within the closed parallel processing system (Figure 3.1) consists of a 10*mm* quartz tube which is connected to a 3*mm* quartz tube to form a U-tube. Connected to these tubes forming the closed line are an oxygen gas reservoir, a liquid oxygen trap, and a peristaltic pump with an oxygen impervious norprene tube. Three such closed systems are centered around a

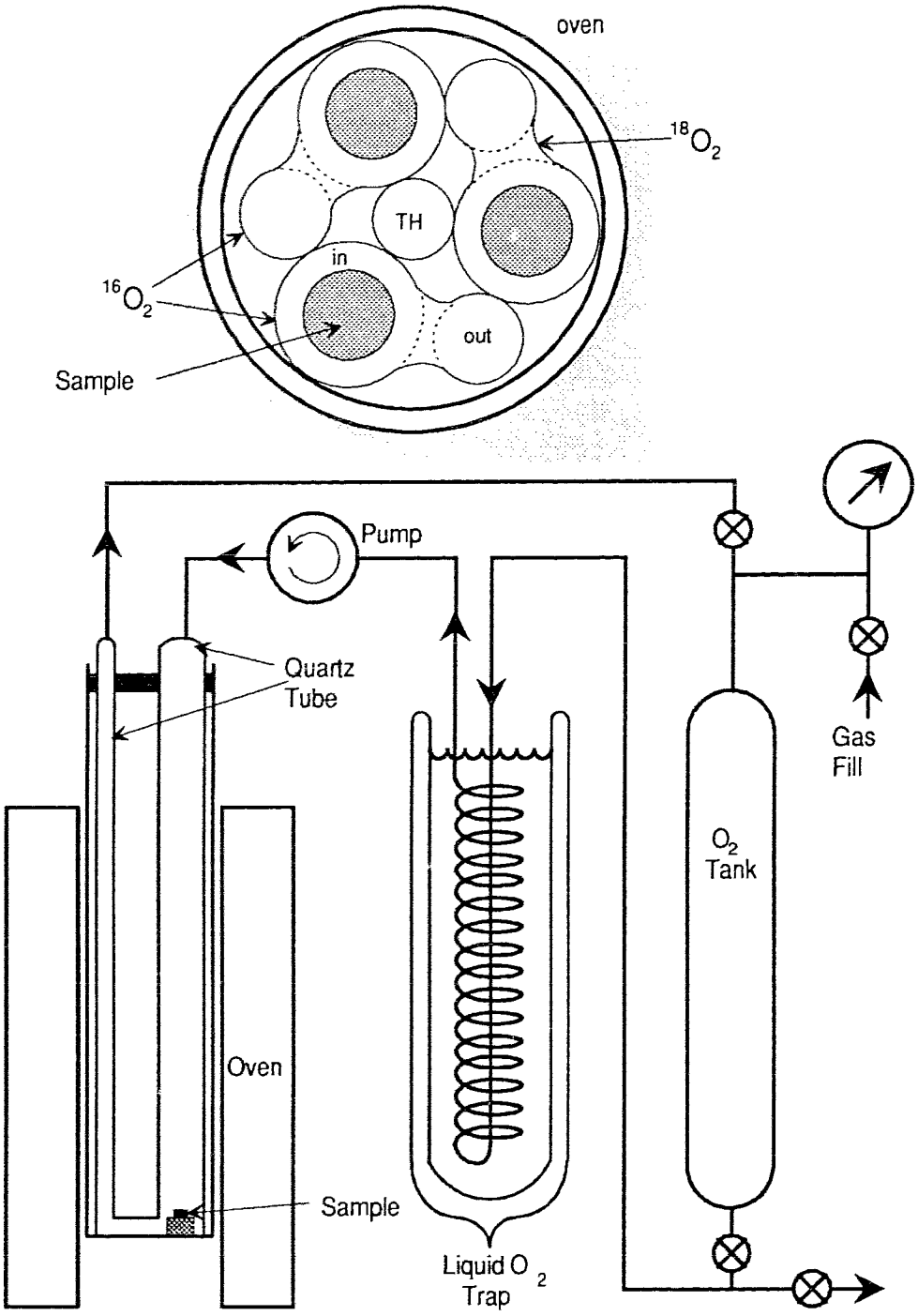

Figure 3.1.

Parallel Processing System.

Top: vertical view of the layout for the three processing lines and the position of the thermometer within the oven.

Bottom: diagram for one of the three identical oxygen flow paths.

Pt-Pt 13% *Rh* thermocouple, also in a quartz tube, and placed in a temperature controlled vertical oven. The symmetry of the three tubes should ensure that each system will experience the same processing conditions. The samples are placed on a gold substrate at the bottom of the large U-tube. The entire closed system is then evacuated for 14-16 hours prior to any heating or oxygen introduction. A one litre supply of oxygen is admitted to each of the three processing lines. The liquid oxygen trap, maintained at the boiling point of oxygen, allows the trapping of unwanted gases such as water vapour and carbon dioxide. This is an excellent way to remove impurities. To keep the oxygen flowing and prevent it from condensing in the oxygen trap, the pressure in the closed system is maintained somewhat below atmospheric pressure at 650-680*mm Hg*.

The resistance vs. temperature profile of identical samples, calcinated and sintered in the three parallel processing lines were compared, and excellent agreement among the samples was found after both the calcination and the sintering procedures (Figure 3.2). Thus we believe that samples placed in the three parallel processing system have undergone the same preparation. Two of the samples prepared have been exposed to ^{16}O and the other to ^{18}O (98.5% atomic purity). The third sample acts as a control allowing the comparison of the two ^{16}O systems' samples, and any differences among the parallel processing systems should result in a difference in the properties of the two ^{16}O pellets.

From each pellet two pieces were cut and shaped: a flat thin bar (0.6*mm* x 1*mm* x 6*mm*) for resistivity measurements and a rod (1*mm* dia. x 6*mm* long) which is roughly cylindrical. The remaining pieces were used for Raman spectroscopy and to obtain the oxygen stoichiometry via SIMS measurement. The ceramic pellets are quite hard and very difficult to cut. They were mounted

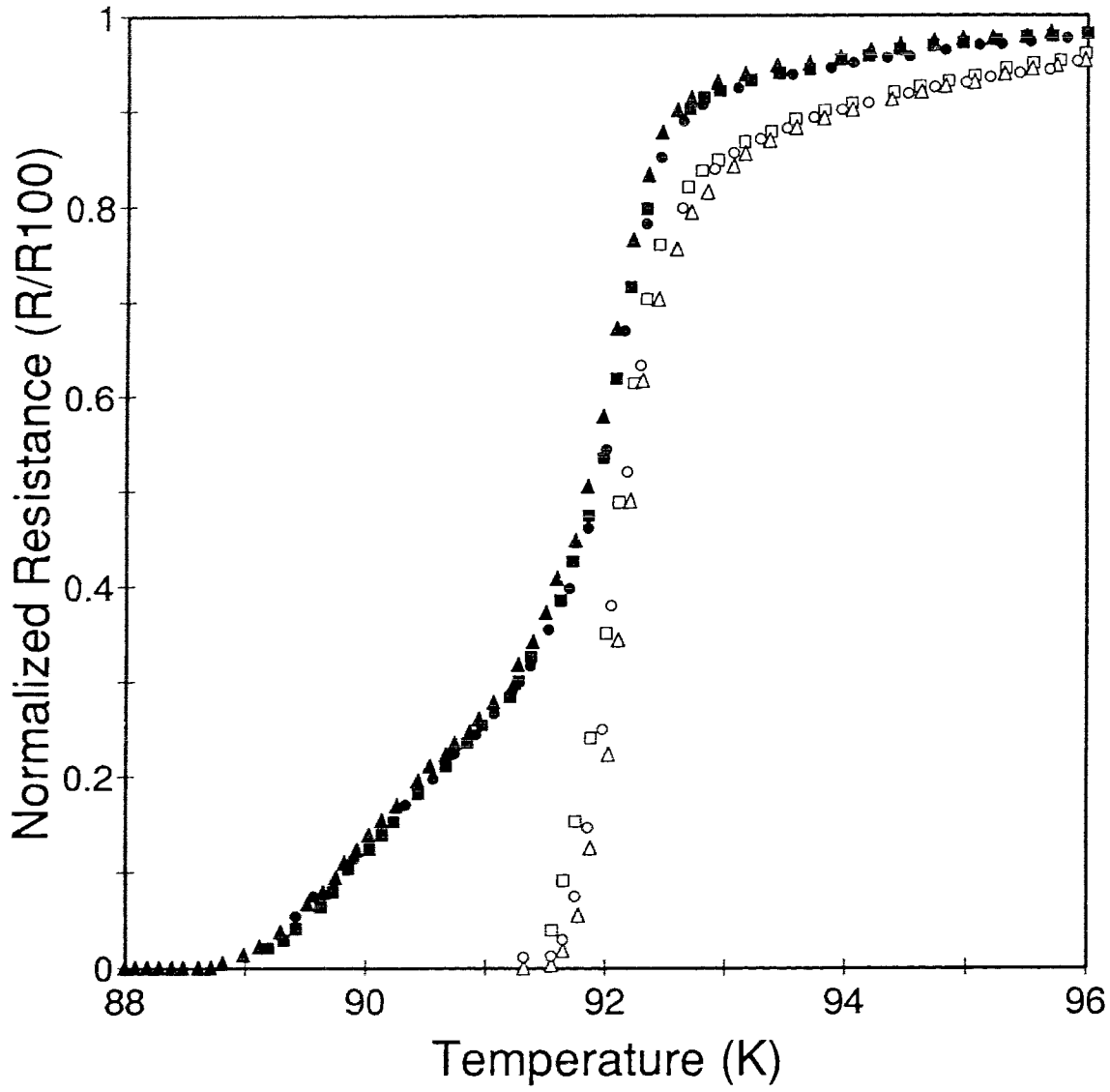

Figure 3.2

Resistance vs. temperature comparison of three ^{16}O samples of $YBa_2Cu_3O_{7-\delta}$ prepared simultaneously in the parallel processing system. The filled symbols represent data taken after the calcination process, and the empty symbols are the same samples after the sintering process.

on $1mm$ thick glass slides with the aid of Crystal Bond, a low melting point adhesive that is soluble in acetone. The samples were then slowly cut with a band saw that utilizes a diamond blade. In order to keep the sample from overheating, the saw blade and sample were kept cool by spraying the blade at the entry point to the sample with methanol from a squeeze bottle. The two desired pieces are then mounted (individually) on an aluminum polishing jig and polished on #600 grit sandpaper to give flat surfaces. In the case of the rod, all four faces were done and the corners were sanded via a small file and #600 grit sandpaper to remove sharp edges. Because of the heating involved in mounting and polishing the samples, as well as the heat created during cutting, the use of acetone to dissolve the Crystal Bond, and the use of methanol in cooling the sample during cutting, it is possible that this sample shaping procedure could affect the critical temperature. Prior to the sample shaping, four probe resistance measurements were performed on the pellets to provide a comparison for the resistivity measurements carried out on the bars. The resistivity curves however show little difference, if any, between them and the resistance curves. Thus, this method for sample shaping appears to have little, if any, effect on the sample characteristics.

3.2 RESISTIVITY MEASUREMENTS

The resistance/resistivity of the sample is measured by a four probe method. A constant current (typically $\mathbf{J} \approx 0.2\ A/cm^2$) is applied and the voltage across the sample is measured. The current is reversed and a second measurement is made and the average is taken. The reversal of the current reduces errors due to thermal emf's in the leads and static charge build-up across the sample.

The temperature profile of the resistance is obtained by lowering the sample, at the end of a sample stick, into a helium bath. The sample holder (Figure 3.3) is an oxygen free, high conductivity (OFHC) copper block at the end of the sample stick. A thin layer of electrically insulating, high thermal conductivity epoxy (Stycast 2850FT) coats the copper where the sample is to be placed. The epoxy layer is also used to permanently mount the electrical solder posts to which contact to the sample is made. The sample is mounted using a small amount of Apiezon L grease to help with the thermal contact to the epoxy. Fine copper wire is used to make contact between the solder posts and the sample. Electrical contact to the sample is accomplished by means of a silver paint - ElectroDag (Acheson Colloids). Just beneath the sample, inside the copper block, a cylindrical thermometer (Lakeshore carbon glass resistor C6853 - calibrated to National Standard over the range $4K$ to $325K$) is mounted in a close tolerance hole with a small amount of grease for thermal contact. An OFHC copper cap that screws onto the block is used to almost completely enclose the sample within an OFHC copper environment. The sample holder also contains a 220Ω resistance heater to allow warming the sample without moving the stick. A small opening in the sample holder allows helium gas in the dip space to enter the sample and act as an exchange gas providing good thermal contact between the sample and the sample holder and hence, the thermometer. Inside the dip stick a thin-walled stainless steel tube contains the electrical connections from the sample and thermometer. These are 30 gauge, insulated copper wires running along the inside from the thermometer and electrical connections on the copper block to a hermetic connector (vacuum/pressure tight) at the top. The thin-walled stainless and thin electrical wires give very little heat conduction from room temperature at the top to the

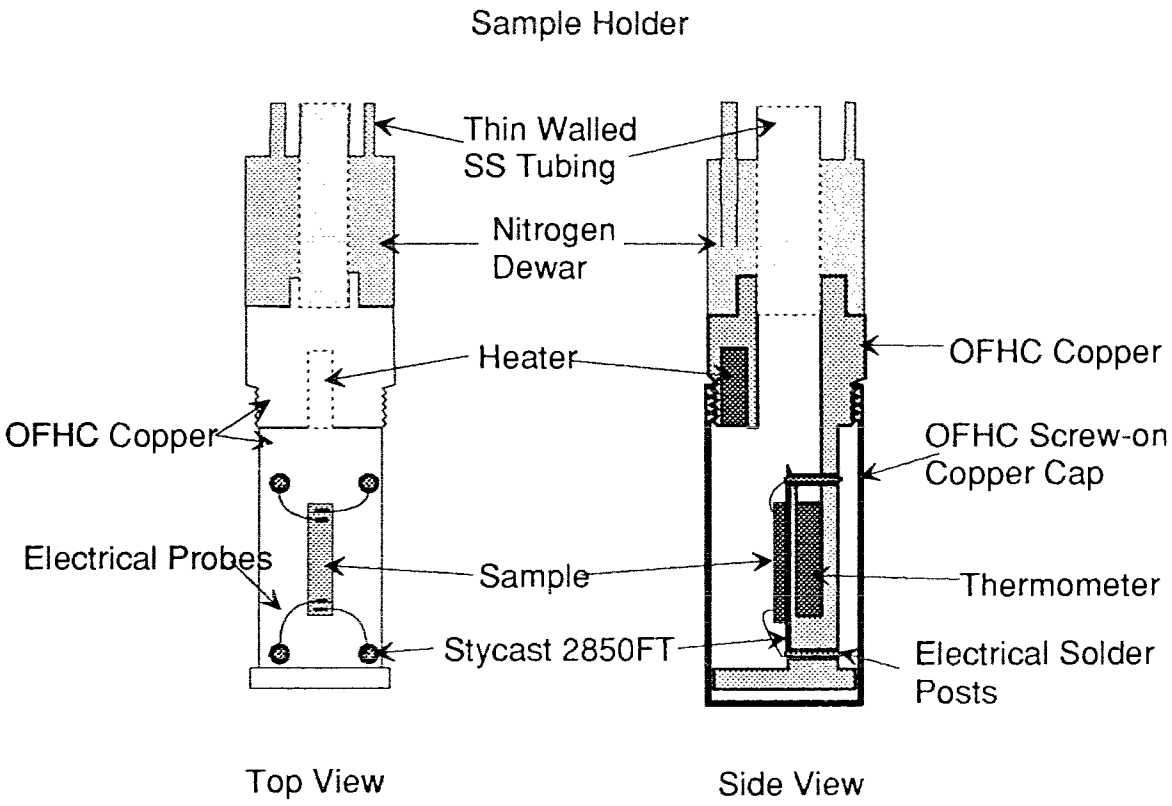

Figure 3.3

Sample holder used for resistivity measurements. The system is drawn to actual size.

minimum of $4K$ attainable at the sample holder. Because the sample and the thermometer are both essentially enclosed within the same OFHC sample holder, the temperature of the sample and that of the thermometer should be the same. Also, the mass of the copper is much greater than that of both the sample and the thermometer together, thus temperature fluctuations between the sample and the thermometer will be small because of the good thermal reservoir of the sample holder.

However, equivalent temperatures for both the thermometer and the sample are likely to occur only in an equilibrium situation. We find two effects predominant when changing temperature and measuring the resistance: the temperature lag between the thermometer and the sample, and the acquisition time involved in measuring the voltages and reading the thermometer (computer acquisition and voltmeter integration times). It is found that if the cooling rate is $\approx 0.05K/sec$ during the transition, then the cooling and warming curves agree to better than a $0.1K$ difference. The thermal contact between the pellet/bar and the copper block does not seem to be important provided both are thermally linked via a thin layer of Apiezon grease. It is believed that the maximum uncertainty between the samples' temperature and the calibrated thermometer is $\pm 0.05K$.

Mounted just above the copper sample holder is a small stainless steel dewar, with a separate supply and exhaust line. This allows the large copper mass to be precooled with liquid nitrogen to minimize the liquid helium boiloff associated with cooling the large copper mass from room temperature to $77K$.

The Quantum Technology Inc. cryogenic cooler, model Quantumcooler $4.2K$[78] (Figure 3.4), is a convenient source of liquid helium. The system

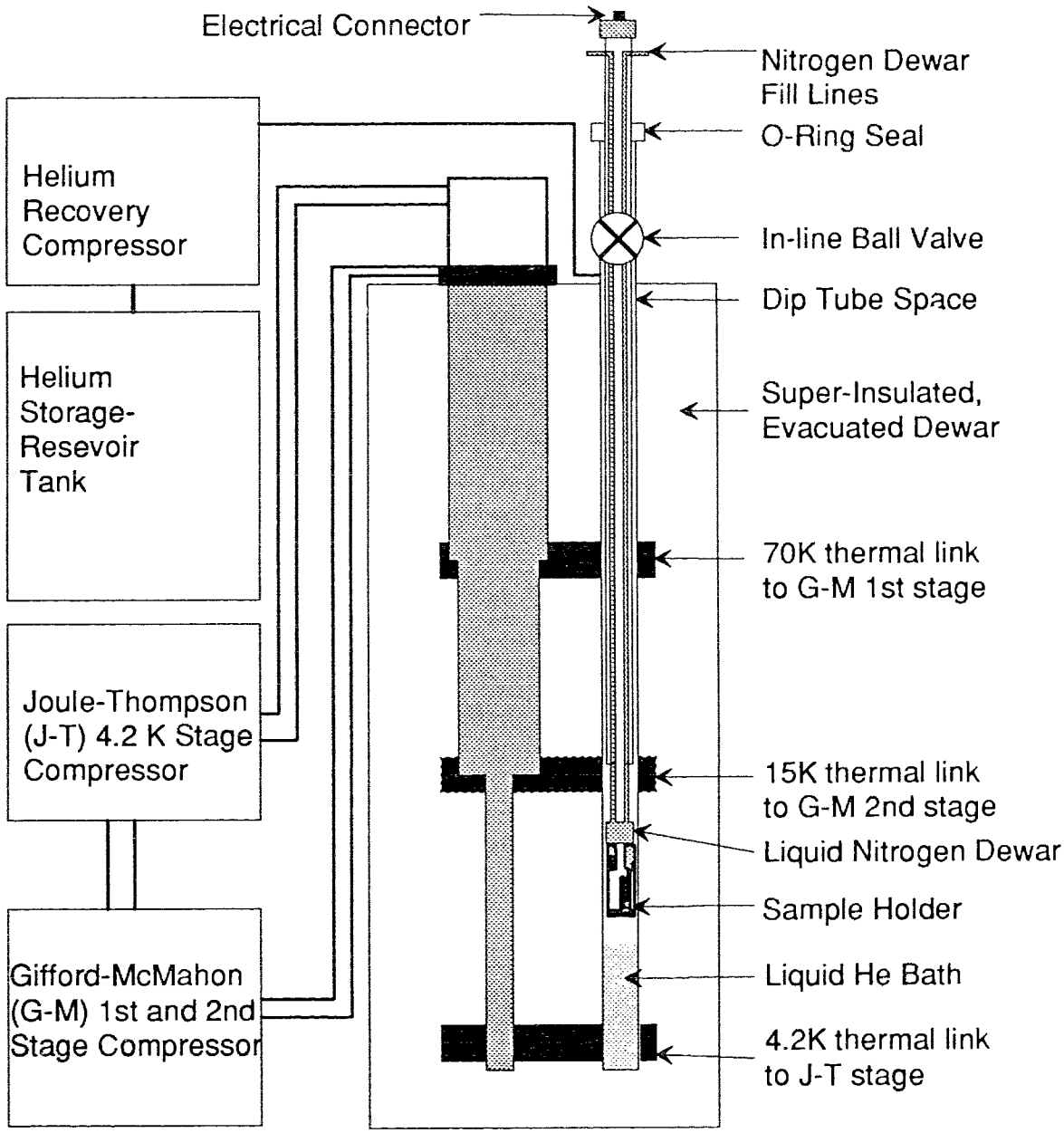

Figure 3.4

Overview of the resistance measuring apparatus.

provides cooling via three helium gas expansion stages, two Gifford-McMahon stages (stage 1 at $90K$ and stage 2 at $14K$) and a Joule-Thompson stage ($4.2K$). The cryocooler provides $1/4W$ of cooling power (at $4.2K$) which maintains a pool of about ½ litre of liquid helium (*LHe*). An in-line ball valve and O-ring seal at the top of the dip tube allow for easy insertion and removal of the sample stick. The dip tube contains helium gas and a relatively linear temperature variation exists between the top of the dewar (at $300K$) and the thermal link between the second stage (at $15K$) and the dip space. At the bottom of the dip tube is the third stage (at $4.2K$) and a pool of liquid helium. From the *LHe* level to the second stage, the temperature variation with distance is highly non-linear. The heat capacity of the cold helium is higher than the specific heat of the copper, and we find that moving the dip stick a small distance can cause large temperature changes and temperature oscillations, resulting in large temperature differences between the sample and the thermometer. This inconvenience is overcome by noting that if the entire sample block is dipped into the *LHe* and then allowed to warm (or is heated), the process occurs much more smoothly. Thus resistance measurements when $T_c < 16K$ are taken in two steps: first, cooling to about $16K$, then moving the sample into the *LHe* to cool to $4.2K$, lifting the sample just out of the liquid, and then measuring while applying a small amount of current to the heater. Even with an easily controlled amount of heat, there are still fluctuations, and it is estimated that the uncertainty in the measurements where $T < 16K$ is approximately $\pm 0.2K$.

3.3 MAGNETIC MEASUREMENTS

Low field magnetic measurements, dc magnetization and ac susceptibility, were carried out on all pairs of samples. These measurements were performed

using a non-commercial SQUID magnetometer. Unlike most commercial magnetometers, this system operates in the static mode - there are no moving coils or samples. This system (Figure 3.5), including the S.H.E. Corporation System 330 SQUID unit and electronics, allows the simultaneous measurement of the dc magnetization, ac susceptibility (in-phase) and ac losses (quadrature) as a function of temperature and/or applied magnetic field. The temperature of the sample can be varied from $4K$ to $> 100K$ in dc fields ranging from 0 to $100Oe$ with an ac field in the range of 0 to $0.1Oe$. The system consists of a liquid helium dewar, a set of magnetic field drive coils, pickup coils and SQUID system (Figure 3.6), and the sample stick and stick space - which allows the insertion of the sample into the magnetic fields. Each of these systems will be described in some detail.

3.3.1 DEWAR

The dewar is a Superconducting Technology Inc. superinsulated dewar. It provides a 15 litre reservoir near the bottom for the *LHe* with a loss rate of about 2 *l/day*. The dewar is constructed from non-magnetic fiberglass and rests inside a μ–metal cylinder closed at the bottom in order to reduce the influence of external magnetic fields. The Earth's magnetic field is effectively shielded down to the order of a few *mGauss*. The whole dewar is mounted in approximately $30cm$ of sand and on a dense rubber pad to help reduce the effects of vibrations (floor or otherwise).

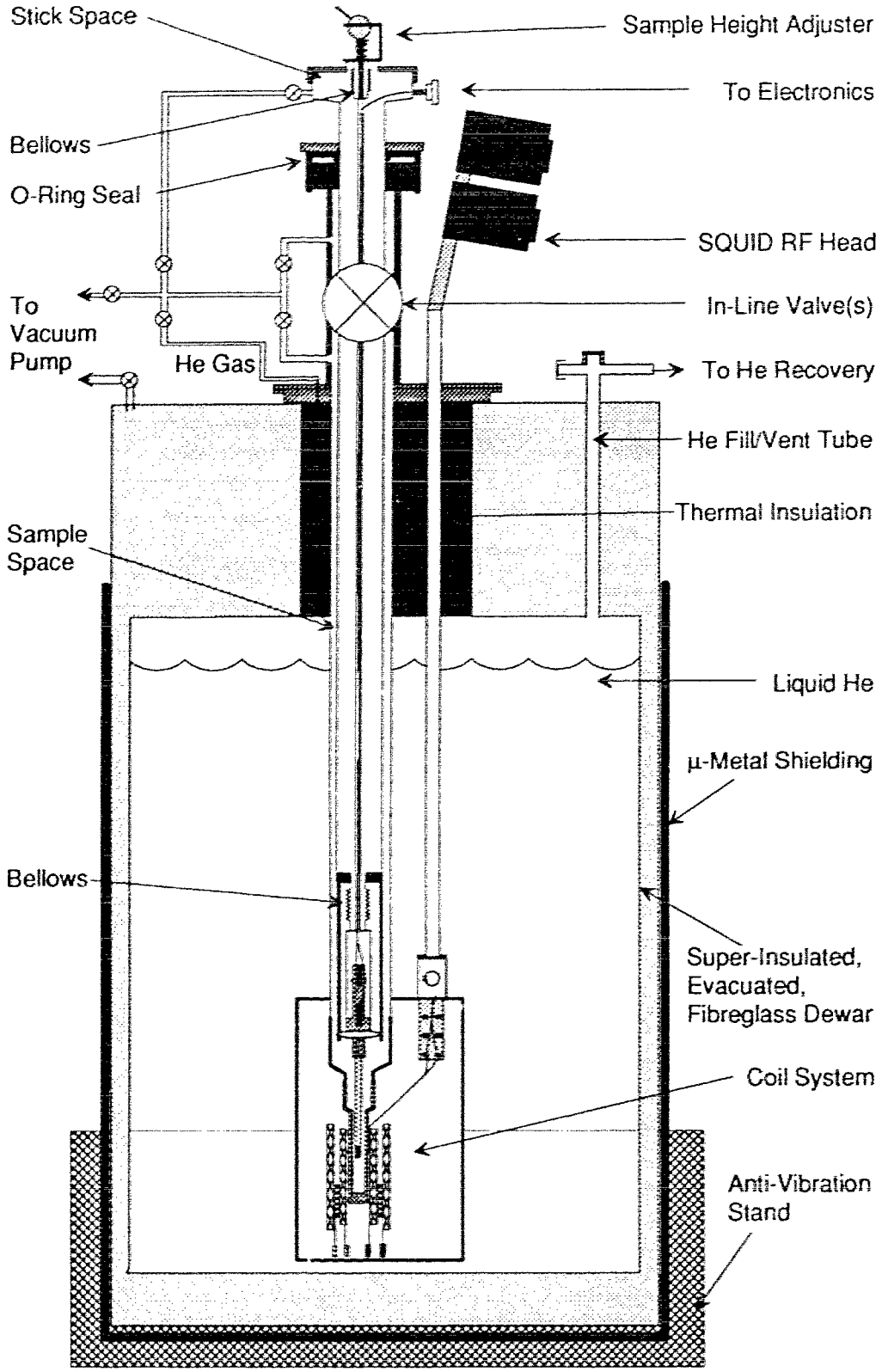

Figure 3.5

Overview of the SQUID Magnetometer.

Figure 3.6

Functional part of the SQUID magnetometer - scale drawing (except the lead shielding cylinder, which is much larger). The relative position of the drive and pickup coils to the sample can be seen. Note the absence of metallic or magnetic materials in close proximity to the sample.

All components shown are immersed in the liquid helium bath. Components that employ superconducting properties are indicated by (SC).

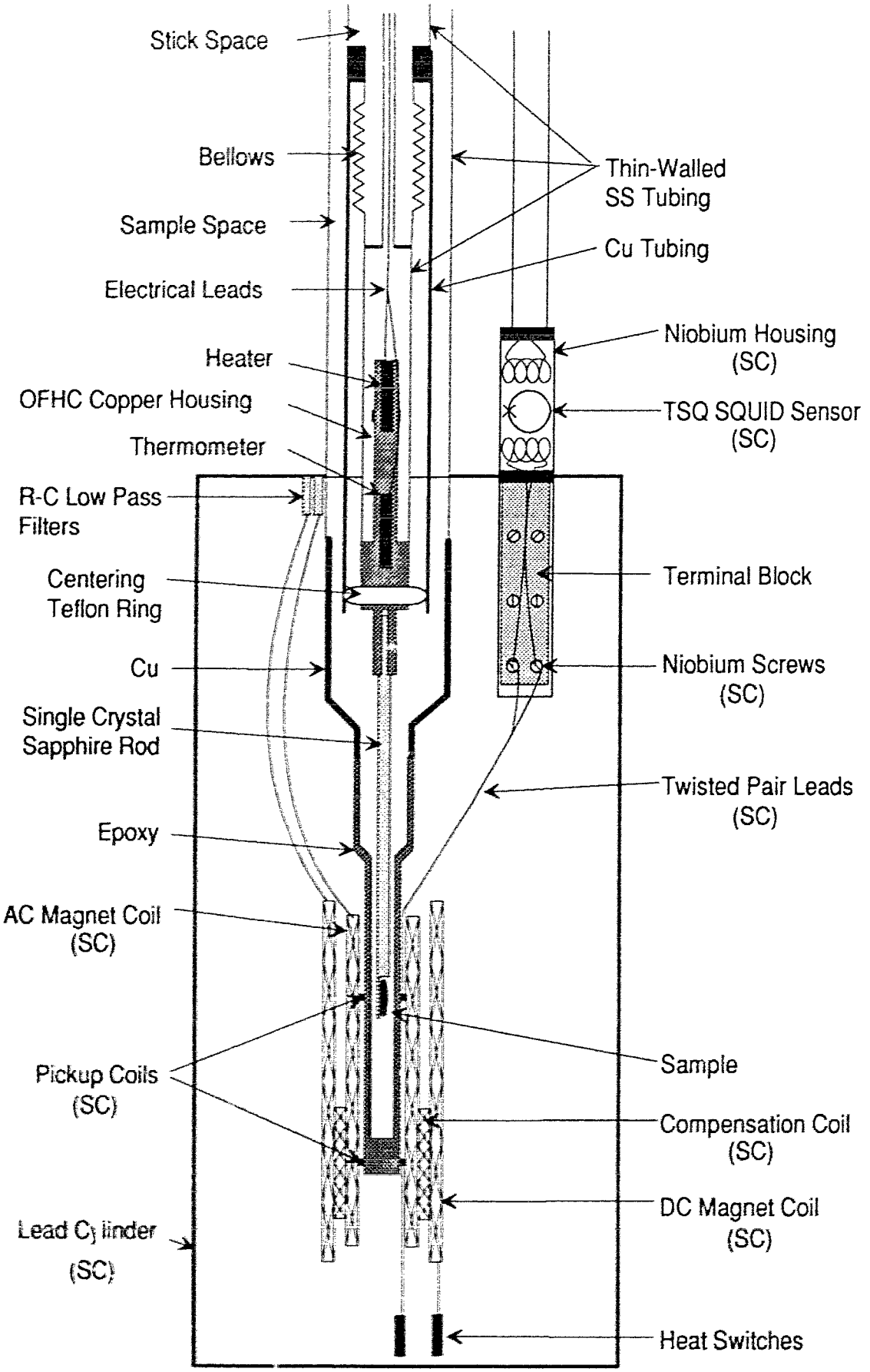
Stick Space
Bellows
Sample Space
Electrical Leads
Heater
OFHC Copper Housing
Thermometer
R-C Low Pass Filters
Centering Teflon Ring
Cu
Single Crystal Sapphire Rod
Epoxy
AC Magnet Coil (SC)
Pickup Coils (SC)
Lead Cylinder (SC)
Thin-Walled SS Tubing
Cu Tubing
Niobium Housing (SC)
TSQ SQUID Sensor (SC)
Terminal Block
Niobium Screws (SC)
Twisted Pair Leads (SC)
Sample
Compensation Coil (SC)
DC Magnet Coil (SC)
Heat Switches

3.3.2 SAMPLE STICK AND STICK SPACE

The sample stick sits in a tube running from the top of the dewar down into the helium bath. The tube is constructed from thin walled stainless steel tubing to minimize heat conduction from the room temperature end to the *LHe* reservoir. An O-ring seal and an in-line valve allow the sample stick to be entered or removed without letting any air into the stick space. The sample space can be (back-) filled with helium gas (boiloff from the liquid reservoir) or evacuated via a liquid nitrogen trapped diffusion pump system. By means of a number of in-line valves, the sample stick can be inserted and removed without exposing the sample space to air. It is extremely important to ensure that air is not trapped in the system as oxygen has a magnetic moment and even a small amount can have an effect on the signal due to the enormous sensitivity of this system. The part of the sample space that lies within the magnet drive and pickup coil system is made from epoxy. Conducting materials in (oscillating) magnetic fields have eddy currents and produce spurious fields. The sample stick is also constructed from thin-walled stainless-steel (SS) tubing and can also be evacuated or filled with helium. The sample stick space must be evacuated prior to insertion. At the bottom of the sample stick our long thin cylindrical sample is mounted vertically on the end of a single crystal sapphire rod (5.5*cm* long). The sapphire rod is cut flat at the end to allow a maximum surface area of the sample to come into contact with the rod. Samples are mounted with a small amount of Apiezon L grease. The high thermal conductivity, good insulator characteristics, and non-magnetic nature of sapphire make it an excellent mount for the sample. The other end of the rod fits snugly into a OFHC copper block. The block also contains a 220Ω resistance heater and a thermometer. The

thermometer is a Lakeshore Cryogenics carbon glass resistor (C11818) calibrated from $4K$ to $325K$. The thermometer leads are thermally anchored to the copper block to prevent heat conduction along the leads. A S.H.E. potentiometric conductance bridge model PCB is used to monitor the conductance of the thermometer and thus provide a temperature reading.

The whole sample assembly can be moved up and down by means of a set of two bellows connecting a small thin-walled SS tube from the copper block at the bottom to a manipulator at the top. By moving the sample in and out of the pickup loop, the maximum amplitude of the expected signal can be determined which allows adjustment of the gain of the measuring equipment to give full scale readings prior to making any measurements. Full scale readings ensure that the maximum S/N ratios are obtained.

By evacuating the sample space and applying current to the resistive heater, the temperature of the sample can be increased. A temperature difference between the thermometer and the sample is expected. There will be a lag due to the difference in heat conduction rates between the heater:copper block:thermometer and the heater:copper block:sapphire rod:sample. It is important that the sample be in a high vacuum in order to minimize thermal conduction between the walls (at $4.2K$) and the sample by cold *He* gas - a good thermal conductor. This is why the LN_2 trapped diffusion pump is used to pump out the space as opposed to just a mechanical pump. By just pumping on the sample space, the vacuum becomes high enough that the heat conduction along the SS tubing and down the electrical leads overcomes the cooling between the cold walls and the sample and the sample begins to warm up very slowly. At this point the heater is switched on, the current for the heater is ramped up slowly over a selected period of time to a desired current. A typical run from $4K$ to

about $100K$ would take roughly $30min$. This gives a temperature rate which is faster at low temperatures and slower at high temperatures (near T_c) where the bulk of the transition occurs. For measurements with lower T_c's, the amount of current is reduced but the time remains the same. All pairs of samples were done at the same settings. Cooling curves were obtained by turning off the current and adding a very small amount of *He* exchange gas into the sample space. The amount of gas administered is difficult to control and thus the cooling rate may differ from run to run. Because of this lack of control on the cooling rate, T_c is not measured from the cooling curves.

To obtain an idea of the temperature variation characteristics, particularly at high temperatures, a $YBa_2Cu_3O_{7-\delta}$ single crystal was measured. The single crystal has a sharp transition making it ideal for this. On this single crystal, a comparison (Figure 3.7) was made among the transitions for the dc magnetization, ac susceptibility and dc resistance. Warming (*70mA/10min*) and cooling measurements were performed for the dc magnetization and the ac susceptibility while the resistance measurement was performed during the cooling process only. The critical temperature computed from the warming curves (ZFC) for both the susceptibility and magnetization (T_c = 94.44K) coincide. The cooling magnetic curves gave a somewhat lower value of T_c = 94.24K, while the zero resistance gave a value of T_c = 94.24K and a linear extrapolation of the resistive transition to zero gives a T_c = 94.28K. The resistance measurement is likely to be the most accurate and this indicates that a difference of 0.2K should be expected for magnetic measurements, with T_c near 100K. Of course, for lower T_c values, one would expect this difference to be smaller. Measurements carried out on lead (T_c = 7K) and niobium (T_c = 17K)

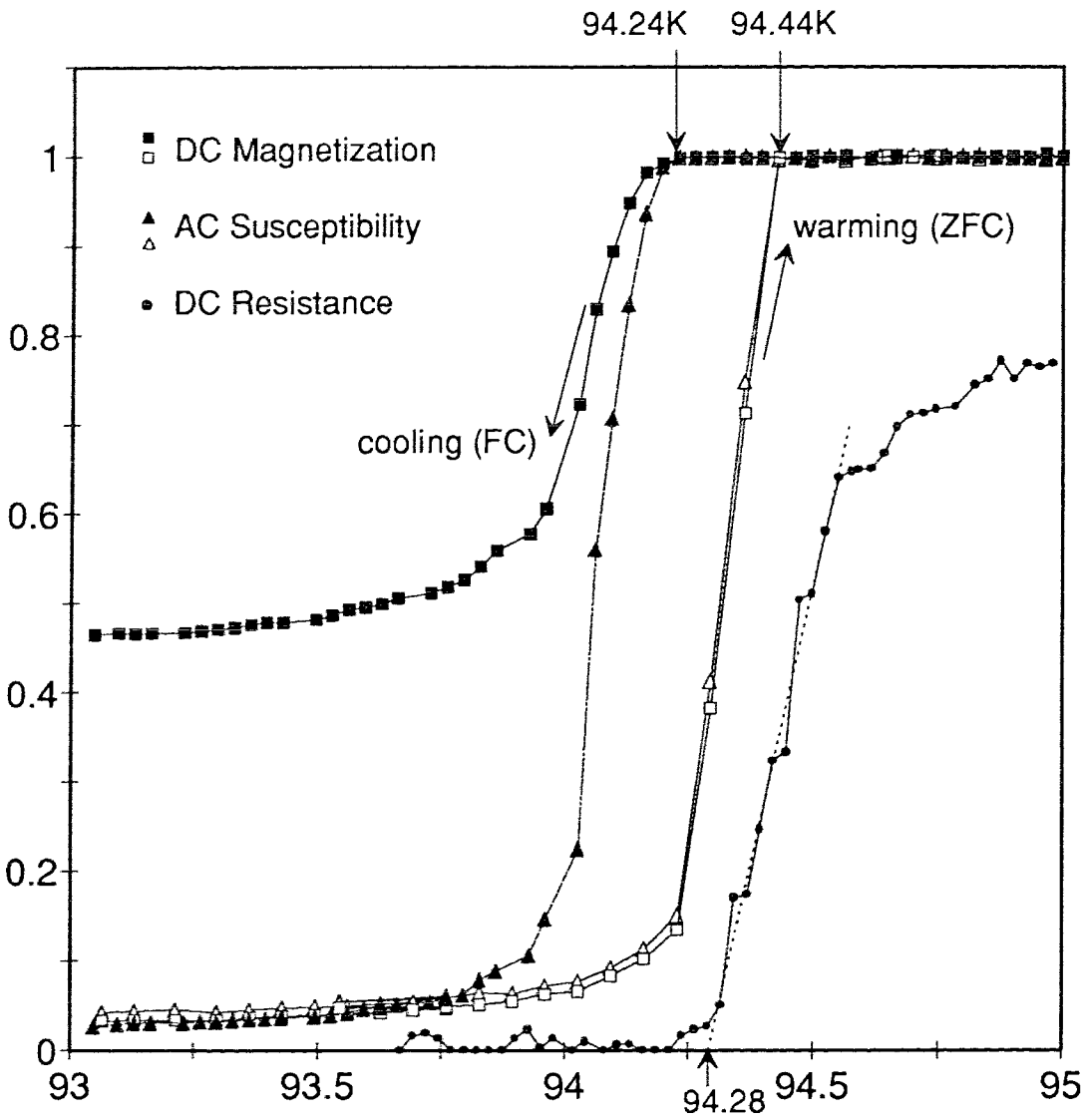

Figure 3.7

Temperature comparison among dc magnetization, ac susceptibility, and resistance measurements.

Comparison of T_c via ZFC, FC, susceptibility (χ'), and resistance measurements performed on a $YBa_2Cu_3O_{7-\delta}$ single crystal. $T_c = 94.28K$ resistively, $T_c = 94.44K$ magnetically upon warming and $T_c = 94.24K$ magnetically upon cooling.

samples indicate no difference within the accuracy of the thermometry of $\pm 0.05K$.

3.3.3 SQUID

The heart of the magnetometer is the S.H.E. model 330 Superconducting QUantum Interference Device (SQUID) system. The system consists of a toroidal SQUID (TSQ) weak-link sensor, rf drive head and control electronics (Figure 3.8). The sensor is located in the helium bath within a superconducting niobium canister to shield it from outside field effects. A rf coil and a signal coil are also within the canister. The rf coil is part of a capacitively tuned circuit that is lightly coupled to the SQUID. The circuit operates at a resonance of $30MHz$ and employs a phase sensitive detector and feedback to detect the effects that occur due to the coupling of the signal coil to the SQUID. The electronics (S.H.E. Model 30 control unit) are tuned to respond to feedback changes that correspond full scale (on its most sensitive setting) to one quantum of flux (Φ_o) change within the SQUID. This flux quantum change corresponds linearly to a $1mA$ feedback current for the TSQ sensor. Thus by monitoring the feedback current, the unit behaves as a microammeter sensitive to a flux resolution of 10^{-4} Φ_o (10^{-10} *Gauss*). As the feedback electronics is set up to maintain a constant amount of flux trapped within the SQUID, this is known as the flux-locked operation of the SQUID. An external digital flux counter (S.H.E. model DFC) keeps track of each integral flux quantum, as well as the fraction of flux quantum, that the pickup coils couple into the SQUID.

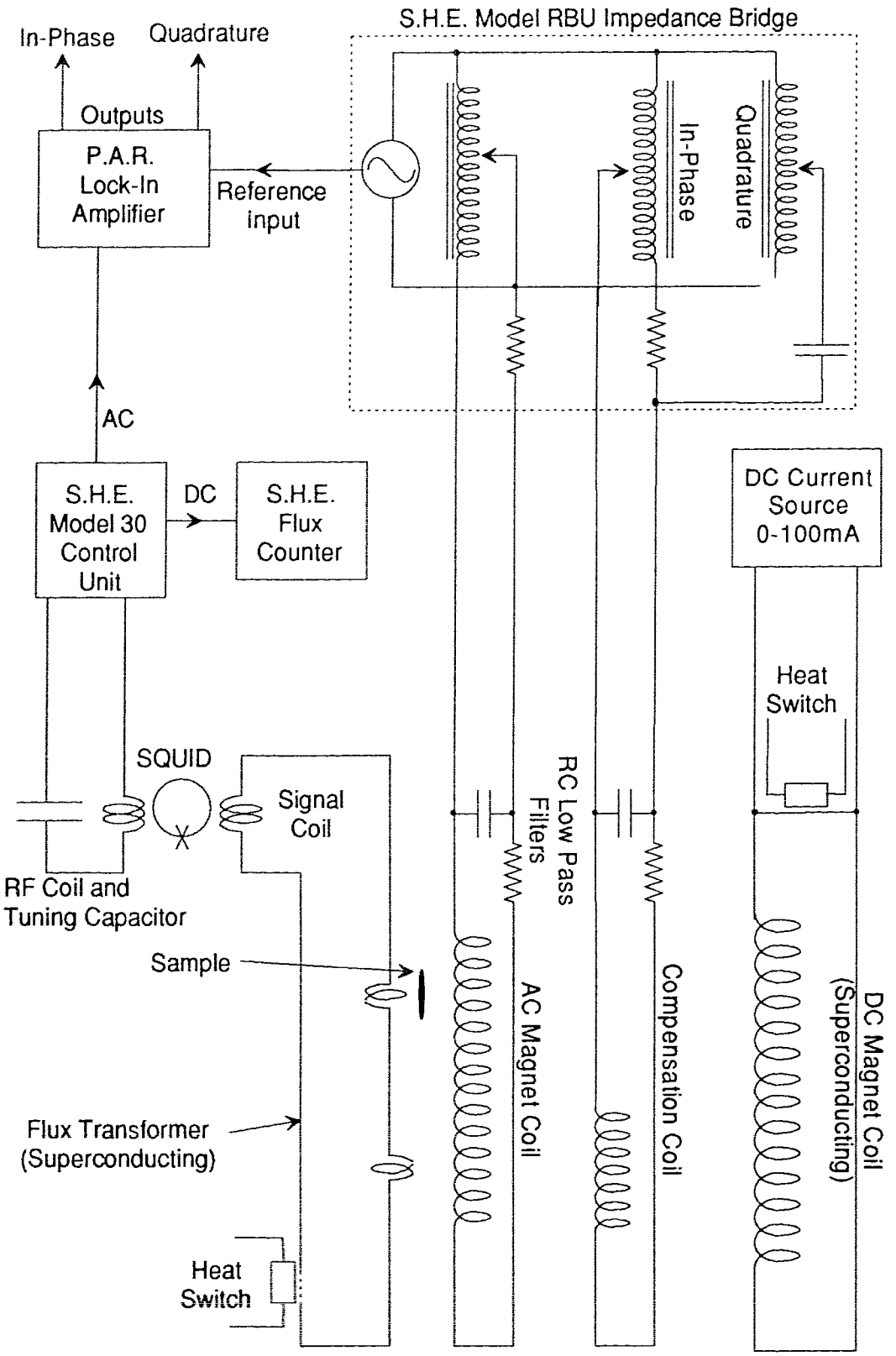

Figure 3.8

Electronic schematic of the SQUID.

3.3.4 FLUX TRANSFORMER

The signal in the sample is coupled to the SQUID by means of a flux transformer. The SQUID signal coil is connected, via a niobium screw block, to two pickup coils residing in the uniform magnetic field regime created by the ac and dc field drive coils. The sample sits within one pickup coil, and the two coils are far enough apart that the sample does not affect the other pickup coil. The two coils are wound in opposition from superconducting wire and along with the superconducting signal coil form the superconducting flux transformer. Thus a change in the magnetization of the sample is coupled into the SQUID.

The leads from the pickup coils are tightly twisted to minimize their self inductance. A resistive heater beside part of the leads allows that part of the flux transformer to go into the normal state. In the normal state, any current induced in the flux transformer by the dc drive coil will quickly decay. This is done to prevent flux from being trapped within the SQUID when introducing or removing a large dc field as well as the fact that large amounts or very rapid changes of flux within the SQUID may affect the flux locked operation or even damage the Josephson junction.

The two pickup coils are 7 turns each, 0.8*mm* long, 5*mm* in diameter and are separated by 28*mm*. The samples used are long cylindrical-like samples approximately 6*mm* in length. The sample is centered in the top pickup loop and remains far enough away from the bottom loop so as not to interfere with its compensation responsibilities.

3.3.5 DC MAGNET COIL

A uniform static field, 0-100*Oe* in strength, is produced inside a solenoid, 60*mm* in length and 16*mm* in diameter, constructed from superconducting Nb_3Sn wire with copper cladding (Supercon T48B). The dc current is supplied by a battery powered S.H.E. constant current supply. The field constant was measured to be approximately 1*Oe/mA*. By driving a section of the closed loop normal, using a resistively heated shunt, a current can be injected (or removed) from the solenoid. Allowing the normal part to go superconducting again traps the current in a circulating "persistent" mode. Thus, a very stable, noise free, static (dc) field can be maintained without the use of an externally supplied voltage.

3.3.6 AC MAGNET COIL

The ac magnet coil is also constructed from superconducting wire although it does not operate in a persistent mode. Its power is supplied via the S.H.E. model RBU ac impedance bridge. The ac operates at a frequency of 160*Hz* and an adjustable amplitude 0-0.1*Oe*. The ac field strength is adjusted so that it is smaller than the dc field. In reality, the two pickup coils will not be in perfect balance and hence another "compensation" coil is added around the lower pickup coil. The ac impedance bridge supplies an inphase and quadrature adjustment, relative to the ac coil, to the compensation coil. Both the ac coil and the compensation coil have low pass filters (attached just above the magnets) to eliminate any rf noise that might interfere with the operation of the SQUID. A frequency signal from the bridge is supplied to a Princeton Applied Research (PAR) model 5204 lock-in analyzer (bi-phase sensitive detector) as a reference

for the ac output of the S.H.E. Model 30 control unit. Both ac and dc measurements are performed at the same time. The dc and ac sensitivities on the lock-in amplifier and ac field strengths on the impedance bridge are adjusted to give a full scale signal for a complete transition from the superconducting to the normal state. The entire coil system is contained within a superconducting lead cylinder closed at the bottom. This provides excellent shielding from external magnetic fields.

3.4 COMPUTER SYSTEM

The S.H.E. digital fluxcounter (DFC) and potentiometric conductance bridge (PCB) have binary coded decimal outputs which are interfaced to an IOTech System-488 digital interface box connected via an IEEE-488 bus to an IBM 386 compatible computer. The ac inphase and quadrature outputs of the P.A.R. lock-in analyzer are connected to the 12 bit MetraByte Model DAS-8PGA analog to digital converter ($0.24mV$ resolution) within the computer. The Lakeshore model 820 thermometer, Keithley model 220 programmable current source, and Keithley model 196 digital multimeter are also controlled on the IEEE-488 bus. The speed at which measurements can be made is dependent on the measuring equipment and not the computer. This can play an important role as transitions can be quite sharp and slow instrumentation may mean the loss of very valuable data during these transitions. All instruments have a minimum integration time in which the measurement is made. The IEEE-488 instruments tend to have the longest integration times and are thus the limiting factor on the number of measurements that can be made per second. The SQUID magnetometer equipment operates quite rapidly obtaining data at a rate as fast as 3 measurements per second. The resistance equipment operates

somewhat slower at 2 measurements per second. To prevent the accumulation of extremely large data files, only during the transition is the data kept at the maximum acquisition rate; at other times, the data is collected only after a specified change in temperature has occurred.

3.5 X-RAY CHARACTERIZATION

The orthorhombic structure of the samples was confirmed via X-ray measurements utilizing the *Cu Kα* (λ=1.540598Å) Bragg diffraction peaks. A typical X-ray measurement spectrogram is given in Figure 3.9 with the [0 0 l] peaks labeled. The lattice constants obtained for the unsubstituted samples were in the range of: a = 3.820 to 3.838 ± 0.003Å, b = 3.880 to 3.892 ± 0.003Å, and c = 11.661 to 11.673 ± 0.003Å, which agree well with the accepted values[44-46]. The effect of the increasing *Pr* substitution was a small linear increase in the lattice constants. There was no observable effect on the lattice parameters for the *Zn* and *Ca* substitutions. Essentially all the peaks observed can be accounted for from the values in Table 3.1 - calculated from the above lattice constants. The main impurities expected have characteristic lines (Figure 3.10) which were not observed to any substantial amount in the spectrum. $BaCuO_2$ has a strong triple peak in the range $2\Theta = 27°–30°$. It was observed (Figure 3.11) that the earlier samples, *Pr* and *Ca* substitutions, had a small amount (< 3%) of this non superconducting phase material present. The other two predominant phases one could expect, $Y_2Cu_2O_5$ and *CuO* with major peaks at $2\Theta = 31.25°$ and 33.25° and $2\Theta = 35.5°$ and 38.75° respectively, are not present. The later samples, the Zn substitutions, did not show any impurity phases at the X-ray detection level.

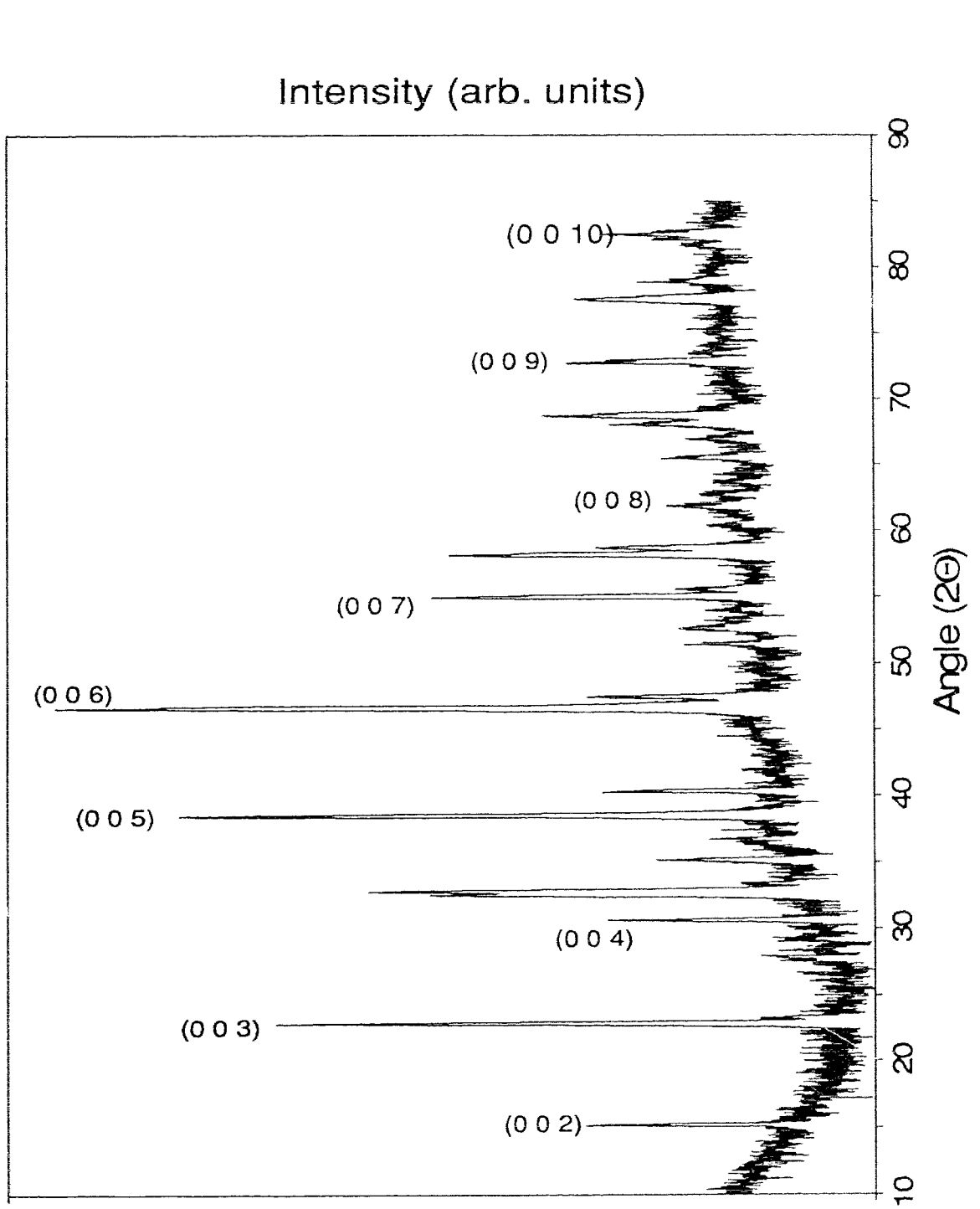

Figure 3.9

Characteristic X-ray sprectrum for a $Y_{0.8}Pr_{0.2}Ba_2Cu_3O_{7-\delta}$ ^{16}O poiycrystalline sample. Numbers in brackets represent the Miller indices (0,0,l) used to determine the *c*-axis parameter. Other peaks can be identified by checking with Table 3.1.

peak	2 theta	h	k	l	peak	2 theta	h	k	l
y	15.176	0	0	2	n	57.538	2	0	4
y	22.848	0	0	3	y	58.223	1	1	6
y	22.866	0	1	0	y	58.248	1	2	3
y	23.211	1	0	0	y	58.723	2	1	3
n	24.119	0	1	1	m	62.115	0	2	5
n	24.448	1	0	1	n	62.275	1	2	4
m	27.558	0	1	2	m	62.724	2	0	5
m	27.849	1	0	2	m	62.732	2	1	4
y	30.626	0	0	4	y	63.766	0	0	8
y	32.547	0	1	3	m	67.247	1	2	5
y	32.797	1	0	3	m	67.686	2	1	5
y	32.810	1	1	0	y	68.173	0	2	6
m	33.721	1	1	1	y	68.754	2	0	6
y	36.332	1	1	2	y	68.784	2	2	0
y	38.552	0	0	5	n	69.319	2	2	1
y	38.563	0	1	4	n	70.912	2	2	2
y	38.779	1	0	4	y	72.913	0	0	9
y	40.359	1	1	3	y	72.979	0	3	0
m	45.295	0	1	5	y	73.091	1	2	6
m	45.485	1	0	5	m	73.500	0	3	1
m	45.494	1	1	4	m	73.514	2	1	6
y	46.675	0	0	6	m	73.535	2	2	3
y	46.713	0	2	0	n	74.246	3	0	0
m	47.395	0	2	1	n	74.764	3	0	1
m	47.450	2	0	0	n	75.057	0	3	2
n	48.125	2	0	1	n	76.312	3	0	2
n	49.399	0	2	2	n	77.150	2	2	4
n	50.107	2	0	2	y	77.628	0	3	3
m	51.500	1	1	5	m	77.773	1	3	0
m	52.587	0	1	6	m	78.284	1	3	1
m	52.613	0	2	3	m	78.869	3	0	3
m	52.757	1	0	6	m	78.876	3	1	0
m	52.792	1	2	0	n	79.385	3	1	1
m	53.290	2	0	3	n	79.810	1	3	2
m	53.299	2	1	0	n	80.906	3	1	2
m	53.416	1	2	1	n	81.185	0	3	4
n	53.919	2	1	1	m	81.725	2	2	5
y	55.054	0	0	7	m	82.338	1	3	3
m	55.261	1	2	2	,n	82.414	3	0	4
n	55.752	2	1	2	y	82.636	0	0	10
m	56.896	0	2	4	n	83.427	3	1	3

Table 3.1. X-ray peak position and assignment for the $YBa_2Cu_3O_{7-\delta}$ system. The X-ray spectrum was calculated using the orthorhombic crystal structure with lattice parameters $a = 3.829$Å; $b = 3.886$Å; and $c = 11.667$Å using the *Cu* X-ray line $K\alpha = 1.540598$Å. The letters in the 'peak' column represent: y = major peak; m = minor peak; n = no peak observed for the given Miller indices h,k,and l.

Figure 3.10

X-ray spectra of common $YBa_2Cu_3O_{7-\delta}$ impurities. The three main impurities that are found are $Y_2Cu_2O_5$, CuO, and $BaCuO_2$. Experimental measurements made on prepared powders of these impurities are shown.

The two peaks of $Y_2Cu_2O_5$ near $2\Theta = 31.25^{\circ}$ and 33.25° are characteristic of this phase.

The two peaks of CuO near $2\Theta = 35.5^{\circ}$ and 38.75° are characteristic of this impurity phase.

The $BaCuO_2$ triplet peak near $2\Theta = 27.75^{\circ}$, 28.5°, and 30.5° is perhaps the most common impurity phase found.

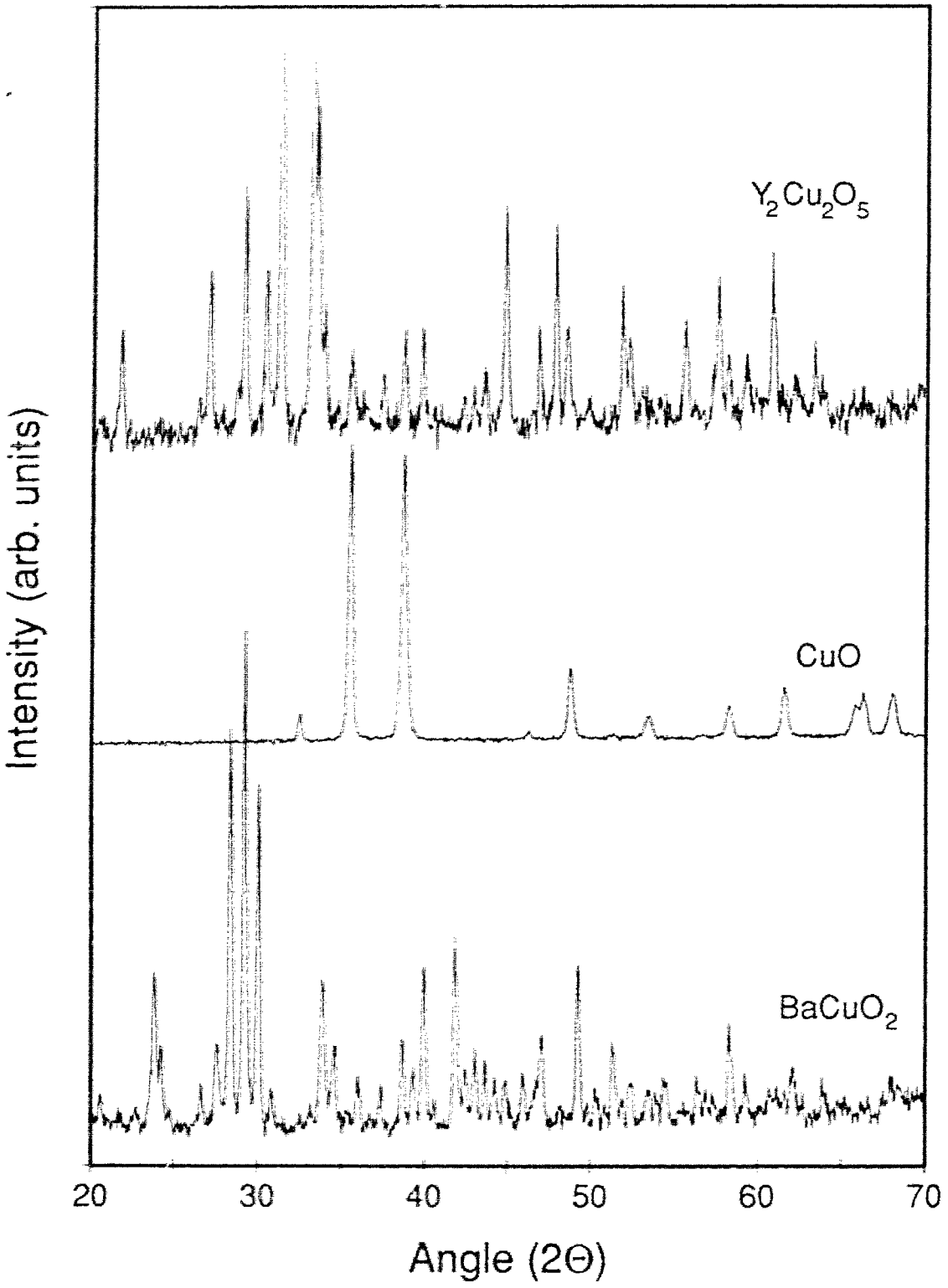
Intensity (arb. units)
$Y_2Cu_2O_5$
CuO
$BaCuO_2$
20
30
40
50
60
70
Angle (2Θ)

Figure 3.11

Comparison of X-ray spectra of $Y_{0.8}Pr_{0.2}Ba_2Cu_3O_{7-\delta}$ and those of the common impurities. The amplitude of the $YBa_2Cu_3O_{7-\delta}$ peaks (solid lines) in the region around the main peaks of the three common impurities (dotted lines) have been enlarged greatly to aid in the comparison of the position of the peaks.

At the top is the $Y_2Cu_2O_5$ phase material. As the characteristic peaks do not appear in the *YBCO* spectrum we conclude that this phase is not present (to within the resolution of the spectrometer).

In the middle is the *CuO* phase material. Again, the characteristic peaks for this phase are not found.

At the bottom is the $BaCuO_2$ phase material. Here we see that these impurity peaks are found in the *YBCO* spectrum. The strength of the impurity signal is quite small. The *YBCO* has been enlarged 25x in comparison to $BaCuO_2$ spectrum in order to see this impurity. Similar measurements at the University of Alberta indicate an upper limit of 3% present of this impurity phase.

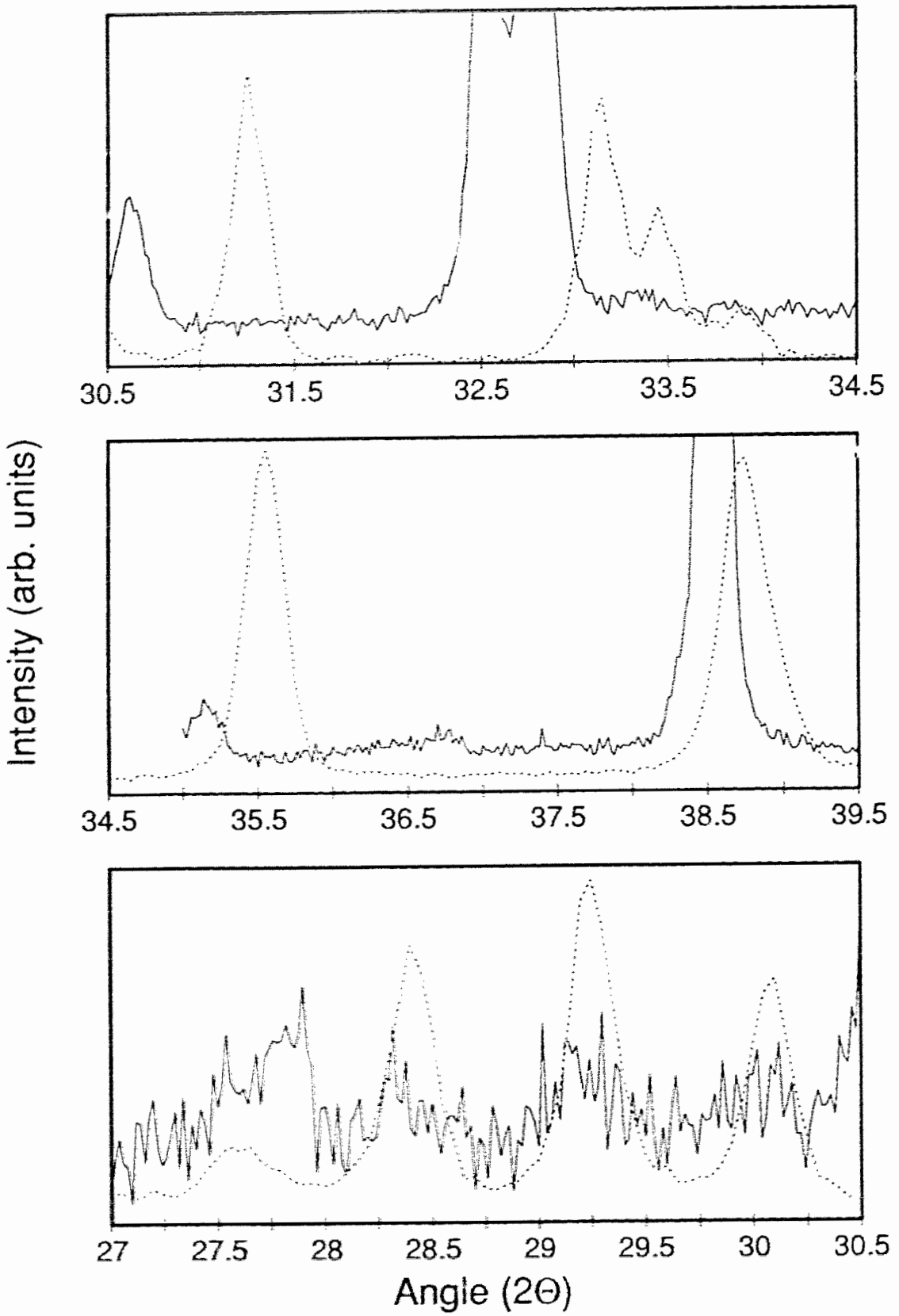
30.5
31.5
32.5
33.5
34.5
34.5
35.5
36.5
37.5
38.5
39.5
27
27.5
28
28.5
29
29.5
30
30.5
Intensity (arb. units)
Angle (2Θ)

3.6 RAMAN CHARACTERIZATION

Raman measurements provide information pertaining to the phonon frequencies within the crystal structure. In investigating the isotope effect, it is necessary to confirm that the isotope substitution has taken place. Because the phonon frequencies are dependent on lattice vibrations which are in turn dependent on the mass of the atoms involved, a shift in the frequencies associated with that element should be seen as evidence that the isotope has been successfully substituted. If we make an analogy with a simple oscillating mass, m, on a spring, of spring constant κ, the mass will have a harmonic frequency of $\omega = (\kappa/m)^{1/2}$. Substituting a higher mass element should then lead to a lower frequency.

There are three main frequency bands associated with the phonons that originate from oxygen vibrations in the $YBa_2Cu_3O_7$ system. They are generallly accepted to be due to:

1) $340cm^{-1}$ - an out-of-phase vertical (*c*-axis) displacement of the *Cu-O* plane oxygen ions *O(2)* and *O(3).*

2) $430cm^{-1}$ - an in-phase vibration mode of *O(2)* and *O(3).*

3) $500cm^{-1}$ - axial stretch mode of the *Cu-O* chain site *O(4)* atom.

There does not appear to be an active Raman mode corresponding to *O(1)* vibrations, but there is an infared mode which does.

The expected shift of these phonon modes with the substitution of ^{18}O for ^{16}O is expected to be 5.0%[79]. As mentioned earlier, the frequency is linked to the oxygen stoichiometry[80]. The $500cm^{-1}$ peak shifts to a lower frequency and

the $430cm^{-1}$ and $340cm^{-1}$ peaks shift to a higher frequency with a decrease in the oxygen stoichiometry. Thus, the observation of a decrease in the frequency shift for all three modes in isotope substitution measurements provides a more convincing argument that the substitution has taken place than measurements by weight change or SIMS analysis.

Far-infared reflectivity measurements along with Raman measurements[80] reveal that all the oxygen active frequencies measured shifted to a lower value when ^{18}O is substituted for ^{16}O and all the shifts correspond closely to the expected theoretical values. It was determined that the oxygen substitution was 86% complete and that all oxygen sites are substituted to some degree. A Raman investigation[81] on the homogeneity of the oxygen substitution indicates that the the apical oxygen site was not as completely substituted as were the *O(2)* and *O(3)* sites. As the apical oxygen is believed to play an important role in the isotope effect[48], this is of some concern.

A typical Raman measurement, performed on the 8.75% *Zn* substituted *YBCO*, is given in Figure 3.12. Here, a downshift in the three active oxygen Raman modes of $17cm^{-1}$ at $340cm^{-1}$, $22cm^{-1}$ at $430cm^{-1}$, and $26cm^{-1}$ at $500cm^{-1}$ with substitution, corresponds to a 5.0%, 5.1% and 5.2% change as is expected. The large background noise found in these measurements is likely due to the handling of the samples prior to making the measurements.

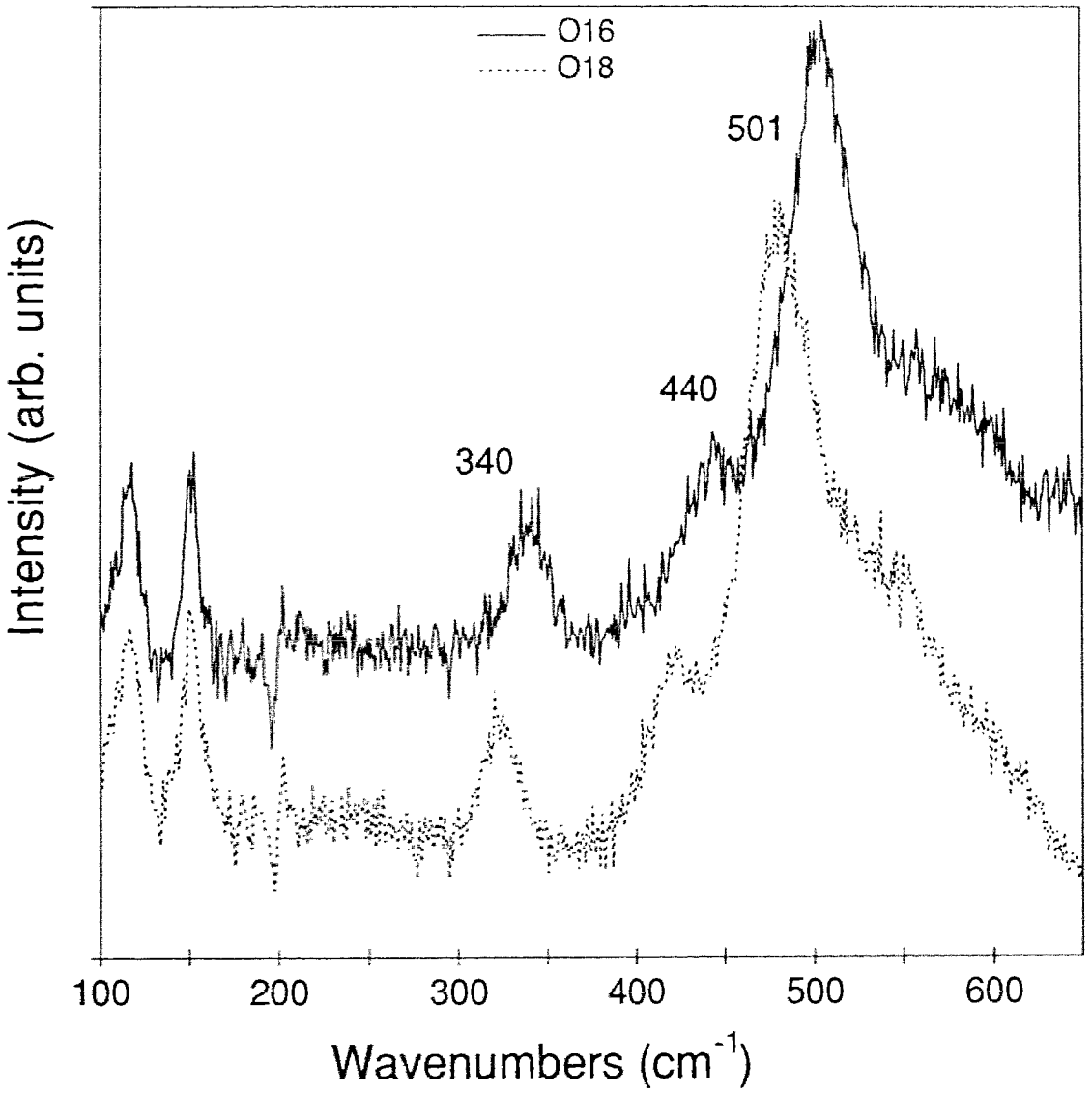

Figure 3.12

Characteristic Raman spectrum for a pair of oxygen $^{16}O/^{18}O$ isotope samples of $YBa_2(Cu_{0.9125}Zn_{0.0875})_3O_{7-\delta}$. The distinct shift to a lower frequency for Raman active oxygen modes: 340 cm^{-1}, 430 cm^{-1} and 501cm^{-1} can be seen with the substitution of the heavier isotope ^{18}O for ^{16}O.

3.7 SIMS CHARACTERIZATION

The extent of the ^{18}O substitution is obtained from SIMS measurements and is reported in a table in each of the respective sections of chapters 6, 7 and 8. Generally, the concentration of atomic ^{18}O, which is indicative of the completeness of the substitution is in the range of 75% to 92%.

The oxygen content was determined by iodometric titration. There was little change in the oxygen stoichiometry, varying from 6.92 ± 0.03 to a maximum of 6.94 ± 0.03. The oxygen stoichiometry is thus not likely to be a factor in any of the measurements.

4.0 THEORY

There is as yet no theory which correctly describes the behaviour of the high temperature superconductors. The BCS theory falls short in explaining many of the characteristics of the new materials. The absence of an isotope effect in early measurements drew much of the theoretical community away from phonons playing an important role in the mechanism for high T_c superconductivity. With the proven existence of an isotope effect, some attention has been refocused on the use of phonons. The discovery of the isotope coefficient's dependency on concentration x in the $La_{2-x}Sr_xCuO_4$ (*LSCO*) system[34] has lead to a number of proposals to account for this dependency. Models such as a phonon modified Fermi-liquid[82], pair breaking[83] and the use of an energy-dependent electronic density of states[84,85] have been proposed.

This chapter is set up into three sections. The first section briefly discusses the BCS theory and how the isotope coefficient is obtained from it. The second section deals with Van Hove singularity (VHS) calculations introduced into the BCS formalism and the last section approaches the isotope effect in high T_c superconductors through the use of the Eliashberg equations. Each section is meant to highlight some of the more important aspects and not as a review of each respective topic. For a review, there exists a large number of books and review articles covering conventional[86,87] and high T_c superconductivity[88-91], Van Hove singularities[92-96] as well as Eliashberg theory[97,98], a few of which are referenced here.

4.1 ISOTOPE EFFECT IN THE BCS THEORY

The motion of an electron through the lattice causes a distortion in the lattice. This distortion gives rise to a phonon which then affects a second electron. The process, being a virtual one, is given visually in Figure 4.1. Here an electron of wave vector, $\mathbf{k}_1$, emits a phonon, $\mathbf{q}$, which is then absorbed by electron, $\mathbf{k}_2$, scattering it into state $\mathbf{k}_2+\mathbf{q}$. As a consequence of the uncertainty principle and the very short lifetime of the phonon, energy does not need to be conserved. The nature of the resulting phonon mediated electron - electron interaction is then dependent on the magnitude of the Coulomb repulsion and the attraction between the second electron and the positive charge fluctuation around the first electron created by the lattice distortion. If the attractive phonon energy, $\hbar\omega_q$, is greater than the repulsive electronic energy, the interaction is attractive and results in a bound Cooper pair. This is the basic interaction responsible for superconductivity.

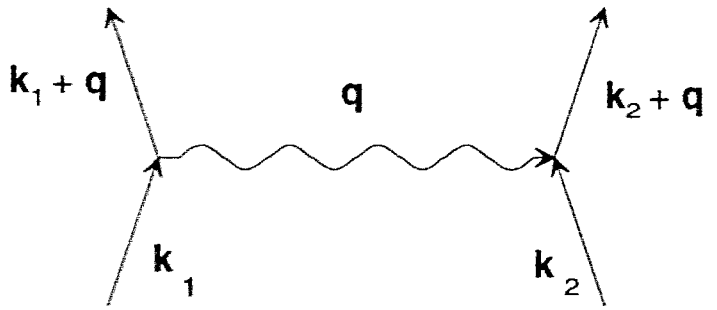

Figure 4.1

Visual representation of the electron-phonon interaction.

Cooper showed that if there was a net attraction between a pair of electrons just above the Fermi surface, these electrons can form a *quasi*-bound pair in a state of lower energy. The electrons for which this can occur (as a result of the phonon interaction) lie in a thin shell of width $\approx \hbar\omega_q$ (average phonon energy of the material). It was also shown that the most general state in which the electrons can be found is a linear superposition of pairs of quasi-particle states, and from conservation of momentum, these states should have a common momentum ($\mathbf{k}_1 + \mathbf{k}_2 = \mathbf{K}$). It is also energetically more favourable to restrict the pairs to those of opposite spin.

The correlation energy for the electron - phonon - electron interaction is quite small $\approx 10^{-3}$-10^{-4} *eV*, compared to the 10 - 20 *eV* for the Fermi energy. The BCS theory makes the assumption that for superconductivity, the zero energy of the system is the normal ground state energy, leaving the ground state energy of the superconducting state due solely to the correlation between the Cooper pair (of opposite spin electrons) and the momentum (by phonon and screened Coulomb interaction). The ground state of this system will occur when we have the largest number of possible transitions, and this occurs when

$$\mathbf{K} = 0,\ \mathbf{k}_1 = -\mathbf{k}_2 = \boldsymbol{k}.$$

The transition of an electron pair from

$$(\boldsymbol{k}\uparrow, -\boldsymbol{k}\downarrow) \text{ to } (\boldsymbol{k}'\uparrow, -\boldsymbol{k}'\downarrow)$$

is given by the matrix element

$$-V_{\boldsymbol{k}\boldsymbol{k}'} = 2\,(\boldsymbol{k}'\uparrow, -\boldsymbol{k}'\downarrow \mid H_{int} \mid \boldsymbol{k}\uparrow, -\boldsymbol{k}\downarrow) \qquad [4.1]$$

where H_{int} is the interaction Hamiltonian.

Because of the similarity in the superconducting characteristics of a number of different materials, BCS made the assumption that $V_{kk'}$ is isotropic and constant relative to the Fermi surface, when the Fermi particle energy, ε_k, is below the average phonon energy, and vanishes elsewhere:

$$V_{kk'} = V \quad ; \quad \varepsilon_k, \varepsilon_{k'} \leq \hbar\omega_q \qquad [4.2]$$

$$= 0 \quad ; \quad \text{otherwise.}$$

Then

let h_k = probability that states k,-k are occupied by a pair of electrons

let f_k = probability of occupation of state k or -k by a single normal electron

$1-2f_k$ = probability that neither state k nor -k is occupied by a single normal electron

the kinetic energy of the system is given by

$$W(T) = 2\sum_k \left\{ |\varepsilon_k| \left(f_k + (1-2f_k)h_k \right) \right\} . \qquad [4.3]$$

The entropy of a Fermi particle is

$$TS = -2k_B T \sum_k \left\{ f_k \ln f_k + (1-f_k)\ln(1-f_k) \right\} . \qquad [4.4]$$

Minimizing the free energy

$$G = W(T) - TS \qquad [4.5]$$

with respect to f_k gives

$$f_k = \left(e^{E_k/k_B T} + 1 \right)^{-1} \qquad [4.6]$$

and minimizing with respect to h_k gives

$$\frac{\sqrt{h_k(1-h_k)}}{1-2h_k}=\frac{V\sum_{k'}\left\{(1-2f_{k'})\sqrt{h_{k'}(1-h_{k'})}\right\}}{2\varepsilon_k}=\frac{\varepsilon(T)}{2\varepsilon_k} \qquad [4.7]$$

were $\varepsilon(T)$ is the energy of the electron pair at temperature T,

$$\varepsilon(T)=V\sum_{k'}\left\{(1-2f_{k'})\sqrt{h_{k'}(1-h_{k'})}\right\}. \qquad [4.8]$$

Setting

$$E_k=\sqrt{(\varepsilon_k^2+\varepsilon^2(T))} \qquad [4.9]$$

and solving for h_k gives

$$h_k=\tfrac{1}{2}\left(1-\frac{\varepsilon_k}{E_k}\right). \qquad [4.10]$$

Solving (self consistently) for $\varepsilon(T)$ we get

$$\varepsilon(T)=\frac{V}{4}\sum_{k'}\left\{\frac{\varepsilon(T)}{\sqrt{\varepsilon_{k'}^2+\varepsilon^2(T)}}\tanh\left(\frac{\sqrt{\varepsilon_{k'}^2+\varepsilon^2(T)}}{2k_BT}\right)\right\}. \qquad [4.11]$$

By converting the sum over $\boldsymbol{k'}$ to an integral, noting that $V = 0$ for energies above $\hbar\omega_q$, and that at the critical temperature, $\varepsilon(T_C) = 0$ as all the pair states are broken up, we are left with

$$1=N(0)V\int_0^{\hbar\omega_q}\frac{d\varepsilon}{\varepsilon}\tanh\left(\frac{\varepsilon}{2k_BT_c}\right) \qquad [4.12]$$

where *N(0)* is the density of electronic states (DOS) of one spin in the normal metal at the Fermi surface. In the limit of $k_B T_C << \hbar\omega_q$, known as the weak coupling limit, this reduces to

$$k_B T_c \equiv 1.13\hbar\omega_q e^{-1/N(0)V} \qquad [4.13]$$

and as $\omega_q \propto M^{-1/2}$, we can see the dependence of the critical temperature on the mass, and hence the isotope effect, with the isotope coefficient $\alpha = 1/2$. The calculation produced here is based on a monatomic superconductor. In the case of more then one element with mass M_i, each will have its own (different) isotope coefficient α_i, such that

$$\alpha = \sum \alpha_i = 1/2 \quad [99]. \qquad [4.14]$$

Not all of the conventional superconductors have their isotope coefficients $\alpha = 1/2$. In fact, a large number of superconductors have $\alpha < 1/2$ (Table 4.1). This is attributed to the simplifying assumptions made in the basic BCS theory. Perhaps the main contribution being neglected is the Coulomb interaction, which may need to be included in order to account for the discrepancy between theory and experiment. Garland[9] chose a *V* that was dependent on the isotopic mass, and arrived at a modified expression for the isotope exponent $\alpha' = \alpha(1-\zeta)$, which was found to give good agreement with a number of materials. Calculations based on modifications to the cutoff energy, $\hbar\omega_q$, have been made by Swihart[10], and Morel and Anderson[11] who obtain deviations from $\alpha = 1/2$ that are in very good agreement with some experimental results and yet, not with others. These calculations are based on the Eliashberg equations which are discussed later in section 4.3.

Element	α (exptl)	α (Garland)	α (Swihart)	α (Morel)
Zn	0.45 ± 0.01	0.415 ± 0.015	0.2	0.35
Cd	0.50 ± 0.10	0.385 ± 0.025	0.34	0.37
Hg	0.50 ± 0.03	0.48 ± 0.005	0.4	0.46
Tl	0.50 ± 0.10	0.48 ± 0.02	0.3	0.43
Sn	0.47 ± 0.02	0.455 ± 0.01	0.3	0.42
Pb	0.48 ± 0.01	0.485 ± 0.005	0.3	0.47
Zr	0.0	0.15 ± 0.17		0.3
Mo	0.33 ± 0.05	0.35 ± 0.075	0.15	0.3
Ru	0.0 ± 0.10	0.065 ± 0.15	0.0	0.35
Os	0.20 ± 0.05	0.225 ± .010	0.1	0.25
Re	0.39 ± 0.01	0.355 ± 0.05		0.41

Table 4.1[100]. Isotope coefficients of some conventional superconductors. BCS theory predicts $\alpha = 1/2$ for all superconductors. The theoretical calculations of Garland, Swihart, and Morel and Anderson are based on modifications to the BCS theory via the Eliashberg equations.

4.2 ISOTOPE EFFECT - VAN HOVE SINGULARITY (HIGH T_c)

The use of a VHS[101] is not unique to high T_c superconductivity. Some models[102], even before the discovery of high T_c superconductivity, have employed them in quasi *2-D* systems. The similarity between the *2-D* nature of the VHS and the *2-D* nature of the conduction band in the high T_c systems, ie. the predominance of superconductivity in the *Cu-O*$_2$ planes, has led to the proposal of a VHS in the DOS.

Tsuei et al.[84] have proposed a logarithmic VHS in the DOS of the BCS determination of the critical temperature calculation as a possible explanation of the isotope behaviour observed by Crawford[34]. In the 2-D limit, the energy bands have saddle points at the Brillouin zone edges. This produces a peak in the electronic density of states, *N(E)*, and the Fermi energy is centered on this peak. In the VHS model, this peak in *N(E)* is represented by a logarthmetic divergence. The carriers (holes) in the DOS are separated into two regimes: those in a high DOS region near the Brillouin zone boundary, at the peak in the DOS, known as heavy holes; and a low DOS region over the rest of the Brillouin zone known as light holes. It is believed that near the VHS, in the *2-D* system, a competition between the formation of charge density waves (CDW) and superconductivity exists. The CDW are believed to be caused by instabilities related to the Fermi surface nesting found in these layered superconductors. Superconductivity is thought to persist either through the suppression of long-range order or in a short-range CDW order. In the first case, *3-D* superconductivity arises from the Josephson coupling between the *2-D* planes. In a short-range CDW order, virtual excitons excited across the CDW gap (VHS exciton[93-96]) could provide an electronic pairing mechanism which could enhance

the phonon effects. The light holes would form a CDW condensate and the heavy holes would form the superconductor condensate (pairing by the virtual excitons).

One of the high T_c band structure features discovered is that the Fermi surface of the *Cu-O*$_2$ planes in *LSCO* is almost exactly at the VHS when $x = 0.15$[103,104], which also corresponds to the maximum T_c of this system. The use of slave-boson mean-field band structure calculations for the CuO_2 systems[104,105] have also indicated that the Fermi level is pinned very close to this logarithmic singularity. Thus, Tsuei et al.[84] have placed the logarithmic VHS very near to the Fermi energy to account for the high T_c*'s* (near 40*K*). By assuming a logarithmic DOS,

$$N(\varepsilon) = N_0 \ln\left(\left|\frac{\varepsilon_f}{\varepsilon - \varepsilon_f}\right|\right) \qquad [4.15]$$

which is symmetric about the singularity, and ignoring the Coulomb interaction, equation [4.12] then becomes

$$\frac{2}{V} = \int_{\varepsilon_f - \hbar\omega_c}^{\varepsilon_f - \hbar\omega_c} \frac{d\varepsilon}{\varepsilon - \varepsilon_f} \tanh\left(\frac{\varepsilon - \varepsilon_f}{2k_B T_c}\right) N_0 \ln\left(\left|\frac{\varepsilon_f}{\varepsilon - \varepsilon_f}\right|\right) = A(\omega_c, T_c) \qquad [4.16]$$

where ω_c is the electron-phonon interaction cutoff frequency. They have taken a large value for the cutoff frequency as a reflection of a pairing mechanism via the apical oxygen modes which lie near the upper cutoff of the phonon frequency spectrum. By approximating the hyperbolic tangent function by:

$$\tanh\left(\frac{\varepsilon - \varepsilon_f}{2\kappa_B T_c}\right) = \frac{\varepsilon - \varepsilon_f}{2k_B T_c} \qquad \text{for } \varepsilon - \varepsilon_f \le 2k_B T_c$$

and [4.17]

$$= 1 \qquad \text{otherwise,}$$

setting δ as the location of the VHS with respect to the Fermi energy, and

$$T_f = \varepsilon_f / k_B$$
$$T_{c0} = \hbar\omega_c / k_B$$

the expressions for T_C and α near the singularity become

$$T_c \equiv 1.36 T_f \exp\left\{-\left[\frac{2}{N_o V} + \left(\ln\frac{T_f}{T_{c0}}\right)^2 - 1 + \frac{\delta^2}{2k_B^2}\left(\frac{1}{4T_c^2} + \frac{1}{T_{c0}^2}\right)\right]^{1/2}\right\} \qquad [4.18]$$

$$\alpha \equiv \frac{1}{2}\left\{\frac{\ln\frac{T_f}{T_{c0}} + \frac{\delta^2}{2k_B^2 T_{c0}^2}}{\ln\frac{1.36T_f}{T_c} - \frac{\delta^2}{8k_B^2 T_c^2}}\right\} \qquad [4.19]$$

where it is assumed that the energy difference $\delta < 2k_B T_C$.

Equations [4.18] and [4.19] are valid only near the singularity, $\delta \approx 0$. They show that α is a minimum when T_C is a maximum. Figure 4.2 gives a plot of α and T_C vs. δ by solving equation [4.16] self consistently for T_C and α, where α was calculated from:

$$\alpha = -\frac{\partial \ln T_c}{\partial \ln M} = -\frac{M}{T_c}\frac{\partial T_c}{\partial \omega_c}\frac{\partial \omega_c}{\partial M} = -\frac{M}{T_c}\frac{\partial A/\partial \omega_c}{\partial A/\partial T_c}\frac{\partial \omega_c}{\partial M} \qquad [4.20]$$

The top graph is the result of the calculation performed by Tsuei et al.[84] to model the results obtained by Crawford[34] on the *LSCO* system which had a maximum T_C of 38*K* and the middle graph is our extension of the calculation of Tsuei et al. to a system in which $T_C = 92K$. In both calculations, the minimum for α is ≈ 0.2 which is much larger than the α ≈ 0.05 that is observed and a maximum value (at the lower T_C's) that exceeds the BCS value of ½. Also, if one compares the α

Figure 4.2

Van Hove singularity calculations for high T_c materials.

Top: VHS calculations of Tsuei et al.[84] to model the *LSCO* system.

Middle: Our extension of the above calculation to a superconductor with a $T_c = 90K$.

Bottom: Modified VHS calculation of Newns[104].

In all cases α is a minimum at the maximum T_c, and then begins to increase with decreasing T_c. The decrease in α at the lowest T_c's seen in the top and middle graphs is not believed to be real but an artifact resulting from the limits imposed on the numerical integration.

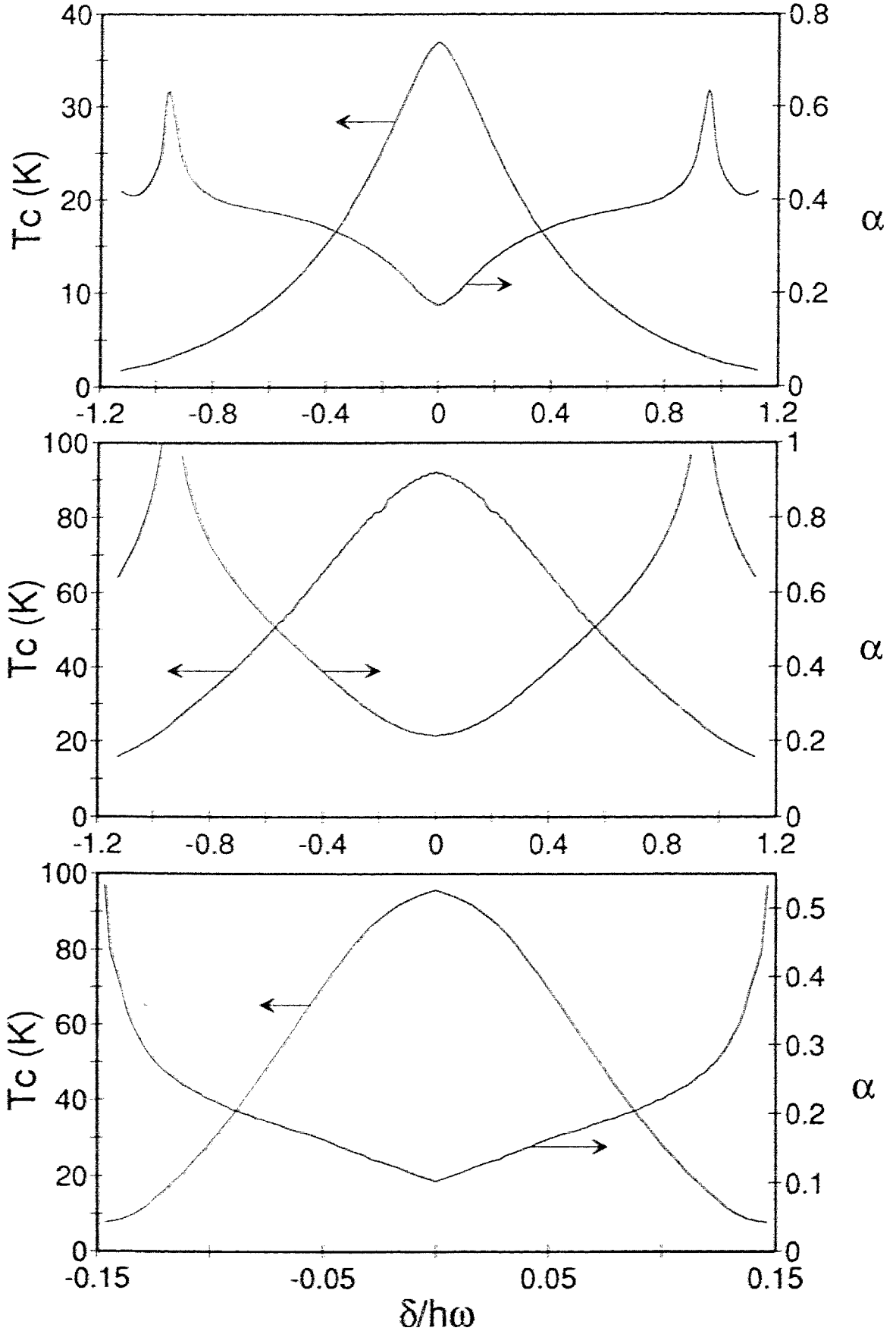
Tc (K)
α
δ/hω
40
30
20
10
0
0.8
0.6
0.4
0.2
-1.2
-0.8
-0.4
0
0.4
0.8
1.2
100
80
60
40
1
-0.15
-0.05
0.05
0.15
0.5
0.3
0.1

with T_c, we note that the higher maximum T_c calculation has a much stronger α variation with T_c, with even larger values of α obtainable.

The mechanism for the pairing of electrons for superconductivity in the high T_c materials seems unlikely to be due entirely to the effects of phonons and some account of an electronic contribution needs to be taken. Newns et al.[107] extended the VHS calculations by removing the constraint of a constant value for the electron pair scattering matrix V to better present a more realistic contribution from the Coulomb interaction. Their goal was to obtain an electron pairing mechanism that would lead to a high T_c and low isotope shifts. The mechanism is based on a strongly interacting *quasi-2D* electron system with a logarithmic VHS near the Fermi energy in the DOS. Some of the underlying physics and mathematical calculations in their paper are beyond the knowledge of the author; however, the importance of the results of their calculations for a material with a T_c of order $90K$ can be seen in the bottom graph of Figure 4.2 (Newns[107]).

Because the DOS is symmetric about the Fermi energy (in all cases), it is not surprising to see that both T_c and α are also symmetric, with their respective maxima and minima corresponding to $\delta = 0$. In comparison with the previous calculations, the addition of the electronic pairing mechanism results in a much less sensitive variation of the isotope coefficient with the changes in the DOS, as well as a much smaller value. The low values of α (minimum of $\alpha = 0.1$) are more reflective of those established in experiments on the $90K$ superconductors ($\alpha = 0.05$) than the previous calculation's value of $\alpha = 0.2$. The critical temperature also drops more rapidly with increasing doping. Low values of α exist for relatively high T_c's, and high α values only for the lowest T_c's, and even then $\alpha = {}^1/_2$.

The relationship between T_c and α is mediated by the energy difference between the peak in the DOS and the Fermi energy. This difference in energy is attributed to the change in the carrier concentration (from its optimum value for a maximized T_c) of the material. Only a linear relationship between the carrier concentration and δ would imply the symmetric behaviour noted here. In the *LSCO* system, this symmetry about the optimum hole concentration does not exist. However, the relationship between the carrier concentration, and the shift in energy, δ, is not yet known.

A number of questions and problems plague the logarithmic VHS method described above. For example, is the need for a logarithmic VHS necessary? R. Combescot[108] and Xing et al.[109] (among others) have noted that any strongly varying DOS will lead to a deviation from $\alpha = 1/2$ and that the extremely low values of the isotope coefficient observed, e.g. $\alpha \approx 0.02$ and the high critical temperatures require unlikely assumptions and values for the parameters in this model. Another question is whether the use of a cutoff frequency at the Debye energy is a valid assumption.

On a qualitative basis, the calculations based on the logarithmic VHS in the DOS are able to account for a number of observed experimental effects[37,84,92-96,106]: the relationship between the hole concentration and the critical temperature; the relationship between the hole concentration and the isotope exponent; the linear normal state resistivity; specific heat properties; and pressure effects. However, there is still much debate on the validity of the methods and the conclusions of these and similar types of theoretical calculations in the community.

4.3 ISOTOPE EFFECT - ELIASHBERG EQUATIONS (HIGH *Tc*)

One of the most successful expansions of BCS theory is the approach taken by Eliashberg[12]. Here, a formal Green's function approach is used to include the details of the electron-phonon interaction into the theory. Although the theory is quite useful in obtaining experimental observables, it lacks an analytical form, and solutions are obtained through numerically solving the equations self-consistently. There are a number of different forms (kernels) for the Eliashberg equations, the choice of which depends on the effect being modeled. In all cases, the important parameters are the spectral function $\alpha^2F(\omega)$ and μ^*. Here $\alpha(\omega)$ is the electron-phonon coupling term (squared indicates that a pair of electrons are involved), $F(\omega)$ is the phonon frequency distribution (phonon DOS), and μ^* is the effective Coulomb repulsion.

At T_C, the linearized Eliashberg equations[110] are given by

$$\Delta(i\omega_n)Z(i\omega_n) = \pi T \sum_{m=-\infty}^{\infty}\left[\lambda(i\omega_m - i\omega_n) - \mu^*(\omega_c)\Theta(\omega_c - |\omega_m|)\right]\frac{\Delta(i\omega_m)}{|\omega_m|} \qquad [4.21]$$

$$Z(i\omega_n) = 1 + \frac{\pi T}{\omega_n}\sum_{m=-\infty}^{\infty}\lambda(i\omega_m - i\omega_n)\,\mathrm{sgn}(\omega_m) \qquad [4.22]$$

where

$$\mu^*(\omega_c) = \frac{\mu(E_F)}{1 + \mu(E_F)\ln\left(E_F/\omega_c\right)} \qquad [4.23]$$

$$\lambda(z) = 2\int_0^{\infty} d\nu \frac{\nu}{\nu^2 - z^2}\alpha^2F(\nu) \qquad [4.24]$$

and

$$\Theta(x) = 1 \qquad \text{if } x < 1; \qquad [4.25]$$
$$0 \qquad \text{if } x > 1;$$

and $i\omega_m = i\pi T(2m\text{-}1)$, $m = 0, \pm1, \pm2,...$ are the Matsubara frequencies for fermions, $\Delta(i\omega_n)$ are the Matsubara gaps, $Z(i\omega_n)$ is the mass renormalization function, and the potential, μ^*, has been renormalized using a cutoff frequency, ω_c, for the Coulomb interaction[11]. The frequency used for the cutoff is typically the highest frequency of the phonon spectrum.

The value of $\alpha^2F(\omega)$ can be experimentally determined from tunneling data but more often the dimensionless parameter, $\lambda = \lambda(0)$ (different from the standard use of λ_L as the penetration depth), is introduced as a measure of the strength of $\alpha^2F(\omega)$ and hence the electron-phonon coupling. A second parameter, ω_{ln}, is also introduced, where

$$\omega_{ln} = \exp\left\{\frac{2}{\lambda}\int_0^\infty d\nu \frac{\ln \nu}{\nu}\alpha^2F(\nu)\right\} \qquad [4.26]$$

The value of λ gives an indication of which phonons in $\alpha^2F(\omega)$ play an important role. For large λ (> 1), it is the low frequency phonons which contribute while if $\lambda \rightarrow 0$, it is the high frequency phonons which are important. The first case is known as the strong-coupling case. The second case is the weak-coupling limit, and in fact, the BCS equations can be obtained in this limit where the BCS *N(0)V* term is replaced by $(\lambda\text{-}\mu^*)/(\lambda+1)$. The parameter ω_{ln} represents the average phonon frequency of the $\alpha^2F(\omega)$ spectrum and is used as a replacement for $\alpha^2F(\omega)$. It is essentially a delta function, at ω_{ln}, the value of which is equal to the area under the $\alpha^2F(\omega)$ spectrum. It can be compared with the cutoff frequency, ω_c, of the BCS theory. By choosing the above delta function, the cutoff frequency employed in the renormalization of μ^* just needs to

be greater then ω_{ln}. To ensure that there is good convergence in the sums of the Eliashberg equations, the cutoff frequency used should be much greater than ω_{ln}. A cutoff of 1000 *meV* has been used in all computations in this thesis.

The Eliashberg equations are then formulated into functions of λ, μ^*, and ω_{ln}. A value for the cutoff frequency, ω_c, which technically should be infinite, is usually not important provided it is much larger than the maximum phonon energy. As no analytic form exists for the Eliashberg equations, some approximate forms for T_c have been derived. The Allen and Dynes[111] refinement of the McMillan equation[112,113], from which the importance of the three parameters introduced, λ, μ^*, and ω_{ln} can be seen, is perhaps the most important one where:

$$k_B T_c = \frac{\hbar\omega_{ln}}{1.2}\exp\left\{-\frac{1.04(1+\lambda)}{\left(\lambda-\mu^*(1+0.62\lambda)\right)^2}(\mu^*)^2\right\} \qquad [4.27]$$

from which the isotope coefficient can be obtained[110]

$$\alpha = \frac{1}{2}\left[1-\frac{1.04(1+\lambda)(1+0.62\lambda)}{\left(\lambda-\mu^*(1+0.62\lambda)\right)^2}(\mu^*)^2\right] \qquad [4.28]$$

Typical values for conventional strong-coupling superconductor (e.g. *Pb*[99]) are $\lambda = 1.55$, $\omega_{ln} = 4.829$ *meV* and $\mu^* = 0.144$.

With the high temperature superconductors, it is difficult to obtain the high T_c of these materials with the Eliashberg equations while keeping the reasonable values of λ, μ^* and ω_{ln} and at the same time accounting for the small isotope coefficients found at these high temperatures. For instance, with $\omega_{ln} = 20$ *meV*, $\mu^* = 0.13$, a $T_c = 90K$ requires $\lambda = 7$ and gives an isotope coefficient of

$\alpha = 0.496$. Lower values of ω_{ln} require higher values of λ to maintain a $T_c = 90K$ and higher values of ω_{ln} still require fairly large λ values, e.g. $\omega_{ln} = 50\ meV$, $\mu^* = 0.18$, $T_c = 90K$ requires $\lambda = 2$ and $\alpha = 0.48$. But again, the isotope coefficient remains much too high to fit the high T_c superconductors.

One method of obtaining a low isotope coefficient and a high critical temperature is if $\mu^* < 0$[114,115]. This can be realized from a joint electron-phonon plus an electronic mechanism. By combining a constant BCS pairing interaction, *N(0)V*, which is large enough to overcome the Coulomb repulsion, μ^*, we can obtain the Coulomb pseudopotential:

$$\mu^*_{eff} = -N(0)V + \mu^* \qquad [4.29]$$

which, when $\mu^*_{eff} < 0$, we have a net attractive interaction. Such a mechanism could involve charge or spin fluctuations, a very-high-energy boson exchange process or some other mechanism. With a set of three parameters: λ, μ^*_{eff} (< 0), and ω_{ln}, practically any set of T_c and α can be fitted. For the *YBCO* system in which $\alpha \approx 0.05$ and $T_c = 90K$, there exist an infinite number of combinations of λ, μ^*_{eff} and ω_{ln} (Figure 4.3) for which these values can be obtained. It then becomes important to determine the validity of the parameters obtained in a fit of the data. One such restriction is that the use of *N(0)V* in μ^*_{eff} is valid only in the BCS limit, and thus values of λ should be small. Gurvitch and Fiory[116] put an upper limit on $\lambda < 0.21$ from resistivity data. The phonon spectrum extends up to 100 *meV* and Weber[117] obtained the spectral density, $\alpha^2F(\omega)$ for *LSCO* from which a value of $\omega_{ln} \approx 15\ meV$ was obtained.

The reduction of T_c due to the substitution of *Pr* for *Y* and *Zn* for *Cu* in *YBCO* may be related to a magnetic pair-breaking mechanism as postulated in section 2.2.1. Carbotte et al.[83] proposed a second modification to the Eliashberg

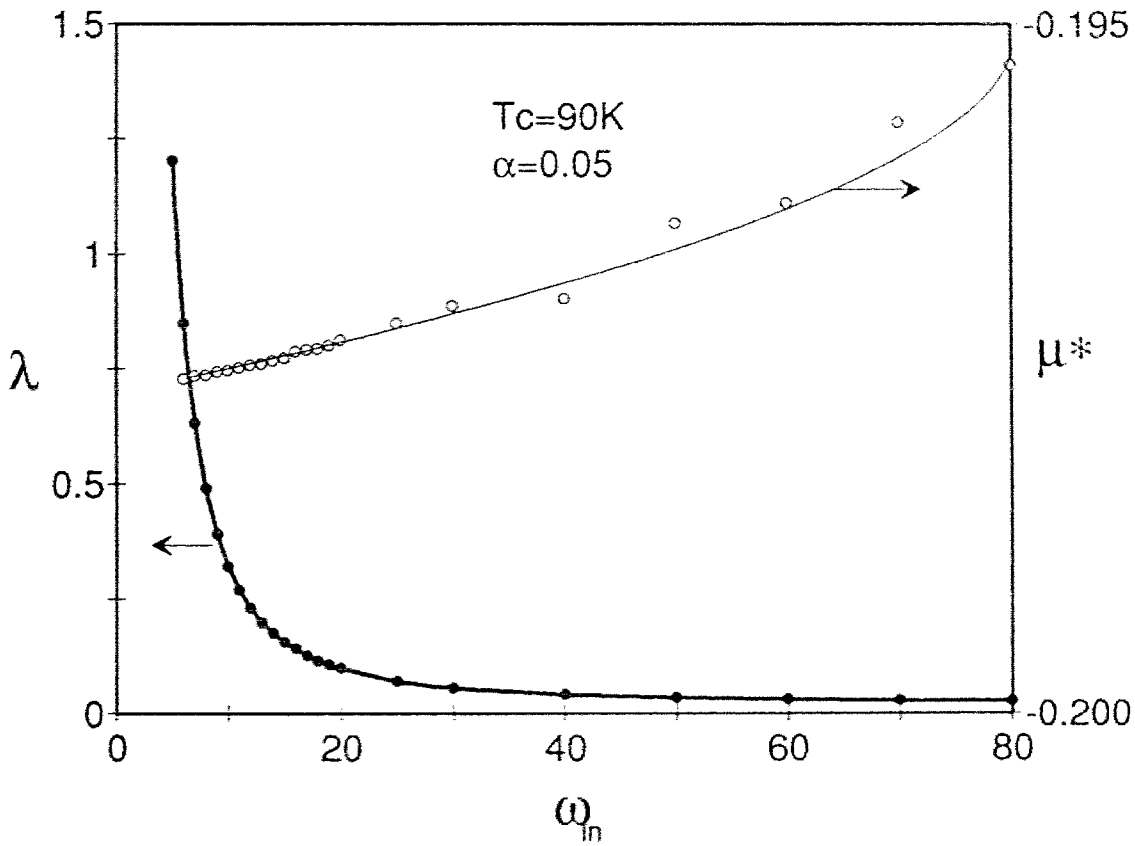

Figure 4.3

Eliashberg calculations for a given T_c = 90K and α = 0.05. The Eliashberg equations are solved self-consistently for μ^* using the values of ω_{ln} and λ that result in a T_c = 90K and an α = 0.05. The solid dots show the required pairs of ω_{ln} and λ while the open circles give the corresponding μ^* value. The change in μ^* is quite small over the entire range (~ 1%).

equations that includes a pair breaking factor, t, as can be seen from the last term in each of the two equations:

$$\Delta(i\omega_n)Z(i\omega_n) = \pi T \sum_{m=-\infty}^{\infty} \left\{ \left[\lambda(i\omega_m - i\omega_n) - \mu^*_{eff}\,\Theta(\omega_c - |\omega_m|) \right] \frac{\Delta(i\omega_m)}{|\omega_m|} \right\} - \frac{\pi t \Delta(i\omega_n)}{|\omega_n|} \qquad [4.30]$$

$$Z(i\omega_n) = 1 + \frac{\pi T}{\omega_n} \sum_{m=-\infty}^{\infty} \lambda(i\omega_m - i\omega_n)\,\mathrm{sgn}(\omega_m) + \pi t\,\mathrm{sgn}(\omega_n) \qquad [4.31]$$

where $t = 1/2\pi\tau_p$. τ_p is the characteristic scattering time associated with the magnetic impurities. As the pair-breaking scattering rate is increased, the critical temperature drops, and the isotope coefficient increases. Thus, values of $\alpha < 0$ (for low T_c) or $\alpha > 1/2$ can achieved.

More regarding the effects of a negative changing μ^*_{eff} and/or t will be discussed in conjunction with our data in chapter 9.

5.0 RESULTS - GENERAL

Twenty pairs of samples were used in this investigation: five *Pr* substitutions, six *Pr* & *Ca* substitutions and nine *Zn* substitutions. This alone represents a total of 200 different measurements consisting of resistance measurements on pellets and bars, magnetization measurements of ZFC and FC curves at 0.05*Oe*, and susceptibility measurements. This does not include the numerous measurements made to ensure that the results were reproducible as well as other resistive and magnetic measurements. Analysis of this data is mainly concerned with the determination of the critical temperature and how to calculate the shift in T_c between isotope pairs. To create an ease of comparison between numerous sets of data, some form of normalization has been carried out on all the data. All isotope comparisons for the magnetic measurements are performed on the ZFC curves as opposed to the FC curves. Although there is no difference in T_c between ZFC and FC measurements, there is greater control over the temperature profile upon warming than there is on cooling and the ZFC measurement gives a larger signal than the FC.

For dc magnetization measurements, the data is normally scaled to the measuring field, *H*, and the molar volume. This is done to reflect the ideal relationship between the magnetization (per unit volume), *M*, and the applied external field, *H*. In the event of no trapped flux, an infinitely small λ_L and no geometric dependencies, the superconductor is perfectly diamagnetic with a susceptibility of χ = -1/4π, that is $\frac{4\pi M}{H} = -1$ at $T = 0K$ and $\frac{4\pi M}{H} = 0$ at $T = T_c$. Because of difficulties arising from demagnetizing effects, differences in the geometry between samples and the calculation of return-flux corrections, the

data was simply normalized from 0 to 1. In the case of comparisons with regard to the Meissner fraction, the FC data was normalized with the same factor as the ZFC data. In the application of different measuring fields, the data was scaled by the applied field and not normalized from 0 to 1 as above.

The dc magnetization and ac susceptibility both have "flat" (zero slope) regions at very low temperatures and above T_c (in the normal state), and are normalized from 0 to 1 corresponding to these two regions. In some cases, a very small background above T_c, which increases linearly with temperature, was found in the data. The origin of this background is unclear but is likely due to either a small amount of dirt or oxygen in the grease used for mounting or perhaps due to air frozen within the stick space and near the pickup coils. In any case, the average slope of the background in the "flat" region well above T_c is computed and the entire data range is corrected by subtracting this background and then the data is renormalized.

Similarly, resistance measurements are also normalized. A "flat" region exists only below T_c where the resistance is zero. Above the transition, the data is more or less linear with temperature. Well above the critical temperature, a linear fit to this region is done and the pair of isotope samples are normalized from 0 to 1 at the same temperature. The temperature of normalization is given on all the presented graphs.

5.1 DETERMINATION OF T_C AND ΔT_C

There are a number of different ways of calculating the critical temperature from the magnetic measurements. The most common method used is to observe the temperature at which the onset of diamagnetic shielding first occurs and take this as the critical temperature. This is the point at which our normalized curves first fall below the normalized value of 1. A second method would be to take a linear extrapolation of the bulk of the transition back to 1 and use the intercept value for T_c. Both methods give the same T_c if one is dealing with single crystals as their magnetic transitions are quite sharp (Figure 3.7) or for samples that have very small (if any) tails at low shielding. Polycrystalline samples tend to have larger tails at small shielding as well as broader transitions. Then the two methods do not agree. Since it is most likely that the bulk reflects the desired superconducting phase, and the small tails are due to impurities, the linear extrapolation method is used to obtain T_c. The temperature obtained from the first method is used as the upper limit in the uncertainty in T_c. Because there is always some noise involved in the measurements, this is not a well defined point. The temperature at which the Simplex fit to the data (described below) first falls below the noise in the data is taken as the upper limit in T_c. The lower limit for T_c, $0.2K$, is taken from the uncertainty in thermometry (section 3.32).

A linear fit, over the range of 0 to 0.5, to the normalized resistance data is used. In the cases where this is not sufficient, a third order polynomial is used. This approach seems to be quite adequate. The temperature at which the resistance goes to zero is used as the critical temperature. In the event that the resistance curves have long tails near zero resistance, the temperature at which

a linear extrapolation of the bulk of the transition intercepts zero is used instead. No fixed method was used for determining the uncertainty in T_c.

The shift between the two isotopic curves is computed based on the fit to the data. For magnetic measurements, the regimes in which the onset of superconductivity occurs, the top 10% of the transitions are compared to obtain the shift in T_c. This is done in order to minimize the effects of sample geometry and demagnetization effects. The discrete data points are fitted to a smoothly varying function by means of a Simplex[118] least square fitting program consisting of three variables. The function used in the Simplex fit is:

$$y = \frac{(\ln(t)/t) - e^{-1}}{s} + 1 \; ; \quad T < T_c \qquad [5.1]$$

$$y = 1 \; ; \quad T \geq T_c$$

where

$$t = e^1 + a(T_c - T)$$

and a, s and T_c are the fitting parameters. For each pair of isotope measurements, the two curves are fitted and the temperature shift between these two curves is computed between 0.90 and 1.00 (on the normalized magnetic scale) for evenly spaced (every 0.02) points to obtain 50 isotope values - ΔT_i. In some cases (such as a rapid change in the shape of the data), the data does not fit well over the entire region, in which case the fit is done in two steps involving two different smaller regions. The shifts in T, ΔT_i, for both the dc magnetization and the ac susceptibility are found in this manner.

The spread of the fitted ΔT_j data reflects the change in the magnetic response of the samples with respect to temperature. Because the small tail effects may be due to impurities, a change in the behaviour of ΔT_j is taken as an indication that the data is no longer representative of the bulk phase. The onset point of this change is used as the upper cutoff in the calculation of the mean in ΔT_j. Because the ΔT_j values are evenly spaced on the magnetic axis as opposed to the temperature axis, the (end of the) bulk transition is much more heavily weighted in the calculation of the mean than the tail. The standard deviation in ΔT_j gives us the uncertainty.

There is no theoretical reason for fitting to this particular function - it is merely due to the similarity in shape between the data at the onset of superconductivity and the $\ln(x)/x$ function, and the desire to fit to a smoothly varying function.

The Simplex fit, the critical temperature, the isotopic shift in temperature, and the uncertainties for a characteristic sample can be seen in Figure 5.1.

Figure 5.1

Simplex fit to data for determining the isotope shift and T_c.

BOTTOM:

Bulk of the magnetic transitions of a ^{16}O and ^{18}O sample. The solid line is a linear extrapolation of the bulk of the ^{16}O magnetic transition to 1 to obtain the critical temperature.

TOP:

An enhancement of the top 10% of the magnetic transition is shown. The filled squares represent the ^{16}O data and the empty squares the ^{18}O data. The solid line following the data represents the Simplex fit to each set of data. The "+" represent the isotopic shift between the two curves calculated at evenly spaced intervals on the magnetization scale.

The vertical dashed line indicates the cutoff point in the calculation of the mean isotope shift. All points to the left of this cutoff are used. The mean of $\Delta T_i = 0.64K$, along with the standard deviation, $\sigma = 0.033K$, are shown.

The value of T_c as well as the upper and lower limits is shown.

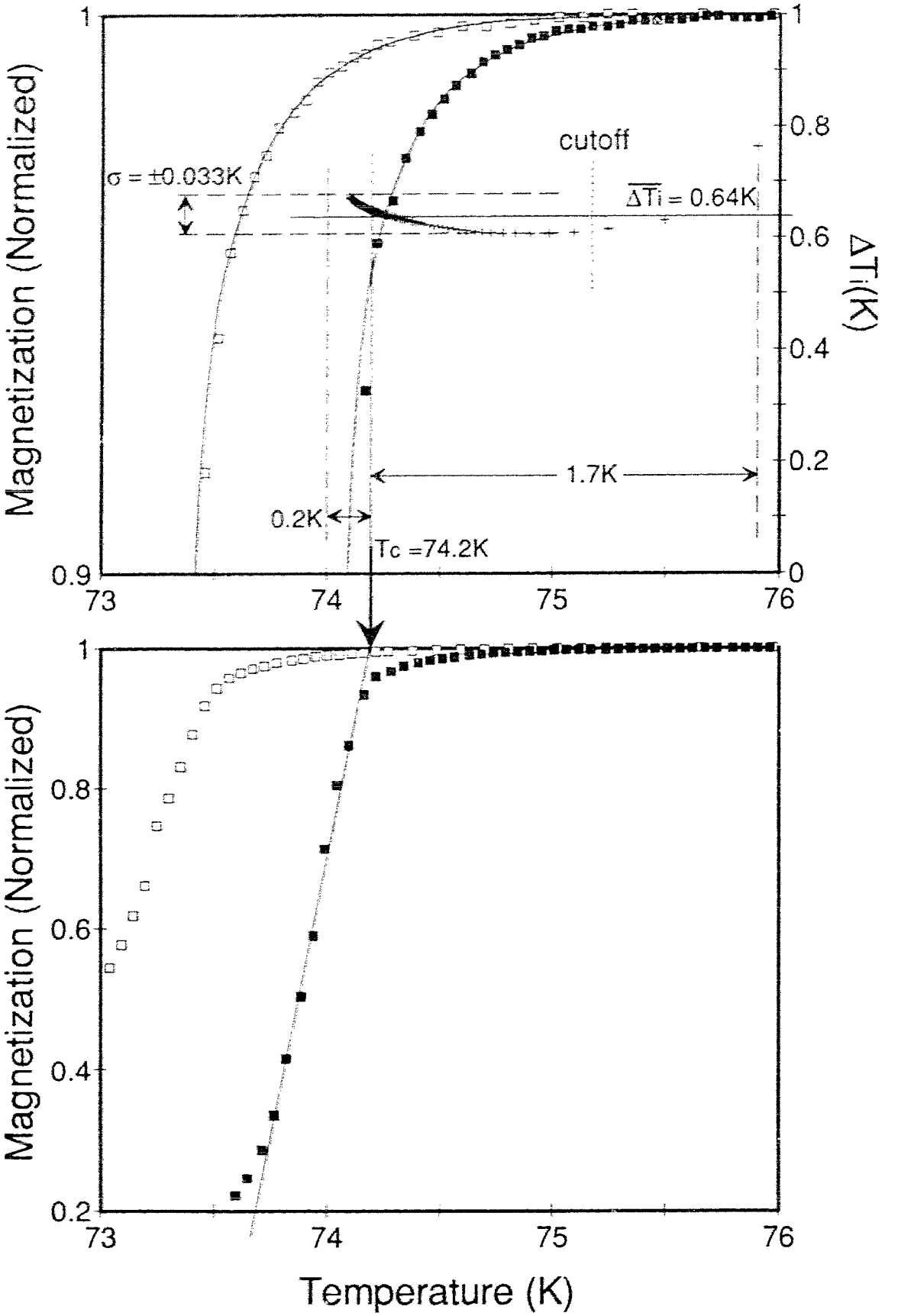
Magnetization (Normalized)
1
0.9
73
74
75
76
cutoff
σ = ±0.033K
ΔTi = 0.64K
1.7K
0.2K
Tc =74.2K
ΔTi(K)
1
0.8
0.6
0.4
0.2
0
Magnetization (Normalized)
1
0.8
0.6
0.4
0.2
73
74
75
76
Temperature (K)

6 RESULTS - PRASEODYMIUM SUBSTITUTION

6.1 SAMPLE PREPARATION

The mixed powders of $(Y_{1-x}Pr_x)Ba_2Cu_3O_{7-\delta}$, with $x = 0.2$, 0.3, 0.4, and 0.5, were calcined in air at 905°*C* for a total of 125 hours. The calcined powders were always quenched to room temperature. Three intermediate grindings were performed to improve the homogeneity. The sintering process consisted of the following temperature treatment in the parallel processing system:

1) heating to 935°*C* and holding for 7 hours; then
2) cool to 450°*C* and hold for 10 hours; then
3) cool to 350°*C* and hold for 10 hours; then
4) cool to 250°*C* and hold for 10 hours; then
5) cool to room temperature.

All sintering cooling processes were at the natural cooling rate of the oven.

The *Pr* results represent the earliest measurements. Field cooled curves and resistivity measurements on shaped bars were not performed. Magnetization (ZFC) and susceptibility were performed on small flakes of various shapes and sizes on the order of a couple of millimeters in size.

The Meissner fractions and resistance measurements were obtained by J. Franck's group. Magnetic measurements were performed in a Quantum Design Magnetometer at an applied field of $H = 20Oe$ and are included in the characteristics in Table 6.1.

6.2 MEASUREMENTS

A comparison of dc magnetization (ZFC), the ac susceptibility, and the resistance measurements for the 20% to 50% *Pr* substitution samples are given in Figures 6.1, 6.2 and 6.3 respectively. A detailed comparison between the dc magnetization, ac susceptibility and the resistance for this system is given in Figure 6.4. The 40% *Pr* substituted sample is taken as a characteristic sample.

The immediate effect that can be seen is that the increase in the *Pr* concentration leads to a continuously decreasing critical temperature (Figure 6.5) as is expected. It is also clear that the substitution of ^{18}O for ^{16}O causes a shift in the bulk of the transition regime to a lower temperature. This isotopic shift appears to be temperature dependent as it becomes larger as the critical temperature becomes smaller. The width of the individual transitions also appear to be temperature dependent as they become wider with the decrease in critical temperature.

The width for the magnetic transitions, both dc and ac measurements, is taken from the temperatures corresponding to 10% and 90% of the full signal. The width of the resistance transition remains a little less definitive: the high temperature end of the transition is taken as the point of change from the linear slope of the normal state resistivity, and the start of the transition is taken as a linear extrapolation of the bulk of the transition to zero. The width of the transition is largest for the magnetization measurements and narrowest for the resistance measurements. The widths are given in Table 6.1.

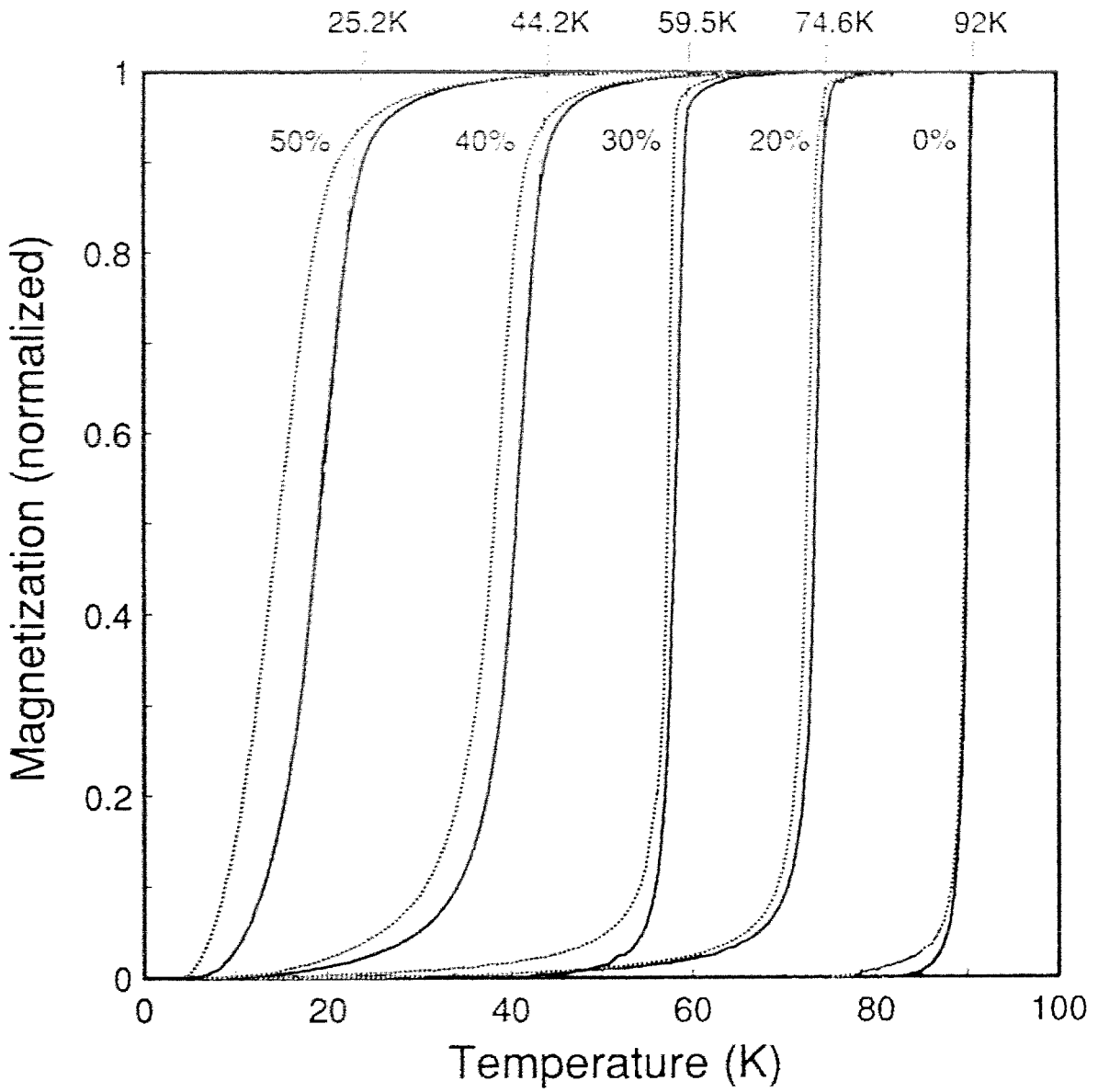

Figure 6.1

DC magnetization vs. temperature for *Pr* substituted *YBCO.* The solid lines represent the ^{16}O data and the dotted lines the ^{18}O data. The dashed lines are a linear extrapolation of the bulk of the transition to 1, the point chosen for T_c. The critical temperatures for each of the ^{16}O samples are given above the graph. Samples were measured in a field of strength $0.05Oe$. An unsubstituted sample is included as a reference ($T_c = 92K$).

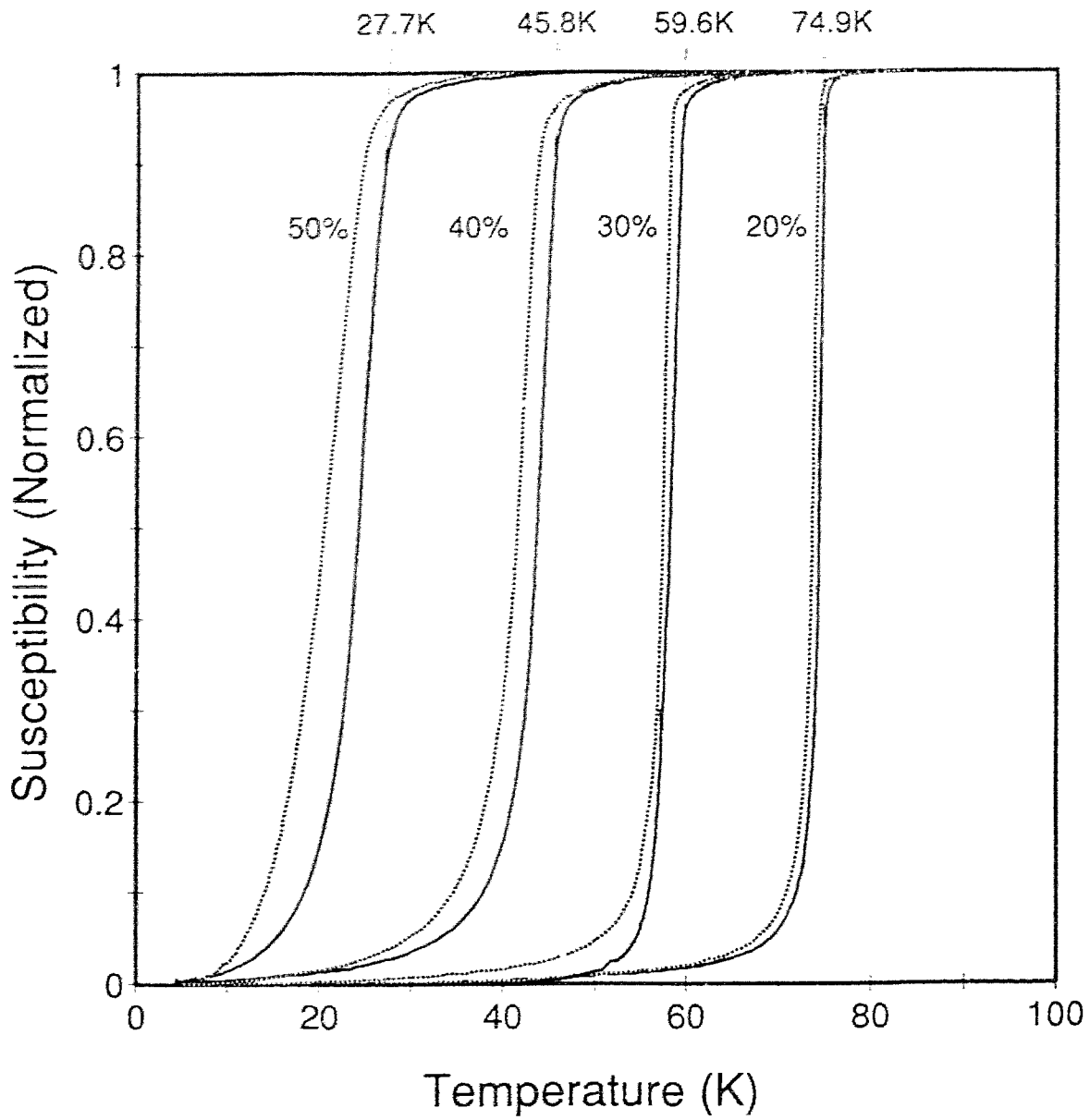

Figure 6.2

AC susceptibility vs. temperature for the *Pr* substituted *YBCO.* The solid line represents the ^{16}O isotope data and the dotted line represents the ^{18}O isotope data. The dashed lines are a linear extrapolation of the bulk of the transition to 1, the point chosen for T_c. The extrapolated critical temperatures are given at the top of the graph.

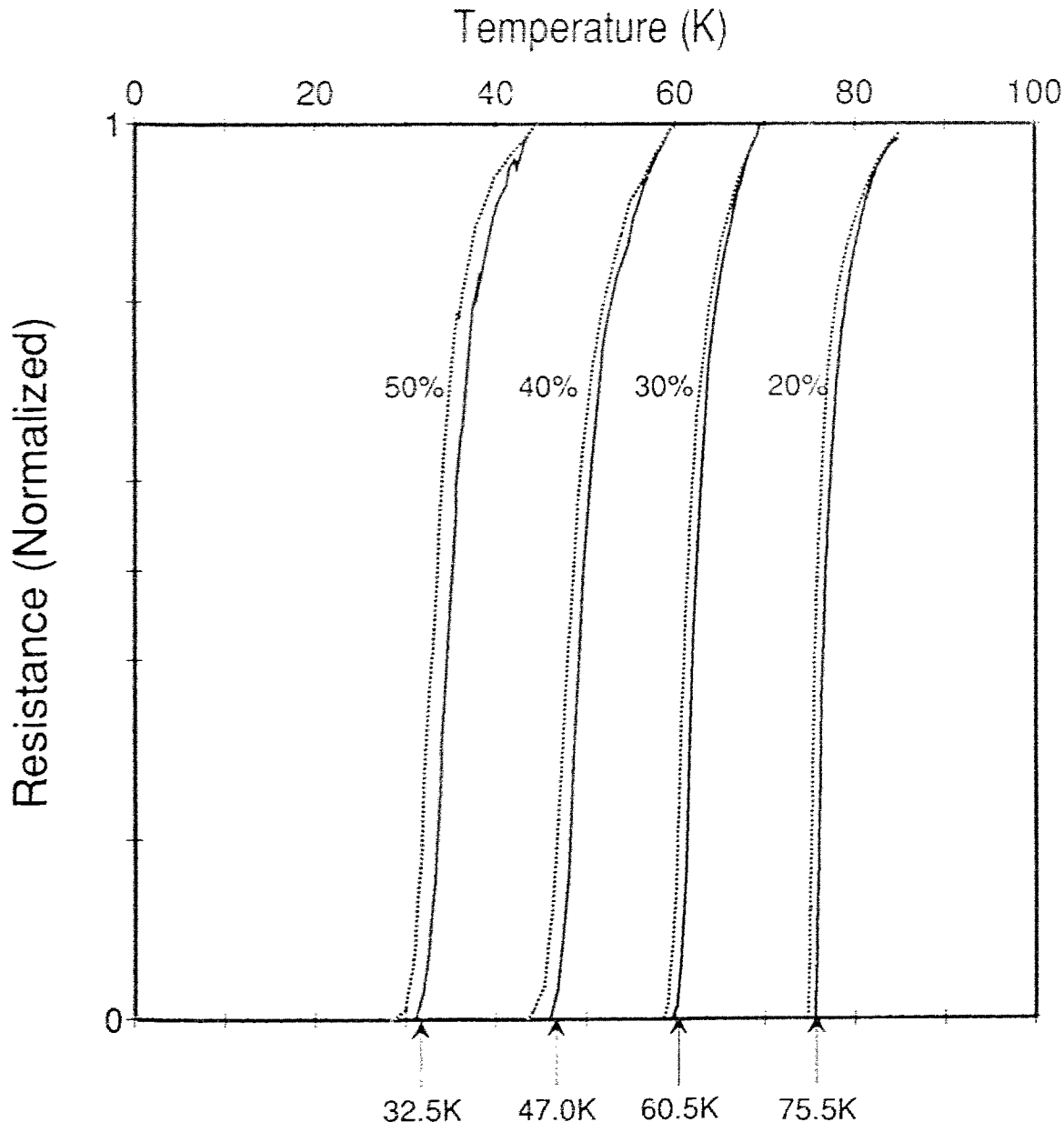

Figure 6.3

DC resistance vs. temperature for *Pr* substituted *YBCO*. The solid lines represent the ^{16}O isotope data and the dotted lines represent the ^{18}O isotope data. The normalization temperatures are 45*K*, 60*K*, 70*K* and 85*K* for the 20%, 30%, 40% and 50% substituted samples respectively. A linear extension of the bulk of the transition to 0 gives us the T_c indicated at the bottom of the graph.

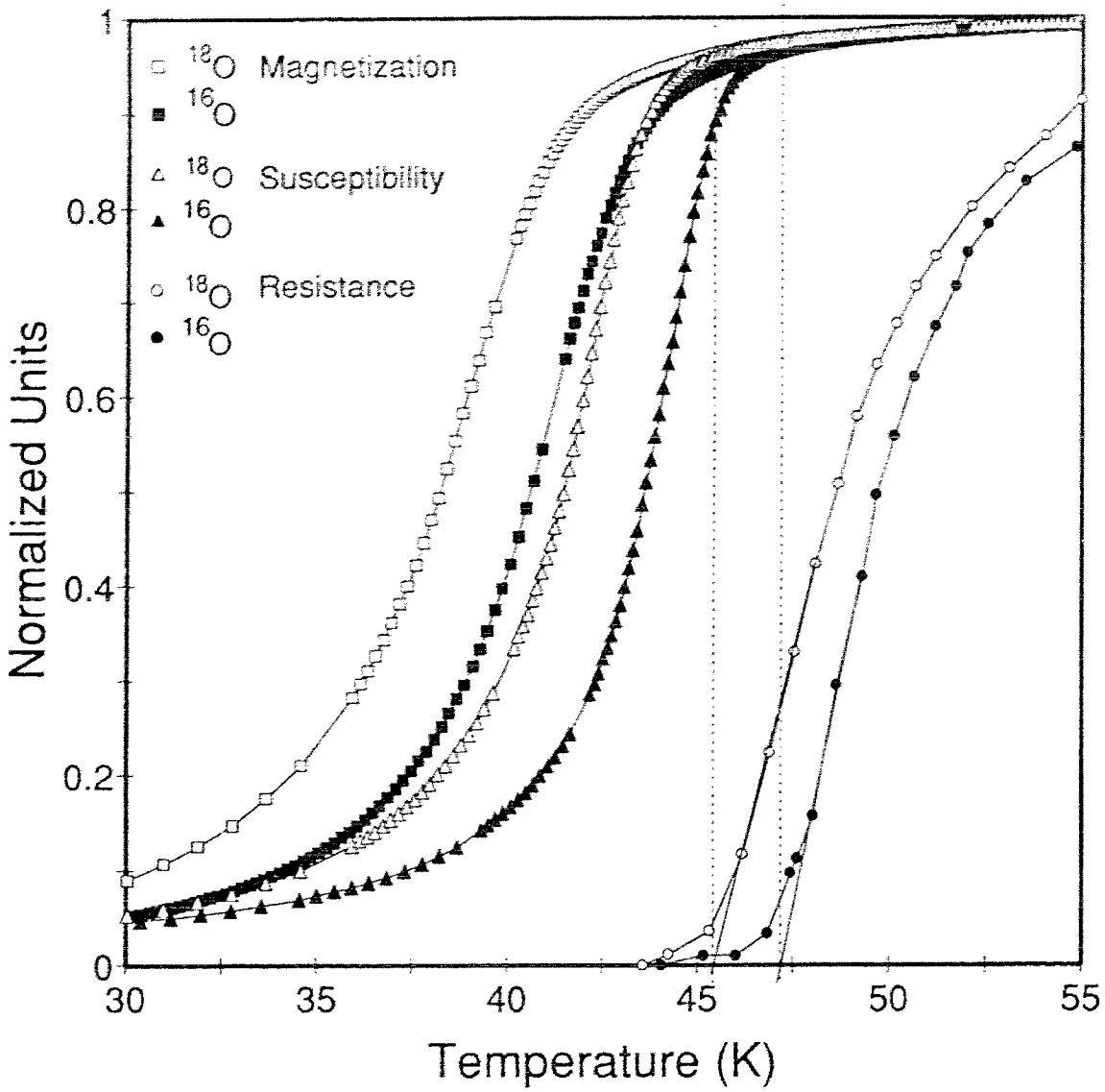

Figure 6.4

Comparison of the dc magnetization, ac susceptibility, and resistance measurements for $Y_{0.6}Pr_{0.4}Ba_2Cu_3O_{7-\delta}$. The resistance is normalized at 60*K*. The symbols represent the data. The solid lines are a guide to the eye to provide continuity between data points. The dotted lines are a visual aid to the critical temperature of the resistive transition (obtained from a straight line extrapolation).

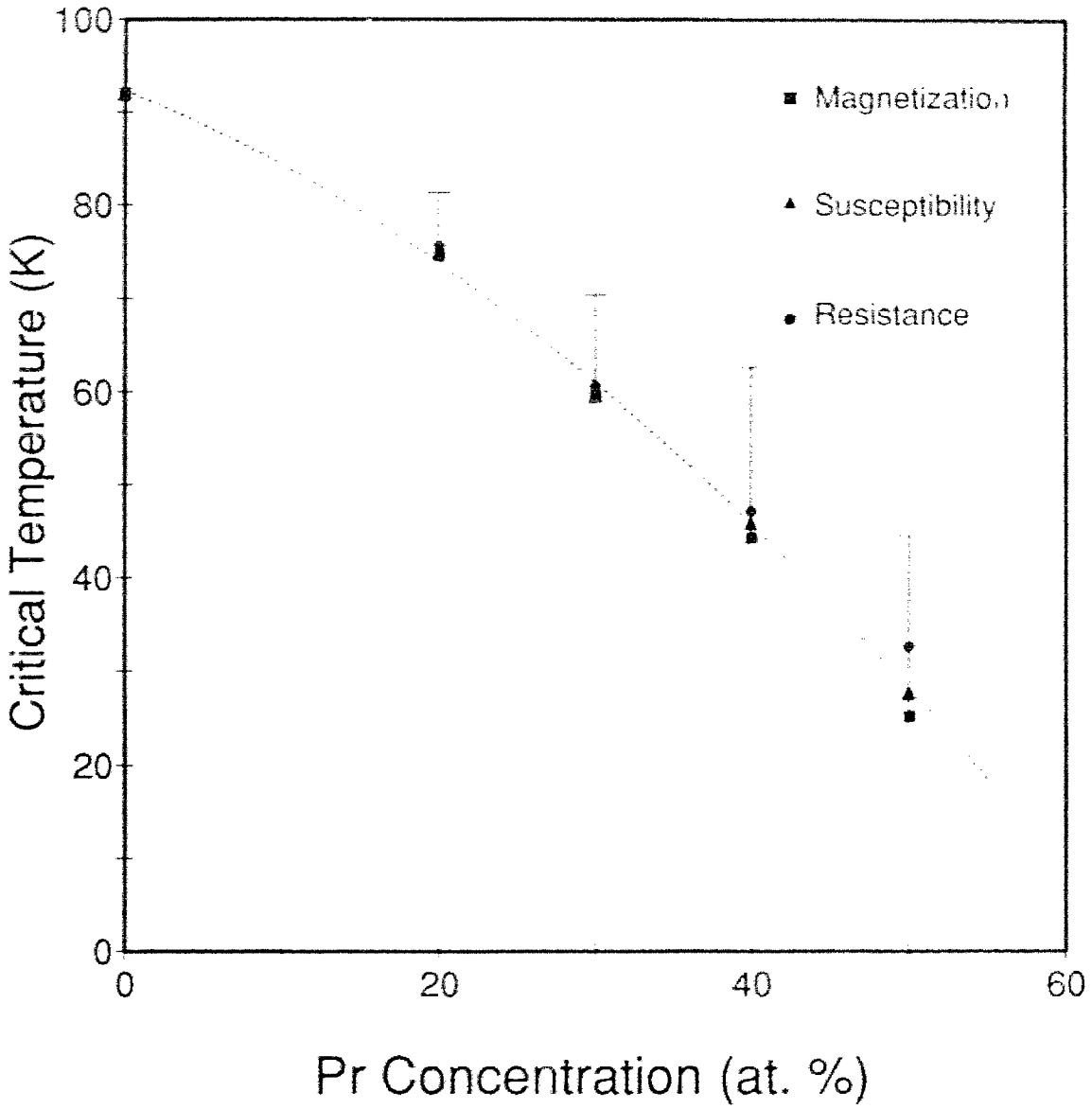

Figure 6.5

Critical temperature vs. *Pr* concentration. The dotted line is the fit of the *Pr* and *Ca* data to the function $T_c(x,y) = T_{co} - A(\gamma - \beta x + y)^2 - Bx$, where x is the *Pr* concentration and y is the *Ca* concentration (next Chapter). The parameters are $T_{co} = 93.6K$, $A = 157K$, $B = 93.3K$, $\gamma = 0.091$ and $\beta = 0.874$.
The error bars reflect the tails in the magnetic measurements (at low shielding).

Pr Concentration	^{18}O Concentration	Meissner Fraction	Transition Width (K)		
(at. %)	(at. %)	@ 20Oe	Mag.	Susc.	Res.
20	84.6	24%	3.8	2.9	1.2
30	79.0	21%	5.0	3.8	2.5
40	85.5	17%	9.0	7.0	4.5
50	85.9	7%	11.0	9.5	6.0

Table 6.1. General characteristics of *Pr* substituted *YBCO*.

The most disturbing characteristic that can be seen with the increasing *Pr* concentration is in the shape of the magnetic transitions. Very long tails at low shielding become more pronounced in the dc magnetization and to a lesser extent in the ac susceptibility data. The net result is that there is a three-fold increase in the transition width with the increase from 20% to 50% *Pr*. Resistively, the transition width increases five-fold. It almost appears as if a second transition is taking place. It does appear that the end of the 'bulk' of the magnetic transition, where we have chosen to take T_c, does agree better with the T_c obtained from the resistance measurements (dashed line in Figure 6.4) than if we were to use the temperature at which the onset of shielding occurs. At the other end of the transition, near the point of full shielding, the 50% *Pr* curves do not exhibit the characteristic slow increase in signal before the bulk of the transition as do the rest of the samples. This will be discussed later.

The data, the Simplex fit to the data, and the calculated shift in the transition between the two isotope curves for the system of $(Y_{1-x}Pr_x)Ba_2Cu_3O_{7-\delta}$, for $x = 0.2$, 0.3, 0.4, and 0.5 are given in figures 6.6 through to 6.9. The critical temperatures, the isotope shifts, and the computed values of the isotope coefficient for this system are given in Table 6.2. The relationship between α and ΔT_c as a function of critical temperature is given in Figure 6.10. We find that ΔT_c increases linearly with increasing *Pr* concentration and that α increases smoothly with increasing *Pr* concentration (decreasing critical temperature) and approaches $\alpha = {}^1/_2$ at the highest Pr concentrations (lowest critical temperature). As noted in Figure 6.10, the three different measurements of ΔT_c and α for the 50% *Pr* samples do not agree well with one another. The values for α have not yet been normalized to 100% ^{18}O substitution. This is done in chapter 9.

In an attempt to understand the long tails at low shielding, the samples of 20%, 30% and 40% *Pr* substituted *YBCO* were ground into a powder and the magnetic measurements performed again. The data for these measurements are given in Figures 6.11 to 6.13. With the smaller particle size in the powder, a wider transition is expected. We find that the data has a much wider transition and the magnetization and susceptibility curves are almost identical. Some deviation is noted in the 40% sample. The computed isotopic shifts are also similar to those before although the 40% sample is somewhat larger. However, the long tails at very low shielding remain essentially unchanged.

Figure 6.6

Oxygen isotope effect in $(Y_{0.8}Pr_{0.2})Ba_2Cu_3O_{7-\delta}$

20% *Pr* Substitution

The empty symbols represent the ^{18}O data and the filled symbols represent the ^{16}O data. The solid line represents the Simplex fit to the data. The "+" symbols represent the shift, ΔT_i, as a function of temperature, between the two fits to the data.

The arrows on the magnetization and susceptibility curves represent the critical temperatures, 74.6*K* and 74.9*K* respectively, obtained earlier. The upper limit for the critical temperature is 80.8*K* in both cases.

The vertical dotted line (magnetic measurements) indicates the cutoff in the calculation of the mean of the isotope shift. The horizontal dotted line indicates this mean, and its value is indicated above the line.

The resistance measurements are normalized at *R*(85*K*).

Not all temperature scales are equivalent.

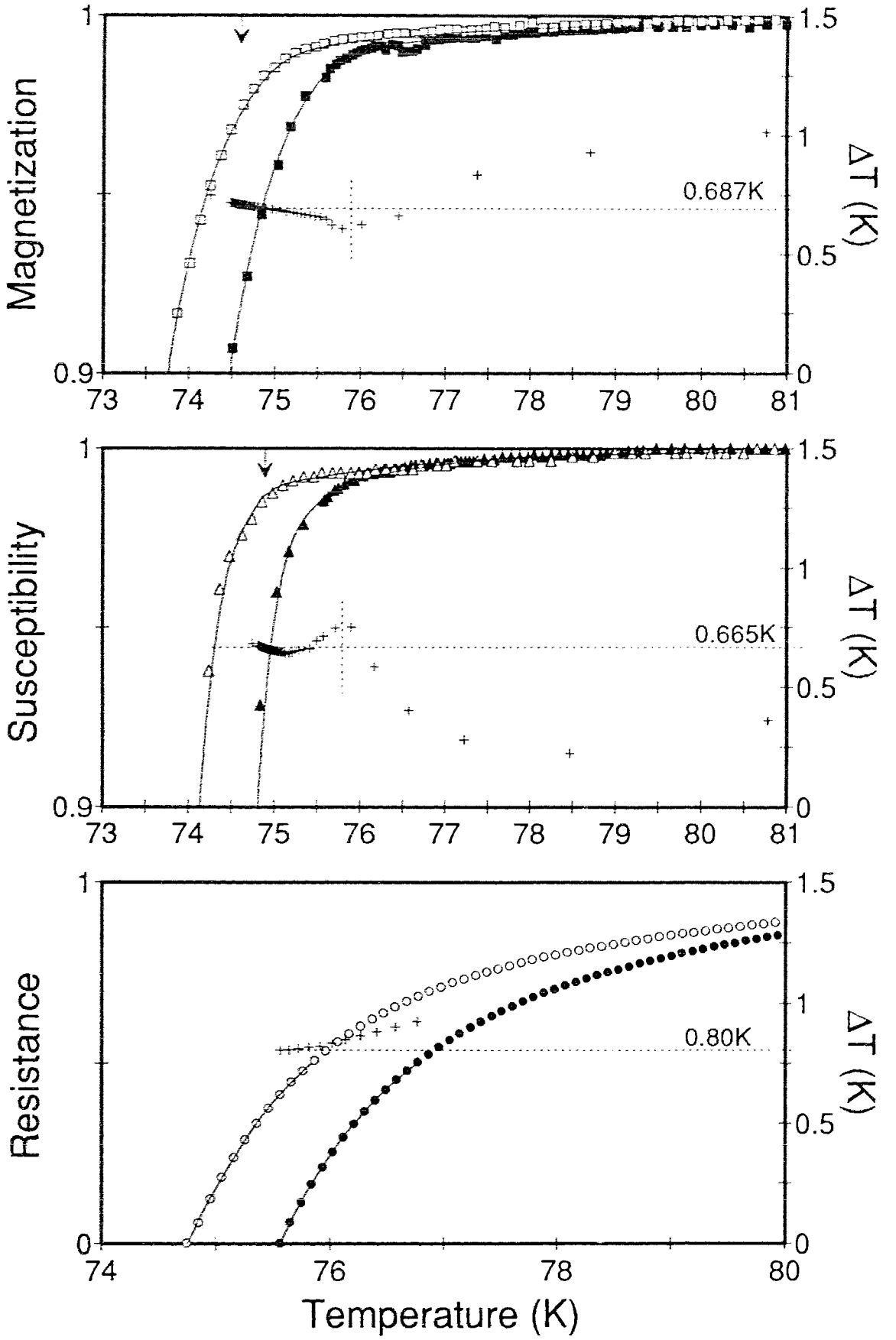
Magnetization
Susceptibility
Resistance
ΔT (K)
0.687K
0.665K
0.80K
Temperature (K)
1
0.9
0
1.5
0.5
73
74
75
76
77
78
79
80
81

Figure 6.7

Oxygen isotope effect in $(Y_{0.7}Pr_{0.3})Ba_2Cu_3O_{7-\delta}$

30% *Pr* Substitution

The empty symbols represent the ^{18}O data and the filled symbols represent the ^{16}O data. The solid line represents the Simplex fit to the data. The "+" symbols represent the shift, ΔT_i, as a function of temperature, between the two fits to the data.

The arrows on the magnetization and susceptibility curves represent the critical temperatures, 59.5*K* and 59.6*K* respectively, obtained earlier. The upper limit for the critical temperature is 69.2*K* and 69.3*K* respectively.

The vertical dotted line (magnetic measurements) indicates the cutoff in the calculation of the mean of the isotope shift. The horizontal dotted line indicates this mean, and its value is indicated above the line.

The resistance measurements are normalized at *R*(70*K*).

Not all temperature scales are equivalent.

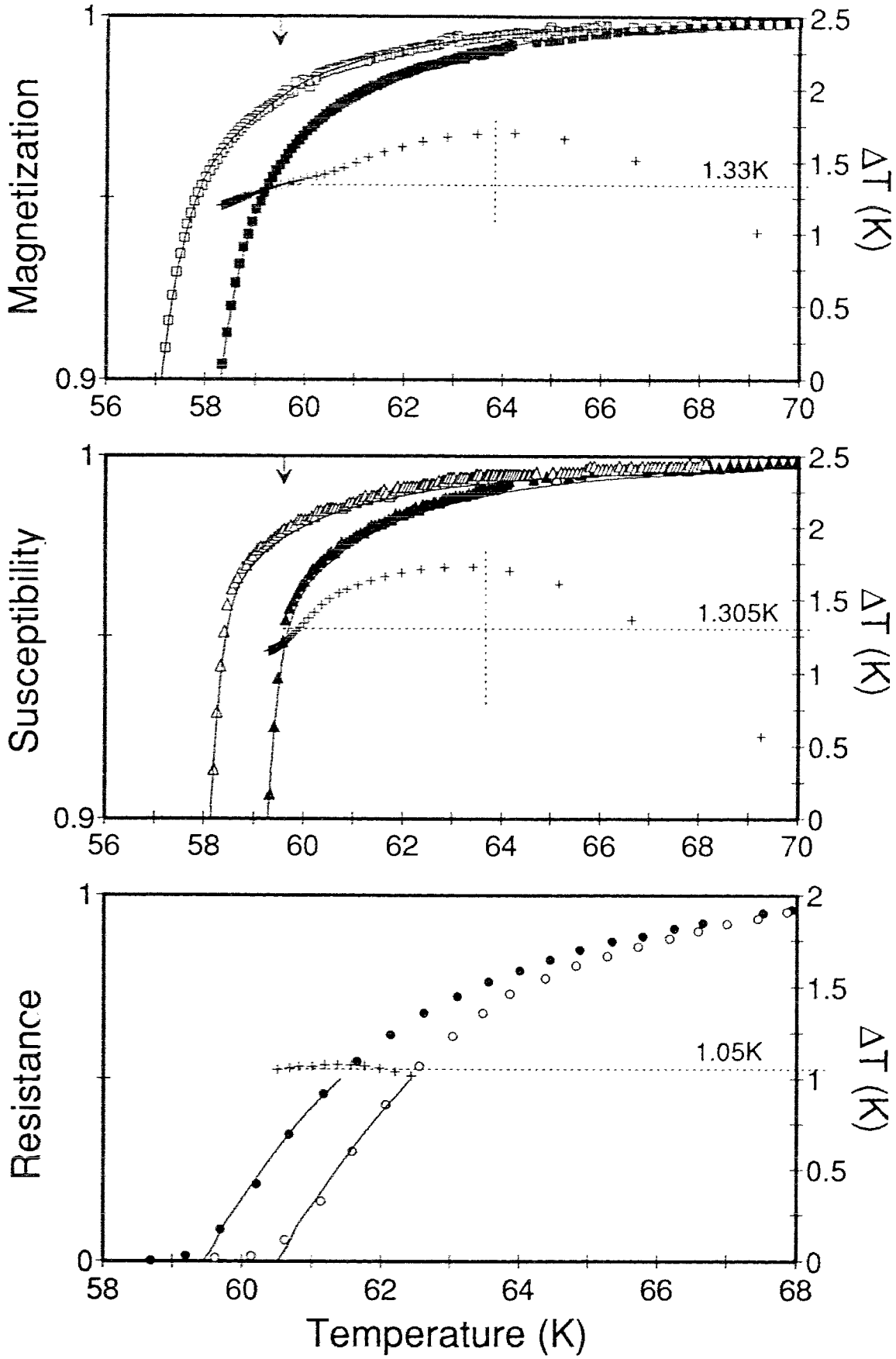
Magnetization
Susceptibility
Resistance
ΔT (K)
1.33K
1.305K
1.05K
Temperature (K)
1
0.9
0
2.5
2
1.5
0.5
56
58
60
62
64
66
68
70

Figure 6.8

Oxygen isotope effect in $(Y_{0.6}Pr_{0.4})Ba_2Cu_3O_{7-\delta}$

40% *Pr* Substitution

The empty symbols represent the ^{18}O data and the filled symbols represent the ^{16}O data. The solid line represents the Simplex fit to the data. The "+" symbols represent the shift, ΔT_c, as a function of temperature, between the two fits to the data.

The arrows on the magnetization and susceptibility curves represent the critical temperatures, 44.2*K* and 45.8*K* respectively, obtained earlier. The upper limit for the critical temperature is 64.6*K* and 62.1*K* respectively.

The vertical dotted line (magnetic measurements) indicates the cutoff in the calculation of the mean of the isotope shift. The horizontal dotted line indicates this mean, and its value is indicated above the line.

The resistance measurements are normalized to *R*(60*K*).

Not all temperature scales are equivalent.

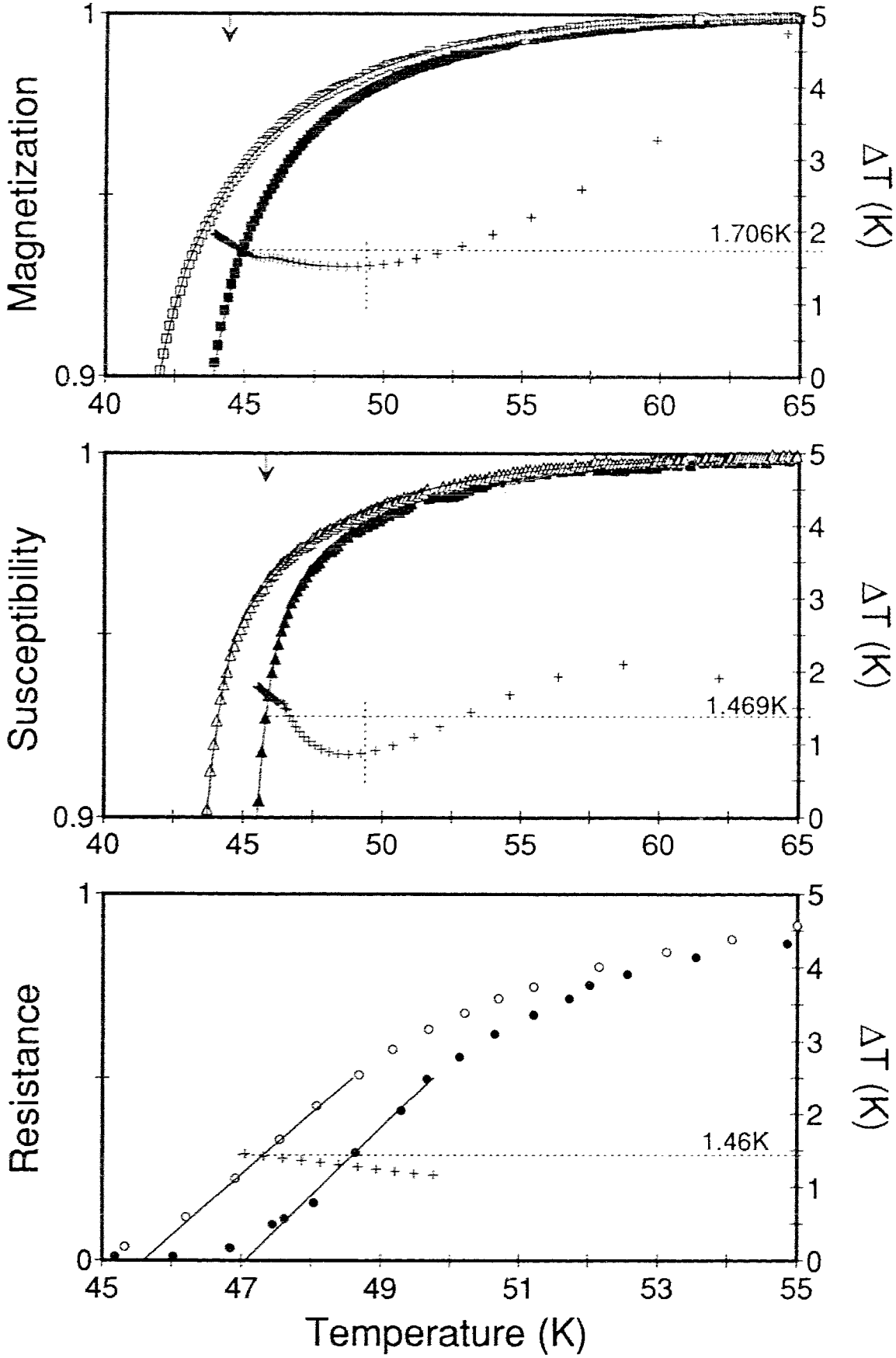
Magnetization
Susceptibility
Resistance
ΔT (K)
1.706K
1.469K
1.46K
Temperature (K)

Figure 6.9

Oxygen isotope effect in $(Y_{0.5}Pr_{0.5})Ba_2Cu_3O_{7-\delta}$

50% *Pr* Substitution

The empty symbols represent the ^{18}O data and the filled symbols represent the ^{16}O data. The solid line represents the Simplex fit to the data. The "+" symbols represent the shift, ΔT_i, as a function of temperature, between the two fits to the data.

The arrows on the magnetization and susceptibility curves represent the critical temperatures, 25.2*K* and 27.7*K* respectively, obtained earlier. The upper limit for the critical temperature is 45.0*K* and 44.9*K* respectively.

The vertical dotted line (magnetic measurements) indicates the cutoff in the calculation of the mean of the isotope shift. The horizontal dotted line indicates this mean, and its value is indicated above the line.

Note that the measured isotope shift for the magnetization is much smaller than that for the susceptibility.

The resistance measurements are normalized at *R*(45*K*).

Not all temperature scales are equivalent.

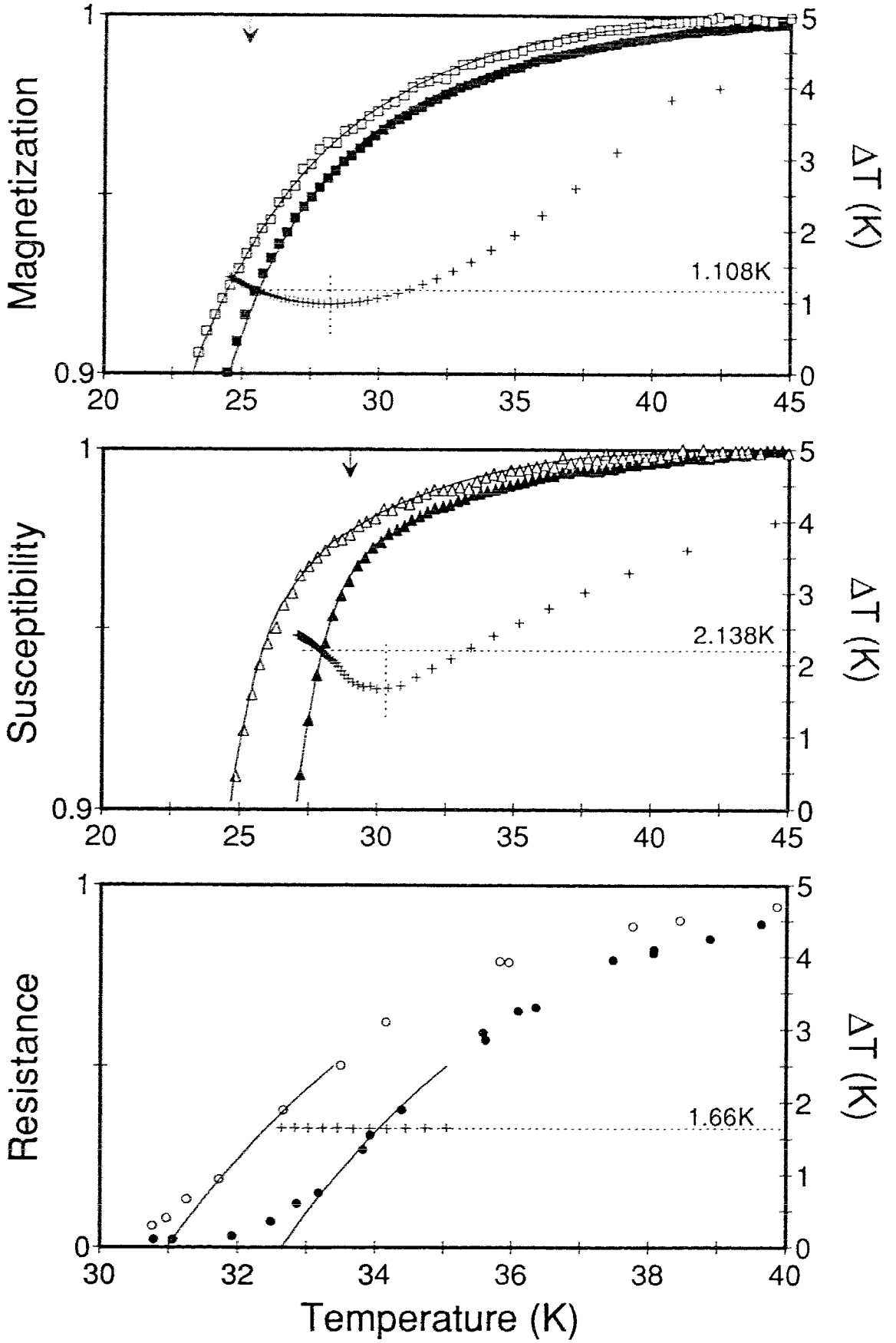
Magnetization
Susceptibility
Resistance
ΔT (K)
1.108K
2.138K
1.66K
Temperature (K)
1
0.9
0
5
4
3
2
1
0
20
25
30
35
40
45
30
32
34
36
38
40

Measurement	Sample	T_c(K)	ΔT_c(K)	α
dc magnetization	20%	$74.6^{-0.2}_{+6.2}$	0.687 ± 0.024	$0.079^{+0.003}_{-0.009}$
	30%	$59.5^{-0.2}_{+9.7}$	1.330 ± 0.137	$0.192^{+0.021}_{-0.044}$
	40%	$44.2^{-0.2}_{+20.4}$	1.706 ± 0.153	$0.334^{+0.032}_{-0.128}$
	50%	$25.2^{-0.2}_{+19.8}$	$*1.108 \pm 0.125$	$0.382^{+0.048}_{-0.194}$
ac susceptibility	20%	$74.9^{-0.2}_{+5.9}$	0.665 ± 0.022	$0.076^{+0.003}_{-0.008}$
	30%	$59.6^{-0.2}_{+9.7}$	1.305 ± 0.195	$0.188^{+0.029}_{-0.051}$
	40%	$45.8^{-0.2}_{+16.3}$	1.469 ± 0.327	$0.277^{+0.064}_{-0.119}$
	50%	$27.7^{-0.2}_{+17.2}$	2.138 ± 0.249	$0.682^{+0.089}_{-0.317}$
dc resistance	20%	75.5 ± 0.2	0.80 ± 0.02	0.090 ± 0.003
	30%	$60.5^{+0.2}_{-0.5}$	1.05 ± 0.02	0.149 ± 0.004
	40%	$47.0^{+0.3}_{-1.0}$	1.46 ± 0.02	$0.268^{+0.097}_{-0.054}$
	50%	$32.5^{+0.3}_{-1.0}$	1.66 ± 0.02	$0.445^{+0.020}_{-0.010}$

Table 6.2. T_c, ΔT_c and α for *Pr* substituted *YBCO.*

*Note that there is some question as to the validity of this data point.

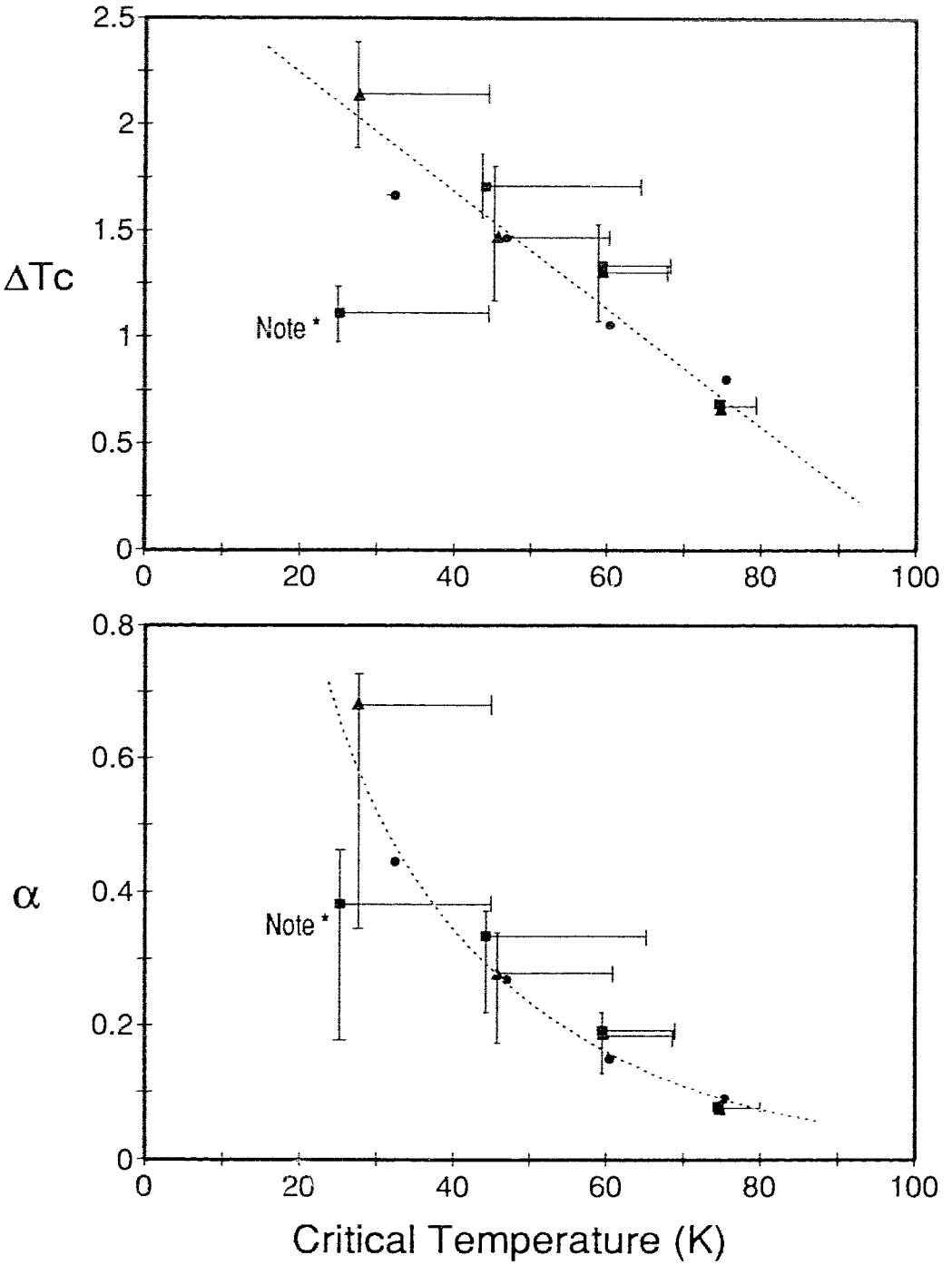

Figure 6.10

ΔT_c and α vs. T_c for *Pr* substituted *YBCO*. The dotted line is merely an aid to the eye and it includes the characteristic values of ΔT_c and α when $T_c = 92K$.

* - Note that there is some question as to the validity of this data point.

Figure 6.11

Oxygen isotope effect in powdered $(Y_{0.8}Pr_{0.2})Ba_2Cu_3O_{7-\delta}$

20% *Pr* substitution - magnetic measurements

The empty symbols represent the ^{18}O data and the filled symbols represent the ^{16}O data. The solid line represents the Simplex fit to the data. The "+" symbols represent the shift, ΔT_i, as a function of temperature, between the two fits to the data.

Shifts measured for these powdered samples are comparable to those measured in the pellets.

Note that the long tails found in the pellets still persist.

At the bottom is a comparision of the magnetization of the pellets and the powder. Note that the magnetization (squares) and susceptibility (triangles) measurements for the powder samples are equivalent and have a much broader transition than do the pellets.

Not all temperature scales are equivalent.

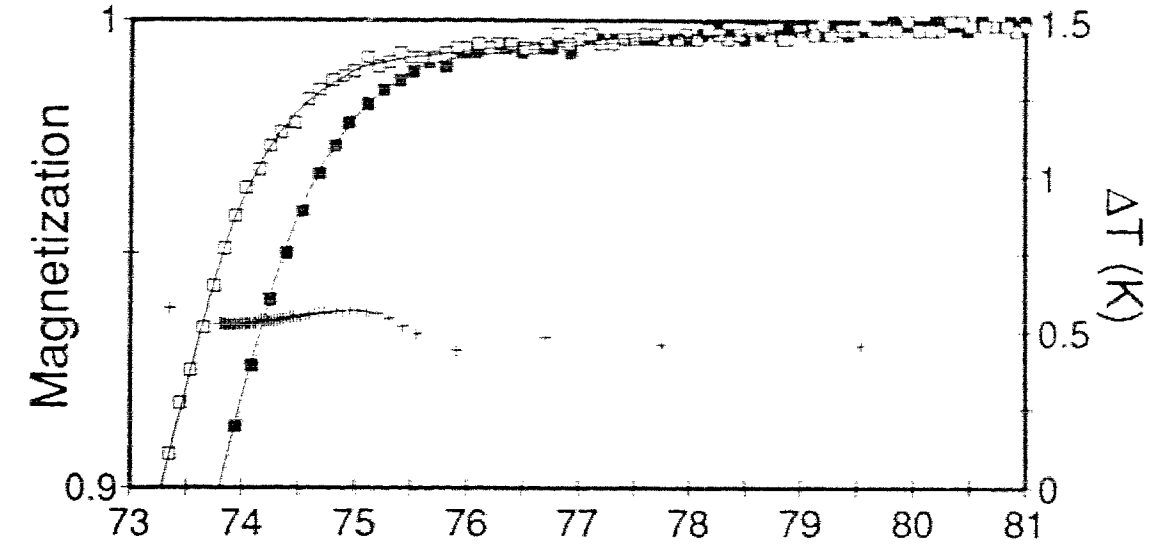
Magnetization
ΔT (K)
1
0.9
1.5
1
0.5
0
73
74
75
76
77
78
79
80
81

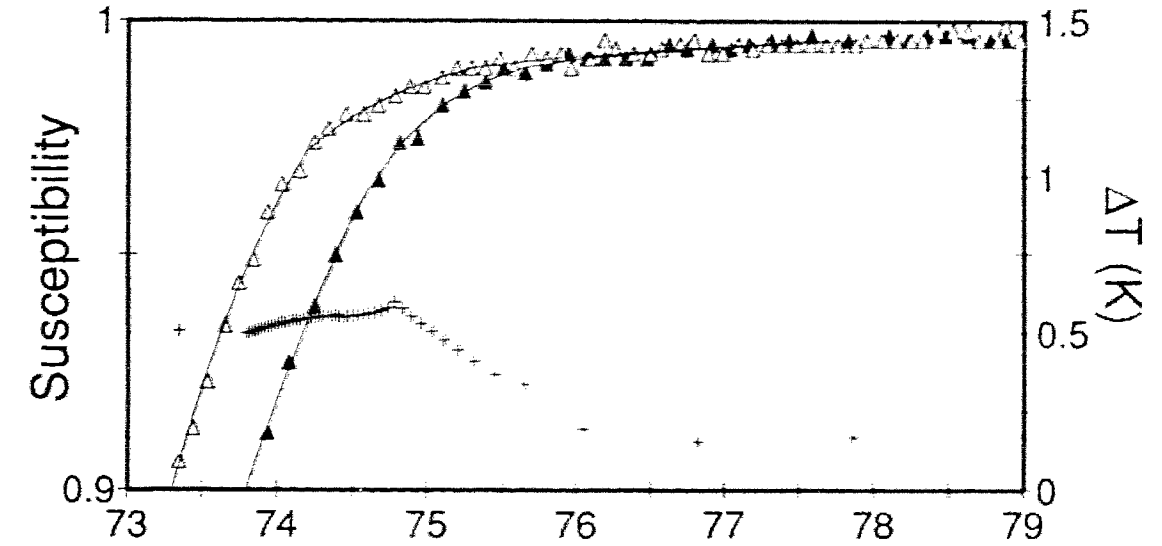
Susceptibility
ΔT (K)
1
0.9
1.5
1
0.5
0
73
74
75
76
77
78
79

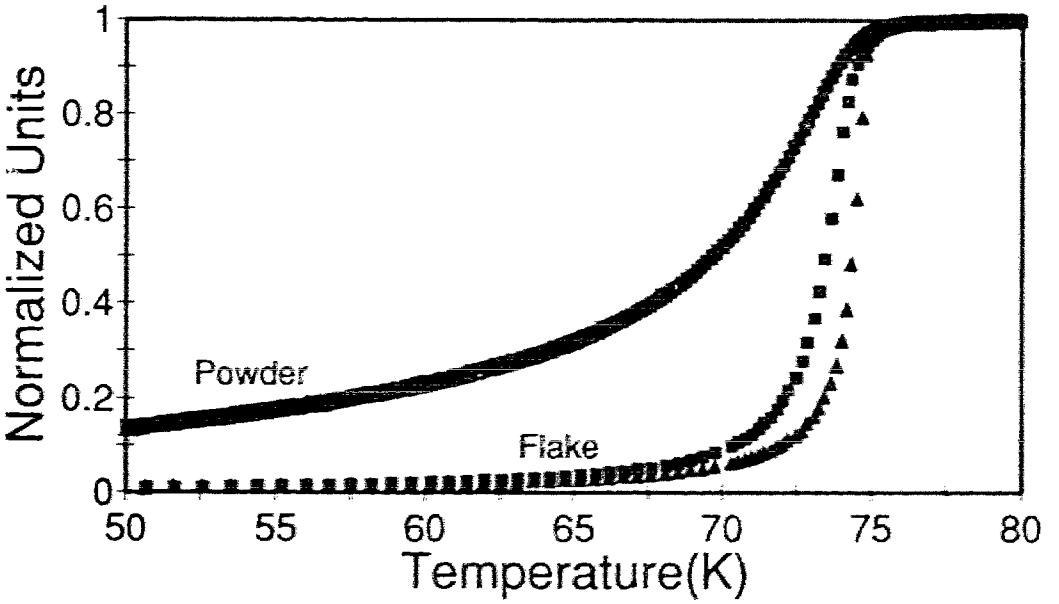
Normalized Units
Temperature(K)
Powder
Flake
1
0.8
0.6
0.4
0.2
0
50
55
60
65
70
75
80

Figure 6.12

Oxygen isotope effect in powdered $(Y_{0.7}Pr_{0.3})Ba_2Cu_3O_{7-\delta}$

30% *Pr* substitution - magnetic measurements

The empty symbols represent the ^{18}O data and the filled symbols represent the ^{16}O data. The solid line represents the Simplex fit to the data. The "+" symbols represent the shift, ΔT_c, as a function of temperature, between the two fits to the data.

Shifts measured for these powdered samples are comparable to those measured in the pellets.

Note that the long tails found in the pellets still persist.

At the bottom is a comparision of the magnetization of the pellets and the powder. Note that the magnetization (squares) and susceptibility (triangles) measurements for the powder samples are equivalent and have a much broader transition than do the pellets.

Not all temperature scales are equivalent.

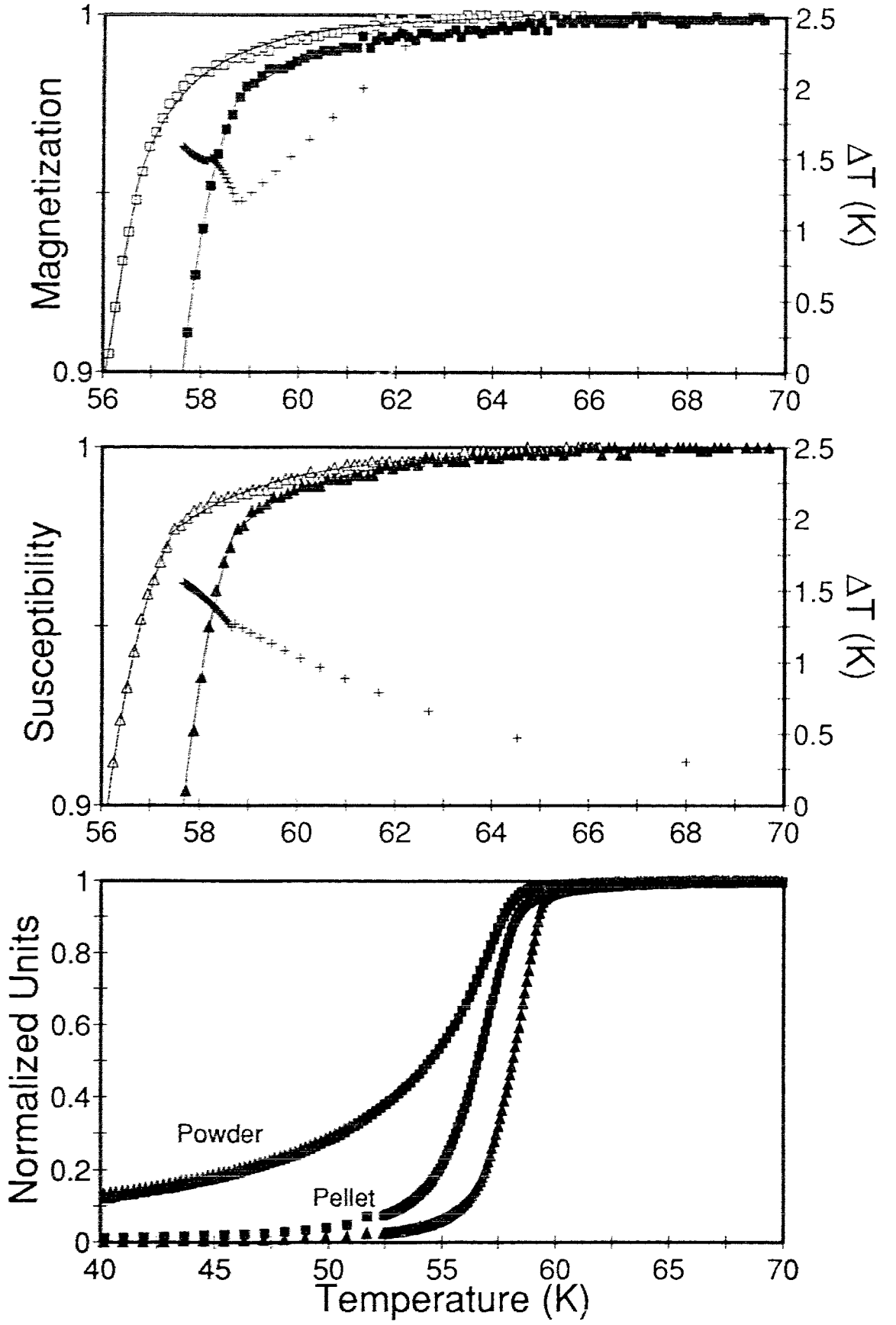
Magnetization
ΔT (K)
1
0.9
2.5
2
1.5
0.5
0
56
58
60
62
64
66
68
70
Susceptibility
ΔT (K)
Normalized Units
Powder
Pellet
0.8
0.6
0.4
0.2
40
45
50
55
60
65
Temperature (K)

Figure 6.13

Oxygen isotope effect in powdered $(Y_{0.6}Pr_{0.4})Ba_2Cu_3O_{7-\delta}$

40% *Pr* substitution - magnetic measurements

The empty symbols represent the ^{18}O data and the filled symbols represent the ^{16}O data. The solid line represents the Simplex fit to the data. The "+" symbols represent the shift, ΔT_i, as a function of temperature, between the two fits to the data.

Shifts measured for these powdered samples are somewhat larger than was found in the pellets.

Note that the long tails found in the pellets still persist.

At the bottom is a comparision of the magnetization of the pellets and the powder. Note that the magnetization (squares) and susceptibility (triangles) measurements for the powder samples are no longer equivalent, as well as a much broader transition than found in the two previous powdered samples.

Not all temperature scales are equivalent.

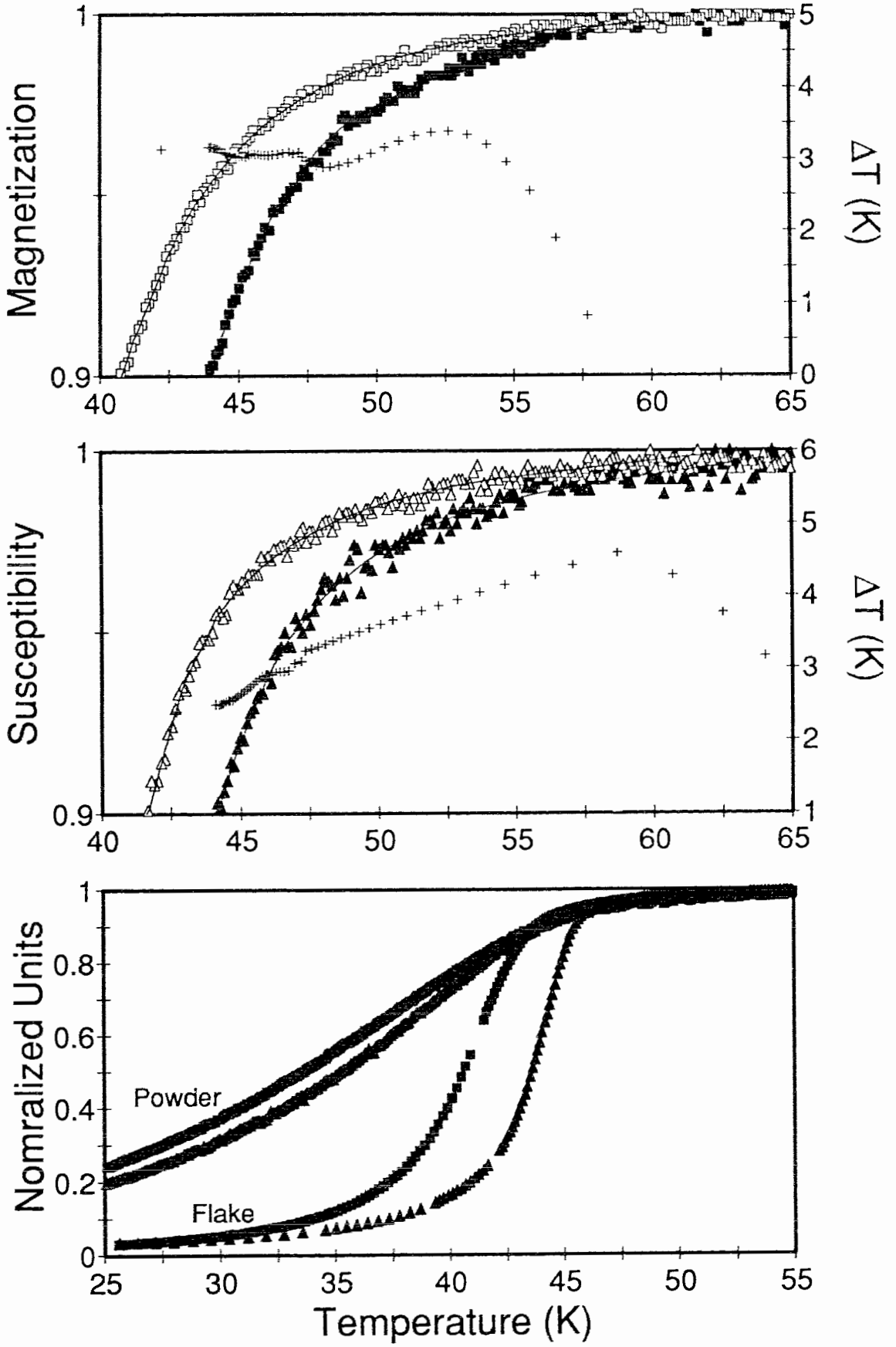
Magnetization
ΔT (K)
Susceptibility
ΔT (K)
Nomralized Units
Powder
Flake
Temperature (K)

6.3 Discussion

The general characteristics of the *Pr* substituted $YBa_2Cu_3O_{7-\delta}$ samples, the reduction in T_c, the decrease in Meissner fraction, and the increase in transition width are all in good agreement with that found in the literature (section 2.2.1). A small amount (< 3%) of impurity phase material, $BaCuO_2$, was detected in the X-ray spectra of our samples .

There could be several reasons for the broadening (long tails) in the transition at low shielding. In the powdered samples, we have essentially removed the coupling between individual grains (which are a few tens of microns in size). The fact that this effect still exists in the powdered samples indicates that this broadening is intrinsic to the material as opposed to being due to a weak coupling effect between grains as one might first suspect. Although tail effects are reported by other groups, they are not as pronounced as they are in our data. The lack of sensitivity and the much larger measuring fields (20*X* larger) used by other groups may be the reason. If the coherence length where related to the *Pr* concentration, the general broadening may then be due to a change in the coherence length, ξ, with increasing *Pr* concentration which affects the size of the fluctuations described in section 2.4. On the other hand, it may be just due to impurities in our samples. However, it is not likely that impurities would have this effect as they would need to be magnetic in nature and thus their effects would continue to temperatures higher than the critical temperature of the superconductor.

Another possibility is that there exists a number of intermediate phases of superconducting $(Y_{1-w}Pr_w)Ba_2Cu_3O_{7-\delta}$ with a variable range of *Pr* concentration, $0 \leq w \leq x$, all contributing a little bit to the signal and then persisting after the bulk

of the material $(Y_{1-x}Pr_x)Ba_2Cu_3O_{7-\delta}$ has gone into the normal state. It does support the method of determination of the critical temperature, taken as the linear extrapolation of the bulk of the transition, as the resistive critical temperature agrees more favourably with the end of the bulk of the magnetic transition and perhaps more correctly reflects the critical temperature of the superconducting material in question. This then raises the question of whether the isotope shift scales with T_c within these long tails. From the data, it is clear that within the tails there is a general trend of the isotope shift, ΔT_i, to increase at the higher temperatures. However, from the above argument, a higher T_c multiphase material would tend to have a smaller shift and not a larger one. In any event, this effect makes it difficult to distinguish between the two isotope curves at low shielding.

The difference in shape in the magnetic measurements (at low temperatures) of the 50% *Pr* samples with the others reflects the inability of these sample(s) to completely shield the measuring field at lowest temperature. This effect is more pronounced in the dc magnetization than in the ac susceptibility as susceptibility measurements are generally sharper (a result of the smaller ac field strength). Thus, even at 4.2*K*, some of the measuring field has penetrated the samples and the normalized curves will not reflect a full signal response and hence the isotopic comparison will be affected. Thus, the normalization of an incomplete transition will cause the transition to be steeper. Because of the lower T_c, this effect is more pronounced in the ^{18}O sample(s) than it is for the ^{16}O sample(s). The net result of this is that the measured ΔT_c will be smaller than it actually is. The sharpness of the transition in these cases will also influence this effect. The broader the transition, the greater the effect. This accounts for the fact that ΔT_c and α are smaller in the magnetization

measurement than in the susceptibility measurement for the 50% Pr substituted sample. This effect occurs more readily in the powdered samples, 40% *Pr* as well as 50% *Pr*, due to the much broader transitions.

The shift between the two isotope transitions are in good agreement for all three measurement methods. However, it is apparent that the critical temperature obtained from resistance measurements is higher than that obtained from the dc magnetization and ac susceptibility which are in fairly good agreement. The difference in T_c between the magnetic and resistive measurements becomes larger the lower the critical temperature, reaching as much as $5K$ for the 50% *Pr* samples. The results of the width of the transition and its relationship to ΔT_c will be discussed at the end of the next chapter.

7 RESULTS - CALCIUM SUBSTITUTION

7.1 SAMPLE PREPARATION

The preparation method of the substitutions of 5% to 25% *Ca*, with a constant 20% *Pr*, into $Y_{0.8}Pr_{0.2}Ba_2Cu_3O_{7-\delta}$ is different from the *Pr* substituted samples and thus a 0% *Ca* substituted sample is included as a comparison for the previous set of measurements.

Mixed powders of $(Y_{0.8-y}Pr_{0.2}Ca_y)Ba_2Cu_3O_{7-\delta}$ for the concentrations of $y = 0.05$, 0.1, 0.15, 0.2, and 0.25 were calcined in air at 905°*C* for a total of 125 hours with several intermediate regrindings to improve the homogeneity of the samples. The sintering process was performed in the parallel processing system and consisted of the following heat treatment:

1) heat to 935°*C* and holding for 48 hours; then
2) cool to 500°*C* and hold for 18 hours; then
3) cool to 400°*C* and hold for 10 hours; then
4) cool to 300°*C* and hold for 10 hours; then
5) cool to room temperature.

All sintering cooling processes were at the natural cooling rate of the oven.

Resistance measurements were performed on the pellets and then shaped rods and bars were made from the pellets. Magnetization, both ZFC and FC data, were performed on the rods and resistivity measurements were performed on the bars.

7.2 MEASUREMENTS

A comparison of the dc magnetization, the ZFC and FC curves, is given in Figure 7.1. The Meissner fractions are tabulated in Table 7.1 along with the transition widths calculated (as described earlier) from the ac susceptibility (Figure 7.2), and resistivity (Figure 7.3) measurements. A characteristic comparison (10% *Ca*) for the *Ca* substitution series of all three measurements is given in Figure 7.4. The *Ca* samples also exhibit the small (< 3%) $BaCuO_2$ impurity that was seen in the *Pr* X-ray measurements.

Ca Concentration	^{18}O Concentration	Meissner Fraction	Transition Width (*K*)		
(at. %)	(at. %)	@ 0.05*Oe*	Mag.	Susc.	Res.
0	(85)	35%	5.2	3.7	2.5
5	84	16%	2.0	1.4	1.3
10	78	12%	1.0	0.9	0.8
15	77	17%	1.9	1.5	1.0
20	76	21%	2.0	1.6	1.0
25	75	24%	1.7	1.4	1.3

Table 7.1. General characteristics of *Ca* substituted *Y(20% Pr)BCO.* A number in parenthesis indicates that this value is an estimate.

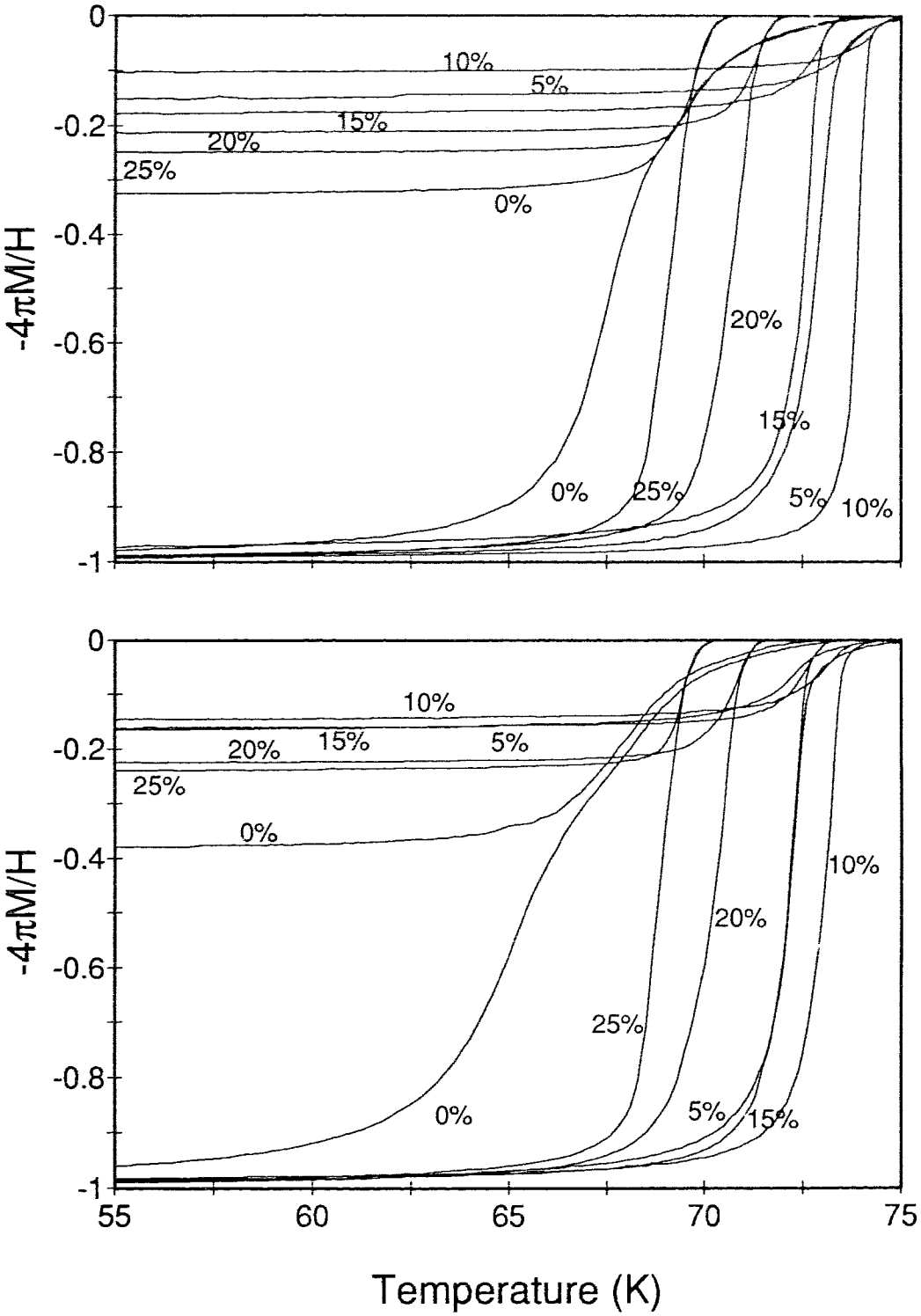

Figure 7.1

DC magnetization vs. temperature for *Ca* substituted *Y(20% Pr)BCO.* Top: ^{16}O data; Bottom ^{18}O data. Both the ZFC and FC data are shown giving the Meissner fraction.

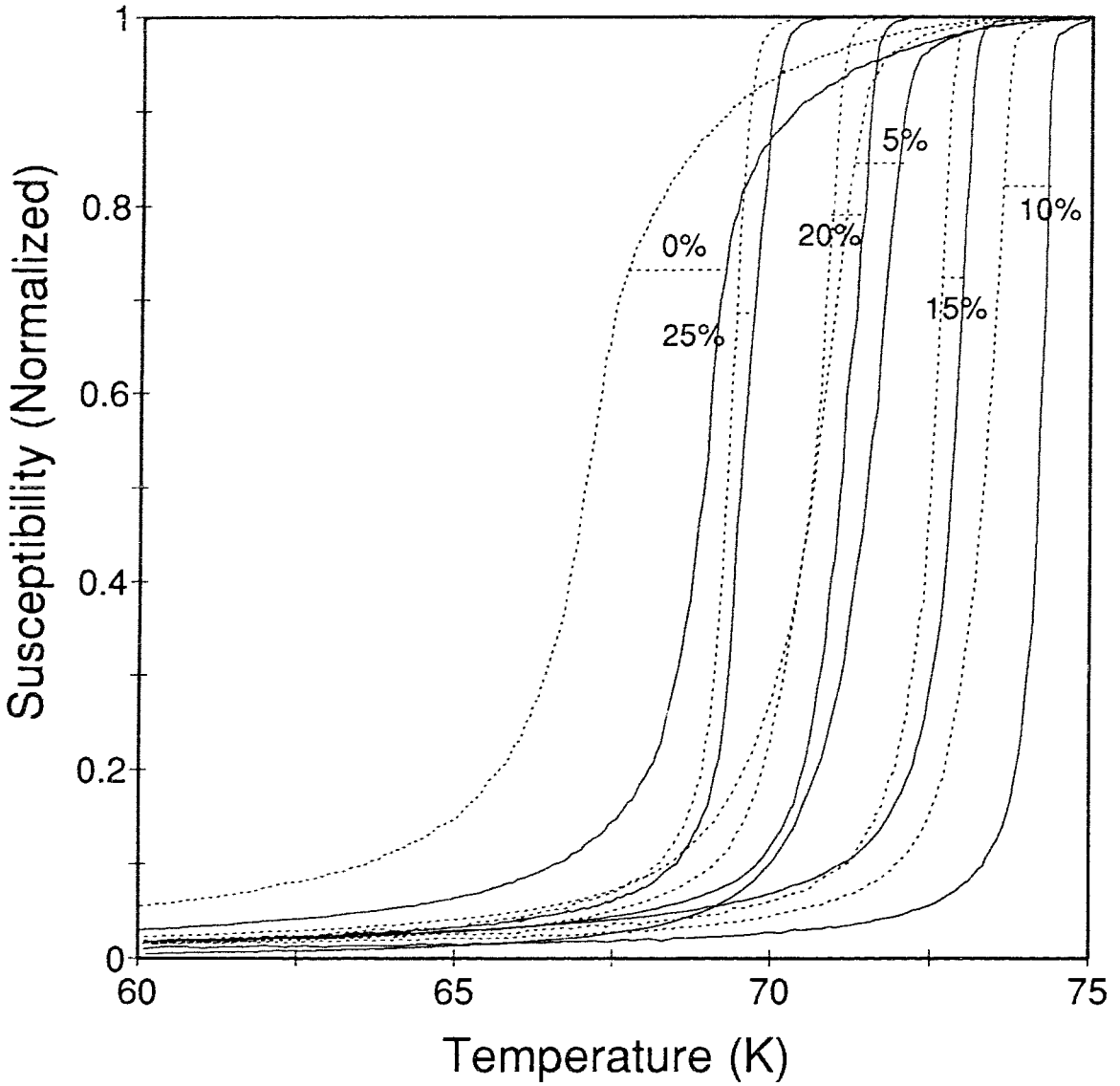

Figure 7.2

AC susceptibility vs. temperature for *Ca* substituted *Y(20% Pr)BCO.* Solid lines represent the ^{16}O isotope data and the dashed lines represent the ^{18}O isotope data. A dashed line between isotope pairs is to help distinguish the curves.

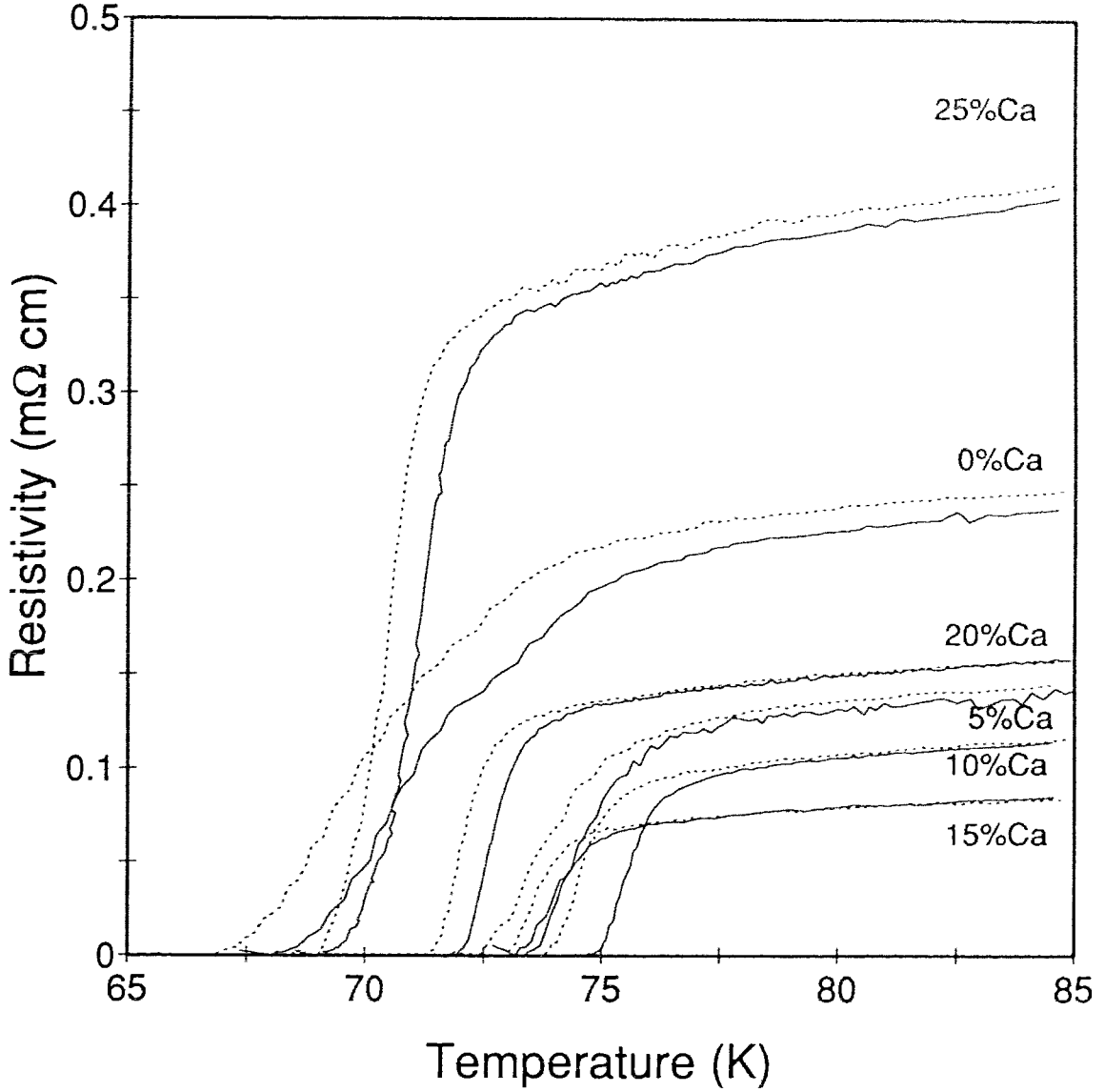

Figure 7.3

DC resistivity vs. temperature for *Ca* substituted *Y(20% Pr)BCO.* The solid lines represent the ^{16}O isotope data and the dashed lines the ^{18}O isotope data.

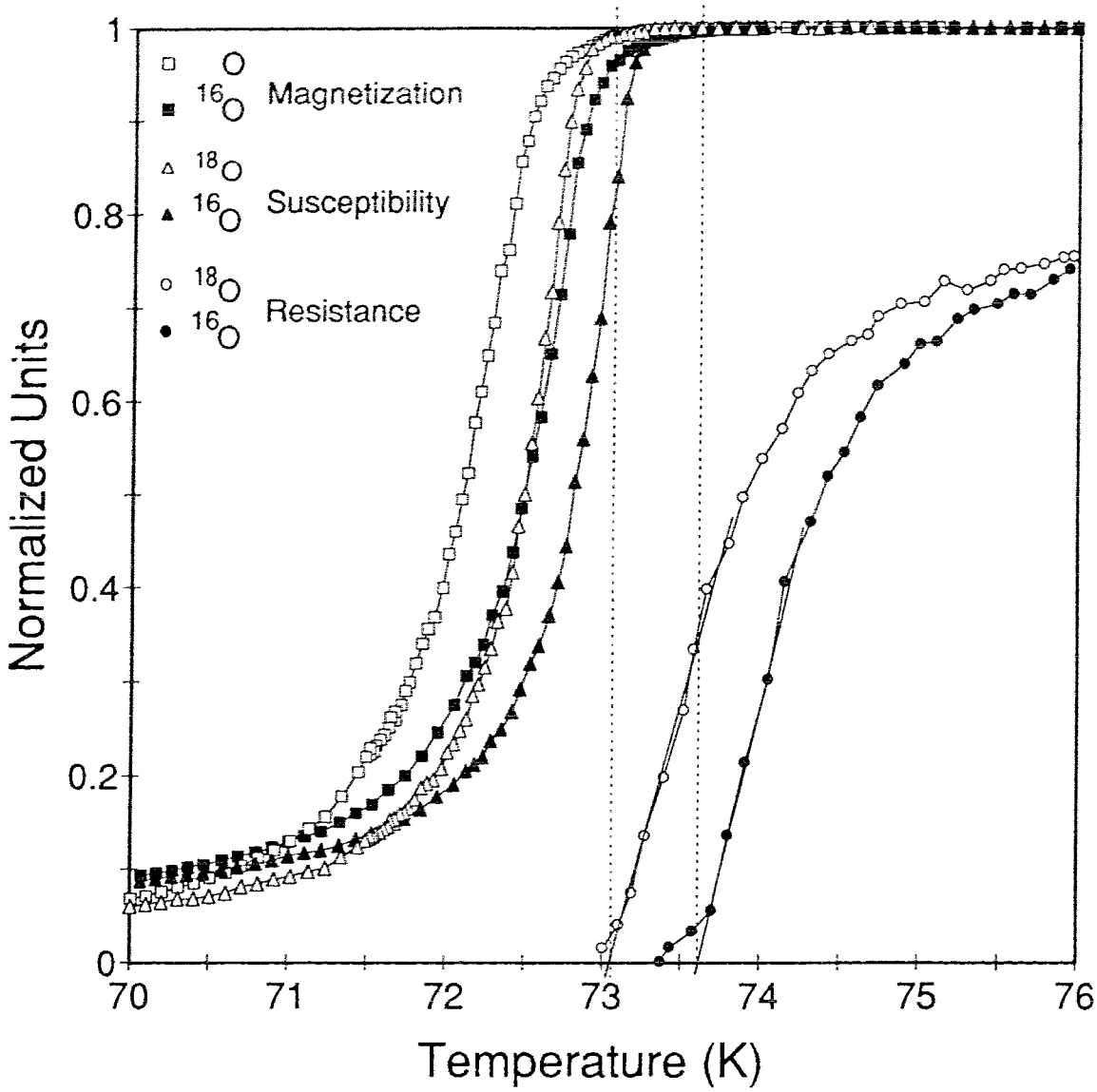

Figure 7.4

Comparison of dc magnetization, ac susceptibility and resistance measurements for $Y_{0.65}Pr_{0.2}Ca_{0.15}Ba_2Cu_3O_{7-\delta}$. The symbols represent the data. The solid lines provide continuity from point to point. The dotted lines are a visual aid for the critical temperature of the resistive transition (obtained from the straight line extrapolation). The resistive transition was normalized to $R(85K)$.

The obvious effect of the addition of *Ca* is an increase in the sharpness of the transition, and the elimination of the long tails at very small shielding. The width of the transition sharpens for all three measurements with the addition of *Ca* and remains fairly constant with the increasing *Ca* concentration. As with the *Pr*, the resistance has the narrowest transition and the dc magnetization has the widest. The isotopic shift measured is similar for both magnetic measurements but the resistivity measurements give a somewhat larger value for the higher concentrations. The size of the isotopic shift is affected also by the addition of *Ca* as it is reduced from that of the 20% *Pr* sample fabricated under the same conditions. The reduction is considerable since the change in T_c is quite small, only about 7*K* throughout the entire substitution range.

The increase in *Ca* concentration in the sample has an effect on a number of properties of this system. First, T_c increases then decreases with a maximum at approximately 10% *Ca*. Second, the Meissner fraction decreases then increases with a minimum at the 10% *Ca*. The normal state resistivity (at $T = 85K$) is also parabolically dependent on the *Ca* concentration although its minimum is the slightly higher concentration of 15% *Ca*.

The parabolic effect in T_c (Figure 7.5) has been reported earlier (section 2.2.3). The T_c data and the corresponding concentrations of both the *Pr, x*, and the *Pr:Ca, y*, series has been fitted to the function proposed by Neumeier et al.[59]. The dotted line in Figure 7.5 indicates this fit to equation [2.1], which gives:

$$T_c(x,y) = 93.6K - (157K)(0.091 - 0.874x + y)^2 - (93.3K)x \qquad [7.1]$$

It should be noted that the last term in equation [7.1], the linear pair-breaking term, is an approximation to the more complicated digamma function which

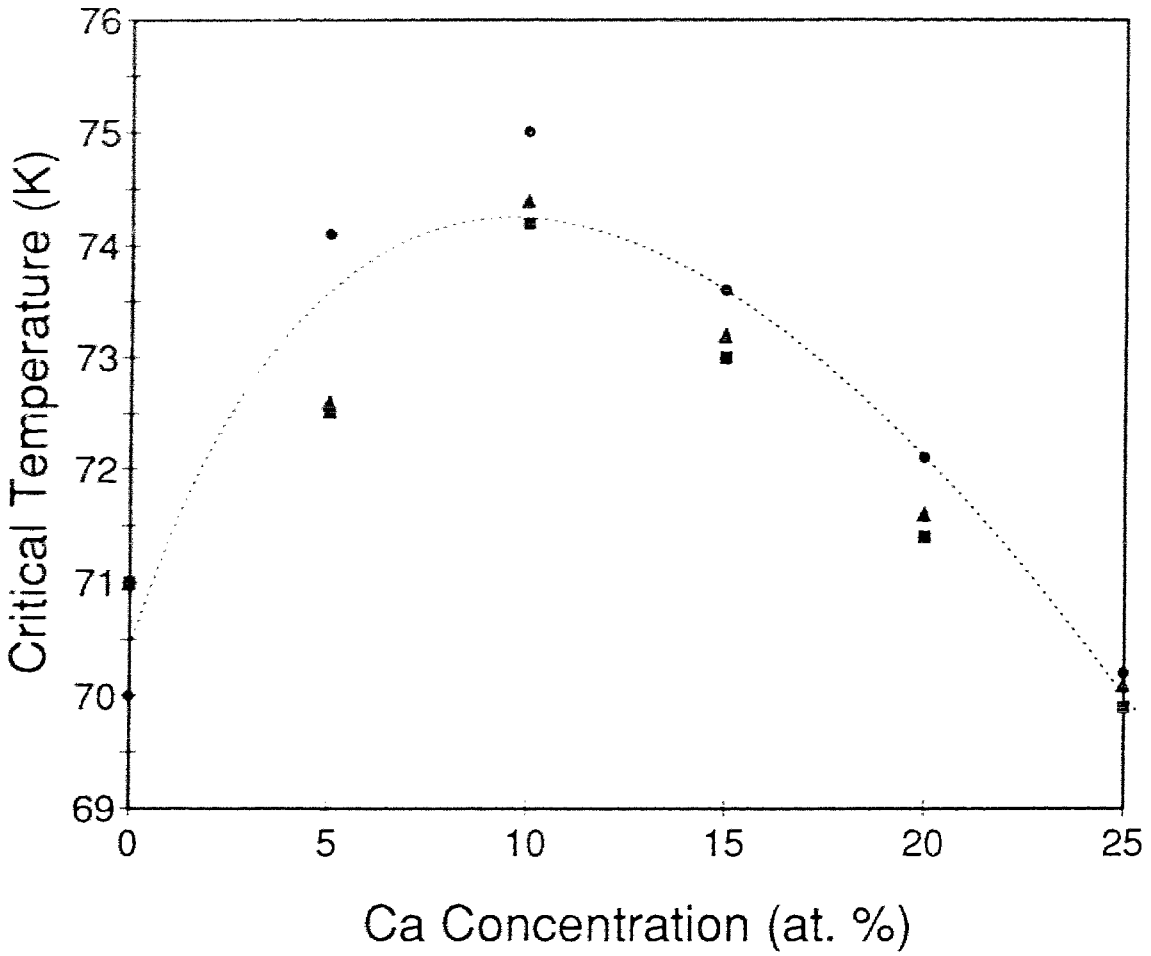

Figure 7.5

Critical temperature vs. *Ca* concentration. The parabolic line is a fit of the data to the function[73] $T_c(x,y) = T_{co} - A(\gamma - \beta x + y)^2 - Bx$, where x is the *Pr* concentration and y is the *Ca* concentration. We obtain $T_{co} = 93.6K$, $A = 157K$, $B = 93.3K$, $\gamma = 0.091$, and $\beta = 0.874$. Both the *Pr* and the *Pr:Ca* data is used in fitting the function.

should be used when dealing with the highest *Pr* concentrations because the pair-breaking here is no longer linear.

The data, the Simplex fit to the data, and the computed isotope shift for the system of $(Y_{0.8-y}Pr_{0.2}Ca_y)Ba_2Cu_3O_{7-\delta}$, $y = 0$, 0.05, 0.1, 0.15, 0.2, 0.25, is given in Figures 7.6 to 7.11 respectively. The critical temperatures, the isotope shifts, and the computed values of the isotope coefficient for this sytem are given in Table 7.2. The relationship between α and ΔT_c as a function of T_c is given in Figure 7.12. Due to the smaller temperature range plotted here, the uncertainty in the temperature values appear large. In fact, they are actually smaller than that obtained in the *Pr* series. The value of T_c reported in the table is that which has been determined from the linear extrapolation technique as explained earlier.

The isotopic shift, ΔT_c, and the value of the isotope coefficient, α, change little over the short spread in critical temperature. The relationship between the critical temperature and α or ΔT_c is not clear. Considering the parabolic nature of the other properties of the system, a possible parabolic fit to α and ΔT_c can be detected in the data (dotted line Figure 7.12). However, the large relative uncertainties also leave the possibility that of a linear relationship or perhaps even no change in ΔT_c at all.

Figure 7.6

Oxygen isotope effect in $(Y_{0.8}Pr_{0.2})Ba_2Cu_3O_{7-\delta}$

0% *Ca*, 20% *Pr* substitution

The empty symbols represent the ^{18}O data and the filled symbols represent the ^{16}O data. The solid line represents the Simplex fit to the data . The "+" symbols represent the shift, ΔT_i, as a function of temperature, between the two fits to the data.

The arrows on the magnetization and susceptibility graphs indicate the critical temperature obtained from a linear extrapolation of the bulk of the transition: 71.0*K* for both the magnetization and susceptibility. The upper limit for T_c is 76.0*K*.

The vertical dotted line (magnetic measurements) indicates the cutoff in the calculation of the mean of the isotope shift. The horizontal line indicates this mean, and its value is indicated above the line.

The resistance measurements are normalized to $R(85K)$.

Not all temperature scales are equivalent.

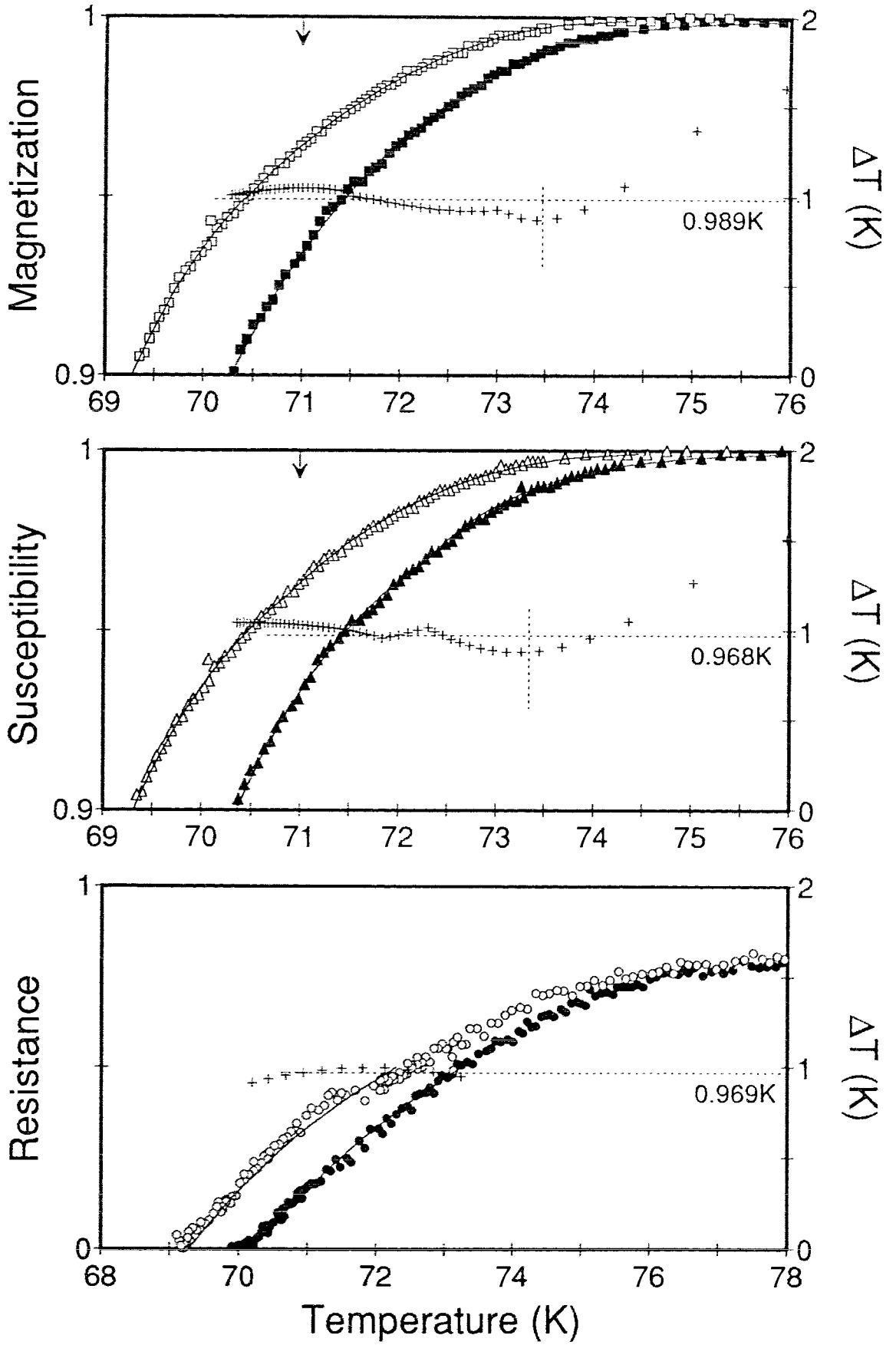
Magnetization
1
0.9
69
70
71
72
73
74
75
76
2
1
0
ΔT (K)
0.989K
Susceptibility
1
0.9
69
70
71
72
73
74
75
76
2
1
0
ΔT (K)
0.968K
Resistance
1
0
68
70
72
74
76
78
2
1
0
ΔT (K)
0.969K
Temperature (K)

Figure 7.7

Oxygen isotope effect in $(Y_{0.75}Pr_{0.2}Ca_{0.05})Ba_2Cu_3O_{7-\delta}$

5% *Ca*, 20% *Pr* substitution

The empty symbols represent the ^{18}O data and the filled symbols represent the ^{16}O data. The solid line represents the Simplex fit to the data . The "+" symbols represent the shift, ΔT_i, as a function of temperature, between the two fits to the data.

The arrows on the magnetization and susceptibility graphs indicate the critical temperature obtained from a linear extrapolation of the bulk of the transition: 72.5*K* for the magnetization (upper limit = 74.8*K*) and 72.6*K* for the susceptibility (upper limit = 74.6*K*).

No cutoff was imposed in the calculation of the mean of the isotope shift. The horizontal line indicates this mean, and its value is indicated above the line.

The resistance measurements are normalized to $R(85K)$.

Not all temperature scales are equivalent.

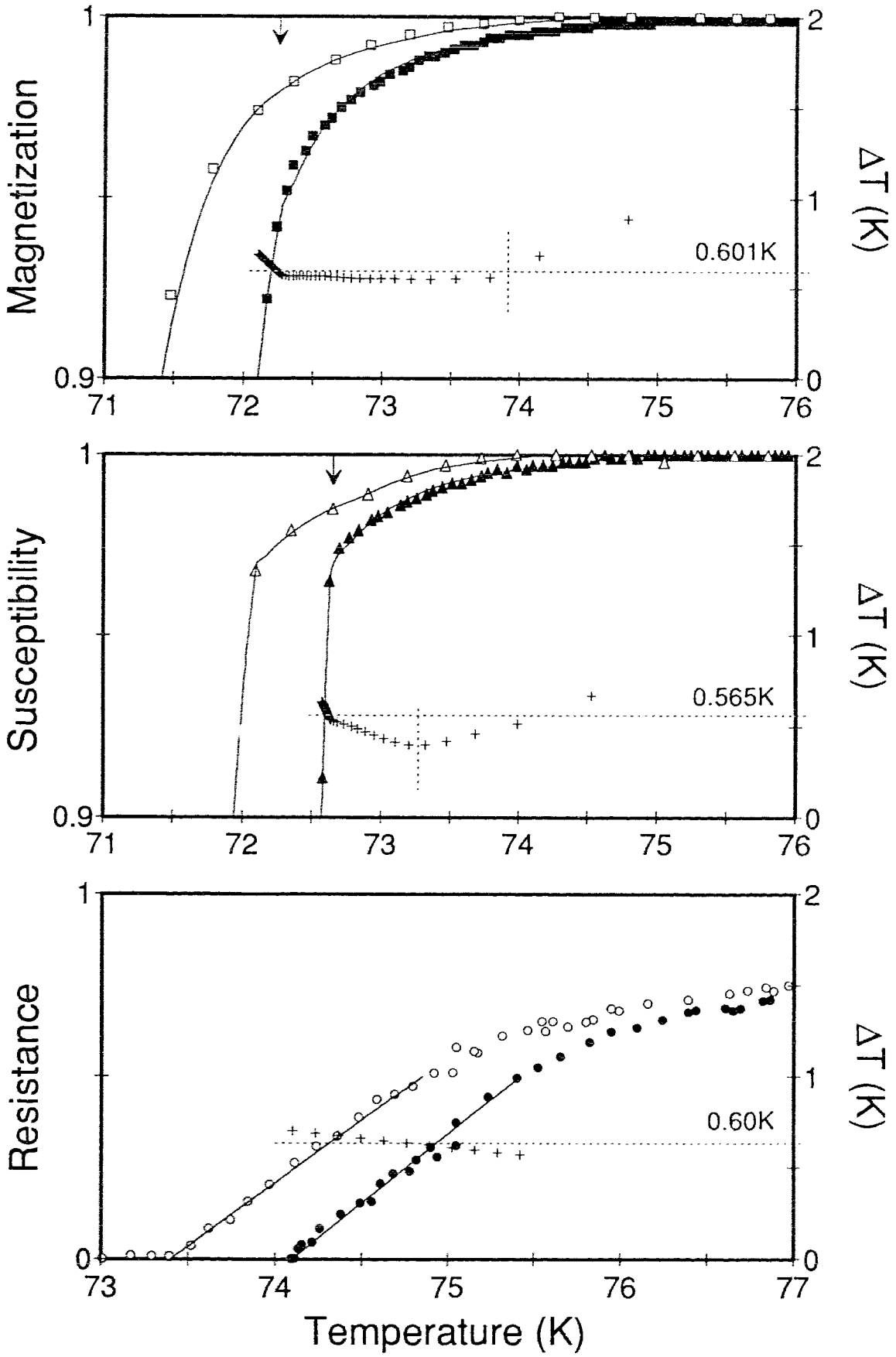
Magnetization
1
0.9
2
1
0
ΔT (K)
0.601K
71
72
73
74
75
76
Susceptibility
1
0.9
2
1
0
ΔT (K)
0.565K
71
72
73
74
75
76
Resistance
1
0
2
1
0
ΔT (K)
0.60K
73
74
75
76
77
Temperature (K)

Figure 7.8

Oxygen isotope effect in $(Y_{0.7}Pr_{0.2}Ca_{0.1})Ba_2Cu_3O_{7-\delta}$

10% *Ca*, 20% *Pr* substitution

The empty symbols represent the ^{18}O data and the filled symbols represent the ^{16}O data. The solid line represents the Simplex fit to the data . The "+" symbols represent the shift, ΔT_i, as a function of temperature, between the two fits to the data.

The arrows on the magnetization and susceptibility graphs indicate the critical temperature obtained from a linear extrapolation of the bulk of the transition: 74.2*K* for the magnetization (upper limit = 75.8*K*) and 74.4*K* for the susceptibility (upper limit = 75.7*K*).

No cutoff was imposed in the calculation of the mean of the isotope shift. The horizontal line indicates this mean, and its value is indicated above the line.

The resistance measurements are normalized to *R*(85*K*).

Not all temperature scales are equivalent.

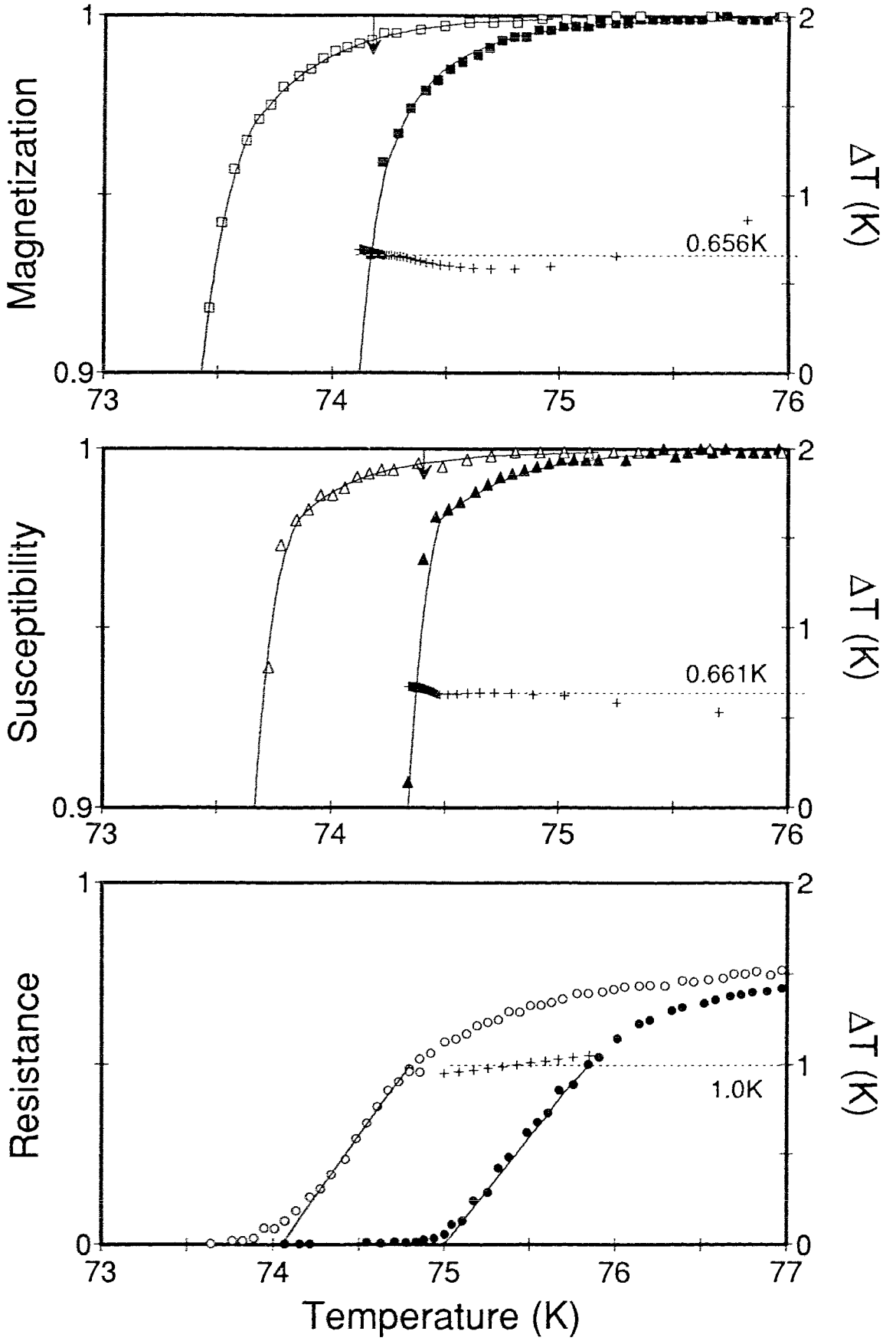
Magnetization
Susceptibility
Resistance
ΔT (K)
0.656K
0.661K
1.0K
Temperature (K)
1
0.9
0
2
73
74
75
76
77

Figure 7.9

Oxygen isotope effect in $(Y_{0.65}Pr_{0.2}Ca_{0.15})Ba_2Cu_3O_{7-\delta}$

15% *Ca*, 20% *Pr* substitution

The empty symbols represent the ^{18}O data and the filled symbols represent the ^{16}O data. The solid line represents the Simplex fit to the data . The "+" symbols represent the shift, ΔT_i, as a function of temperature, between the two fits to the data.

The arrows on the magnetization and susceptibility graphs indicate the critical temperature obtained from a linear extrapolation of the bulk of the transition: 73.0*K* for the magnetization (upper limit = 74.0*K*) and 73.2*K* for the susceptibility (upper limit = 73.8*K*).

No cutoff was imposed in the calculation of the mean of the isotope shift. The horizontal line indicates this mean, and its value is indicated above the line.

The resistance measurements are normalized to *R*(85*K*).

Not all temperature scales are equivalent.

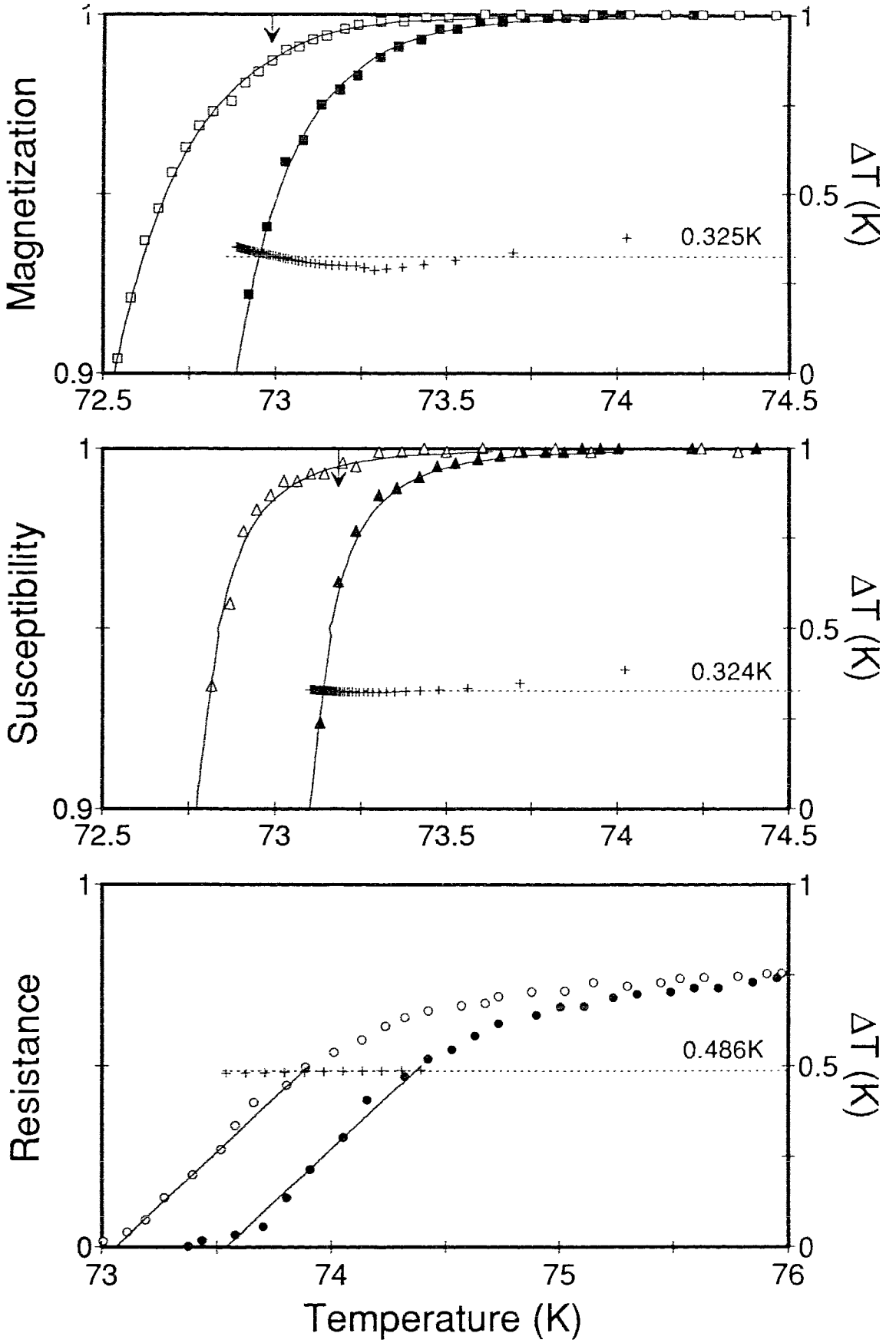
Magnetization
Susceptibility
Resistance
ΔT (K)
0.325K
0.324K
0.486K
1
0.9
0.5
0
72.5
73
73.5
74
74.5
75
76
Temperature (K)

Figure 7.10

Oxygen isotope effect in $(Y_{0.6}Pr_{0.2}Ca_{0.2})Ba_2Cu_3O_{7-\delta}$

20% *Ca*, 20% *Pr* substitution

The empty symbols represent the ^{18}O data and the filled symbols represent the ^{16}O data. The solid line represents the Simplex fit to the data . The "+" symbols represent the shift, ΔT_i, as a function of temperature, between the two fits to the data.

The arrows on the magnetization and susceptibility graphs indicate the critical temperature obtained from a linear extrapolation of the bulk of the transition: $71.4K$ for the magnetization (upper limit = $72.5K$) and $71.6K$ for the susceptibility (upper limit = $72.6K$).

No cutoff was imposed in the calculation of the mean of the isotope shift. The horizontal line indicates this mean, and its value is indicated above the line.

The resistance measurements are normalized to $R(85K)$.

Not all temperature scales are equivalent.

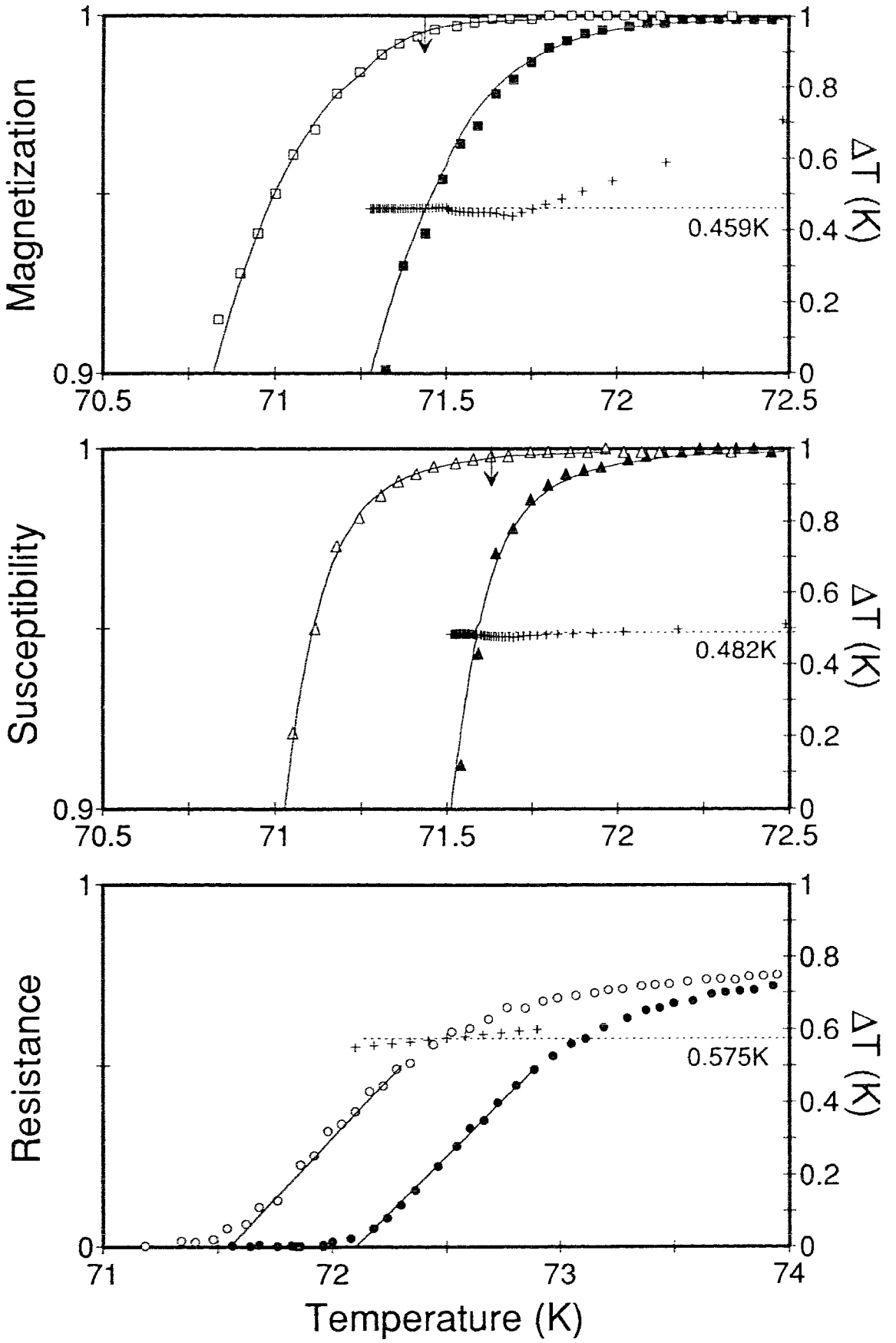
Magnetization
Susceptibility
Resistance
ΔT (K)
0.459K
0.482K
0.575K
Temperature (K)
1
0.9
0
0.2
0.4
0.6
0.8
70.5
71
71.5
72
72.5
73
74

Figure 7.11

Oxygen isotope effect in $(Y_{0.55}Pr_{0.2}Ca_{0.25})Ba_2Cu_3O_{7-\delta}$

25% *Ca*, 20% *Pr* substitution

The empty symbols represent the ^{18}O data and the filled symbols represent the ^{16}O data. The solid line represents the Simplex fit to the data . The "+" symbols represent the shift, ΔT_i, as a function of temperature, between the two fits to the data.

The arrows on the magnetization and susceptibility graphs indicate the critical temperature obtained from a linear extrapolation of the bulk of the transition: 69.9*K* for the magnetization (upper limit = 70.9*K*) and 70.1*K* for the susceptibility (upper limit = 71.2*K*).

No cutoff was imposed in the calculation of the mean of the isotope shift. The horizontal line indicates this mean, and its value is indicated above the line.

The resistance measurements are normalized to *R*(85*K*).

Not all temperature scales are equivalent.

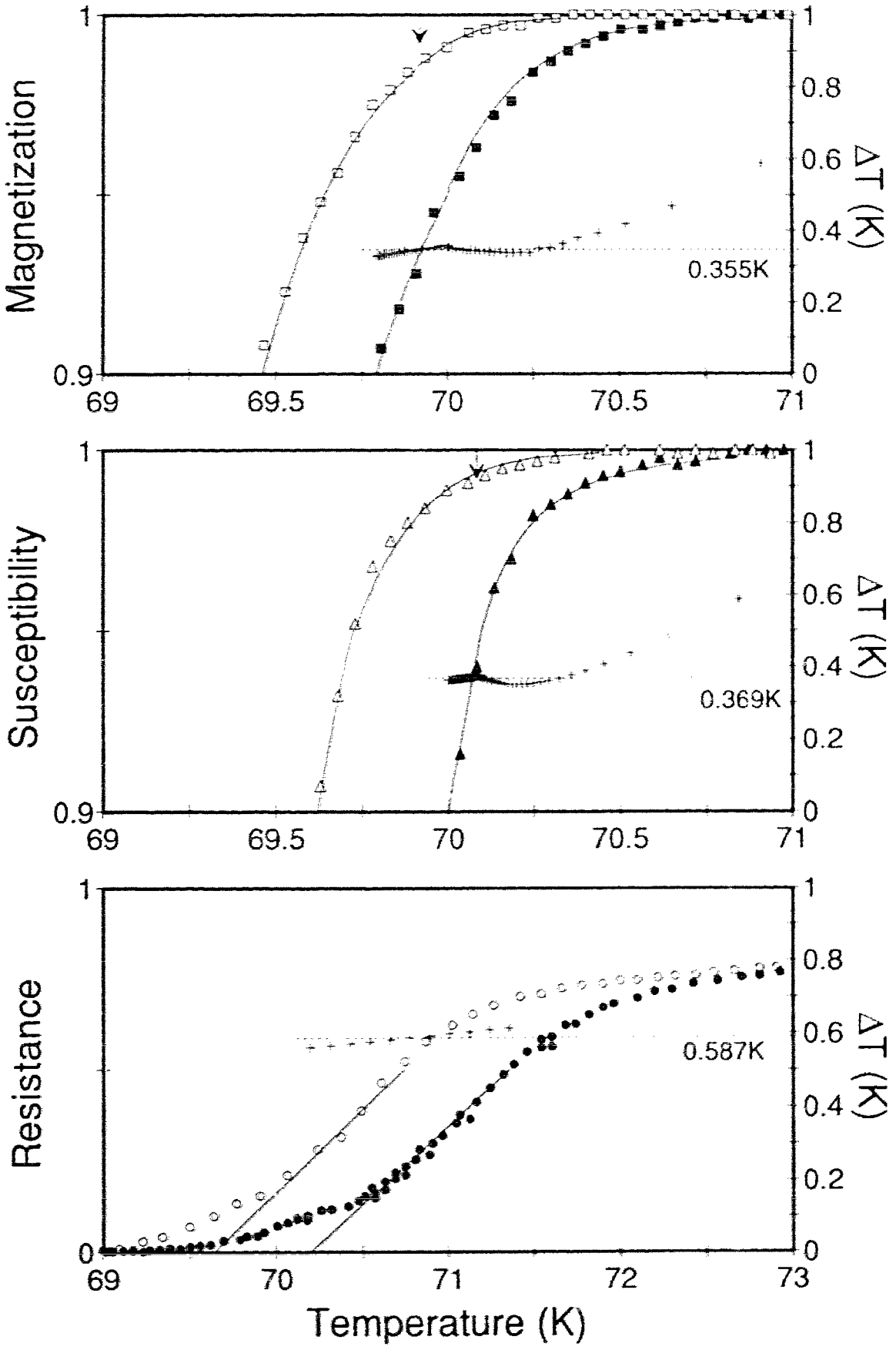
Magnetization
Susceptibility
Resistance
ΔT (K)
0.355K
0.369K
0.587K
Temperature (K)
1
0.9
0
0.2
0.4
0.6
0.8
69
69.5
70
70.5
71
72
73

Measurement	Sample	$T_c(K)$	$\Delta T_c(K)$	α
dc magnetization	0%	$71.0^{-2.0}_{+5.0}$	0.989 ± 0.055	0.119 ± 0.012
	5%	$72.5^{-0.2}_{+2.3}$	0.601 ± 0.047	0.071 ± 0.006
	10%	$74.2^{-0.2}_{+1.6}$	0.656 ± 0.030	0.075 ± 0.004
	15%	$73.0^{-0.2}_{+1.0}$	0.325 ± 0.020	0.038 ± 0.003
	20%	$71.4^{-0.2}_{+1.1}$	0.459 ± 0.042	0.055 ± 0.005
	25%	$69.9^{-0.2}_{+1.0}$	0.355 ± 0.041	0.043 ± 0.005
ac susceptibility	0%	$71.0^{-2.0}_{+5.0}$	0.968 ± 0.013	0.117 ± 0.008
	5%	$72.6^{-0.2}_{+2.0}$	0.565 ± 0.060	0.066 ± 0.007
	10%	$74.4^{-0.2}_{+1.3}$	0.661 ± 0.020	0.074 ± 0.008
	15%	$73.2^{-0.2}_{+0.6}$	0.324 ± 0.095	0.040 ± 0.011
	20%	$71.6^{-0.2}_{+1.0}$	0.482 ± 0.042	0.057 ± 0.005
	25%	$70.1^{-0.2}_{+1.1}$	0.369 ± 0.028	0.045 ± 0.004
dc resistance	0%	$70.0^{-0.3}_{+0.3}$	0.969 ± 0.028	0.118 ± 0.004
	5%	$74.1^{-0.1}_{+0.1}$	0.600 ± 0.082	0.073 ± 0.010
	10%	$75.0^{-0.3}_{+0.1}$	1.000 ± 0.010	0.111 ± 0.002
	15%	$73.6^{-0.1}_{+0.1}$	0.486 ± 0.011	0.059 ± 0.001
	20%	$72.1^{-0.2}_{+0.1}$	0.575 ± 0.002	0.071 ± 0.003
	25%	$70.2^{-0.7}_{+0.1}$	0.587 ± 0.048	0.072 ± 0.006

Table 7.2. T_c, ΔT_c and α for *Ca* substituted *Y(20% Pr)BCO.*

Figure 7.12

ΔT_c and α vs. T_c for *Ca* substituted *Y(20% Pr)BCO*. The positive error bars in temperature reflect the length of the tails in the magnetic measurements. Due to the temperature range plotted, the error bars appear, erroneously, larger than that of the previous *Pr* data.

The filled symbols are the *Pr:Ca* data while the empty symbols are the 20% *Pr* samples from the *Pr* data and are included for comparison.

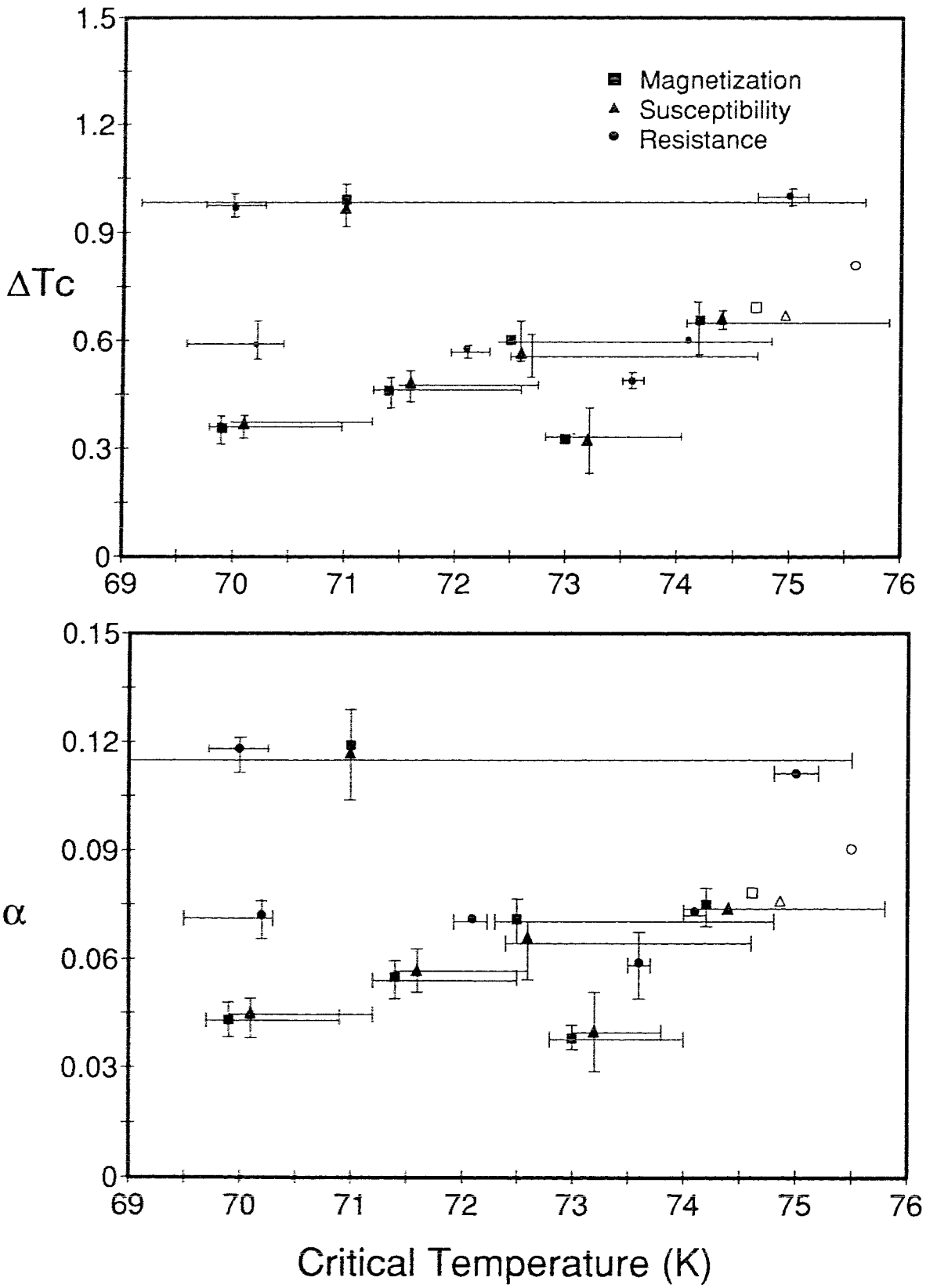
Magnetization
Susceptibility
Resistance
ΔTc
α
Critical Temperature (K)
1.5
1.2
0.9
0.6
0.3
0
0.15
0.12
0.09
0.06
0.03
0
69
70
71
72
73
74
75
76

7.3 DISCUSSION

The fit of T_c to the concentrations of *Pr, x,* and *Ca, y,* to equation [2.1] fit very well. The maximum obtainable T_{co} (in the *YBCO* system) from our calculations is 93.6*K*, which appears to be a more reasonable value than Neumeier's 97*K*[59]. We obtain an effective valence of +3.874 for the *Pr*, slightly smaller than Neumeier's +3.95, which is consistent with the measurements that indicate a mixed valence between +3 and +4 (section 2.2.1). With the optimum hole concentration, γ (= 0.091), being slightly smaller than Neumeier's (γ = 0.1), the predicted (relative) change in mobile hole concentration will also be very similar. In fact, only one parameter is significantly different from Neumeier's, and that is the coefficient *A*. Our value of *A* = 157*K* is 37% of Neumeier's *A* = 425*K*. The smaller value of *A* suggests that T_c would be more strongly affected by pair-breaking than by a change in hole concentration.

The 20% *Pr*, 0% *Ca* sample made for comparison, is quite different from that of the *Pr* 20-50% system. Its T_c is about 5*K* lower than before, the magnetic transition width is much broader (~1.4*X*) and its isotope shift is also larger (~1.5*X*). Clearly the preparation technique greatly affects the characteristics and hence the quality of the samples. As the highest quality materials, single crystals, tend to have very sharp transitions, and the polycrystalline materials have broader transitions, the relationship between the isotope shift and the width of the transition was investigated (Figure 7.13) for both the *Pr* and *Pr:Ca* substituted materials. A linear correlation between the ΔT_c and the transition width is found. The intercept for a zero-width transition remains finite, in the range of 0.3*K* to 0.4*K*. This result poses the question of whether the isotope shift should actually be taken as a constant for this system.

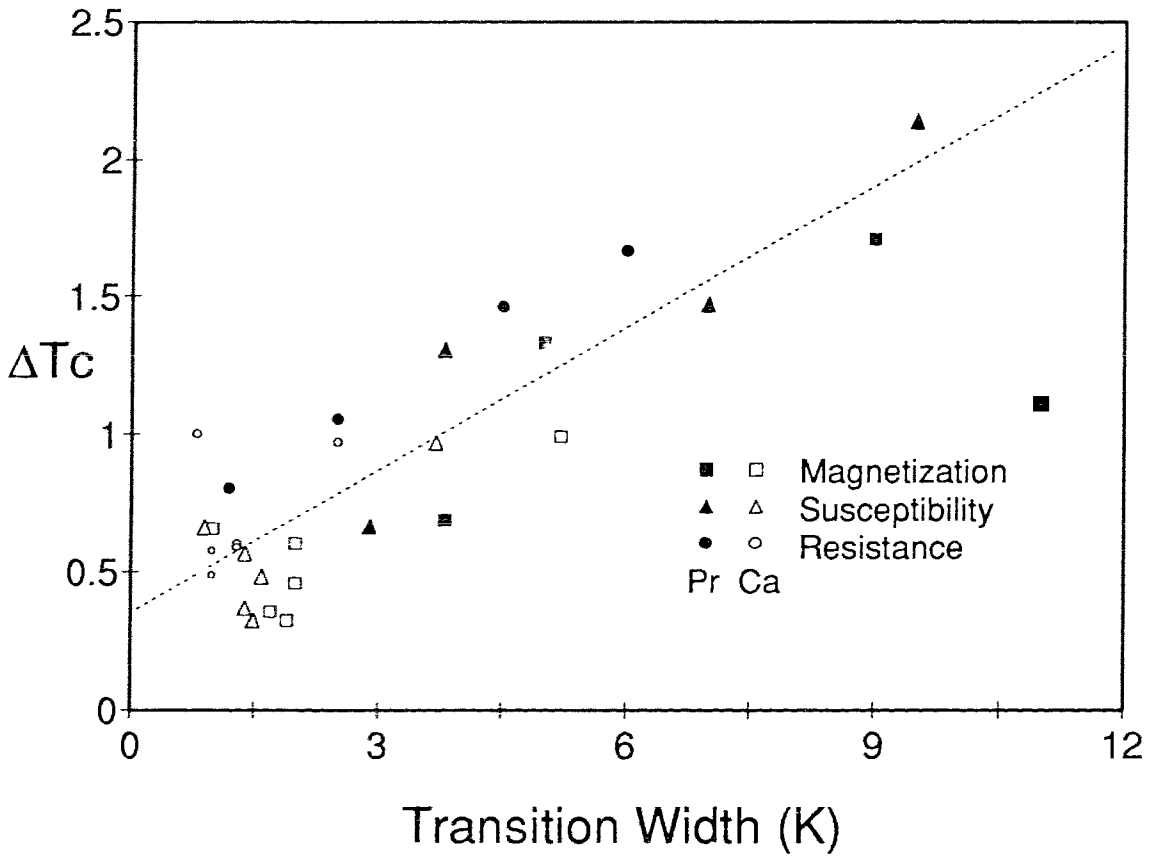

Figure 7.13

ΔT_c vs. transition width for both the *Pr* and the *Pr:Ca* systems. The dotted line is a linear fit to the data and indicates a possible relationship between the magnitude of the isotope shift, ΔT_c, and the width of the transition.

In the *Pr* system, we noted that the tails in the magnetic measurements become much larger with the increase in *Pr* concentration as do the transition widths, and the isotope shifts. The *Ca* data with its much sharper transitions and lack of low shielding tails do not exhibit this same effect. As both sets of samples have similar impurity lines in the X-ray data, it is unlikely that the long tails can be attributed solely to the impurities within the samples. Of course, the *Ca* substitution does not have the large effect on T_c that the *Pr* does and it may then be argued that ΔT_c, the transition width, as well as the isotope shift are dependent on T_c.

8 RESULTS - ZINC SUBSTITUTION

8.1 SAMPLE PREPARATION

The stoichiometric proportions for the *Zn* system $YBa_2(Cu_{1-z}Zn_z)_3O_{7-\delta}$ with $z = 0.02$, 0.025, 0.04, 0.05, 0.06, 0.07, 0.075, 0.08, 0.085, and 0.0875 were prepared in a different manner than the previous two systems. The calcination procedure was as follows:

1) heat to 925°*C* in air and hold for 20 hours, then cool and regrind;

2) repeat step 1;

3) heat to 930°*C* in ^{16}O and hold for 12 hours; then

4) cool to 475°*C* and hold for 18 hours; then

5) cool to 375°*C* and hold for 12 hours; then

6) cool to room temperature.

The sintering process was as follows:

1) heat to 925°*C* and hold for 12 hours; then

2) cool to 475°*C* and hold for 24 hours; then

3) cool to 375°*C* and hold for 18 hours; then

4) cool to room temperature.

All cooling processes were at the natural cooling rate of the oven.

8.2 MEASUREMENTS

The substitution of *Zn* for *Cu* in $YBa_2Cu_3O_{7-\delta}$ causes a more rapid depression in the critical temperature with the increase in *Zn* concentration than it did with the *Pr* subsitution. The resistivity measurements (Figure 8.1) show a smooth drop in the critical temperature with the increase of *Zn* substitution, from about 70*K* at 2% *Zn* to just under 10*K* at 8.75% *Zn*. A substitution of 9% *Zn* remained in the normal state down to 1.8*K*. These measurements also indicate an increase in the normal state resistivity with the drop in T_c and the increase in *Zn* concentration.

A comparison of the dc magnetization, ac susceptibility and resistivity measurements is given in Figure 8.2. The 4% *Zn* substitution is given as a characteristic sample. The *Zn* system has the sharpest transitions of all three of the systems studied. The transition width remains sharp and independent of the *Zn* concentration (and critical temperature). There is good agreement between the calculated isotopic shifts as well as the critical temperatures determined from the three different measurement methods. The difference between T_c obtained magnetically and that obtained resistively is highest for the 4% *Zn* samples. The linear relationship between the critical temperature and the concentration can be seen in Figure 8.3.

The ZFC and FC data for several *Zn* concentrations are given in Figure 8.4, and the Meissner fractions are indicated in Table 8.1. The Meissner fraction drops rapidly with the initial increase in *Zn* substitution but then quickly levels out around 10%. At the highest concentrations of *Zn*, 8%, 8.5% and 8.75%, the Meissner fraction no longer remains small or predictable.

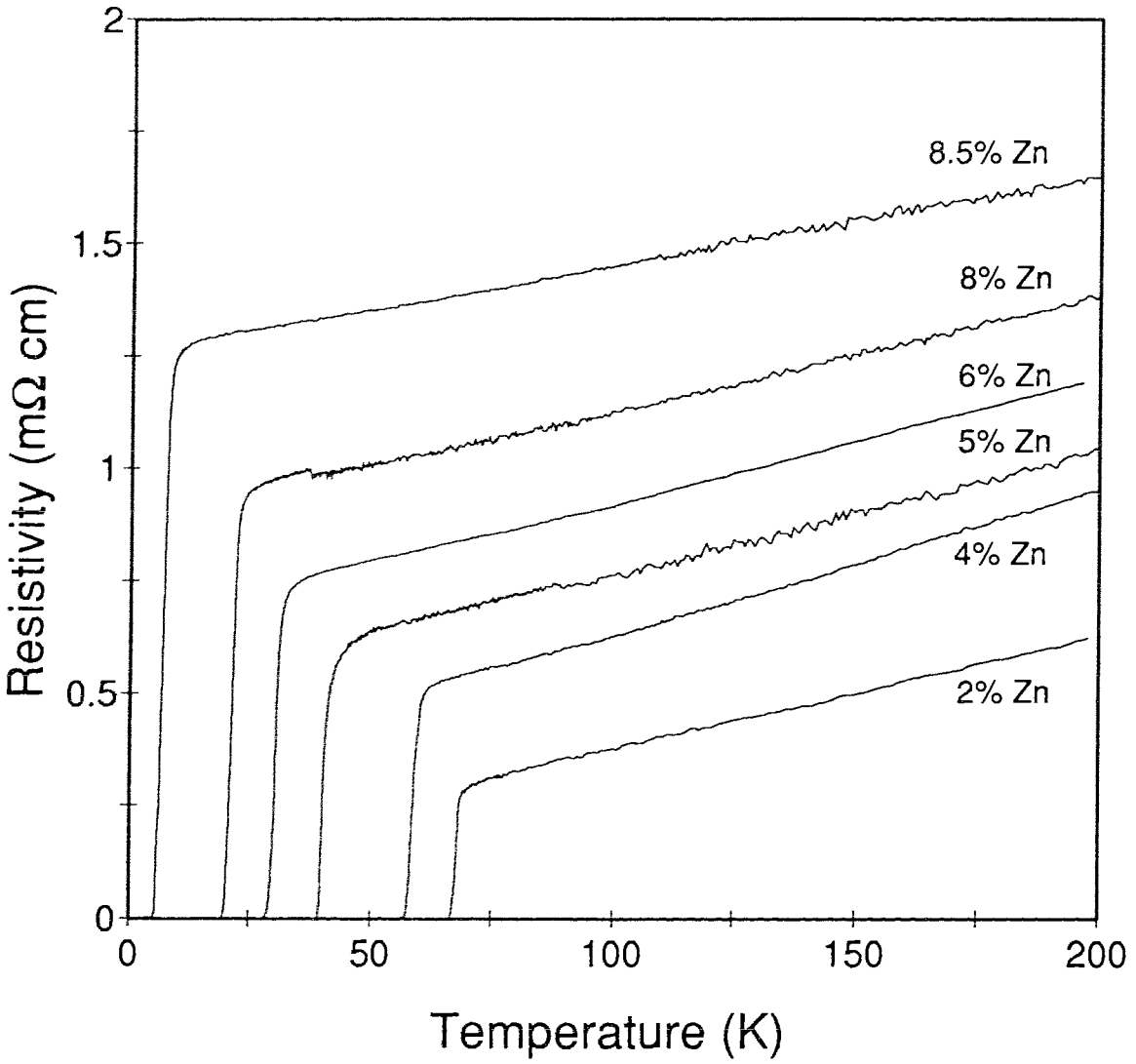

Figure 8.1

DC resistivity vs. temperature for *Zn* substituted *YBCO*. Only the measurements on the some of the ^{16}O samples are shown. Note the linear slope of the samples in the normal state.

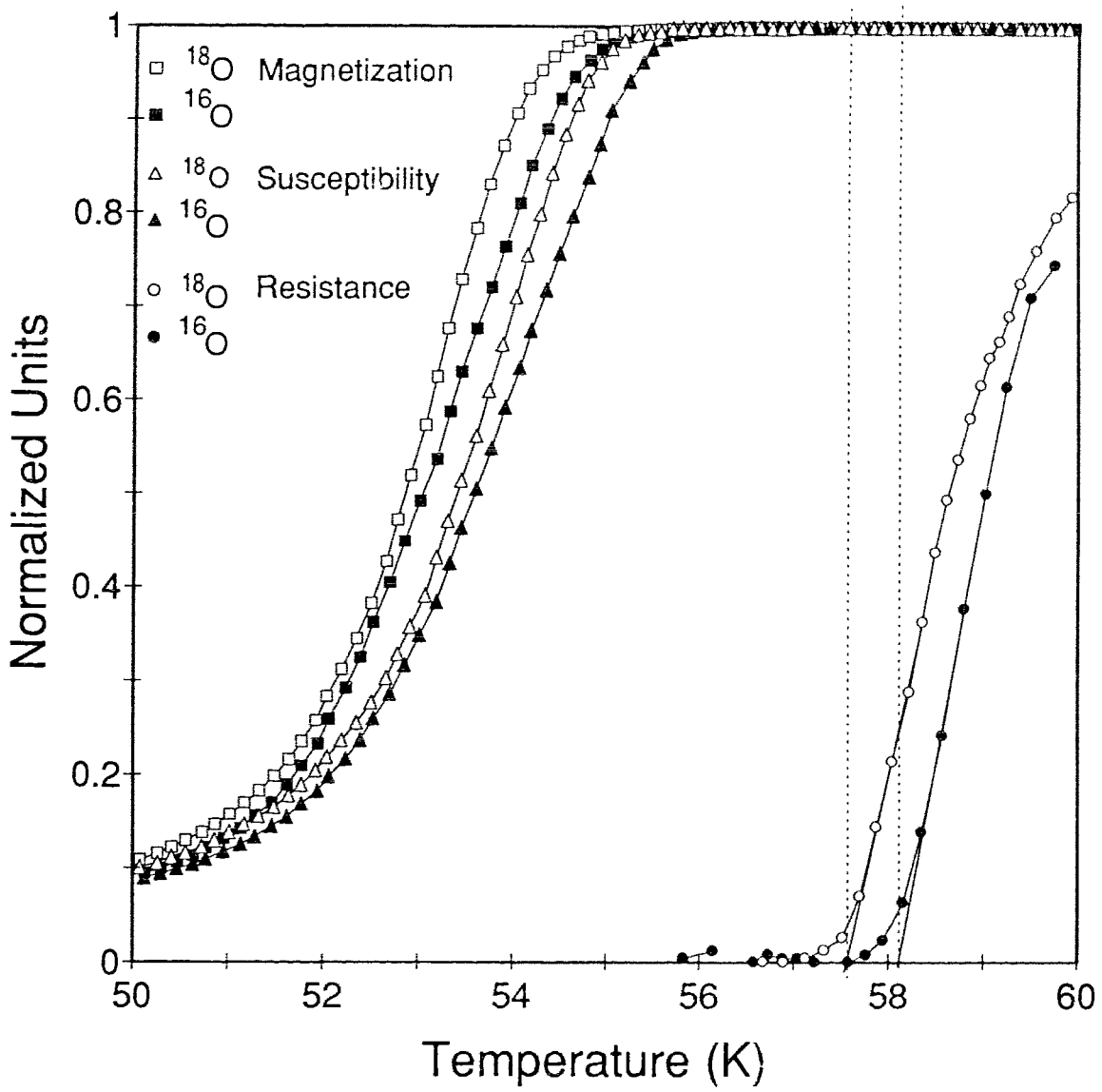

Figure 8.2

Comparison of dc magnetization, ac susceptibility and resistance measurements for $YBa_2(Cu_{0.96}Zn_{0.04})_3O_{7-\delta}$. The symbols represent the data. The solid lines provide continuity from point to point. The dashed lines are a visual aid for the critical temperature of the resistive transition (obtained from the straight line approximation). The resistance was normalized to $R(72K)$.

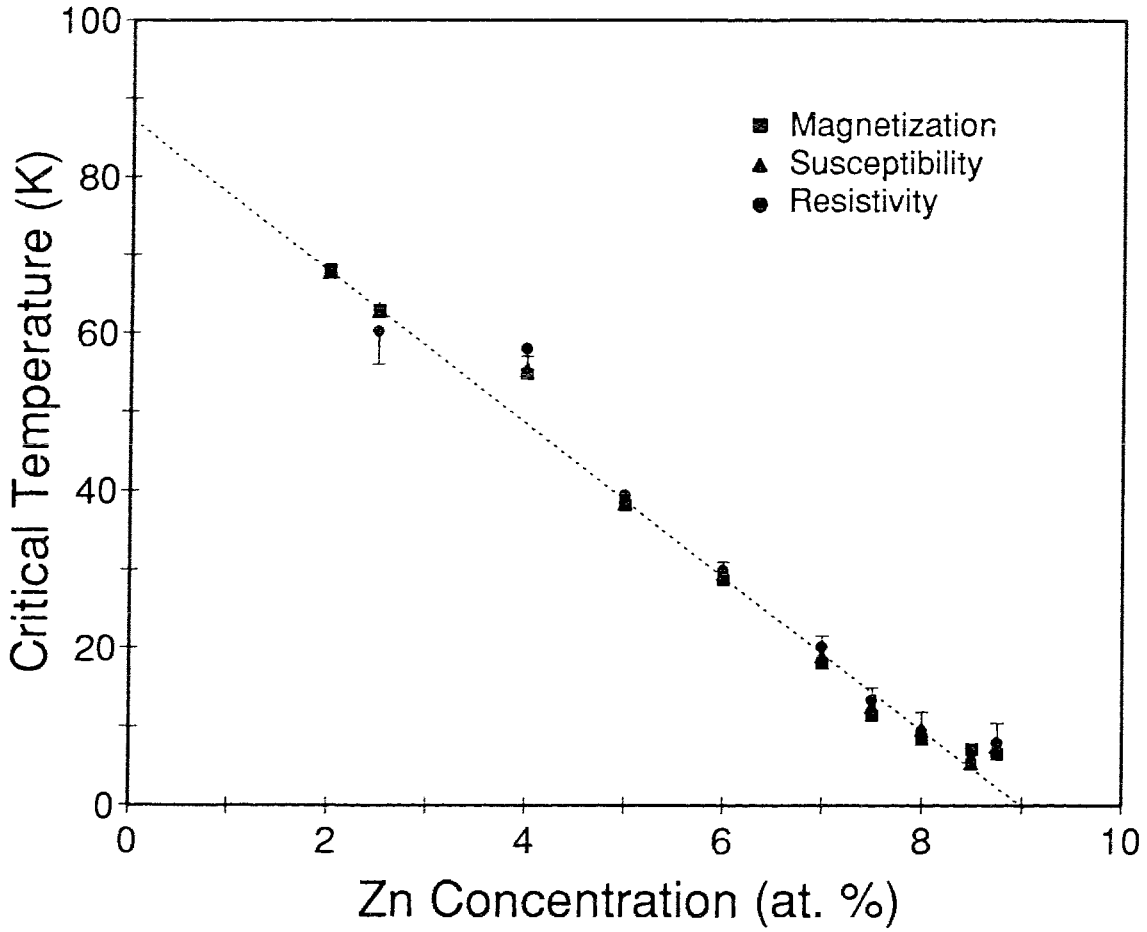

Figure 8.3

Critical temperature vs. *Zn* concentration. The dotted line is a linear fit to the data and indicates the linear relationship between the concentration and T_c.

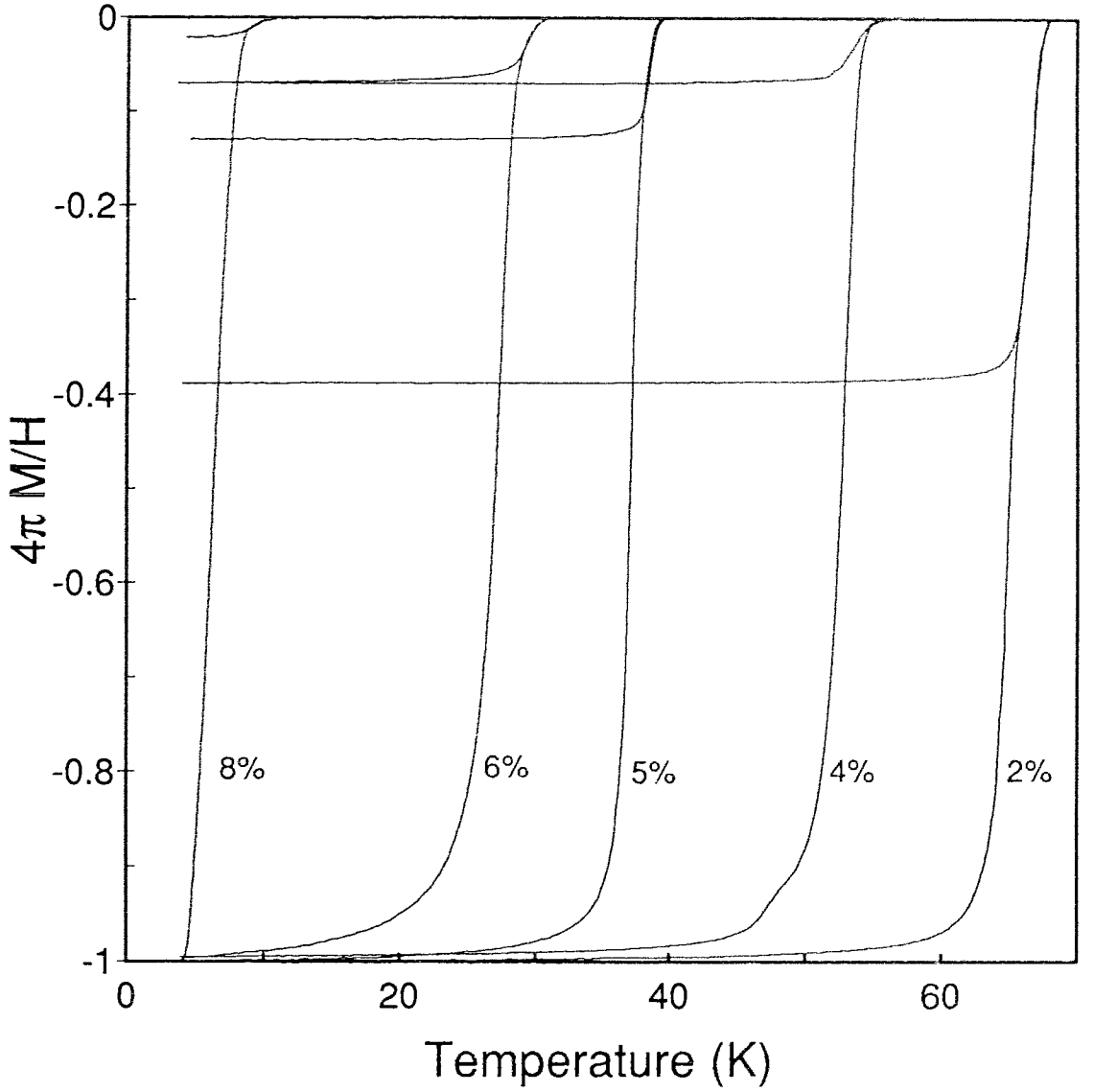

Figure 8.4

Meissner effect in *Zn* substituted *YBCO*. Both the ZFC and FC curves are shown from which the Meissner fraction has been obtained for the 2%, 4%, 5%, 6%, and 8% Zn samples. Samples were measured in a field of strength 0.05*Oe*.

Zn Concentration	^{18}O Concentration	Meissner Fraction	Transition Width *(K)*		
(at. %)	(at. %)	@ 0.05*Oe*	Mag.	Susc.	Res.
2	92	40%	3.5	3.5	1.0
2.5	(92)	60%	22	22	6
4	92	7%	3.9	4.5	1.5
5	92	13%	3.0	2.0	1.3
6	(92)	7%	5.0	3.0	1.6
7	86	6%	4.0	2.5	2.2
7.5	88	5%	3.9	2.6	2.0
8*	(92)	2%, 11%	2.9	2.4	2.0
8.5*	92	74%, 60%	2.3	2.2	2.0
8.75*	92	5%, 25%	2.0	2.0	2.0

Table 8.1. General characteristics of *Zn* substituted *YBCO*.

* - both ^{16}O and ^{18}O Meissner fractions are given. A number in parentheses indicates that this value is an estimate.

Our results on the resistivity, critical temperature, and the generally narrow transitions involved in *Zn* substitution agree quite favourably with what exists in the literature (section 2.2.2). No information on the Meissner effect is available.

The data, the Simplex fit to the data, and the isotope shift for the dc magnetization, ac susceptibility and resistivity measurements for the *Zn* substitutions of 2% to 8.75% are given in Figures 8.5 to 8.14. The critical temperatures and the computed isotope shifts are given in Table 8.2. The isotopic shift, ΔT_c, and the isotope coefficient, α, are plotted against T_c in Figure 8.15. The isotope shift appears constant or there may even be a slight decrease in its magnitude with decreasing critical temperature. Only the magnetic measurements for the 8.5% and 8.75% samples, as well as all measurements on the 8% samples have large ΔT_c's.

The *Zn* samples do not show (to within the limits of the equipment) any impurity lines within the X-ray spectra; they have sharp transitions; and thus, tend to be better quality samples than the *Pr* or *Pr:Ca* series. The quality of the 2.5% *Zn* substituted sample is questionable as it has an extremely broad transition, however it does give an isotopic shift that is comparable to the other measured shifts.

The 4% and 7% *Zn* samples were subjected to different measuring fields ranging from 0.05*Oe* to 50*Oe* to study the effect of the penetration of the measuring field into the sample. The effects on the ZFC curves are shown in Figure 8.16. On the low T_c sample, 7% *Zn*, a measuring field of only 1*Oe* has already begun to penetrate the sample causing a substantial decrease in signal. Not only is the magnitude of the transition lessened, but indeed the shape of the entire transition is altered. Even samples with high T_c's (4% *Zn*) can be influenced by their measuring fields although this occurs only at lower fields. There appears to be a critical field at which there is a large change in the

(note: text continues on page 143)

Figure 8.5

Oxygen isotope effect in $YBa_2(Cu_{0.98}Zn_{0.02})_3O_{7-\delta}$

2% *Zn* Substitution

The empty symbols represent the ^{18}O data and the filled symbols represent the ^{16}O data. The solid line represents the Simplex fit to the data. The "+" symbols represent the shift, ΔT_c as a function of temperature, between the two fits to the data.

The arrows on the magnetization and susceptibility graphs indicate the T_c obtained from a linear extrapolation of the bulk of the transition - $68.1K$ for the magnetization (upper limit = $68.7K$) and $67.9K$ (upper limit = $68.9K$) for the susceptibility.

No cutoff was imposed in the calculation of the mean of the isotope shift for the magnetic measurements. A lower limit cutoff was imposed on the resistance owing to the long resistive tails. The cutoff was taken at the point at which the fit broke away form the straight line extrapolation which was extended to 0.7.

The resistance measurements are normalized to $R(80K)$.

Not all temperature scales are equivalent.

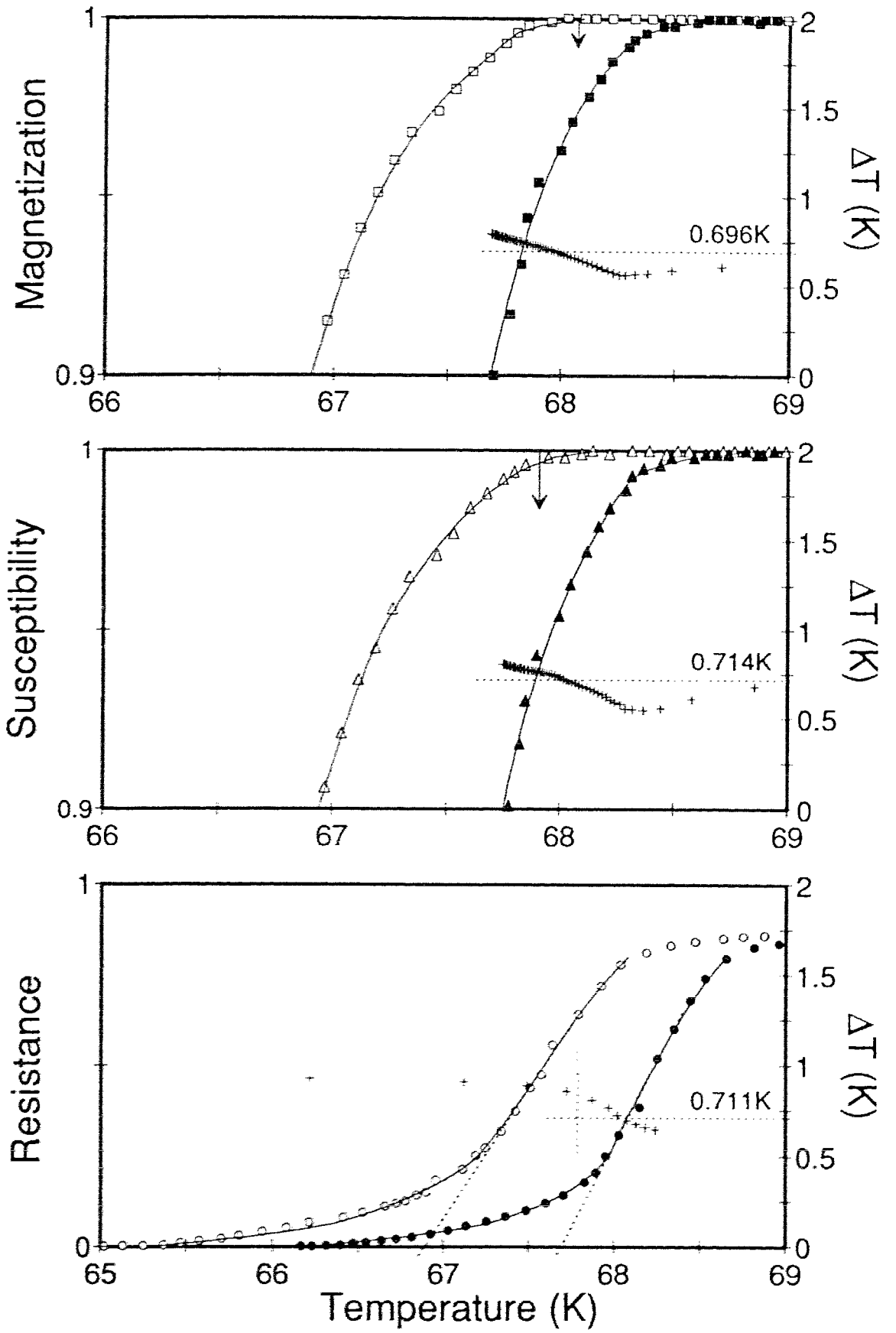
Magnetization
Susceptibility
Resistance
ΔT (K)
0.696K
0.714K
0.711K
Temperature (K)
1
0.9
2
1.5
0.5
0
66
67
68
69
65

Figure 8.6

Oxygen isotope effect in $YBa_2(Cu_{0.975}Zn_{0.025})_3O_{7-\delta}$

2.5% *Zn* Substitution

The empty symbols represent the ^{18}O data and the filled symbols represent the ^{16}O data. The solid line represents the Simplex fit to the data. The "+" symbols represent the shift, ΔT_i, as a function of temperature, between the two fits to the data.

The arrows on the magnetization and susceptibility graphs indicate the T_c obtained from a linear extrapolation of the bulk of the transition - 62.9*K* for the magnetization (upper limit = 63.4*K*) and 63.0*K* (upper limit = 63.7*K*) for the susceptibility.

No cutoff was imposed in the calculation of the mean of the isotope shift for the magnetic measurements. Although the resistive transition is quite poor, the temperature shift, ΔT_i, between curves remains constant and thus no cutoff limit was imposed.

The resistance measurements are normalized to *R*(100*K*).

Not all temperature scales are equivalent.

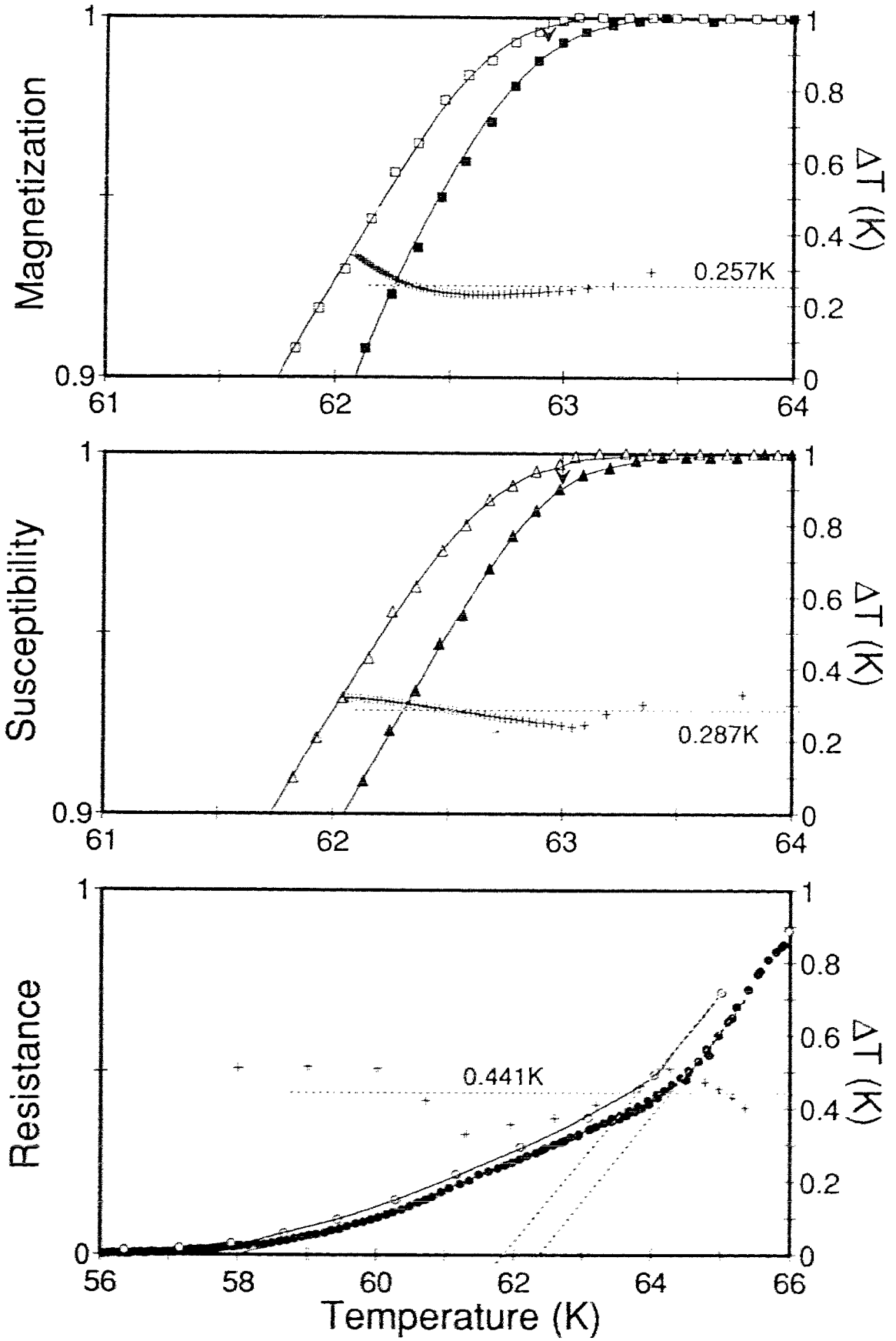
Magnetization
1
0.9
61
62
63
64
0.257K
ΔT (K)
0
0.2
0.4
0.6
0.8
1
Susceptibility
0.287K
Resistance
0.441K
56
58
60
62
64
66
Temperature (K)

Figure 8.7

Oxygen isotope effect in $YBa_2(Cu_{0.96}Zn_{0.04})_3O_{7-\delta}$

4% *Zn* Substitution

The empty symbols represent the ^{18}O data and the filled symbols represent the ^{16}O data. The solid line represents the Simplex fit to the data. The "+" symbols represent the shift, ΔT_i, as a function of temperature, between the two fits to the data.

The arrows on the magnetization and susceptibility graphs indicate the T_c obtained from a linear extrapolation of the bulk of the transition - 54.8*K* for the magnetization (upper limit = 56.9*K*) and 55.4*K* (upper limit = 56.6*K*) for the susceptibility.

No cutoff was imposed in the calculation of the mean of the isotope shift for either the magnetic or resistance measurements.

The resistance measurements are normalized to *R*(70*K*).

Not all temperature scales are equivalent.

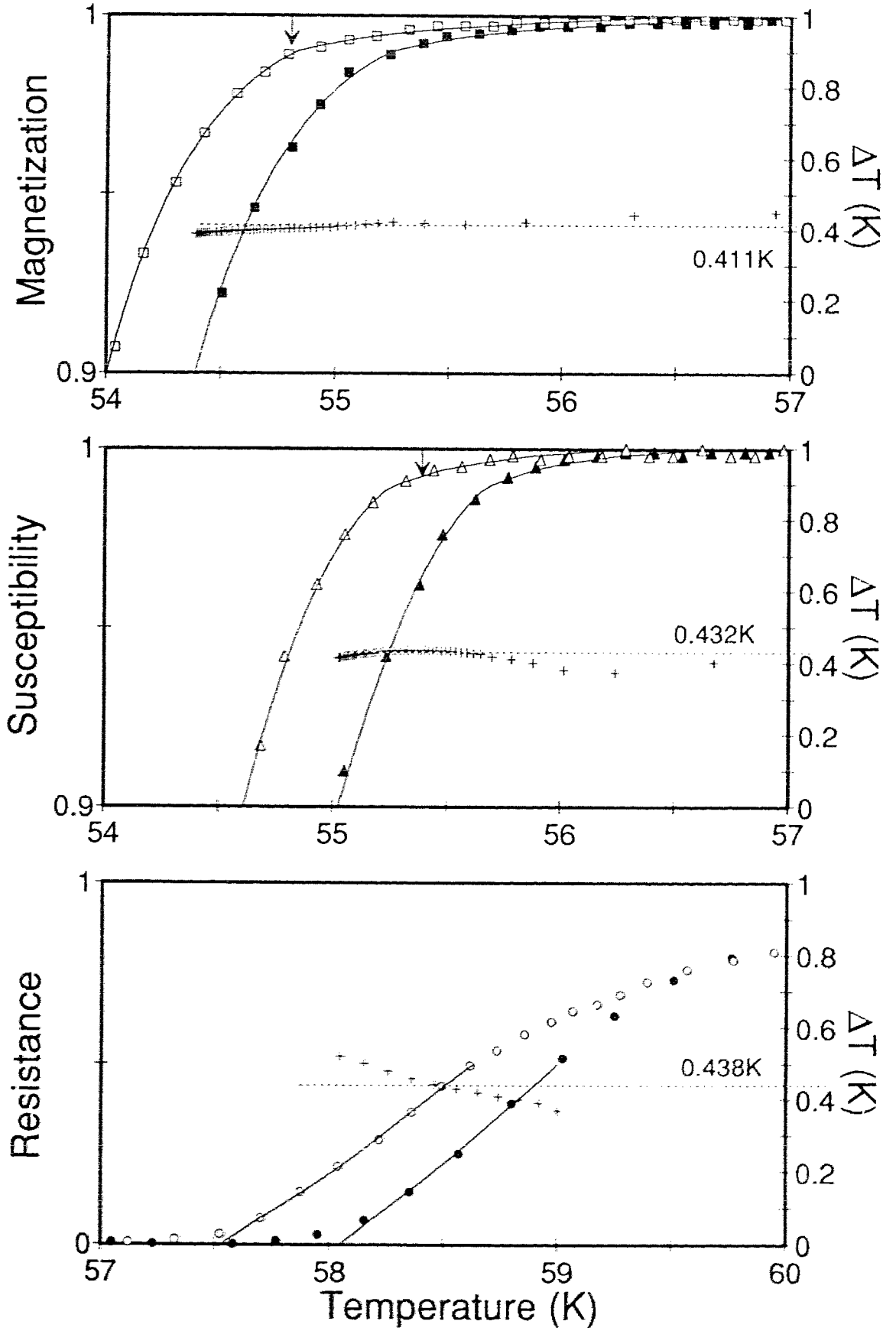
Magnetization
Susceptibility
Resistance
ΔT (K)
0.411K
0.432K
0.438K
Temperature (K)
1
0.9
0
0.2
0.4
0.6
0.8
54
55
56
57
58
59
60

Figue 8.8

Oxygen isotope effect in $YBa_2(Cu_{0.95}Zn_{0.05})_3O_{7-\delta}$

5% *Zn* Substitution

The empty symbols represent the ^{18}O data and the filled symbols represent the ^{16}O data. The solid line represents the Simplex fit to the data. The "+" symbols represent the shift, ΔT_i, as a function of temperature, between the two fits to the data.

The arrows on the magnetization and susceptibility graphs indicate the T_c obtained from a linear extrapolation of the bulk of the transition - $38.1K$ for the magnetization (upper limit = $39.6K$) and $38.4K$ (upper limit = $39.7K$) for the susceptibility.

No cutoff was imposed in the calculation of the mean of the isotope shift for either the magnetic or resistance measurements.

The resistance measurements are normalized to $R(70K)$.

Not all temperature scales are equivalent.

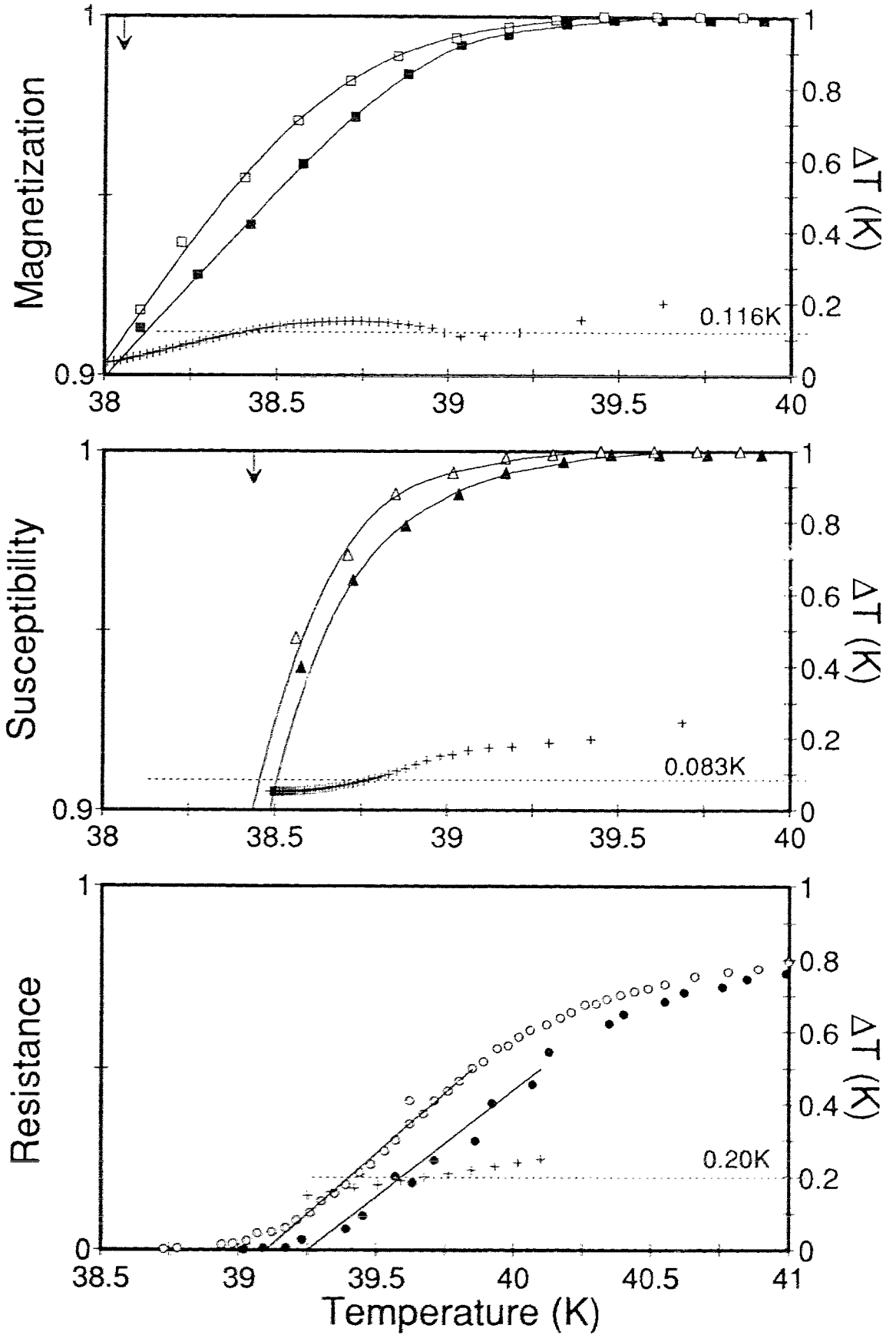
Magnetization
Susceptibility
Resistance
ΔT (K)
0.116K
0.083K
0.20K
Temperature (K)
1
0.9
0
0.8
0.6
0.4
0.2
38
38.5
39
39.5
40
40.5
41

Figure 8.9

Oxygen isotope effect in $YBa_2(Cu_{0.94}Zn_{0.06})_3O_{7-\delta}$

6% *Zn* Substitution

The empty symbols represent the ^{18}O data and the filled symbols represent the ^{16}O data. The solid line represents the Simplex fit to the data. The "+" symbols represent the shift, ΔT_i, as a function of temperature, between the two fits to the data.

The arrows on the magnetization and susceptibility graphs indicate the T_c obtained from a linear extrapolation of the bulk of the transition - 28.7*K* for the magnetization (upper limit = 31.4*K*) and 29.6*K* (upper limit = 31.0*K*) for the susceptibility.

The vertical dotted line indicates the cutoff in the calculation of the mean of the isotope shift. The horizontal line indicates this mean, and its value is indicated above the line.

The resistance measurements are normalized to *R*(45*K*).

Not all temperature scales are equivalent.

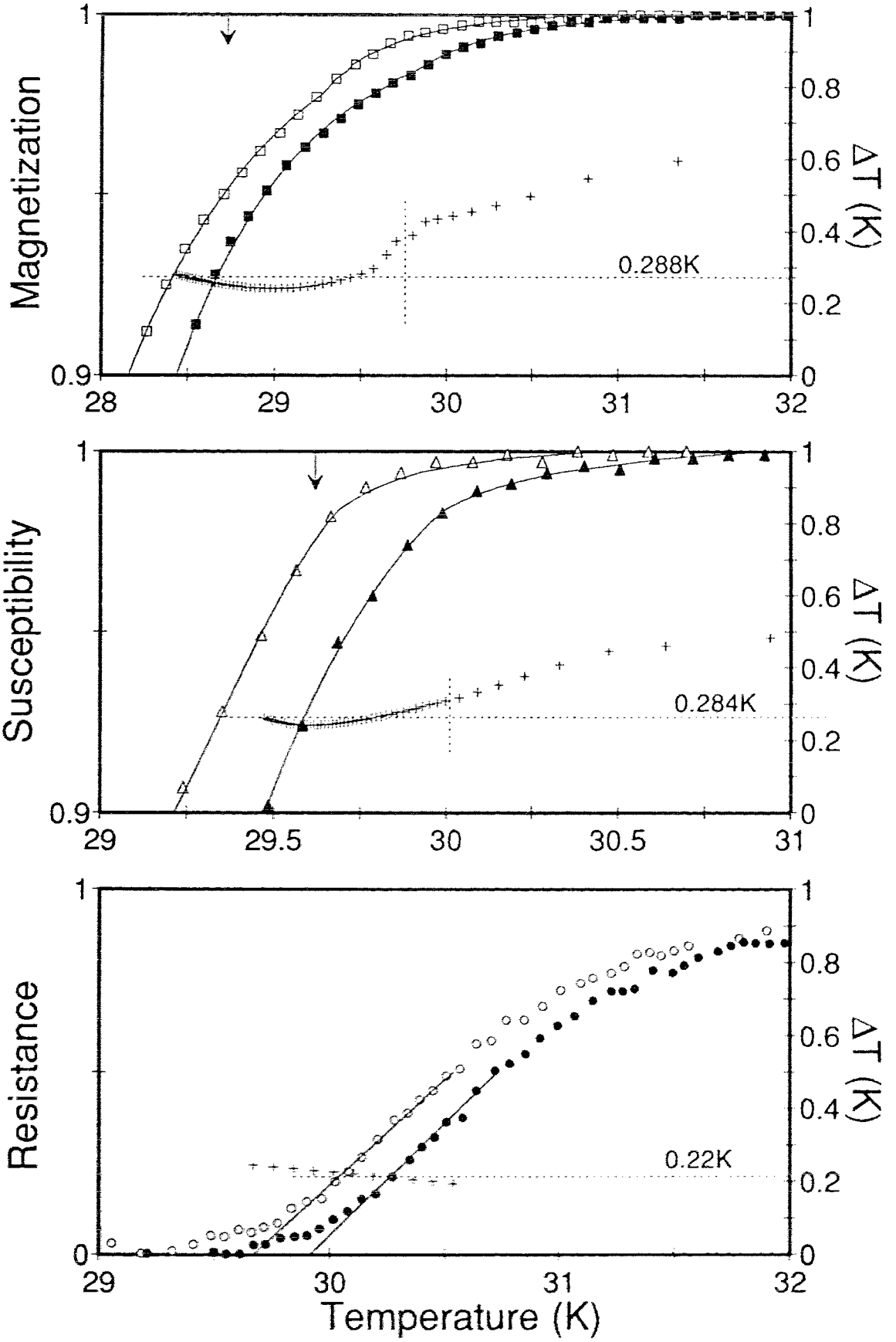
Magnetization
1
0.9
28
29
30
31
32
0.288K
Susceptibility
29
29.5
30
30.5
31
0.284K
Resistance
0
0.22K
Temperature (K)
ΔT (K)
0
0.2
0.4
0.6
0.8

Figure 8.10

Oxygen isotope effect in $YBa_2(Cu_{0.93}Zn_{0.07})_3O_{7-\delta}$

7% *Zn* Substitution

The empty symbols represent the ^{18}O data and the filled symbols represent the ^{16}O data. The solid line represents the Simplex fit to the data. The "+" symbols represent the shift, ΔT_i, as a function of temperature, between the two fits to the data.

The arrows on the magnetization and susceptibility graphs indicate the T_c obtained from a linear extrapolation of the bulk of the transition - 18.1*K* for the magnetization (upper limit = 21.4*K*) and 19.1*K* (upper limit = 21.8*K*) for the susceptibility.

The vertical dotted line indicates the cutoff in the calculation of the mean of the isotope shift. The horizontal line indicates this mean, and its value is indicated above the line.

The resistance measurements are normalized to *R*(40*K*).

Not all temperature scales are equivalent.

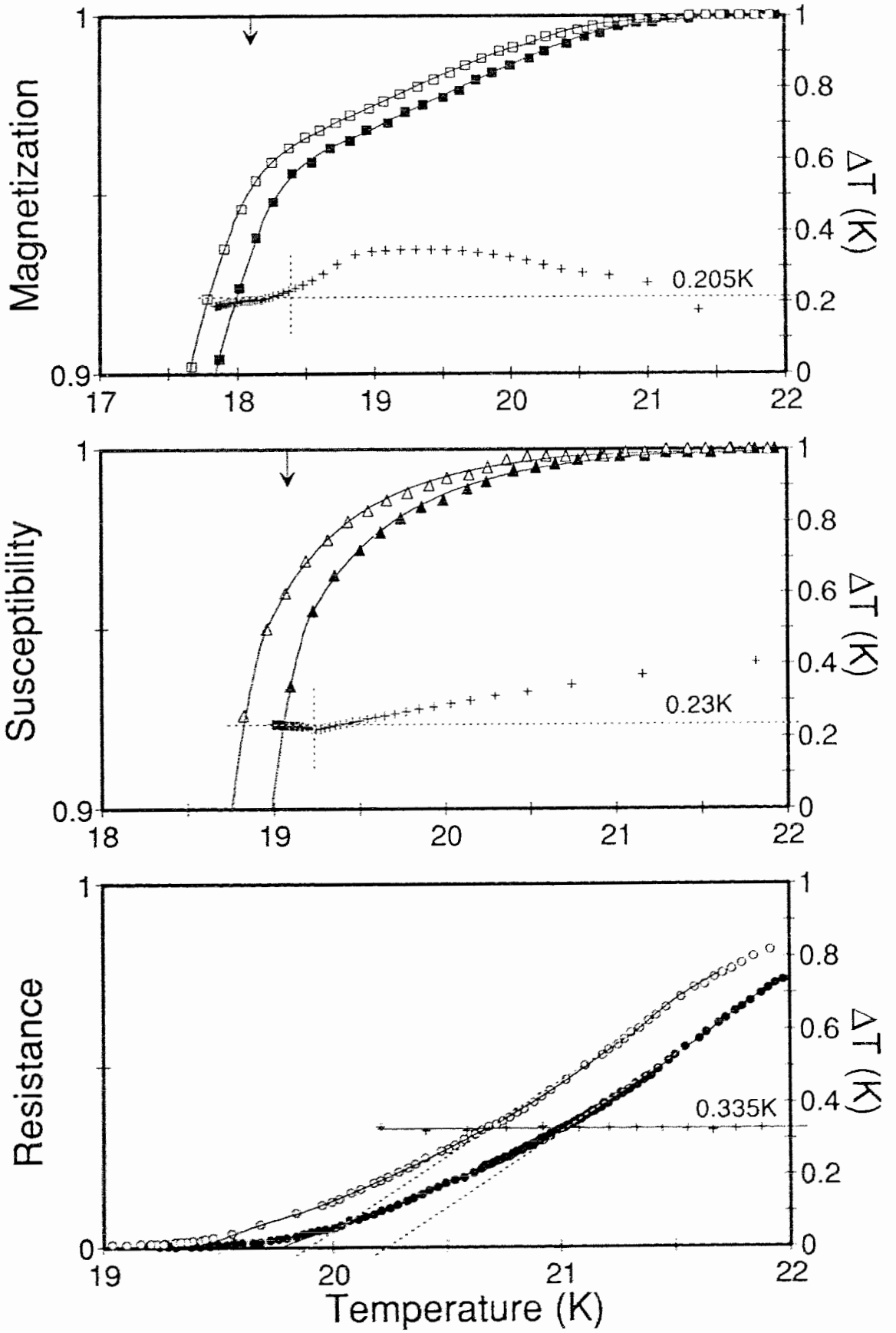
Magnetization
Susceptibility
Resistance
ΔT (K)
0.205K
0.23K
0.335K
Temperature (K)

Figure 8.11

Oxygen isotope effect in $YBa_2(Cu_{0.925}Zn_{0.075})_3O_{7-\delta}$

7.5% *Zn* Substitution

The empty symbols represent the ^{18}O data and the filled symbols represent the ^{16}O data. The solid line represents the Simplex fit to the data. The "+" symbols represent the shift, ΔT_c, as a function of temperature, between the two fits to the data.

The arrows on the magnetization and susceptibility graphs indicate the T_c obtained from a linear extrapolation of the bulk of the transition - 11.59*K* for the magnetization (upper limit = 14.6*K*) and 12.7*K* (upper limit = 14.8*K*) for the susceptibility.

The vertical dotted line indicates the cutoff in the calculation of the mean of the isotope shift. The horizontal line indicates this mean, and its value is indicated above the line.

The resistance measurements are normalized to *R*(25*K*).

Not all temperature scales are equivalent.

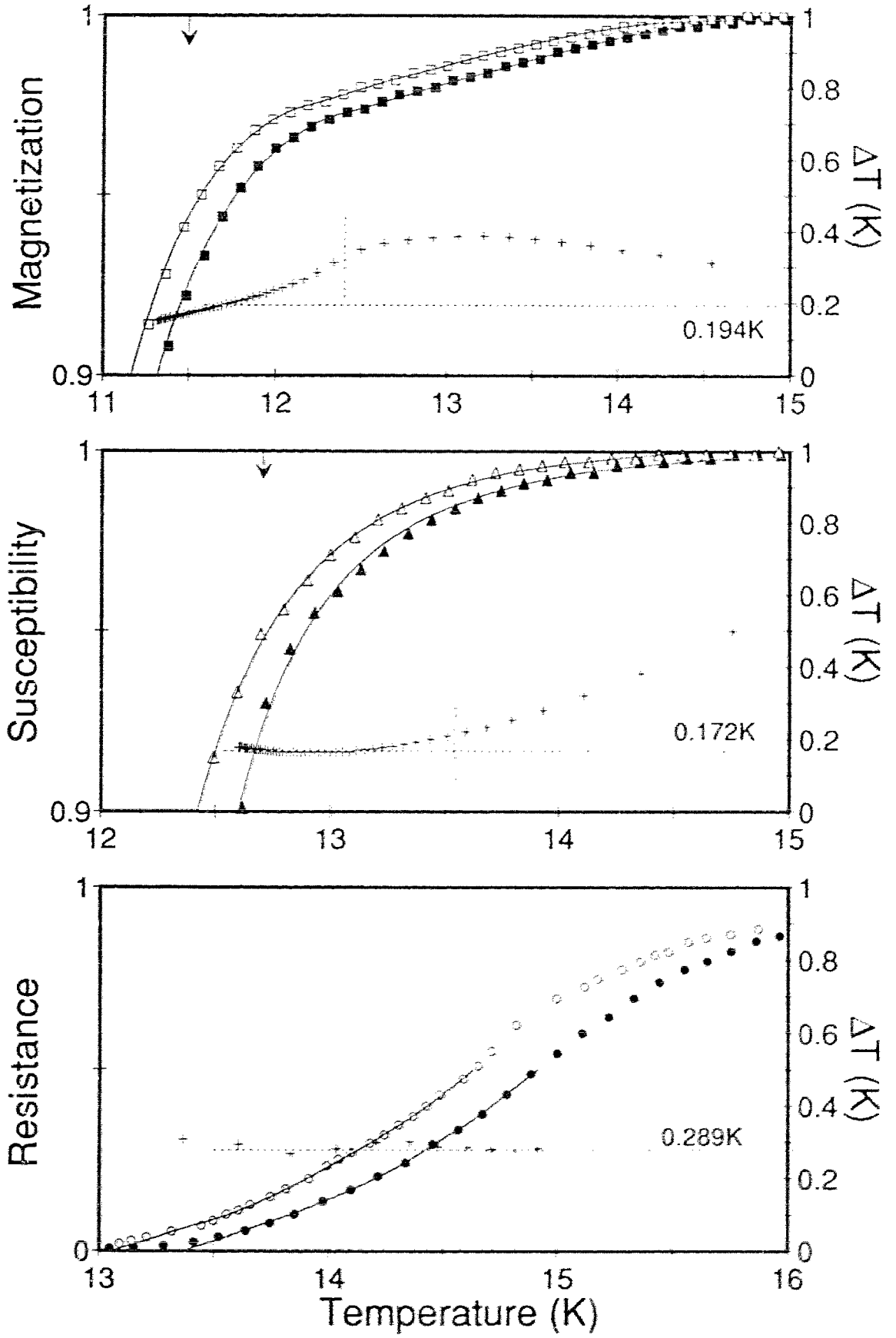
Magnetization
Susceptibility
Resistance
ΔT (K)
Temperature (K)
0.194K
0.172K
0.289K
1
0.9
0
0.2
0.4
0.6
0.8
11
12
13
14
15
16

Figure 8.12

Oxygen isotope effect in $YBa_2(Cu_{0.92}Zn_{0.08})_3O_{7-\delta}$

8% *Zn* Substitution

The empty symbols represent the ^{18}O data and the filled symbols represent the ^{16}O data. The solid line represents the Simplex fit to the data. The "+" symbols represent the shift, ΔT_c, as a function of temperature, between the two fits to the data.

The arrows on the magnetization and susceptibility graphs indicate the T_c obtained from a linear extrapolation of the bulk of the transition - 8.5*K* for the magnetization (upper limit = 11.6*K*) and 9.8*K* (upper limit = 11.3*K*) for the susceptibility.

The vertical dotted line indicates the cutoff in the calculation of the mean of the isotope shift. The horizontal line indicates this mean, and its value is indicated above the line.

The resistance measurements are normalized to *R*(25*K*).

Not all temperature scales are equivalent.

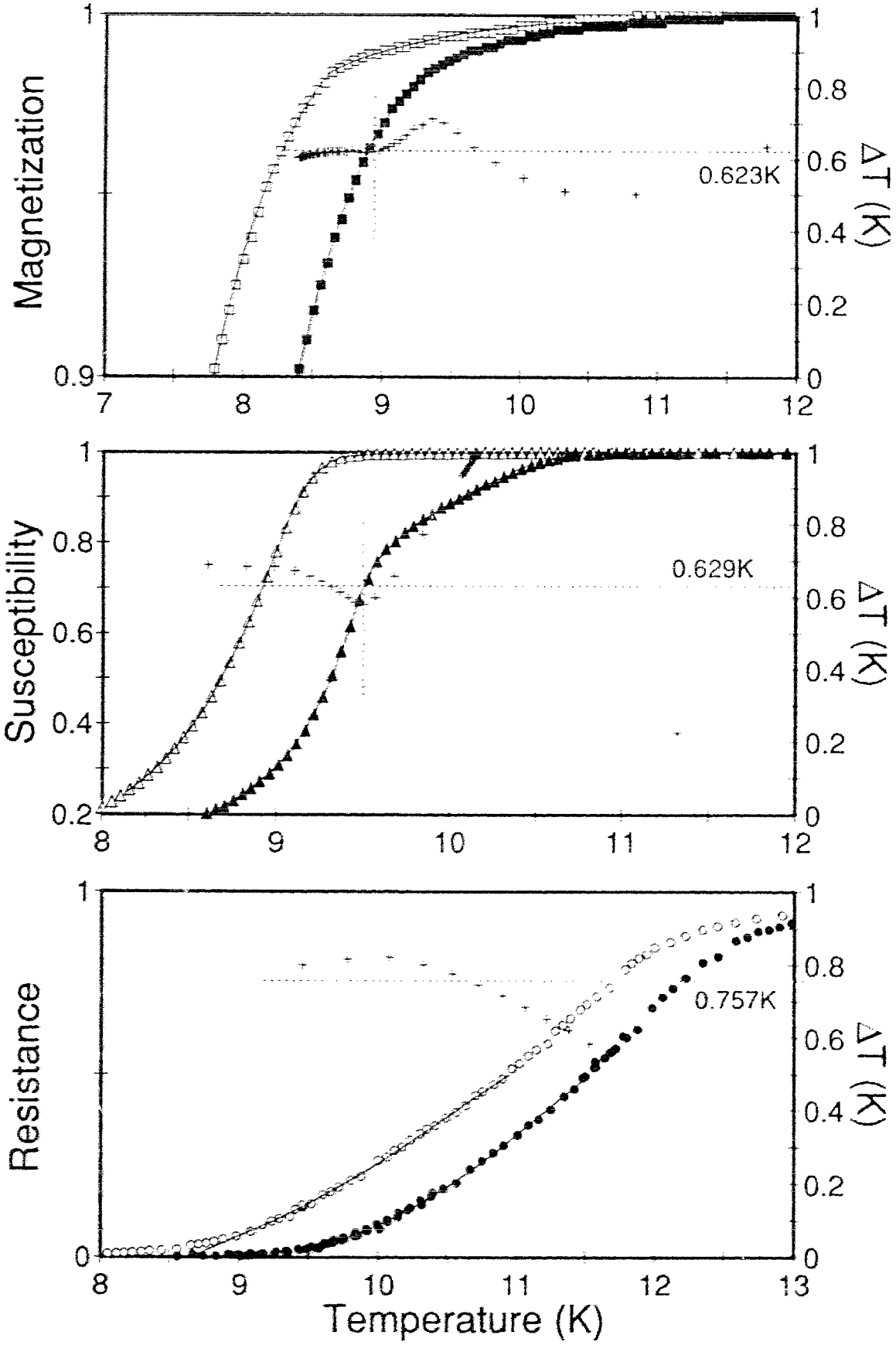
Magnetization
1
0.9
7
8
9
10
11
12
0.623K
ΔT (K)
1
0.8
0.6
0.4
0.2
0
Susceptibility
1
0.8
0.6
0.4
0.2
8
9
10
11
12
0.629K
ΔT (K)
1
0.8
0.6
0.4
0.2
0
Resistance
1
0
8
9
10
11
12
13
0.757K
ΔT (K)
1
0.8
0.6
0.4
0.2
0
Temperature (K)

Figure 8.13

Oxygen isotope effect in $YBa_2(Cu_{0.915}Zn_{0.085})_3O_{7-\delta}$

8.5% *Zn* Substitution

The empty symbols represent the ^{18}O data and the filled symbols represent the ^{16}O data. The solid line represents the Simplex fit to the data. The "+" symbols represent the shift, ΔT_i, as a function of temperature, between the two fits to the data.

The arrows on the magnetization and susceptibility graphs indicate the T_c obtained from a linear extrapolation of the bulk of the transition - $7.2K$ for the magnetization (upper limit = $8.2K$) and $5.6K$ (upper limit = $8.3K$) for the susceptibility.

Note the difference in the two susceptibilty data. The vertical dotted line indicates the cutoff in the calculation of the mean of the isotope shift. The horizontal line indicates this mean, and its value is indicated above the line.

The resistance measurements are normalized to $R(20K)$.

Not all temperature scales are equivalent.

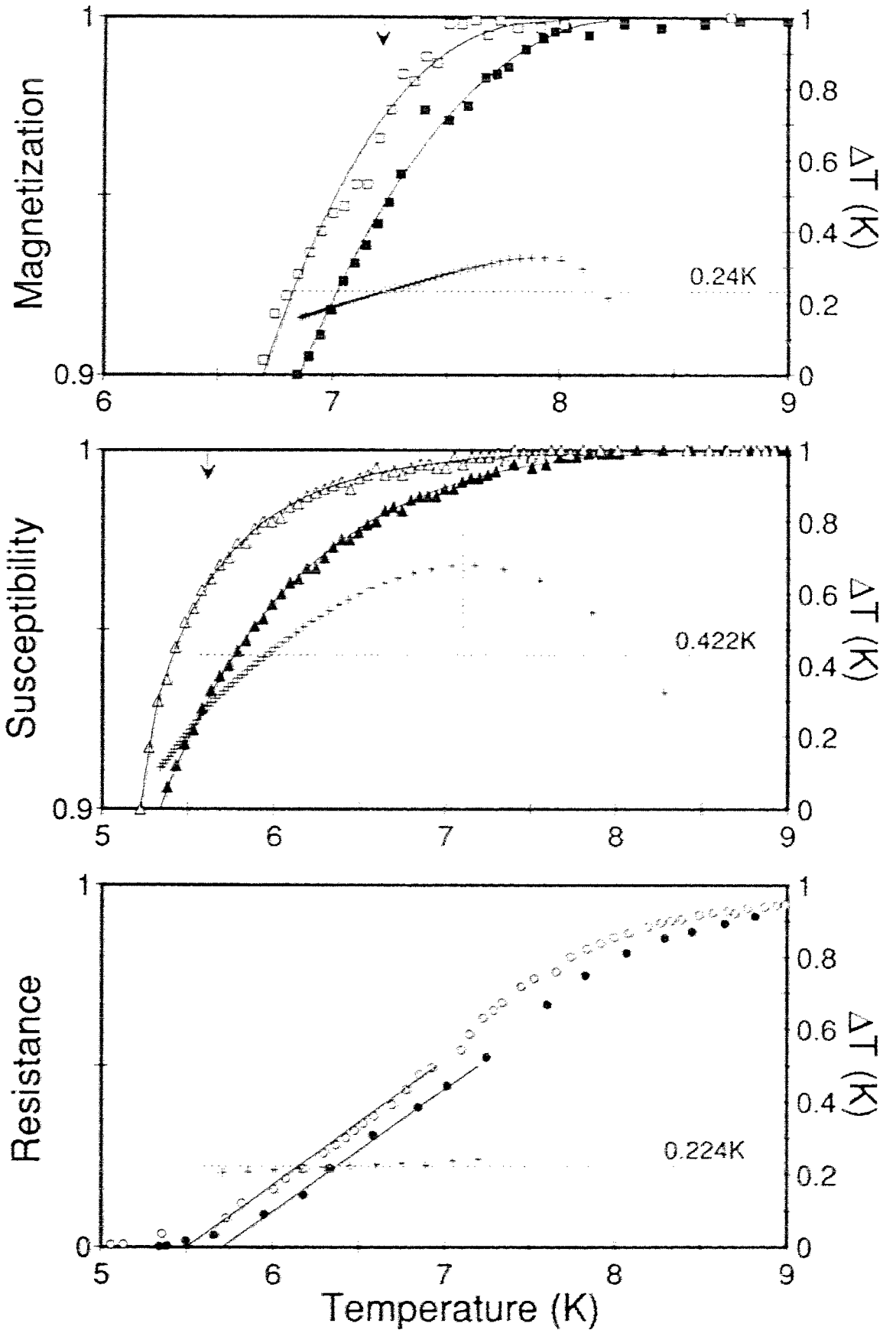
Magnetization
1
0.9
6
7
8
9
0.24K
ΔT (K)
0
0.2
0.4
0.6
0.8
1
Susceptibility
1
0.9
5
6
7
8
9
0.422K
ΔT (K)
0
0.2
0.4
0.6
0.8
1
Resistance
1
0
5
6
7
8
9
0.224K
ΔT (K)
0
0.2
0.4
0.6
0.8
1
Temperature (K)

Figure 8.14

Oxygen isotope effect in $YBa_2(Cu_{0.9125}Zn_{0.0875})_3O_{7-\delta}$

8.75% *Zn* Substitution

The empty symbols represent the ^{18}O data and the filled symbols represent the ^{16}O data. The solid line represents the Simplex fit to the data. The "+" symbols represent the shift, ΔT_c as a function of temperature, between the two fits to the data.

The arrows on the magnetization and susceptibility graphs indicate the T_c obtained from a linear extrapolation of the bulk of the transition - 6.6*K* for the magnetization (upper limit = 9.9*K*) and 7.7*K* (upper limit = 8.8*K*) for the susceptibility.

The vertical dotted line indicates the cutoff in the calculation of the mean of the isotope shift. The horizontal line indicates this mean, and its value is indicated above the line.

The resistance measurements are normalized to *R*(20*K*).

Not all temperature scales are equivalent.

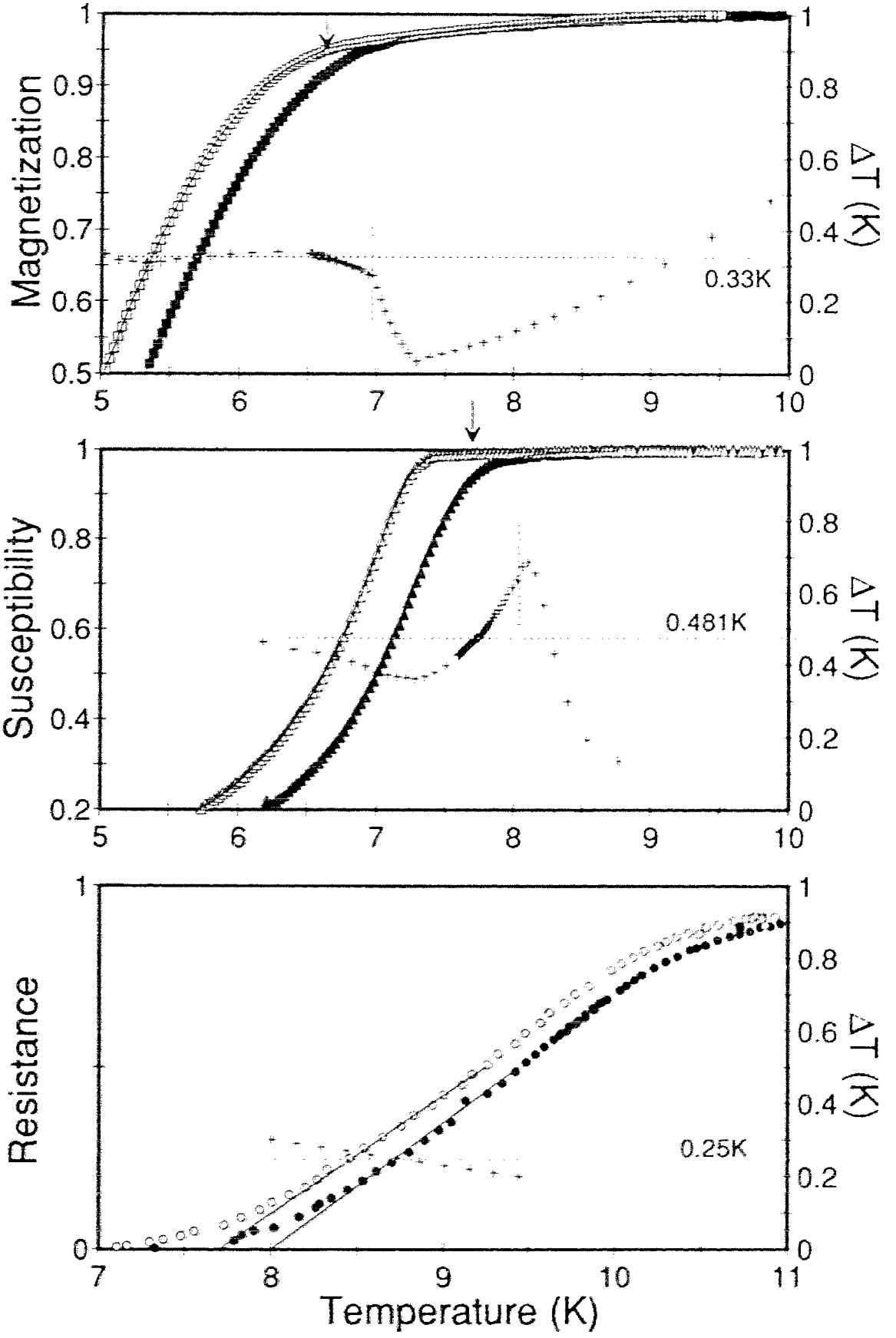
Magnetization
Susceptibility
Resistance
ΔT (K)
0.33K
0.481K
0.25K
Temperature (K)

Measurement	Sample	$T_c(K)$	$\Delta T_c(K)$	α
dc magnetization	2%	68.1 $^{-0.2}_{+0.6}$	0.696 ± 0.072	0.087 ± 0.010
	2.5%	62.9 $^{-0.2}_{+0.5}$	0.257 ± 0.031	0.035 ± 0.004
	4%	54.8 $^{-0.2}_{+2.1}$	0.411 ± 0.065	0.064 ± 0.011
	5%	38.1 $^{-0.2}_{+1.5}$	0.116 ± 0.045	0.026 ± 0.010
	6%	28.7 $^{-0.2}_{+2.7}$	0.288 ± 0.032	0.086 $^{+0.010}_{-0.016}$
	7%	18.1 $^{-0.2}_{+3.3}$	0.205 ± 0.049	0.097 $^{+0.025}_{-0.035}$
	7.5%	11.5 $^{-0.2}_{+3.0}$	0.194 ± 0.043	0.144 $^{+0.035}_{-0.055}$
	8%	8.5 $^{-0.2}_{+3.3}$	0.623 ± 0.033	0.646 $^{+0.053}_{-0.211}$
	8.5%	7.2 $^{-0.2}_{+1.1}$	0.240 ± 0.052	0.288 $^{+0.074}_{-0.098}$
	8.75%	6.6 $^{-0.2}_{+3.3}$	0.330 ± 0.040	0.435 $^{+0.070}_{-0.183}$
ac susceptibility	2%	67.9 $^{-0.2}_{+1.0}$	0.714 ± 0.078	0.090 ± 0.011
	2.5%	63.0 $^{-0.2}_{+0.7}$	0.287 ± 0.025	0.039 ± 0.004
	4%	55.4 $^{-0.2}_{+1.2}$	0.432 ± 0.092	0.066 ± 0.015
	5%	38.4 $^{-0.2}_{+1.3}$	0.083 ± 0.044	0.018 ± 0.010
	6%	29.6 $^{-0.2}_{+1.4}$	0.284 ± 0.036	0.082 ± 0.012
	7%	19.1 $^{-0.2}_{+2.7}$	0.230 ± 0.023	0.103 $^{+0.012}_{-0.022}$
	7.5%	12.7 $^{-0.2}_{+2.1}$	0.172 ± 0.020	0.116 $^{+0.016}_{-0.028}$
	8%	9.8 $^{-0.2}_{+1.5}$	0.629 ± 0.038	0.563 $^{+0.048}_{-0.107}$
	8.5%	5.6 $^{-0.2}_{+2.7}$	0.422 ± 0.188	0.665 $^{+0.352}_{-0.422}$
	8.75%	7.7 $^{-0.2}_{+1.1}$	0.481 ± 0.100	0.548 $^{+0.137}_{-0.172}$
dc resistance	2%	67.7 $^{-1.5}_{+0.1}$	0.711 ± 0.060	0.090 ± 0.010
	2.5%	60.2 $^{-4.4}_{+0.2}$	0.441 ± 0.087	0.062 ± 0.015
	4%	58.0 ± 0.2	0.438 ± 0.043	0.064 ± 0.006
	5%	39.3 ± 0.2	0.200 ± 0.050	0.043 ± 0.011
	6%	29.9 ± 0.2	0.220 ± 0.025	0.062 ± 0.008
	7%	20.2 $^{-0.5}_{+0.2}$	0.335 ± 0.020	0.142 ± 0.011
	7.5%	13.4 ± 0.3	0.289 ± 0.012	0.185 ± 0.012
	8%	9.6 ± 0.3	0.757 ± 0.061	0.697 ± 0.082
	8.5%	5.7 ± 0.2	0.224 ± 0.031	0.340 ± 0.060
	8.75%	8.0 ± 0.4	0.250 ± 0.050	0.270 ± 0.068

Table 8.2. T_c, ΔT_c and α for *Zn* substituted *YBCO*.

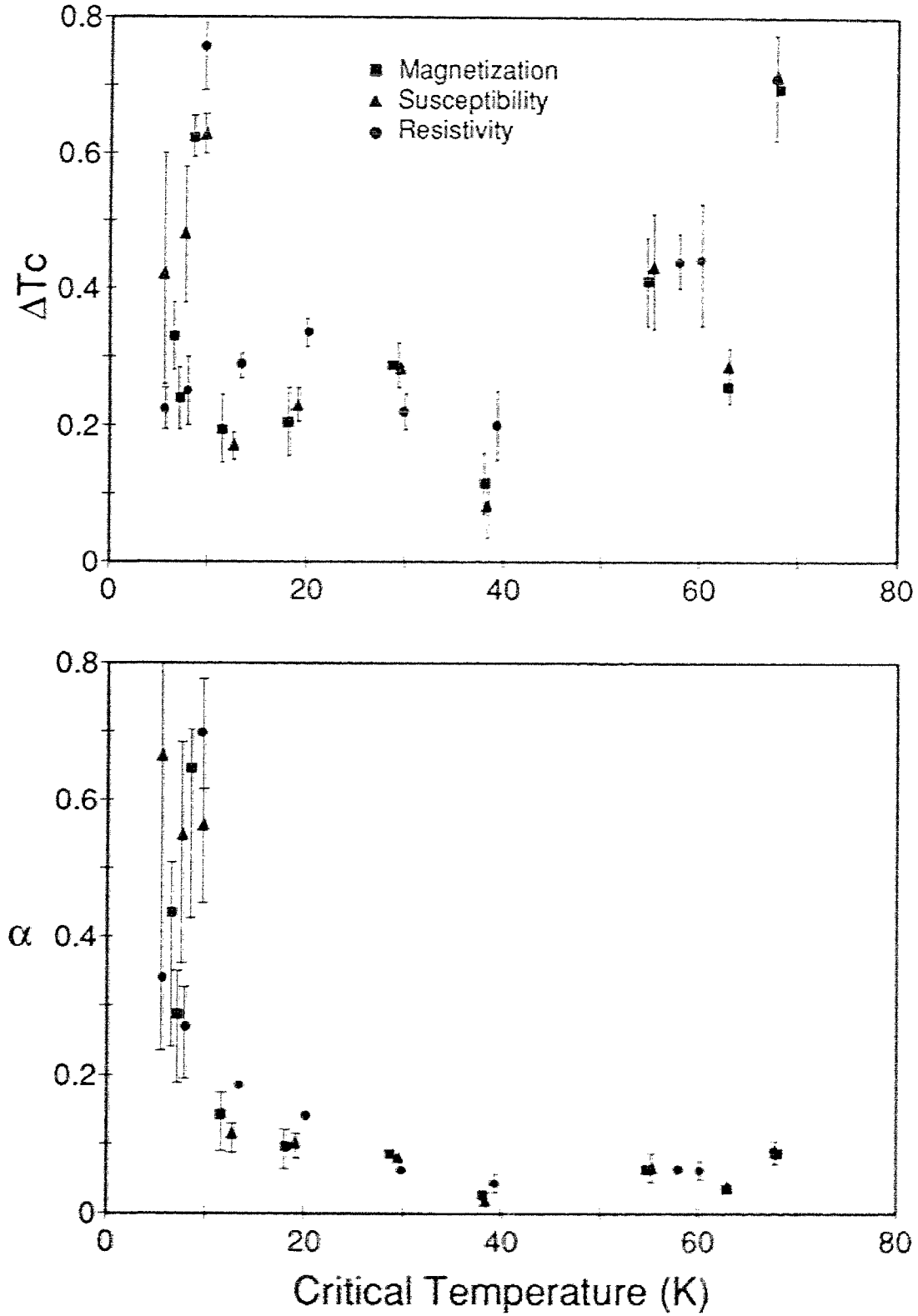

Figure 8.15

ΔT_c and α vs. T_c for *Zn* substituted *YBCO*.

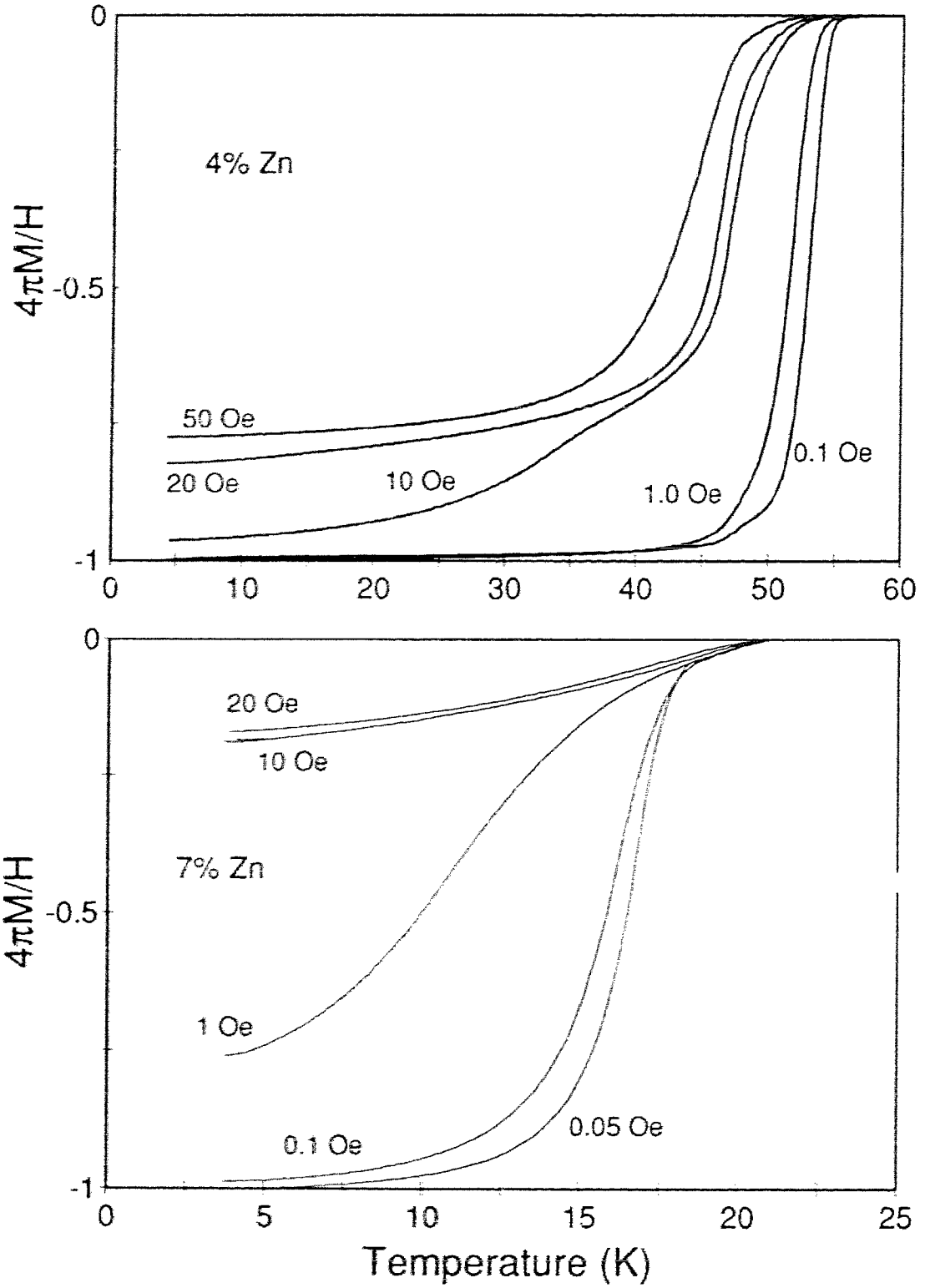

Figure 8.16

Field dependence of the 4% & 7% *Zn* substituted *YBCO* samples.

transition characteristics. Below this field, the penetration effects are small and above this field the penetration effects saturate. For the 4% *Zn* sample, this field is near $H = 10 Oe$ and for the 7% *Zn* it occurs near $H = 1 Oe$.

A logarithmic plot of $-4\pi M/H$ vs. temperature (Figure 8.17) for the different measuring field strengths shows that the strong field dependence still remains in the top 10% of the transition. There does, however, appear to be some convergence to a common T_c. Near the onset of superconductivity the level of noise begins to overwhelm the change in signal and it becomes difficult to determine if all fields converge to the same point. The noise is proportionally less for the higher fields and if we take T_c as the point at which the signal emerges from the noise, there is good agreement between the T_c's for the different fields. The isotope shift has been calculated for fields of $H = 0.05$, 1, 10, 20 and $50 Oe$ for the 4% *Zn* and 7% *Zn* data (Figure 8.18). From this data we can see no clear field dependence in the shift.

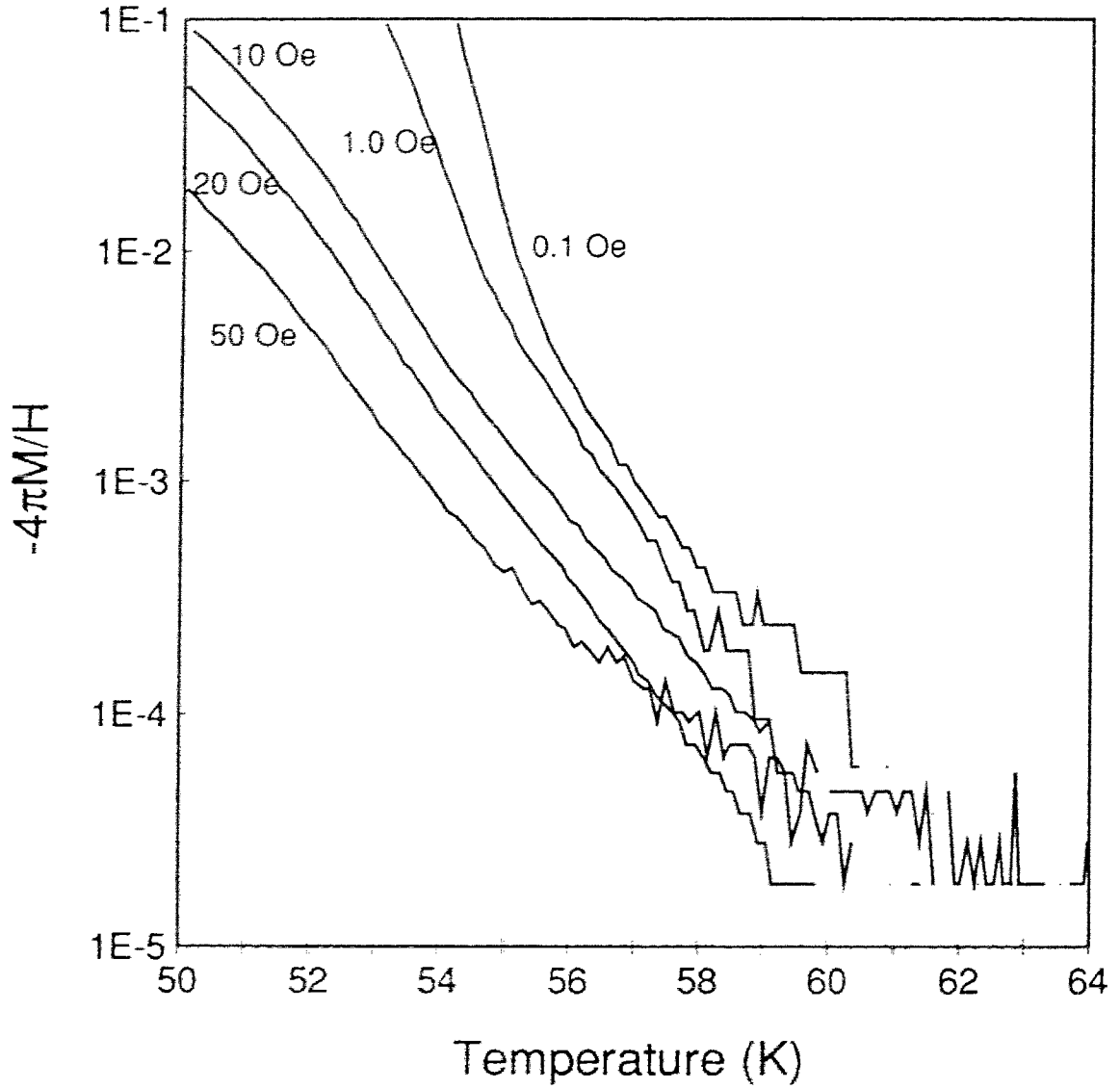

Figure 8.17

Log ($-4\pi M/H$) vs. T showing convergence near T_c as a function of applied field. All curves are ZFC magnetization measurements performed on the ^{16}O samples.

Figure 8.18

The isotope shift in the 4% and 7% *Zn* substituted samples at different applied measuring fields. The filled symbols represent the ^{16}O isotope data and the empty symbols represent the ^{18}O isotope data. The solid line is the Simplex fit to the data.

The filled symbols not fitted are the computed isotope shifts for the specified applied measuring fields.

All data are ZFC magnetization measurements.

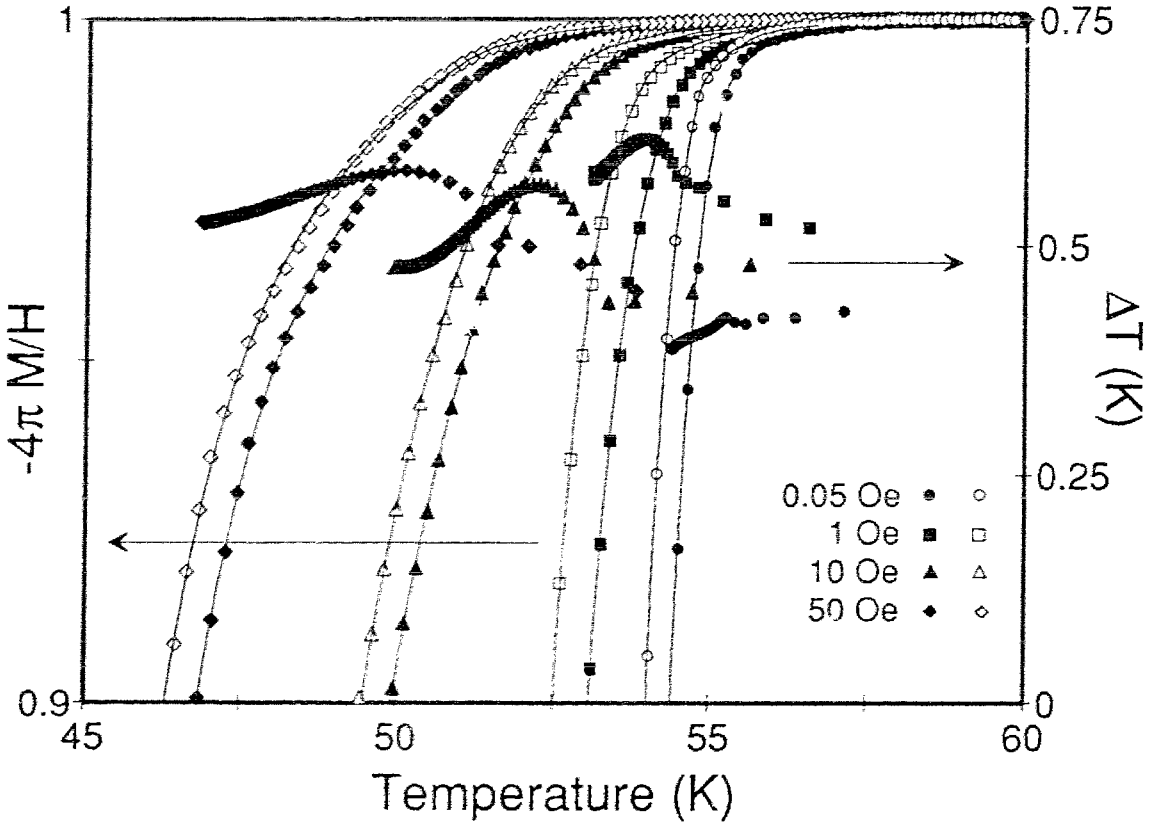
1
0.9
0.75
0.5
0.25
0
-4π M/H
ΔT (K)
0.05 Oe
1 Oe
10 Oe
50 Oe
45
50
55
60
Temperature (K)

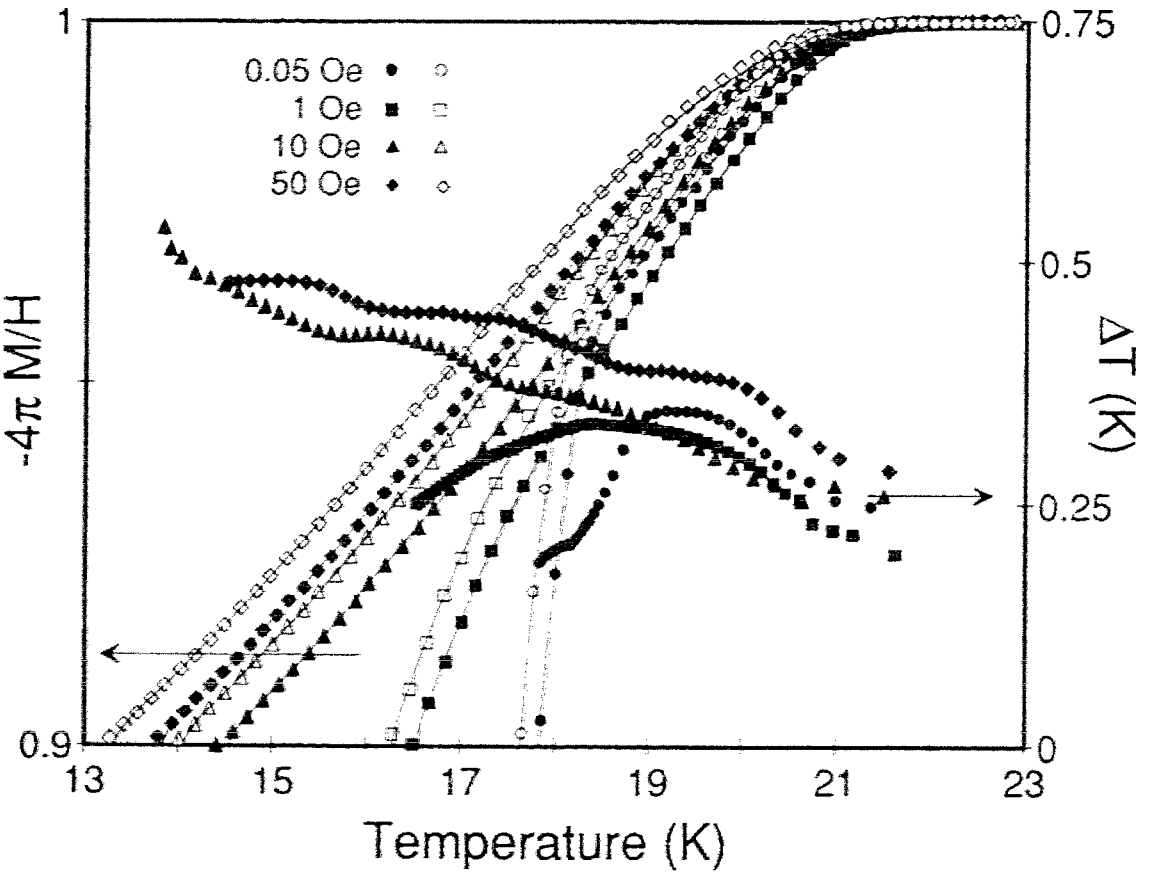
1
0.9
0.75
0.5
0.25
0
-4π M/H
ΔT (K)
0.05 Oe
1 Oe
10 Oe
50 Oe
13
15
17
19
21
23
Temperature (K)

8.3 DISCUSSION

The magnetization data was corrected for effects of field penetration at low temperatures by taking into account the cross sectional area (molar volume) of the sample and the magnitude of the ac susceptibility and comparing them with the 2% *Zn* sample. The corrected magnetization (Figure 8.19) is unaffected to within a few percent on all but the lowest T_c samples at *Zn* concentrations of 8%, 8.5%, and 8.75%.

The penetration of the measuring fields into the samples with a low T_c means that the complete expulsion of the magnetic flux from the sample, at the lowest temperatures obtainable in the magnetometer *(4K)*, is not possible. Thus even in a field as low as 0.05*Oe* a temperature sweep from 4*K* to above T_c does not represent a full scale transition. It is clear that the lower the critical temperature, the greater this effect becomes. This will then affect any calculation of the Meissner effect on samples with a low T_c which accounts for the large difference (between $^{18}O/^{16}O$ pairs) in the Meissner fractions for the 8%, 8.5%, and 8.75% *Zn* concentrations reported in Table 8.1. The lack of correlation between the Meissner fraction for the different isotopes (8%, 8.5%, and 8.75%) indicate that the effect the measuring field has on each isotope is also different.

As the shape of the 8%, 8.5%, and 8.75% transitions are already affected by the penetration of the measuring field, normalizing the transitions in order to compute the isotope shift will likely create an even larger error in obtaining a value of ΔT_c and hence α for these samples. It would be wrong to surmise that the actual shift should be larger than measured as was done for the 50% *Pr* samples. In those samples, the effects of a premature field penetration were

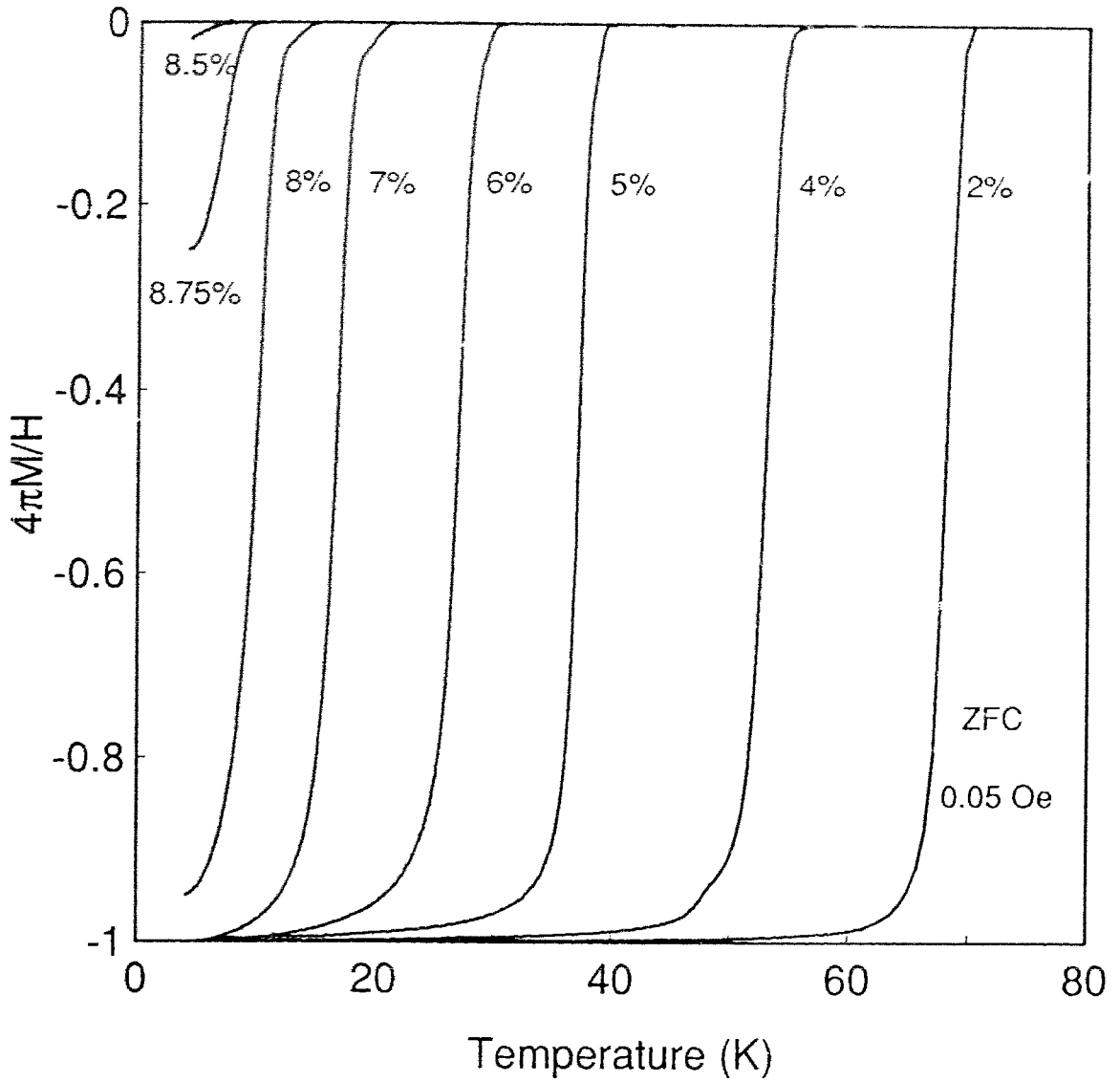

Figure 8.19

DC magnetization vs. temperature for *Zn* substituted *YBCO*. The magnetization has been corrected for molar volume and field strength. Note that the low T_c materials do not give a full transition.

small and the shape of the transition was preserved. In the 8% *Zn* sample however, there is not even a hint of the characteristic low temperature tail in the ^{16}O sample transition (Figure 8.4). It is clear that at 4.2*K*, the transition has already begun. The field measurements on the 7% and 4% samples indicate that a measuring field of 10*Oe* and 1*Oe* respectively has a distorting effect on the shape and size of the transition. Clearly, a measuring field of 0.05*Oe* will be sufficient to have a large distortion effect on the even lower T_c samples of 8%, 8.5% and 8.75% *Zn*. For these samples, the shift obtained from the resistive measurements will be more accurate. In two of these samples, 8.5% and 8.75% *Zn*, the resistance measurement does not give the large shift obtained from the magnetic measurements but instead gives the same constant shift noted for the other samples. The large isotope shift in the 8% *Zn* samples cannot be explained. Both the magnetic and the resistive measurements are in agreement. It seems unreasonable for this concentration to present such a large shift in view of the results of the other concentrations.

To alleviate the problems of field penetration, many groups measure the isotope shift on the FC data as opposed to the ZFC data as we do. In most of the cases, we do not believe this is a problem because the isotopic shift is the same (Figure 8.20) for the reversible/irreversible regime of the data. However, our experimental setup does not have the temperature accuracy for measurements decreasing in temperature (FC) as it does for those increasing in temperature (ZFC).

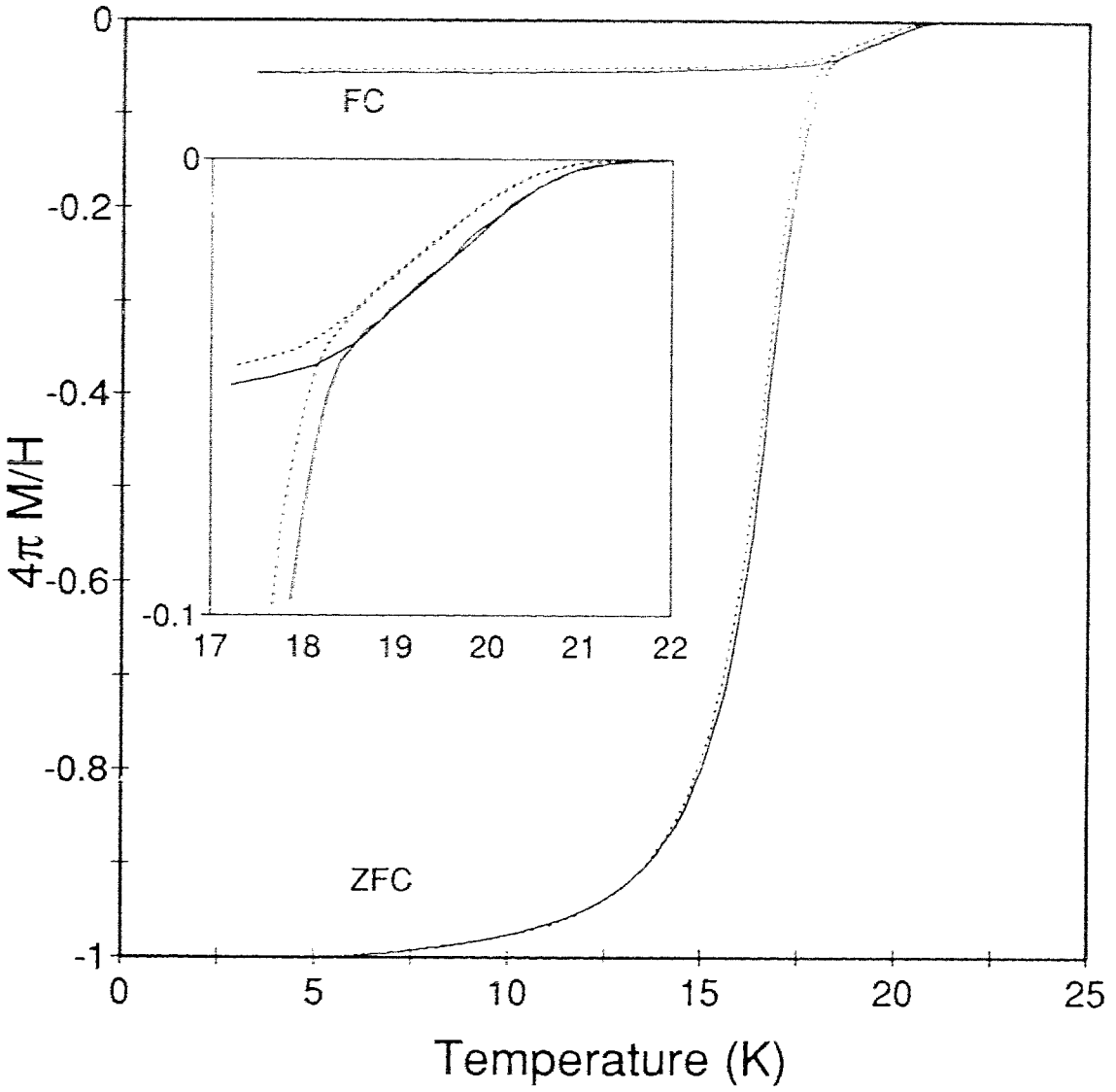

Figure 8.20

Relationship between the isotope effect and the reversible - irreversible point of the magnetic transition. Inset is an enlargement of the point of separation of the ZFC data from the FC data. Solid lines are ^{16}O isotope and dashed are the ^{18}O isotope. Measurements were made on the 7% *Zn* substituted sample at a field strength of 0.05*Oe*.

9.0 DISCUSSION

Our work on the determination of the isotope coefficients and critical temperatures from resistance, dc magnetization, and ac susceptibility measurements for all three systems of substitution is summarized in Figure 9.1. The top graph presents α as it is related to T_c and the bottom gives α and T_c as a function of the mobile hole concentration. In these summary graphs the values of α have been corrected for their incomplete ^{18}O substitution and are given in Table 9.1 together with the estimated Δp_h. All three systems have a very small isotope coefficient near the maximum T_c. This is typical of almost all the high T_c isotope studies done to date. The large isotope values found in the *Pr* and the *Zn* systems, at the lower T_c's, are not typical and in fact are reminiscent of the conventional superconductors. To minimize the amount of clutter within the graphs, the uncertainties (see Figures 6.10, 7.12, and 8.15) were left out.

As the SIMS measurements indicate that the ^{18}O substitution is not complete, a linear extrapolation was used to provide α at 100% ^{18}O. The validity of such an assumption is quite debatable. The effect would only be linear if all oxygen sites were substituted to the same degree and if all oxygen sites play similar roles in the mechanism for superconductivity. But consider the apical oxygen site *O(4)*. Raman[81] measurements have shown that this site is more difficult to substitute than the other oxygen sites. It has also been shown[62,63] that increasing the *Pr* concentrations leads to an increase in the *Ba-O(4)* distance, as well as an increase in the *c*-axis *O(4)* vibration frequency. This mode shows a strong electron-phonon interaction[64,119] and the localization of holes about the *Ba* is thus strongly dependent on the *Ba-O(4)* distance. Thus, the isotopic substitution of oxygen at the *O(4)* site may affect the amount of localization of

Figure 9.1

Oxygen isotope effect in *Pr*, *Ca*, and *Zn* doped $YBa_2Cu_3O_{7-\delta}$.

Top: the oxygen isotope effect as a function of the critical temperature.

Bottom: the oxygen isotope effect and critical temperature as a function of the mobile hole concentration. $\Delta p_h = 0$ corresponds approximately to a sheet hole concentration of $p_{sh} = 0.22$ holes per $Cu\text{-}O_2$ sheet. Empty symbols are the α values and filled symbols are the T_c's.

All isotope values have been linearly extrapolated to obtain a value corresponding to 100% ^{18}O content.

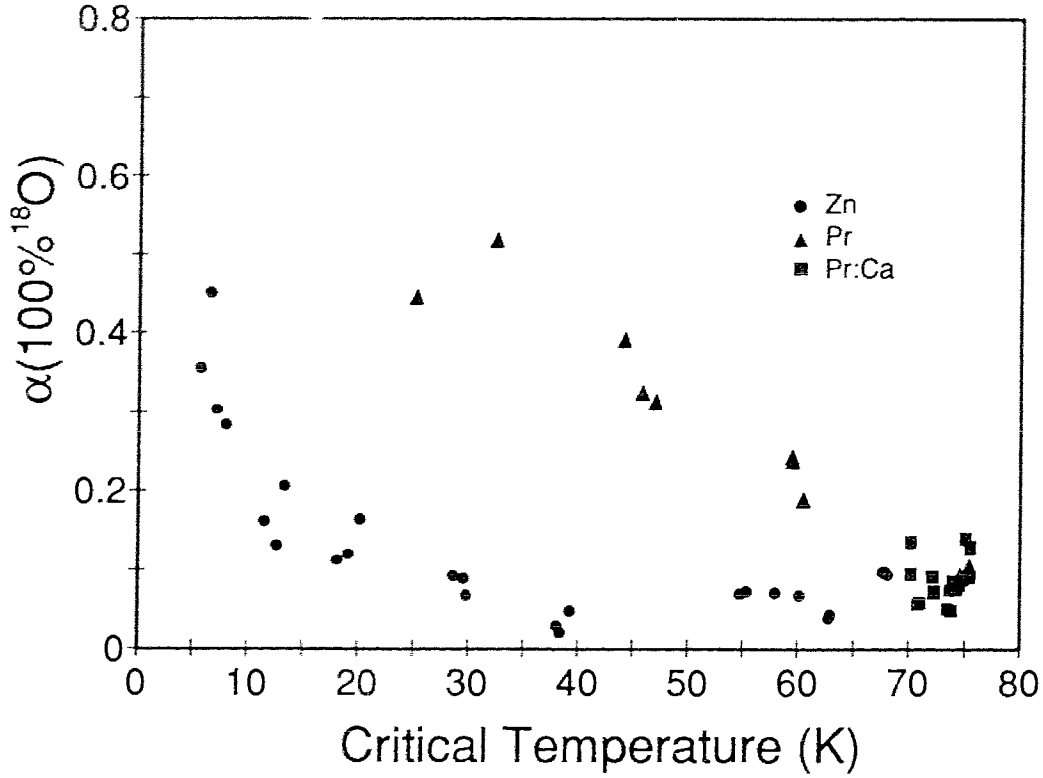
0.8
0.6
0.4
0.2
0
α(100%^{18}O)
Zn
Pr
Pr:Ca
0
10
20
30
40
50
60
70
80
Critical Temperature (K)

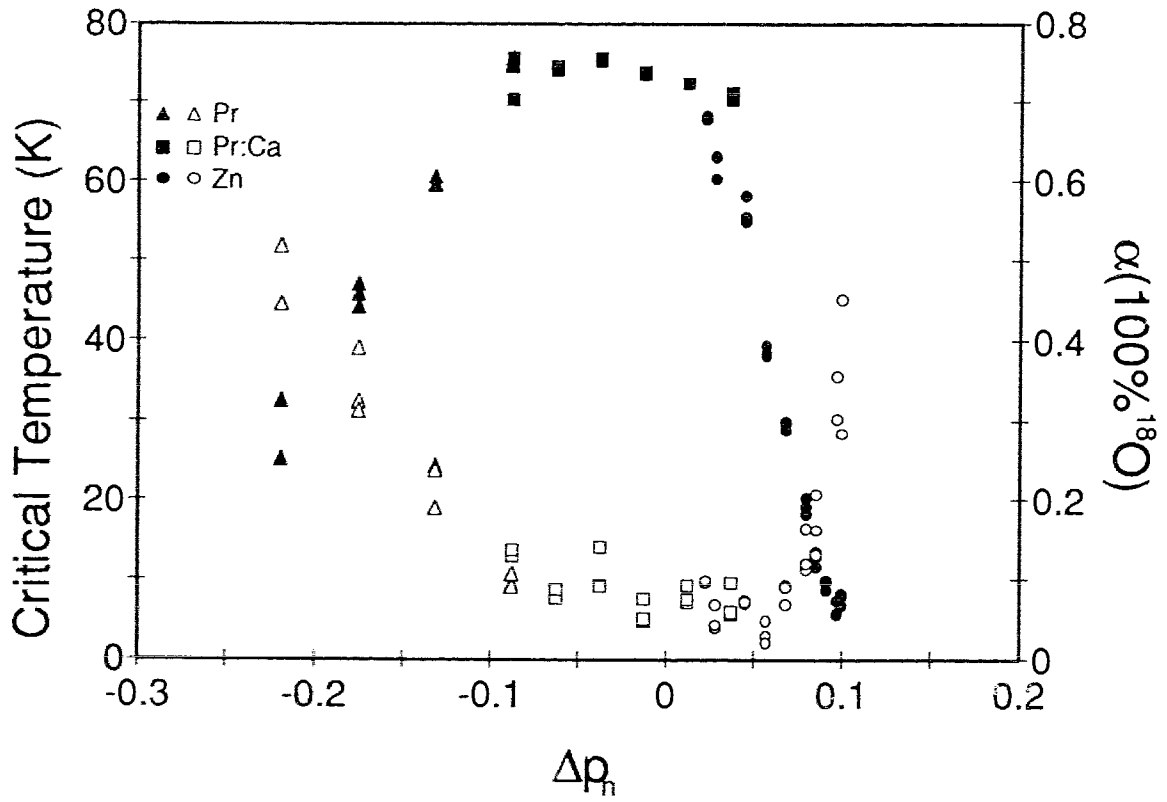
80
60
40
20
0
Critical Temperature (K)
Pr
Pr:Ca
Zn
0.8
0.6
0.4
0.2
0
α(100%^{18}O)
-0.3
-0.2
-0.1
0
0.1
0.2
Δp$_n$

Substitution	$\%^{18}O$	Δp_h	$T_c(K)$			α (100$\%^{18}O$)		
			mag	susc	res	mag	susc	res
20% Pr	84.6	–0.0874	74.6	74.9	75.5	0.093	0.090	0.106
30% Pr	79	–0.1311	59.5	59.6	60.5	0.243	0.238	0.189
40% Pr	85.5	–0.1748	44.2	45.8	47.0	0.391	0.324	0.313
50% Pr	85.9	–0.2185	25.2	27.7	32.5	–	–	0.518
20% Pr, 0% Ca	85	–0.0874	71.0	71.0	70.0	0.131	0.128	0.136
20% Pr, 5% Ca	84	–0.0624	72.5	72.6	74.1	0.081	0.076	0.086
20% Pr, 10% Ca	78	–0.0374	74.2	74.4	75.0	0.092	0.090	0.140
20% Pr, 15% Ca	77	–0.0124	73.0	73.2	73.6	0.048	0.051	0.075
20% Pr, 20% Ca	76	+0.0126	71.4	71.6	72.1	0.071	0.074	0.092
20% Pr, 25% Ca	75	+0.0376	69.9	70.1	70.2	0.056	0.059	0.095
2% Zn	92	+0.0229	68.1	67.9	67.7	0.094	0.097	0.097
2.5% Zn	92	+0.0286	62.9	63.0	60.2	0.038	0.042	0.067
4% Zn	92	+0.0457	54.8	55.4	58.0	0.069	0.072	0.070
5% Zn	92	+0.0571	38.1	38.4	39.3	0.028	0.020	0.047
6% Zn	92	+0.0686	28.7	29.6	29.9	0.092	0.088	0.067
7% Zn	86	+0.0800	18.1	19.1	20.2	0.112	0.119	0.163
7.5% Zn	88	+0.0857	11.5	12.7	13.4	0.161	0.130	0.206
8% Zn	92	+0.0914	8.5	9.8	9.6	–	–	–
8.5% Zn	92	+0.0971	7.2	5.6	5.7	0.302	–	0.355
8.75% Zn	92	+0.1000	6.6	7.7	8.0	0.450	–	0.283

Table 9.1 Estimated change in mobile hole concentration, Δp_h, and oxygen isotope coefficient. The value of the coefficient has been extrapolated (linearly) to give a 100% ^{18}O content.

holes around *Ba* and hence the critical temperature and the isotope shift. The analysis given by Tsuei (section 4.2) also reflects the importance of the apical oxygen sites as they determine the phonon cutoff frequency from the apical oxygen modes. Other groups have also expressed the importance of the apical oxygen in the high T_c superconductors[48,120]. We have measured the completeness of ^{18}O as a whole and not on a site-by-site basis. It was revealed that the substitution was 74-92% complete. Even though α may not be linear with substitution and would then not increase as much as speculated, at the worst α will not change. We can see no reason why a more complete substitution would have a smaller α.

Sections 9.1 to 9.3 discuss the measurement technique, sample quality, and the relationship between the width of the transition and the isotope coefficient. Section 9.4 presents our results as they relate to the estimated mobile hole concentration. Comparisons with the theoretical calculations involving the logarithmic VHS as well as the possibility of a universal relationship between the hole concentration and T_c are discussed here. Section 9.5 discusses the use of Eliashberg equations in fitting our data, and some general remarks are given in section 9.6.

9.1 MEASUREMENTS

The preparation method employed for the samples, the measurement technique used, and the consistency of our results leads us to conclude that the shift in T_c that is observed in our data is the result of the isotopic substitution of ^{18}O for ^{16}O and not the result of some other spurious effect such as a different oxygen stoichiometry between pairs of samples or other impurity effects.

The majority of the measurements on the samples have been redone, often several times and on different days, to ensure the reproducibility of the results. The use of a standardized cylindrical sample for the magnetic measurements was a significant improvement over the small flakes that were used in the early *Pr* data. It would have been best if the samples had been prepared in their finished form, cylindrical "rods" and flat "bars", prior to the heat treatment as opposed to making pellets and then cutting and sanding them into the desired shape afterwards.

It is also clear that when making magnetic measurements on these samples that the penetration effects of the measuring field need to be taken into consideration. From the field measurements on the 4% & 7% *Zn* samples, we can see that even small measuring fields can affect the shape of the transitions, as well as the Meissner effect. The degree to which the measurement is affected depends on both the magnitude of the applied measuring field and the critical temperature of the material. The higher the field or the lower the T_c, the greater this effect becomes and, if neglected, erroneous measurements of ΔT_c, and hence α, can be obtained. We believe that the majority of the values of α for samples with a low T_c are incorrect due to these field penetration effects. Thus, we have neglected the previously mentioned five *Zn* α values and two *Pr*

magnetic α values during the comparison and fitting with the theoretical calculations that follow.

9.2 SAMPLE QUALITY

Sample preparation is a long and difficult process. Control over this process was maintained by the group at the University of Alberta. The three sets of data reflect the three stages of this investigation. The earliest measurements were made on the system $(Y_{1-x}Pr_x)Ba_2Cu_3O_{7-\delta}$ for the substitution range $x = 0.2$ to 0.5, then on $(Y_{0.8-y}Pr_{0.2}Ca_y)Ba_2Cu_3O_{7-\delta}$ for the range $y = 0$ to 0.25 and finally the *Zn* system $YBa_2(Cu_{1-z}Zn_z)_3O_{7-\delta}$ for the range $z = 0$ to 0.0875. As more is learned regarding the relationship between the sample characteristics and the preparation process, it is very likely the qualities of the three sets of samples are not equivalent. The poorest samples are probably the earliest with the sample quality improving with preparation experience.

The *Pr* samples do have impurities, primarily $BaCuO_2$ as determined by the X-ray measurements. The transitions are wide with long tails at low shielding and increase in width and length with the increase in *Pr* concentration. Widening tails and broader transitions are characteristic of a deterioration in sample quality. We believe that the primary cause may be due to too high a temperature during the sintering process which promotes the formation of impurity phases.

The *Pr* and *Ca* substituted samples also exhibit the $BaCuO_2$ X-ray impurity lines. The connection between the addition of *Ca* and the narrowing of the transition width and the loss of the long tails at low shielding is not known. It does appear that the quality of the samples has improved. A pair of isotope

samples in the *Pr:Ca* set was made with 0% *Ca*. Here it was found that the transitions are actually broader and that the critical temperature is different than in the initial *Pr* set. As the preparation conditions were different between the two sets, this clearly indicates that the preparation method can strongly affect the characteristics and/or quality of the sample.

The *Zn* substituted samples were the latest samples prepared. They did not show the $BaCuO_2$ impurity peaks characteristic of the previous sets of samples. Here, the transition widths were quite narrow and did not exhibit the long low shielding tails. Thus we believe the *Zn* to be the best samples of this investigation. Perhaps this time the preparation conditions were more ideal.

We have speculated that the deterioration of the sample quality is linked with non ideal preparation conditions - perhaps the ideal preparation conditions are different for each different substitution. However, this may not be the only, or even the primary, cause of the change in sample quality. Even though the $BaCuO_2$ impurity phase is still present in the *Pr:Ca* data, the addition of *Ca* appears to improve the transition width and low shielding tails - i.e. the sample quality. Maybe the broader transitions and/or low shielding tails are intrinsic to the substitution of *Pr* and then the *Ca* would tend to counteract this behaviour. Although the properties of our samples are quite similar to those of other polycrystalline *Pr* samples discussed in the literature, the uncertainty involved in sample preparation will cast some doubt over the conclusions that can be drawn.

A high degree of quality, as found in single crystals, is just not found in the polycrystalline materials and even less so in the mixed phase systems that we are dealing with. The questions concerning the sample quality that arise in this investigation also plague the isotope research performed by other groups on

similar polycrystalline samples. Ideally, one would like to perform such measurements on a single crystal mixed phase system; however, such samples are rare and there exists a difficulty in preparing single crystal isotope samples.

9.3 TRANSITION WIDTH vs. α

One of the surprising results is the apparent linear relationship between the width of the transition, and the magnitude of the isotope shift (Figure 7.13). In the *Pr* system the increase in *Pr* resulted not only in a decrease of T_c, but also in a widening of the transition. This relationship is also found in the *Pr:Ca* system but to a lesser extent. In the *Zn* system, there is little change in the width of the transitions with a corresponding small change in the magnitude of the isotope shift. The constant width of each transition for the *Zn* samples does tend to corroborate the hypothesis that there is a link between the size of the shift, ΔT_c, and the transition width.

As the quality of the *Pr* and *Pr:Ca* samples is believed to be poorer than that of the *Zn* samples, this may indicate that the isotopic shift is independent of the elemental substitution and the increase in ΔT_c is due to sample quality. Thus we would have an α which is dependent only on the critical temperature of the samples and will thus have the relationship $\alpha = constant/T_c$ (provided we have $T_c >> \Delta T_c$). If the isotope shift is a constant, then the question arises - why should the isotope shift be dependent on the quality of the sample? The identical preparation method for the pairs of samples leaves only the isotopic substitution of $^{18}O/^{16}O$ as the cause. Thus it seems unlikely that the isotope shift is . To this question, we have no answer.

The other possibility is that the isotope shift and the transition width are not constant and in fact do change with the change in *Pr*, *Pr:Ca* substitution, even in a good quality samples, although perhaps not as much as we have observed. The differences in the location of substitution of the *Pr* and *Ca* with that of the *Zn* may account for the difference in the behaviour of ΔT_c between these systems. The *Pr* and *Ca* substitute for the *Y* in the charge reservoir and thus play an important role not only in the concentration of holes, but also in the coupling between *Cu-O*$_2$ planes, both of which are likely to affect ΔT_c. The *Zn* substitutes for the *Cu* in the *Cu-O*$_2$ planes and thus the effect on the mechanism for superconductivity will be different from that of *Pr* and *Ca*. This may imply that the transition width may be an intrinsic property that is somehow related to the mechanism of superconductivity and hence ΔT_c.

Until more information can be obtained, an explanation for the observed relationship between ΔT_c and the transition width and/or sample quality remains unknown.

9.4 T_c & α vs. HOLE CONCENTRATION

The substitution of *Pr*, *Ca* and *Zn* into *YBCO* changes the mobile hole concentration within the superconductor. Here we will consider changes in the mobile hole concentration, Δp_h, from the nominal value that exists in the optimum oxygenated $YBa_2Cu_3O_{6.9}$. The changes in Δp_h are obtained as mentioned in sections 2.2.2 and 2.2.3.

The theoretical calculations of Tsuei[84] and Newns[127] (section 4.2) predict a relationship between α and T_c with respect to Δp_h via the parameter δ, where δ is the difference between the Fermi energy and the location, in energy, of the

logarithmic VHS in the DOS. The relationship between Δp_h and δ, however, is unclear. A comparison of our data and the theoretical calculations of Tsuei and Newns (section 4.2) is given in Figure 9.2. The top figure compares our extension of Tsuei's calculation for a 90*K* superconductor with the data and the bottom figure compares our data to Newns' calculation. These particular comparisons were made because the α dependence with δ is somewhat broader in Newns' model than it is in Tsuei's which is similar to what is found in our data. In the data, we also find that Δp_h is broader in the *Zn* system than it is in the *Pr* system. Thus, we have fitted Tsuei's model to the *Pr* data (top graph) and the Newns' model to the *Zn* data. The parameter δ has been (linearly) adjusted so that the depression in T_c within the model can be fitted to the T_c change with Δp_h, and no adjustment is made to fit for the isotope coefficient. The adjustment of δ for each case is different and as the two models are derived somewhat differently, this is not surprising.

The qualitative similarities between both T_c and α vs. Δp_h, and the theoretical calculations of Tsuei and Newns, where we have taken δ to be linearly related to Δp_h, are quite good when we consider that these calculations are based on a fairly simplistic model. The general trend of a high T_c near $\Delta p_h = 0$ and the decrease in T_c with increasing Δp_h is in agreement with our data. The change in isotope coefficient also shows good agreement with the predictions of Tsuei, although quantitatively, they are not as good as the T_c predictions, and in both cases, the predicted minimum value for α is too high. The lack of symmetry about $\Delta p_h = 0$ is also quite substantial.

There are a number of possible explanations for the poor symmetrical fit. The relationship between the parameter δ and Δp_h is unknown, as mentioned earlier, and a more complex relationship between δ and Δp_h may exist rather

Figure 9.2

Comparison of Van Hove singularity calculations for α and T_c.

Top: Comparison of the calculations of Tsuei with our data. The scale for the parameter δ has been adjusted to give a fit to the *Pr* T_c data.

Bottom: Comparison of the calculations of Newns with our data. The scale for the parameter δ has been adjusted to give a fit to the *Zn* T_c data.

Empty symbols are the T_c data and filled symbols are the α data. Both are plotted as a function of mobile hole concentrations.

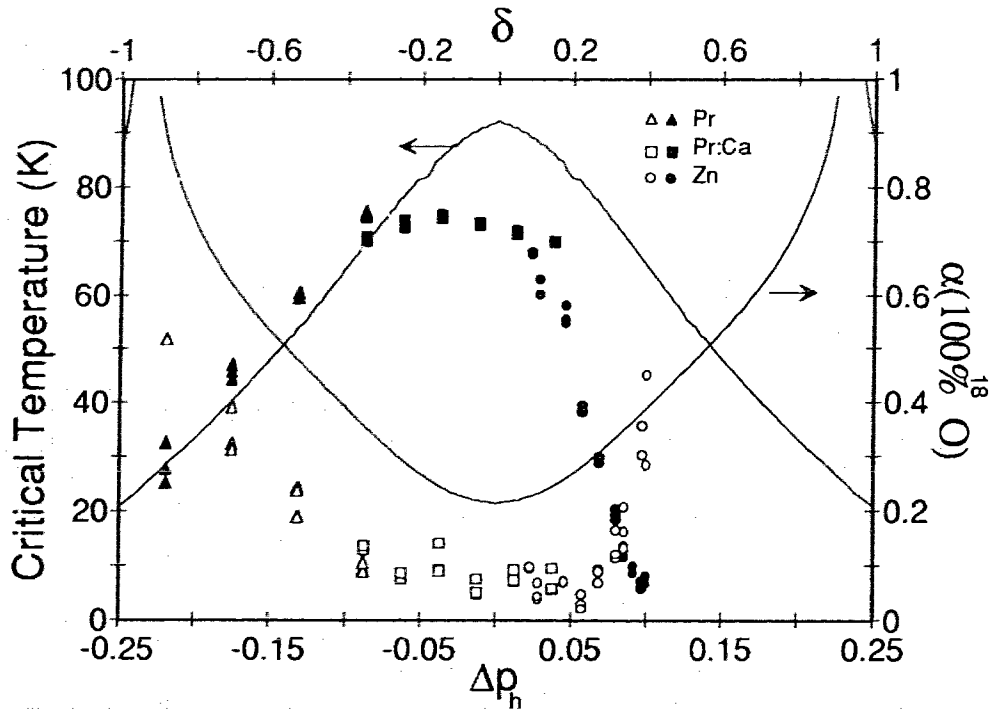
δ
-1
-0.6
-0.2
0.2
0.6
1
Pr
Pr:Ca
Zn
Critical Temperature (K)
α(100% ^{18}O)
Δp_h
-0.25
-0.15
-0.05
0.05
0.15
0.25

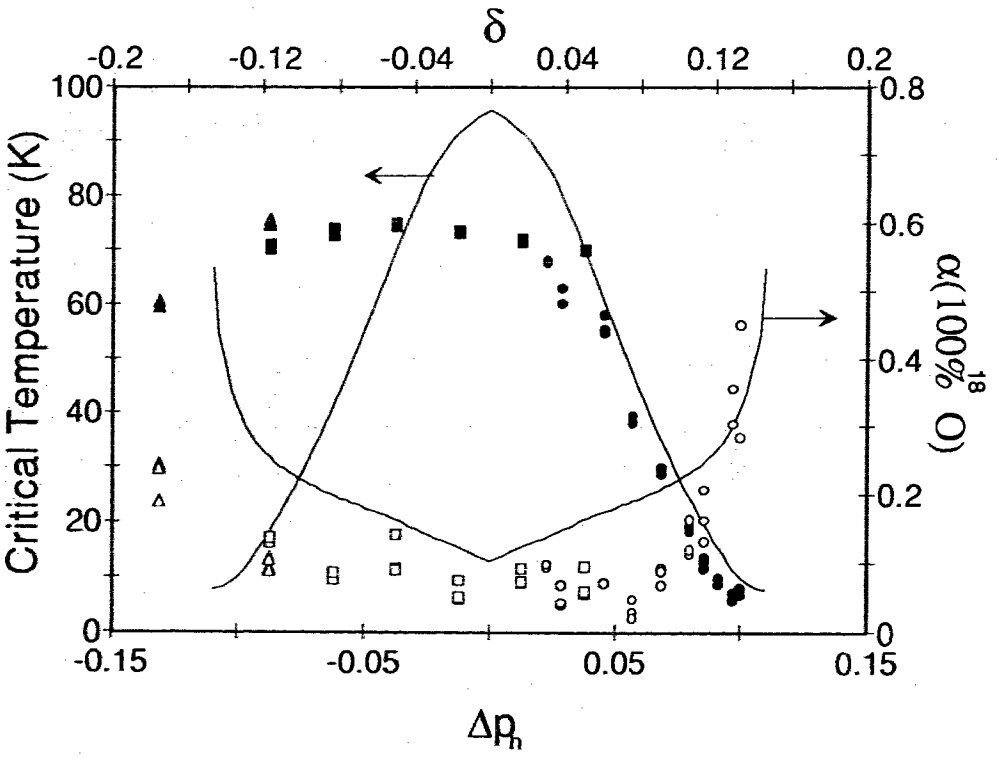
δ
-0.2
-0.12
-0.04
0.04
0.12
0.2
Critical Temperature (K)
α(100% ^{18}O)
Δp_h
-0.15
-0.05
0.05
0.15

than the simple linear one used here. The relationship between the Δp_h and the *Zn* concentration is still uncertain. It may also be that the relationship between Δp_h and the *Pr* concentration is overestimated. The VHS calculations are symmetric only because a symmetric logarithmic singularity was used in the DOS, and thus the dissimilar effects of the *Pr* and *Zn* substitutions have not been accounted for. Also, the quantitative results are affected by the values selected for the parameters: E_f, $\hbar\omega_q$, and *N(0)V* which are used in the calculations by Tsuei and Newns. The values for these parameters are also not well known. Modification of any of these conditions may result in a better fit between the data and this model. What is important here is that the general trends of our data do fit these theoretical calculations.

In the event that ΔT_c were a constant, the isotope exponent in the *Pr* samples would behave similarly to that of the *Zn* - a much broader change in α with α becoming large only at low T_c. This broader change in α with respect to Δp_h would then favour Newns' more sophisticated model, which exhibits this broader characteristic, over Tsuei's. The difference in α with respect to Δp_h in the *Zn* and *Pr* data still leaves some symmetry problems. But here, an incorrect estimate of Δp_h and the concentration of the substituted element may be the cause.

A universal relationship between $t_c\ (= T_c/T_{c\,max})$ and p_{sh}, the hole concentration in the *Cu-O*$_2$ sheets, in the *p-type* superconductors has been recently proposed by H. Zhang et al.[121]. Here, a broad plateau, as opposed to a parabolic dependence, in t_c exists over a range of $\Delta p_{sh} = 0.14$ and on either side t_c decreases linearly with the change in p_{sh}. Although the primary source of information for their conclusions comes from data in which the oxygen

stoichiometry is altered as opposed to an elemental substitution as we have done to manipulate the hole concentration, a striking similarity between their results and ours can be seen (Figure 9.3). Not only does T_c of our results follow this behaviour, but it appears that the isotope effect also has a similar behaviour. A plateau of width $\Delta p_h = 0.12$ for T_c and $\Delta p_h = 0.15$ for α exists in our data, quite comparable in size to the plateau range in T_c reported by Zhang et al. The lack of symmetry between *Pr* and *Zn* data with Δp_h is again apparent in comparison with that reported by Zhang, which does exhibit a symmetric behaviour to a large degree. The rapid change in T_c, with respect to the estimated Δp_h for the *Zn* substitution, is more closely matched to Zhang's universal relationship than the slow change in T_c observed with the *Pr* system. Here, an overestimation of the relationship between the *Pr* substitution and the loss of mobile holes could explain this difference. In the event that ΔT_c is a constant, the 'universal relationship' would then also predict the same symmetry in α as is found in T_c.

In the VHS model, the Eliashberg equation calculations, and from the universal relationship between Δp_h and T_c, it is clear that the mobile hole concentration in the high temperature superconductors plays an important role in determining their characteristics, particularly the critical temperature and the isotope effect. However, it is clear that more information regarding the elemental substitution of *Pr*, *Ca* and *Zn* and their effect on the mobile hole concentration is required.

The value of the VHS model is not only that it gives a good phenomenological account of the trends that we have observed in T_c and α with changing hole concentration, but also that it is consistent with the *2-D* nature (*Cu-O*$_2$ planes) of the high T_c superconductors which has been used to explain other features observed in these materials (section 4.2). It should not be

Figure 9.3

Comparison of the data with the 'universal relationship between T_c and hole content'.

Top: the universal relationship between T_c and hole content proposed by Zhang et al.[121] using the T_c data of a number of different groups on different high T_c materials. All critical temperatures have been normalized to the maximum T_c obtainable for each respective superconductor family ($t_c = T_c/T_{c\,max}$). Note the plateau extending from $p_{sh} = 0.11$ to about 0.26 holes per $Cu\text{-}O_2$ sheet (plane).

The same symbols are used as in Zhang's paper.

Bottom: Isotope effect and T_c vs. mobile hole concentration for our data. The solid line is a guide to the eye to suggest a similar "plateau effect" as noted in the above universal relationship. Filled symbols are the T_c data and empty symbols are the α data.

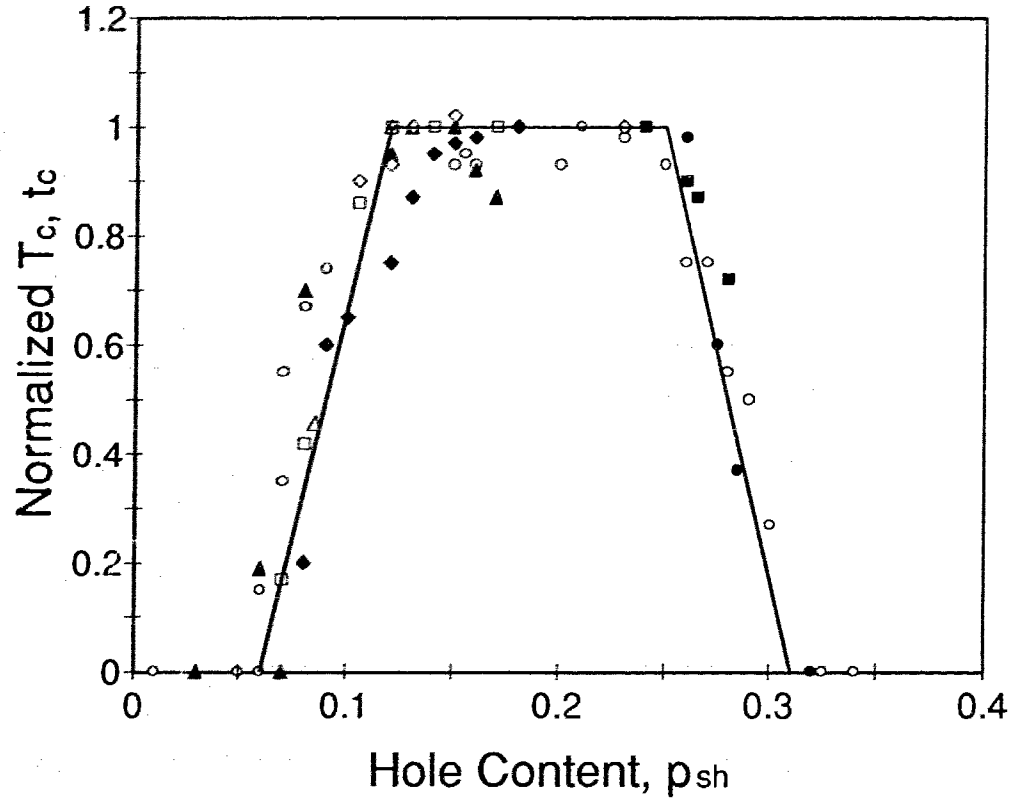
Normalized T_c, t_c
1.2
1
0.8
0.6
0.4
0.2
0
0
0.1
0.2
0.3
0.4
Hole Content, p_{sh}

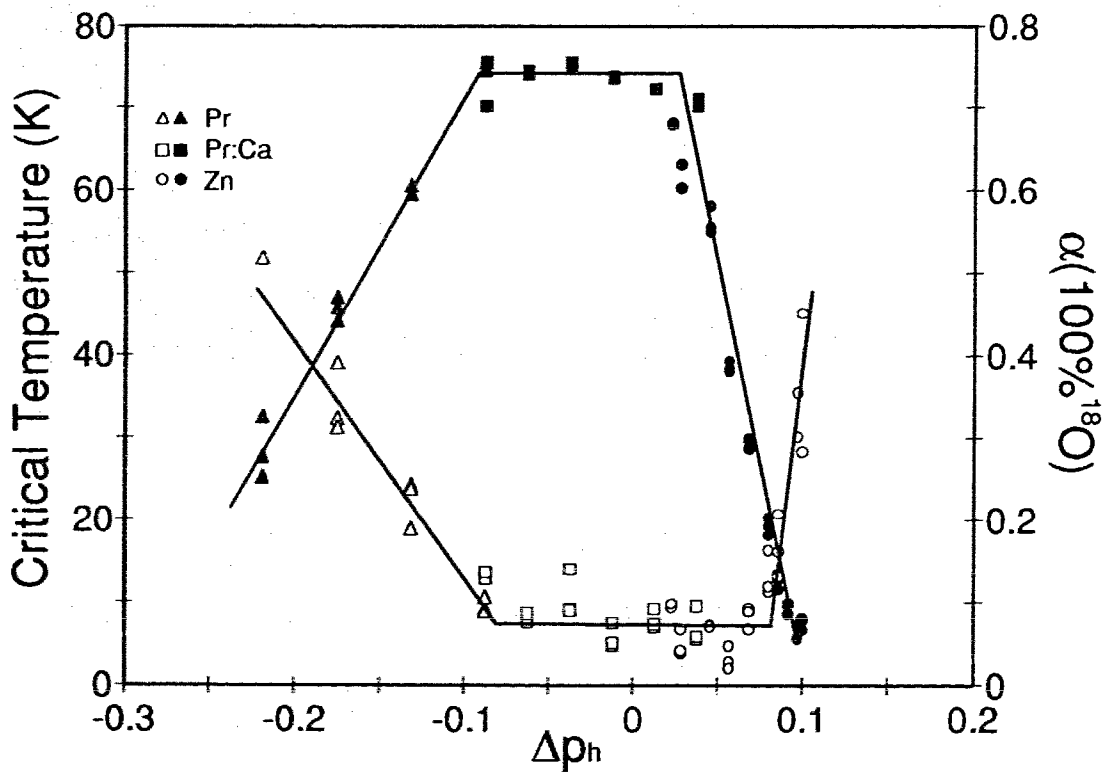
Critical Temperature (K)
80
60
40
20
0
Pr
Pr:Ca
Zn
-0.3
-0.2
-0.1
0
0.1
0.2
Δp_h
0.8
0.6
0.4
0.2
0
$\alpha(100\%^{18}O)$

overlooked, however, that the VHS is a *2-D* phenomena and although the high T_c superconductors have strong *2-D* tendencies, they are still a *3-D* system and such a *2-D* model will have its shortcomings.

9.5 α vs. T_c

An attempt was made to fit the data using Eliashberg equations (section 4.3) where we relate α to T_c. The fitting parameters for the Eliashberg equations are the average phonon frequency - ω_{ln} *(meV)*, a dimensionless parameter which is representative of the electron-phonon interaction - λ, the pair breaking factor - *t (meV)*, and T_c *(K)*. With these parameters, the Eliashberg equations are capable of fitting any values of α and T_c simultaneously. There are three basic limits to which we have restricted the values of these parameters.

First, we considered those values which may be physically feasible. The values of ω_{ln} used range from that found in conventional superconductors ($\omega_{ln} \sim 5$ *meV*) to the upper limits of the phonon spectrum found in the high T_c superconductors ($\omega \sim 100$ *meV*). Typically, the values of λ that lie within the BCS approximation are $\lambda < 1$. The relative magnitude of the pair-breaking factor is unknown, and of course, T_c must reflect the range found in our data.

Second, all values of the pair (ω_{ln} , λ) were chosen to reflect the T_c and α of undoped $YBa_2Cu_3O_{7-\delta}$, i.e. a $T_c = 90K$ and $\alpha = 0.05$. Figure 4.3 gives a range of the pairs of values that correspond to the above limits imposed on ω_{ln} and λ. The value of the pair (ω_{ln} , λ) was held constant while fitting over an entire system. Thus, only through a change in T_c and/or t will there be a change in α. By maintaining a constant ω_{ln} and λ over an entire system, we have assumed

that the electron-phonon interaction, as well as the phonon spectrum, do not change appreciably with the depression of T_c, i.e. with the addition of impurities.

Third, as the amount of pair-breaking is probably proportional to the impurity concentration, *t* will have to change accordingly. As a linear relationship exists between T_c and the *Zn* concentration and as the relationship between T_c and *Pr* concentration is also (nearly) linear, it has been assumed that the amount of pair-breaking would then be linearly dependent on T_c. Instead of the T_c dependence, a constant factor, *t' (meV/K),* has been introduced to reflect the strength of this linear relationship giving $t = (90 - T_c)\ t'$. t' is then a fitting parameter over an entire system.

For each T_c (and corresponding *t*) value we solved the Eliashberg equation for μ^*_{eff} self consistently. Several pairs of ω_{ln} and λ were used. Once μ^*_{eff} was determined, the corresponding value for α was computed. The result, α vs. T_c, is plotted in Figure 9.4. A number of remarks can be made.

1) A fairly good fit to our data can be achieved using Eliashberg theory. The necessity of the pair-breaking term is clear although the significance of the magnitude of this term is unclear. The fit to the data in the absence of pair-breaking ($t' = 0$) is quite poor. Including a small pair-breaking factor ($t' = 0.002$ *meV/K*) is sufficient to fit the *Zn* data. A much larger pair-breaking factor ($t' = 0.05 meV/K$) is required to fit to the *Pr* data, but even here the fit is quite good. According to Tinkham[122], one has for the Abrikosov-Gorkov-type magnetic impurity pair-breaking parameter:

$$\frac{1}{\tau_s} = \frac{n_m J^2}{\hbar E_f} \qquad [9.1]$$

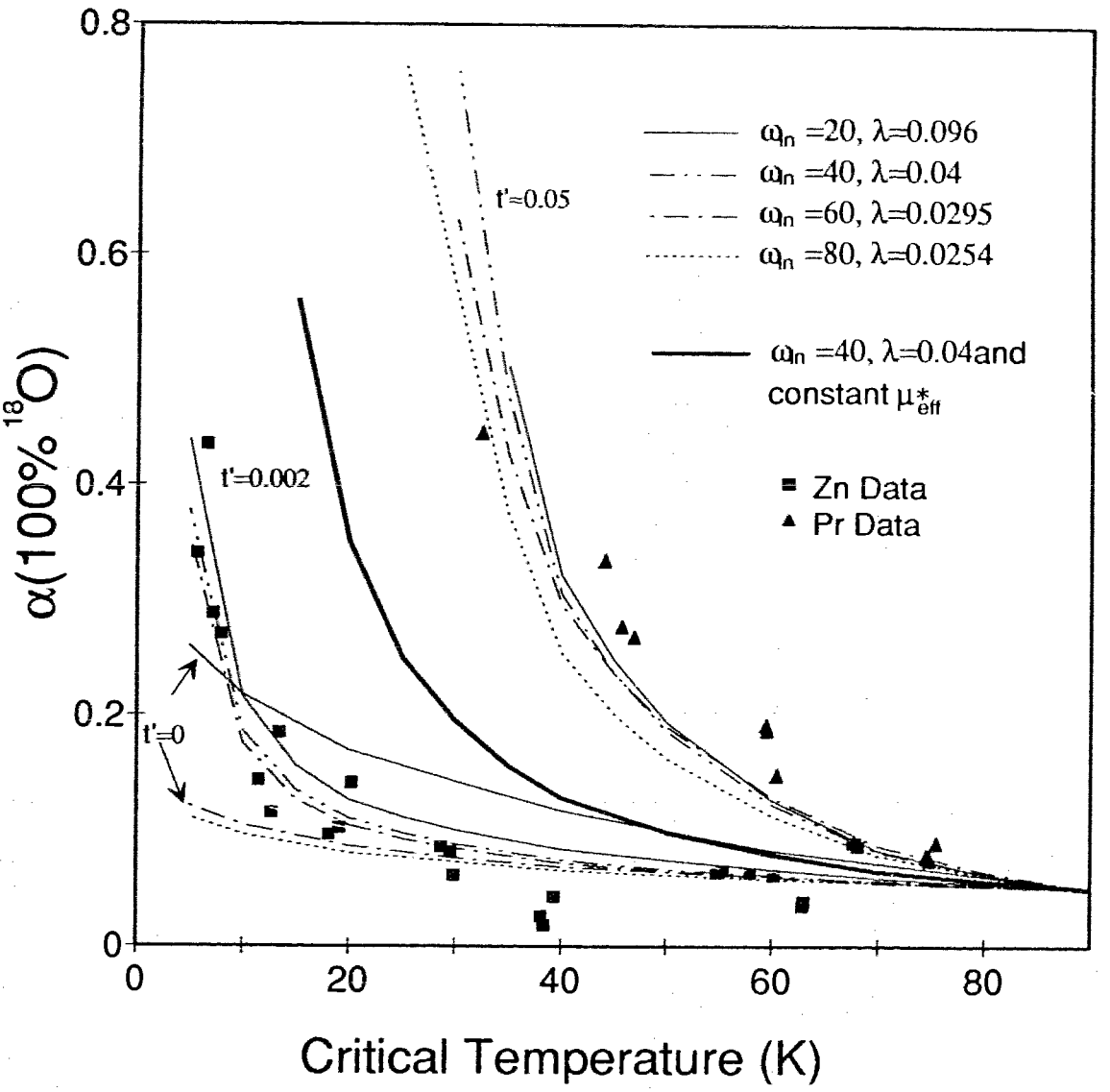

Figure 9.4

Comparison of Eliashberg calculations with the data.

Isotope coefficient as a function of the critical temperature. Different sets of ω_{ln} and λ have been chosen to give $\alpha = 0.05$ at $T_c = 90K$. The pair-breaking factor, t', used to obtain the fit is given.

Symbols are the data points and the lines are the theoretical calculations.

where n_m is the magnetic impurity concentration, and **J** is the magnetic impurity per electron spin exchange interaction and τ_s is the characteristic scattering time.

Using the relation between t and τ_s:

$$t = \frac{1}{2\pi\tau_s} \qquad [9.2]$$

along with the linear relationship between the spin, **J**, and the magnetic moment, μ, we obtain for the ratio of t'_{Pr} to t'_{Zn} :

$$\frac{t'_{Pr}}{t'_{Zn}} = \frac{\tau_s(Zn)}{\tau_s(Pr)} = \frac{n_m(Pr)J^2_{Pr}}{n_m(Zn)J^2_{Zn}} = \frac{n_m(Pr)}{n_m(Zn)} \times \frac{\mu^2_{Pr}}{\mu^2_{Zn}} \qquad [9.3]$$

As the change in T_c is approximately the same for both the *Zn* (0 to 9%) and *Pr* (0 to 50%) systems, the ratio of the concentration of *Zn* to *Pr* is:

$$\frac{n_m(Pr)}{n_m(Zn)} \approx 5 \qquad [9.4]$$

From our calculations, we obtained the ratio of pair-breaking factors:

$$\frac{t'_{Pr}}{t'_{Zn}} = \frac{0.05}{0.002} = 25 \qquad [9.5]$$

This gives a ratio of the magnetic moments for the *Zn*, μ_{Zn}, and *Pr*, μ_{Pr}, of:

$$\mu_{Pr} \cong 2.24\mu_{Zn} \qquad [9.6]$$

Xiao et al.[73] have experimentally determined that the addition of the non-magnetic impurity *Zn*, for the magnetic Cu, introduces a moment of μ_{Zn} = 1.0 to 1.2. This then gives μ_{Pr} = 2.24 to 2.69, which is in very good agreement with what is found for μ_{Pr} experimentally (μ_{Pr} = 2.7[56,58,59]).

2) In keeping with the limits suggested for λ (< 0.21) by Gurvitch[116] and the value of ω_{ln} (15*meV*) by Weber[117], only the range ω_{ln} = 20 to 80*meV* has been plotted. We find that within this range of physically reasonable values, the choice of pairs of (ω_{ln} , λ) makes little difference.

3) The use of a constant μ^*_{eff}, for $\omega_{ln} = 40meV$ and $\lambda = 0.04$, does give an increase in α with the depression of T_c, however, it fits neither the *Zn* nor the *Pr* data. A pair-breaking term was required to obtain a constant μ^*_{eff} with the change in T_c but the factor τ' was no longer constant for the entire system as it increased approximately 25%. Again, other pairs of ω_{ln} and λ give similar results.

4) The values obtained for $-\mu_{eff}^*$ as a function of critical temperature are plotted in Figure 9.5. In all cases we find that $\mu_{eff}^* < 0$, and from equation [4.29]:

$$\mu^*_{eff} = -N(0)V + \mu^* \qquad [9.6]$$

this implies that $-\mu^*_{eff}$ is a net attractive interaction. In fact, at 90K ($\alpha = 0.05$), the value of $-\mu_{eff}^*$ for the range of ω_{ln} (and λ), from 3*meV* to 100*meV*, varies by only 1% from the value of $-\mu_{eff}^* = 0.197$. Clearly, the value of $-\mu_{eff}^*$ is dependent not only on T_c but on the amount of pair-breaking present that exists (Figure 9.5). The large pair-breaking term needed to fit the *Pr* data results in an increase in the value of $-\mu_{eff}^*$ while the small τ' needed for the *Zn* data requires a decrease in $-\mu_{eff}^*$. Interpretation of what makes μ^*_{eff} negative is not clear. Our Eliashberg calculations use a constant value for λ, and a constant λ is essentially equivalent to a constant electron-phonon interaction term. Thus, the change in μ^*_{eff} must be associated with the change in the electronic behaviour of the system. As a negative μ_{eff}^* is the result of the presence of an attractive electronic interaction

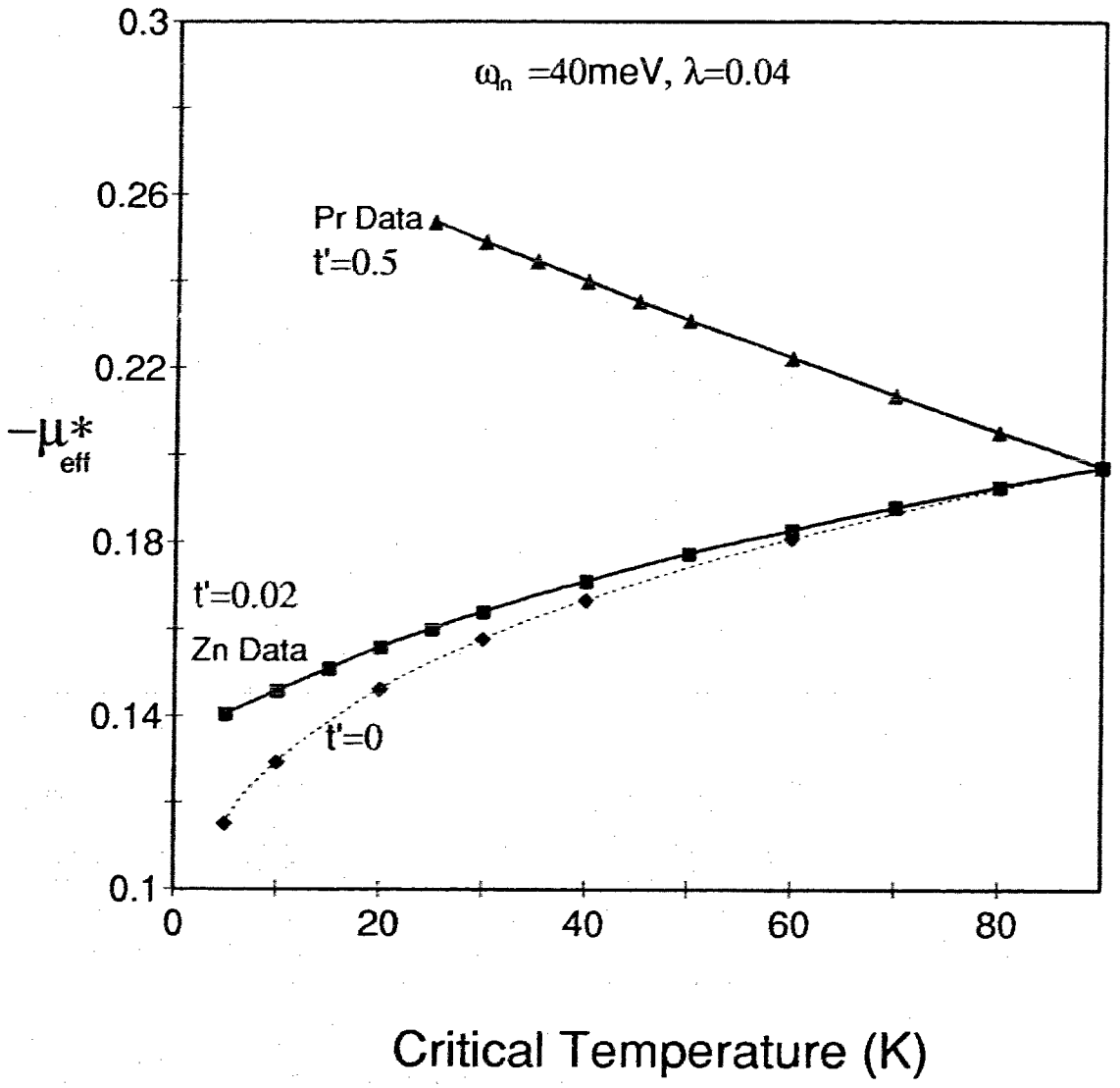

Figure 9.5

Coulomb pseudopotential as a function of T_c.

Pair-breaking *(t')* used to obtain the fit to the *Pr* ($t' = 0.05 meV/K$) and *Zn* ($t' = 0.002 meV/K$) as well as that obtained without any pair-breaking ($t' = 0$).

as well as the Coulomb repulsion term, this strongly suggests that a relationship between the mechanism involved and the hole concentration exists. However, the details of such a mechanism are unknown.

One could speculate that an increase in the number of holes means an increase in the electronic DOS and hence an increase in *N(0)V*. But this alone would have the opposite effect to what is observed. Consider the *Zn* system. Here we have an increase in the number of holes; however, we see a decrease in $-\mu_{eff}^*$ which implies a decrease in *N(0)V*. Similarly for the *Pr* system, we have a decrease in holes and hence *N(0)V*, but here, we have an increase in $-\mu_{eff}^*$. It is likely that the change in hole concentration will not only affect *N(0)V*, but the Coulomb repulsion, μ^*, as well. This would mean then that we would need a larger change in μ^* than in *N(0)V* to correctly account for the change in μ_{eff}^*. However, we have not considered how *V* changes with Δp_h, nor have we considered variations in the DOS with which an increase/decrease in Δp_h may change μ^* in a manner other than what we expect.

If the isotope shift were a constant, then it is possible that both the *Zn* and the *Pr* data could be fitted with one curve. In this case, the possible relationship between Δp_h and μ^*_{eff} would not exist as described above. A relationship between Δp_h and μ^*_{eff} could be established in this case if we considered only the magnitude of the shift in Δp_h from its 'optimum' value at the maximum T_c. In this case, however, we would have the same pair-breaking factor for both the *Pr* and the *Zn* data. Then the previous attempt to link the pair-breaking factors with the magnetic moments would fail.

In view of the fact that these Eliashberg calculations are successful in fitting our data, it appears that a relationship between the mobile hole

concentration and the Coulomb pseudopotential exists and in fact, is quite important. The role of the pair-breaking, due to magnetic impurities, is also an important factor. Ultimately, more of the details of the mechanism need to be considered before the relationship between μ^*_{eff} and $\Delta\rho_h$ can be established.

9.6 REMARKS ON THE MODELS

The relative success of the calculations based on the VHS in the density of states and, to an even greater extent, the use of the Eliashberg equations in modeling the isotope effect and the critical temperature indicates that some aspects of the BCS theory are still present within these high T_c superconductors. Basic to BCS theory is the electron-phonon interaction which we have shown has some influence, however small. Our results, and the relationship between T_c and α with $\Delta\rho_h$ indicate that it is more likely that an electron-electron interaction is the driving force behind the mechanism for high T_c superconductivity and any new theoretical model must take this into account. In view of the fact that even for the conventional superconductors with their relatively simple structure, modifications to the simple BCS theory are required to better describe these materials, it should not be too surprising that, because of the complexity of the structure of the high T_c superconductors, a complex mechanism will be required. The apparent relationship between the hole concentration and both T_c and α, as well as the similarity between our T_c data and the proposed 'Universal relationship between T_c and hole content', lead to the conclusion that this electron-electron interaction should be strongly linked to the presence of the charge carriers.

The large degree of anisotropy in the high T_c superconductors are of concern in these two models. The over-simplified VHS model takes this anisotropy to the extreme limit of a *2-D* system whereas the form of the Eliashberg equations employed here also assumes an extreme limit for these materials: that we are dealing with an isotropic *3-D* superconductor. Perhaps incorporating some of the *2-D* features of the VHS model, specifically those shown to be of importance in this research, into the Eliashberg equations could result in a more promising model that more correctly represents the anisotropy in the high T_c superconductors. Carbotte et al.[110,114] have done some preliminary Eliashberg calculations involving the VHS and a Lorentzian shaped peak in the DOS.

There is still some uncertainty as to whether or not a relationship between the width of the transition and the isotope shift exists. A number of our conclusions and speculations are significantly affected by whether or not ΔT_c is in fact a constant. As this uncertainty is believed to be tied to the sample quality, similar isotope measurements on high quality single crystals may help clear up whether this is so.

10 CONCLUSIONS

There does exist, in the high temperature superconducting systems of $(Y_{1-x}Pr_x)Ba_2Cu_3O_{7-\delta}$, $(Y_{0.8-y}Pr_{0.2}Ca_y)Ba_2Cu_3O_{7-\delta}$, and $YBa_2(Cu_{1-z}Zn_z)_3O_{7-\delta}$ an oxygen isotope effect. In all cases, the dc magnetization, the ac susceptibility and the dc resistive measurements show that the substitution of the heavier ^{18}O isotope for ^{16}O leads to a reduction in the critical temperature. For the *Pr* data, the isotope shift in T_c, ΔT_c, increases with increasing concentration; hence α also increases and at the highest concentration is approximately $^1/_2$. The *Zn* data has a relatively constant or perhaps even a slightly decreasing ΔT_c with increasing concentration. Consequently α increases to approximately $^1/_3$ as T_c drops.

The critical temperature and isotope coefficient were modeled using a modification to the BCS theory involving a logarithmic Van Hove singularity in the density of states. This model proved relatively successful in that it predicts the general trends found in our data: the small α at the highest T_c, and an increase in α as T_c drops. The range of change for α predicted is reasonable although the actual values are somewhat larger than observed. The response of the VHS model relies heavily on the parameter δ, the difference between the singularity in the DOS and the Fermi energy. The smaller δ becomes, the more the isotope shift is reduced. Thus this model indicates that the difference between the peak in the DOS and the Fermi energy is an important feature.

The Eliashberg approach proved even more successful in fitting the data. The theory requires the use of both a pair-breaking mechanism and an attractive (electronic) pairing interaction which is necessary to overcome the Coulomb repulsion in order to give a net attractive effective Coulomb pseudopotential.

The behaviour of this parameter μ_{eff}^* suggests that there exists a relationship between it and the mobile hole concentration, Δp_h, and hence, that both α and T_c are dependent on the change in mobile hole concentration.

There are still some questions and concerns with regard to the samples that will need to be addressed. Of primary interest are:

1). To improve the quality of our samples. Both the relationship between the width of the transition and the size of ΔT_c (or α) and the existence (in the measurements) of tails at low shielding are believed to be dependent on sample quality. A further investigation on high quality (single crystal?) samples will be required before we can be confident of the results of this oxygen isotope investigation.

2) The relationship between the mobile hole concentration and the elemental substitutions of *Pr, Ca,* and *Zn* needs to be clarified.

3) The role of an incomplete oxygen isotope substitution, with respect to the different oxygen sites, on the magnitude of α are also of concern.

4) The effects of field penetration on magnetic measurements of low T_c superconductors are an experimental concern when comparing the transitions to obtain ΔT_c.

From our Eliashberg calculation it appears that a joint mechanism is involved in high T_c superconductors. The existence of an isotope effect is evidence for an electron-phonon contribution to the mechanism. Our calculations suggest that at the optimal T_c, where the isotope coefficient is small, the mechanism is predominantly electronic in nature. As T_c drops, the electron-electron contribution becomes smaller, the electron-phonon interaction is emphasized and the isotope coefficient increases.

REFERENCES

[1] H. Kamerlingh Onnes, Leiden Comm., 124c (1911).

[2] W. Meissner and R. Ochsenfeld, Naturwissenschaften, **21**, 787 (1933).

[3] B.D. Josephson, Phys. Rev. Lett., **5**, 147,464 (1960).

[4] E. Maxwell, Phys. Rev., **78**, 477 (1950).

[5] C.A. Reynolds, B. Serin, W.H. Wright and L.B. Nesbitt, Phys. Rev., **78**, 487 (1950).

[6] J. Bardeen, L.N. Cooper and J.R. Schrieffer, Phys. Rev. **108**, 1175 (1957).

[7] J.J. Schooley, W.R. Hosler and M.L. Cohen, Phys. Rev. Lett., **12**, 474 (1964).

[8] J.R. Gavaler, Appl. Phys. Lett., **23**, 480 (1973).

[9] J.W. Garland Jr., Phys. Rev. Lett., **11**, 114 (1963); Phys. Rev., **153**, 460 (1964).

[10] J.C. Swihart, IBM J. Res. Dev., **6**,14 (1962).

[11] P. Morel and P.W. Anderson, Phys. Rev., **125**, 1263 (1962).

[12] G.M. Eliashberg, Sov. Phys. (JETP), **11**, 696 (1960).

[13] J.G. Bednorz and K.A. Müller, Z. Phys. B, **64**, 189 (1986).

[14] S. Uchida, H. Takagi, K. Kitazawa, S. Tanaka, Jpn. J. Appl. Phys. Lett., **26**, L1 (1987).

[15] C.W. Chu, P.H. Hor, R.L. Mong, L. Gao, Z.J. Huang and Y.Q. Wang, Phys. Rev. Lett., **58**, 405 (1987).

[16] R.J. Cava, R.B. van Dover, B. Batlogg and E.A. Rietman, Phys. Rev. Lett., **58**, 408 (1987).

[17] M.K. Wu, J.R. Ashburn, C.J. Torng, P.H. Hor, R.L. Meng, L. Gao, Z.J. Huang, Y.Q. Wang and C.W. Chu, Phys. Rev. Lett., **58**, 908 (1987).

[18] H. Maeda, Y. Tanaka, M. Fukutomi and T. Asano, Jpn. J. Appl. Phys., **27**, L209 (1988).

[19] Z.Z. Sheng and A.M. Hermann, Nature, **332**, 138 (1988).

[20] A. Schilling, M. Cantoni, J.D. Guo and H.R. Ott, Nature, **363**, 56 (1993).

[21] W.L. McMillan and J.M. Rowell, Superconductivity, Editor R.D. Parks, Dekker, New York, Vol. 1, 561-611 (1969).

[22] L.C. Bourne, M.F. Crommie, A. Zettl, H.C. zur Loye, S.W. Keller, K.L. Leary, A.M. Stacy, K.J. Chang, M.L. Cohen and D.E. Morris, Phys. Rev. Lett., **58**, 2337 (1987).

[23] T. Hidaka, T. Matsui and Y. Nakagawa, Jpn. J. Appl. Phys., **27**, L553 (1988).

[24] T. A. Faltens, W. K. Ham, S.W. Keller, K.J. Leary, J.N. Michaels, A.M. Stacy, H.C. zur Loye, D.E. Morris, T.W. Barbee III, L.C. Bourne, M.L. Cohen, S. Hoen and A. Zettl, Phys. Rev. Lett., **59**, 915 (1987).

[25] L. Quan, Y. Wei, Q. Yan, G. Chen, P. Zhang, Z. Shen, Y. Ni, Q. Yang, C. Liu, T. Ning, J. Zhao, Y. Shao, S. Han and J. Li, Solid State Comm., **65**, 869 (1988).

[26] B. Batlogg, R.J. Cava, A. Jayaraman, R.B. van Dover, G.A. Kourouklis, S. Sunshine, D.W. Murphy, L.W. Rupp, H.S. Chen, A. White, K.T. Short, A.M. Mujsce and E.A. Rietman, Phys. Rev. Lett., **58**, 2333 (1987).

[27] B. Batlogg, G. Kourouklis, W. Weber, R.J. Cava, A. Jayaraman, A.E. White, K.T. Short, L.W. Rupp and E.A. Rietman, Phys. Rev. Lett., **59**, 912 (1987).

[28] H.C. zur Loye, K.J. Leary, S.W. Keller, W.K. Ham, T.A. Faltens, J.N. Michaels and A.M. Stacy, Science, **238**, 1558 (1987).

[29] K.J. Leary, H.C. zur Loye, S.W. Keller, T.A. Faltens, W.K. Ham, J.N.Michaels and A.M. Stacy, Phys. Rev. Lett., **59**, 1236 (1987).

[30] D.E. Morris, R.M. Kuroda, A.G. Markeiz, J.H. Nickel and J.Y.T. Wei, Phys. Rev. B, **37**, 5936 (1988).

[31] S. Hoen, W.N.Creage, L.C. Bourne, M.F. Crommie, T.W. Barbee III, M.L. Cohen and A. Zettl, Phys. Rev. B, **39**, 2269 (1989).

[32] H. Katayama-Yoshida, T. Hirooka, A.J. Mascarenhas, Y. Okabe, T. Takahashi, T. Sasaki, A. Ochiai, T. Suzuki, J.I. Pankove, T.F. Ciszek and S.K. Deb, Jpn. J. Appl. Phys., **26**, L2085 (1987).

[33] H. Katayama-Yoshida, T. Hirooka, A. Oyamada, Y. Okabe, T. Takahashi, T. Sasaki, A. Ochiai, T. Suzuki, A.J. Mascarenhas, J.I. Pankove, T.F. Ciszek, S.K. Deb, R.B. Goldfarb and Y. Li, Physica C, **156**, 481 (1988).

[34] M.K. Crawford, M.N. Kunchur, S.J. Poon, Phys. Rev. B, **41**, 282 (1990).

[35] H.J. Bornemann and D.E. Morris, Phys. Rev. B, **44**, 5322 (1991).

[36] A. I. Kingon, S. Chevacharoenkul, S. Pejovnik, R. Velasquez, R. Porter, T. Hare and H. Palmour, High Temperature Superconducting Materials, editors W. E. Hatfield and J.H. Miller, Marcel Dekker Inc., New York, 327 (1988).

[37] C.C. Tsuei, Physica A, **168**, 238 (1990).

[38] J.S. Shier and D. M. Ginsberg, Phys. Rev., **147**, 384 (1966).

[39] P.P. Frietas, C.C. Tsuei and T.S. Plaskett, Phys. Rev. B, **36**, 833 (1987).

[40] B. Oh, K. Char, A.D. Kent, M. Naito, M.R. Beasley, T.H. Geballe, R.H. Hammond, A. Kapitulnik, J.M. Graybeal, Phys. Rev. B, **37**, 7861 (1988).

[41] D. Chen, J. A. Brug, and R. B. Goldfarb, IEEE Transactions on Magnetics, **27**, 3601 (1991).

[42] M. Denhoff, S. Gygax and J.R. Long, Cryogenics, **July**, 400 (1981).

[43] R.B. Goldfarb, M. Lental, C.A. Thompson, *Alternating-Field Susceptometry and Magnetic Susceptibility of Superconductors*, Magnetic Susceptibility of Superconductors and Other Spin Systems, editors R.A. Hein, T.L. Francavilla and D.H. Liebenberg, Plenum Press, New York, 49 (1992).

[44] J.D. Jorgensen, B.W. Veal, A.P. Paulikas, L.J. Nowicki, G.W. Crabtree, H. Claus and W.K. Kwok, Phys. Rev. B, **41**, 1863 (1990).

[45] Y. Ueda and K. Kosuge, Physica C, **156**, 281 (1988).

[46] R.J. Cava, B. Batlogg, C.H. Chen, E.A. Rietman, S.M. Zahurak and D. Werder, Phys. Rev. B, **36**, 5719 (1987); Nature, **329**, 423 (1987).

[47] F. Beech, S. Miraglia, A. Santoro and R.S. Roth, Phys. Rev. B, **35**, 8778 (1987).

[48] K.A. Müller, Z. Phys. B, **80**, 193 (1990).

[49] B.W Veal, A.P. Paulikas, H. You, H. Shi, Y. Fang and J.W. Downey, Phys. Rev. B, **42**, 6305 (1990).

[50] J.L. Tallon and N.E. Flower, Physica C, **204**, 237 (1993).

[51] J.P. Franck, J. Jung, G. Salomons, W.A. Miner, M.A.K. Mohamed, J. Chrzanowski, S. Gygax, J.C. Irwin, D.F. Mitchell and G.I. Sproule, Physica C, **172**, 90 (1990).

[52] K.C. Ott, J.L. Smith, J.O. Willis, R. M. Aikin, E. Garcia, M. Goldblatt, W.B. Hutchinson, G.H. Kwei, C.B. Pierce, J.F. Smith, J.D. Thompson and T.E. Walker, Los Alamos National Laboratory, unpublished work, (1988).

[53] P.J. Yvon, R.B. Schwarz, C.B. Pierce, L. Bernardez, A. Connor and R. Meisenheimer, Phys. Rev. B, **39**, 6690 (1989).

[54] P.H. Hor, R.L. Meng, Y.Q. Wang, L. Gao, Z.J. Huang, J. Bechtold, K. Rorster and C.W. Chu, Phys. Rev. Lett., **58**, 1891 (1987).

[55] M.B. Maple, Y. Dalichaouch, J.M. Ferreira, R.R. Hake, B.W. Lee, J.J. Neumeier, M.S. Torikachvili, K.N. Yang and H. Zhou,Physica B, **148**, 155 (1987).

[56] Y. Dalichaouch, M.S. Torikachvili, E.A. Early, B.W. Lee, C.L. Seaman, K.N. Yang, H. Zhou and M.B. Maple, Solid State Comm., **65**, 1001 (1988).

[57] J.Peng, Phys. Rev. B, **40**, 4517 (1989).

[58] L. Soderholm, K. Zhang, D.G. Hinks, M.A. Beno, J.D. Jorgensen, C.U. Segre and Ivan K. Schuller, Nature, **328**, 604 (1987).

[59] J.J. Neumeier, T. Bjornholm, M.B. Maple and I.K. Schuller, Phys. Rev. Lett., **63**, 2516 (1989).

[60] A. Matsuda,K. Kinoshita, T. Ishii, H. Shibata, T. Watanabe and T. Yamada, Phys. Rev. B, **38**, 2910 (1988).

[61] E.E. Alp, G.K. Shenoy, L. Soderholm, G.L. Goodman, D.G. Hinks and B.W. Veal, Mater. Res. Soc. Symp. Proc., **99**, 177 (1988).

[62] J. Fink, N. Nücker, H. Romberg, M. Alexander, M.B. Maple, J.J. Neumeier and J. W. Allen, Phys. Rev. B, **42**, 4823 (1990).

[63] In-Sang Yang, A.G. Schrott and C.C. Tsuei, Phys. Rev. B, **41**, 8921 (1990).

[64] In-Sang Yang, G. Burns, F.H. Dacol and C.C. Tsuei, Phys. Rev. B, **42**, 4240 (1990).

[65] F.W. Lytle, Phys. Rev. B, **41**, 8955 (1990).

[66] R.Fehrenbacher and T.M. Rice, Phys. Rev. Lett., **70**, 3471 (1993).

[67] B. Jayaram, S.K. Agarwal, C. V. Rarasimaha Rao and A.V. Narlikar, Phys. Rev. B, **38**, 2903 (1988).

[68] G. Xiao, M.Z. Cieplak, D. Musser, A. Gavrin, F.H. Streitz, C.L. Chien, J.J. Rhyne and J. A. Gotaas, Nature, **332**, 238 (1988).

[69] G. Xiao, M.Z. Cieplak, A. Gavrin, F.H. Streitz, A. Bakhshai and C.L. Chien, Phys. Rev. Lett., **60**, 1446 (1988).

[70] M. Mehbod, W. Biberacher, A. G. M. Jansen and P. Wyder, Phys. Rev. B, **38**, 11813 (1988).

[71] M. Affronte, D. Pavuna, O. Martin, F. Licci, T. Besagni, S. Cattni, Solid State Comm., **70**, 951 (1989).

[72] T. Kajitani, K. Kusaba, M. Kikuchi, Y. Syono and M. Hirabayashi, Jap. J. of App. Phys., **27**, L354 (1988).

[73] G. Xiao, M.Z. Cieplak, J.Q. Xiao and C.L. Chien, Phys. Rev. B, **42**, 8752 (1990).

[74] H. Alloul, P. Mendels, H. Casalta, J.F. Marucco and J. Arabski, Phys. Rev. Lett., **67**, 3140 (1991).

[75] M.W. Shafer, T. Penney, B.L. Olson, R.L. Greene and R.H. Koch, Phys. Rev. B, **39**, 2914 (1989).

[76] Y. Tokura, J.B. Torrance, T.C. Huang and A.I. Nazzal, Phys. Rev. B, **38**, 7156 (1988).

[77] K.C. Ott, R.M. Aikin, L. Bernardez, A. Connor, M.J. Fluss, E. Garcia, M. Goldblatt, W.B. Hutchinson, G.H. Kwei, C.J. Maggiore, J.A. Martin, R. Meisenheimer, M. Nastasi, Eric J. Peterson, Eugene J. Peterson, C. B. Pierce, R. B. Schwarz, J.F. Smith, J.L. Smith, J.R. Tesmer, T.E. Walker, J.O. Willis and P.J. Yvon, Phys. Rev. B **39**, 4285 (1989).

[78] QTC Cryocooler 4.K, Quantum Technology Corporation, Surrey, British Columbia.

[79] M. Cardona, R. Liu, C. Thomsen, W. Kress, E. Schönherr, M. Bauer, L. Genzel and W. König, Solid State Commun. **67**, 789 (1988).

[80] C. Thomsen, Solid State Commun. **65**, 55 (1988).

[81] J.C. Irwin, J. Chrzanowski, E. Altendorf, J.P. Franck and J. Jung, J. Mater. Res., **5**, 2780 (1990).

[82] E.J. Nicol and J.P. Carbotte, Phys. Rev. B, **44**, 12511 (1991).

[83] J.P. Carbotte, M. Greeson and A. Perez-Gonzalez, Phys. Rev. Lett., **66**, 1789 (1991).

[84] C.C. Tsuei, D.M. Newns, C.C. Chi and P.C. Pattnaik, Phys. Rev. Lett., **65**, 2724 (1990).

[85] E. Schachinger, M.Greeson and J.P. Carbotte, Phys. Rev. B, **42**, 406 (1990).

[86] R.D. Parks, Superconductivity Volumes 1 & 2, Marcel Dekker, Inc., New York (1969).

[87] E. Lynton, E. A., Superconductivity, John Wiley & Sons Inc. (1962).

[88] J.W. Lynn, High Temperature Superconductivity, Springer-Verlag, New York (1990).

[89] W.E. Hatfield, J.H. Miller Jr., High-Temperature Superconducting Materials, Marcel Dekker Inc., New York (1988).

[90] V.D. Hunt, Superconductivity Sourcebook, John Wiley & Sons Inc., (1989).

[91] J.C. Phillips, Physics of High-Tc Superconductors, Academic Press Inc., San Diego (1989).

[92] R.S. Markiewicz and B.G. Giessen, Physica C, **160**, 497 (1989).

[93] R.S. Markiewicz, J. Phys. Cond. Matt., **1**, 8911 (1989).

[94] R.S. Markiewicz, J. Phys. Cond. Matt., **1**, 8931 (1989).

[95] R.S. Markiewicz, Physica B, **165 & 166**, 1053 (1990).

[96] R.S. Markiewicz, J. Phys. Cond. Matt., **2**, 665 (1990).

[97] G. Grimvall, The Electron-Phonon Interaction in Metals, North Holland, Amsterdam (1981).

[98] R. Akis, Some Applications of Eliashberg Theory, PhD Thesis, McMaster University (1991).

[99] J.P. Carbotte, Rev. Mod. Phys., **62**, 1027 (1990).

[100] R. Meservey and B.B. Schwartz. Superconductivity. Marcel Dekker, Inc. New York. editor R.D. Parks., 126 (1969).

[101] L. Van Hove, Phys. Rev., **89**, 1189 (1953).

[102] J.E. Hirsch and D.J. Scalapino, Phys. Rev. Lett., **56**, 2732 (1986).

[103] L. Mattheiss, Phys. Rev. Lett., **58**, 1058 (1987).

[104] J.H. Xu, T.J. Watson-Yang,J. Yu and A.J. Freeman, Phys. Lett. A, **120**, 489 (1987).

[105] D.M. Newns, P.C. Pattnaik, and C.C. Tsuei, Phys. Rev. B, **43**, 3075 (1991).

[106]C.C. Tsuei, C.C. Chi, D.M. Newns, P.C. Pattnaik, and M. Daumling, Phys. Rev. Lett., **69**, 2134 (1992).

[107]D.M. Newns, H.R. Krishnamurthy, P.C. Pattnaik, C.C. Tsuei, and C.L. Kane, Phys. Rev. Lett., **69**, 1264 (1992).

[108]R. Combescot, Phys. Rev. Lett., **68**, 1089 (1992).

[109]D.Y. Xing, M. Liu, and C.D. Gong, Phys. Rev. Lett., 1090 (1992).

[110]J.P. Carbotte, Proceedings of the First Cinvestav-Superconductivity Symposium, editor R. Baquero, World Scientific, Singapore, 98 (1991).

[111]P.B. Allen and R.C. Dynes, Phys. Rev. B, **12** , 905 (1975).

[112]W.L. McMillan, Phys. Rev., **167**, 33 (1968).

[113]W.L. McMillan and J.M. Rowell, Phys. Rev. Lett., **14**, 108 (1965).

[114]J.P. Carbotte and R. Akis, Solid State Comm., **82**, 613 (1992).

[115]J.P. Carbotte and E.J. Nicol, *Isotope Effect and Electronic Mechanisms*, Proceedings of the Conference on Lattice Effects in High-Tc Superconductors, editors Y.Bar-Yam, T. Egami, J. Mustre-de Leon and A.R. Bishop, World Scientific, Singapore, 189 (1992).

[116]M. Gurvitch and A.T. Fiory, Phys. Rev. Lett., **59**, 1337 (1987).

[117]W. Weber, Phys. Rev. Lett., **58**, 1371, 2154 (1987).

[118]M.S. Caceci and W.P. Cacheris, Byte, **May**, 340 (1984).

[119]E. Altendorf, J. Chrzanowski, J.C. Irwin and J. Franck, Solid State Comm., **76**, 391 (1990).

[120]A.R. Bishop, R.L. Martin, K.A. Müller and Z. Tesanovic, Z. Phys. B, **76**, 17 (1989).

[121]H. Zhang and H. Sato, Phys. Rev. Lett., **70**, 1697, (1993).

[122]M. Tinkham, Introduction to Superconductivity, McGraw-Hill, New York, 267 (1975).